
Dynamic structural colour in thin film stacks and patterned nanoparticle arrays

A PhD Thesis

by:

Keith Mark Wilson

Supervisor:

Prof. Louise Bradley



School of Physics

Trinity College Dublin

2018

Declaration

I declare that this thesis has not been submitted as an exercise for a degree at this or any other university and it is entirely my own work with the exception of assistance and collaboration recognised in the acknowledgements and throughout the thesis where applicable.

I agree to deposit this thesis in the University's open access institutional repository or allow the library to do so on my behalf, subject to Irish Copyright Legislation and Trinity College Library conditions of use and acknowledgement.

I have read and I understand the plagiarism provisions in the General Regulations of the University Calendar for the current year, found at <http://www.tcd.ie/calendar>.

I have also completed the Online Tutorial on avoiding plagiarism "Ready Steady Write", located at <http://tcd-ie.libguides.com/plagiarism/ready-steady-write>.

Keith Wilson

Abstract

In this thesis a number of metal nanostructures have been investigated for structural colour at sub-micron scales. These structures have utilised localised surface plasmon resonance (LSPR) to produce near-field interactions between components, generating sharp spectral features in reflectance. The use of phase change materials (PCMs) have also been investigated, for dynamic tuning of colour after fabrication of the structures, with a view towards display applications.

An aluminium nanodisc-nanohole array structure is explored for colour generation in reflection. The structure consists of a square dielectric pillar array, with aluminium coating the top of the pillar and the backreflector to produce the disc and hole components. Simulation is carried out by the finite-difference time-domain (FDTD) method, with varying geometry parameters to determine the colour gamut of the structure. The strong LSPR of the disc and hole interact in a Fano resonance condition, resulting in sharp spectral features in the visible region. A 5 mm square array with 400 nm pitch and 200 nm diameter pillars have been fabricated by electron beam lithography (EBL), with close correlation between simulated and measured spectra. A diffraction effect has been observed, following a first order diffraction profile with grating constant of 400 nm, consistent with this sample. The limited viewing angle presented by this structure leads research towards alternative materials, capable of colour generation at smaller dimensions.

A hybrid metal nanostructure consisting of Au discs on a polymer thin film and Ag backreflector has been investigated for vibrant structural colour in reflectance with a minimal unit cell size. The structure benefits from the strong LSPR of Au nanodiscs, high reflectivity of Ag and the optical cavity produced by the transparent polymer layer generating a strong Fano resonance that results in near-zero reflection in a narrow wavelength range. A cyclical colour trend is observed as polymer layer thickness is varied, with a repetition periodicity every 180 nm thickness change. The dependency of optical path length in the polymer, and material component composition on the colour produced is examined. Arrays

measuring $100 \times 100 \mu\text{m}$, of 150 nm diameter discs with a 300 nm pitch have been fabricated using EBL. Assessment of the polymer film by ellipsometry revealed that the fabrication process caused negligible damage, and good agreement is found between arrays simulated by FDTD and those fabricated.

A thin film stack consisting of layers of Indium Tin Oxide (ITO) with an intermediate Vanadium Oxide (VO_2) layer with an Ag backreflector is explored for dynamic structural colour. Compared with other phase change materials (PCMs), such as Germanium Antimony Telluride (GST), VO_2 can be considered as a lower power consumption alternative. It has been overlooked in the visible region, due to its smaller refractive index change below 700 nm . The sensitivity of the visible reflectance spectrum to the change in phase of a 30 nm VO_2 layer is shown to increase after it is incorporated in a thin film stack, with comparable performance other phase change materials. An improved maximum ΔR is observed, with 20% recorded in structures containing GeSbTe (GST) and AgInSbTe (AIST) increasing to 30% in a 10-30-25-100 nm ITO- VO_2 -ITO-Ag thin film stack. CIE separation is also shown to increase in this VO_2 stack configuration. Inclusion of a top ITO layer is also shown to improve the chromaticity change on phase transition.

Finally, these VO_2 thin films have been combined with Au nanoparticle arrays. Several nanoparticle shapes have been investigated, in positions on-top of the VO_2 layer, and imbedded within it, to determine colour change potential of a combined nanostructure architecture. Change in reflectance of the thin film VO_2 stack, as well as the modification LSPR response of the disc component as the surrounding media is altered, combine to increase the colour change of the overall structure. Imbedded particles are shown to result in the decrease of the maximum ΔR to 20%. However, this architecture results in the largest separation in CIE values of any architecture examined, with particle shape having little impact on the colour change observed.

Acknowledgements

First and foremost, I would like to thank my supervisor, **Prof. Louise Bradley** for the opportunity to undertake my PhD in her research group. Her advice and encouragement has been invaluable to my completion of this undertaking.

I would also like to thank the members of the research group, with whom I have spent much of my time working with over the last few years. In particular **Dr. Cristian Marocico**, who has been mentored me in theory and simulation a great deal throughout the project, even after departure from the group.

I would also like to thank **John Gough**, a great friend and colleague, that has been instrumental to my success in the lab. My thanks also go to the other members of the group, **Graham Murphy, Luke Higgins, Vasilios Karanikolas, Jorge Garcia**, and **Xia Zhang** for their very helpful discussions.

Thanks are in order for the members of the wider research group, in particular **Brian Jennings, David McCloskey**, and **Chris Smith** for their expertise in the lab when issues arose. I must also thank **Allan Bell**, for his excellent training and help in fabrications of samples throughout the first two years.

My thanks to the extremely helpful and infinitely patient technicians in the workshop **Dave Grouse** and **Pat Murphy** for all the contraptions, and the ever wise and helpful IT wizards **Ken Concannon** and **Alan O'Meara**.

My friends, who have helped me get through the stressful patches.

A very special acknowledgement to my parents **Mark** and **Karen**, and sister **Claire**, who have always been supportive and encouraging in all my studies, and have helped me so much in this endeavour.

Finally, to my girlfriend **Gloria**, for putting up with me and supporting me through sleepless nights, and grumpy days.

List of Publications and Conference contributions

Publications

1. Graham P Murphy, John J. Gough, Luke J. Higgins, Vasilios D. Karanikolas, **Keith M. Wilson**, and A Louise Bradley, "Ag colloids and arrays for plasmonic non-radiative energy transfer from quantum dots to a quantum well", *Nanotechnology* 28(11), 115401 (2017).
2. **Keith M. Wilson**, Cristian A. Marocico, and A. Louise Bradley, "Dynamic structural colour using Vanadium Dioxide thin films", *J. Phys. D. Appl. Phys.* 51(25), 2018.
3. **Keith M. Wilson**, Cristian A. Marocico, Chris Smith, and A. Louise Bradley, "Hybrid metal nanostructure arrays for colour printing", Manuscript submitted, *Nanoscale*, August 2018.
4. **Keith M. Wilson**, Cristian A. Marocico, Esteban Pedreuzza, and A. Louise Bradley, "Angular diffractive effects and structural colour in aluminium plasmonic nanopillar array", Manuscript in preparation, 2018.

Conference contributions

1. **Keith M. Wilson** and A. Louise Bradley. "Dynamic structural colour using Vanadium dioxide thin films". Photonics Ireland 2017. 13th-15th September 2017, Galway, Ireland. (Poster)
2. **Keith M. Wilson**, Cristian A. Marocico, Esteban Pedreuzza, Chris Smith, and A. Louise Bradley. "Hybrid metal nanostructure arrays for colour printing". ICTON 2016. 10nd-14th July 2016, Trento, Italy. (Oral presentation)
3. **Keith M. Wilson**, Cristian A. Marocico, and A. Louise Bradley. "Design of metallic nanostructured arrays for display applications". Photonics Ireland 2015. 2nd-4th September 2015, Cork, Ireland. (Poster)

Contents

Declaration	i
Abstract.....	iii
Acknowledgements.....	v
List of Publications and Conference contributions.....	vi
Contents	vii
1 Motivation	1
2 Background	13
2.1 Thin films	14
2.1.1 Interference.....	14
2.1.2 Absorption.....	16
2.1.3 Phase Change Materials	19
2.2 Plasmons.....	22
2.2.2 Surface Plasmon Polaritons	23
2.2.3 Localised Surface Plasmon Resonance	26
2.3 Fano resonance	30
2.4 Array effects.....	32
2.4.1 Diffraction.....	32
2.5 Colour theory.....	34
2.5.1 CYMK.....	35
2.5.2 RGB.....	36
2.5.3 CIE	38
2.6 Conclusion	40
3 Methods	41

3.1	Simulation	42
3.1.1	Transfer Matrix Method	42
3.1.2	Finite Difference Time Domain	45
3.1.3	Discrete Dipole.....	51
3.1.4	Refractive Index information	52
3.1.5	Colour conversion of spectra to sRGB and CIE xyY	52
3.2	Fabrication.....	56
3.2.1	Lithography	57
3.2.2	Resists and Development	60
3.2.3	Material Deposition.....	61
3.3	Characterisation.....	62
3.3.1	Structural parameters.....	62
3.3.2	Normal incidence measurements.....	63
3.3.3	Angular measurements	65
3.4	Conclusion.....	66
4	Aluminium Nanostructure	67
4.1	Simulation	67
4.1.1	Validation	69
4.1.2	Al nanostructured array	72
4.1.3	Geometries.....	81
4.2	Experimental.....	89
4.2.1	Fabrication	89
4.2.2	Characterisation.....	90
4.2.3	Diffraction effects.....	94
4.3	Conclusion.....	99

5 Hybrid Nanostructure	101
5.1 Simulation	102
5.1.1 Hybrid nanostructure array	103
5.1.2 Geometries.....	113
5.1.3 Material Composition	121
5.2 Experimental.....	124
5.2.1 Fabrication	124
5.2.2 Characterisation.....	126
5.3 Conclusion	131
6 VO₂ thin films.....	133
6.1 Simulation	134
6.1.1 AIST and GST structures.....	134
6.1.2 Vanadium Oxide thin films	139
6.1.3 ITO-VO ₂ -ITO stacks	142
6.1.4 VO ₂ Thickness	145
6.1.5 Impact of the ITO top contact.....	148
6.2 Conclusion	151
7 Metal nanoparticle-VO₂ structures	153
7.1 Simulation	154
7.1.1 Hybrid structure with VO ₂ layer.....	155
7.1.2 Discs on VO ₂	160
7.1.3 Particle shapes on VO ₂	163
7.1.4 Discs imbedded in VO ₂	170
7.1.5 Particle shapes imbedded in VO ₂	175
7.2 Conclusion	179

8 Conclusion.....181

 Summary.....181

 Outlook.....185

Appendix A187

Appendix B.....195

Appendix C.....197

References.....211

Chapter 1

Motivation

The human eye is a wonder of nature that grants the most information-packed sense of all; colour vision. Over the past 30 years, huge leaps have been made in display technology, from the very earliest in the form of cathode ray tubes (CRTs) [1], to the incredibly high resolution and high contrast organic light emitting diode (OLED)[2] displays. With the advent of mobile devices that are becoming more powerful and power-hungry, the battery technology that powers these devices struggles to keep up[3]. Focus has shifted towards low-power display technology for mobile phones and tablets, as developments are made to provide lower cost alternatives to the active displays used across most technologies. The implementation of passive displays is in its infancy[4], with much improvement required before widespread adoption of these systems can be achieved.

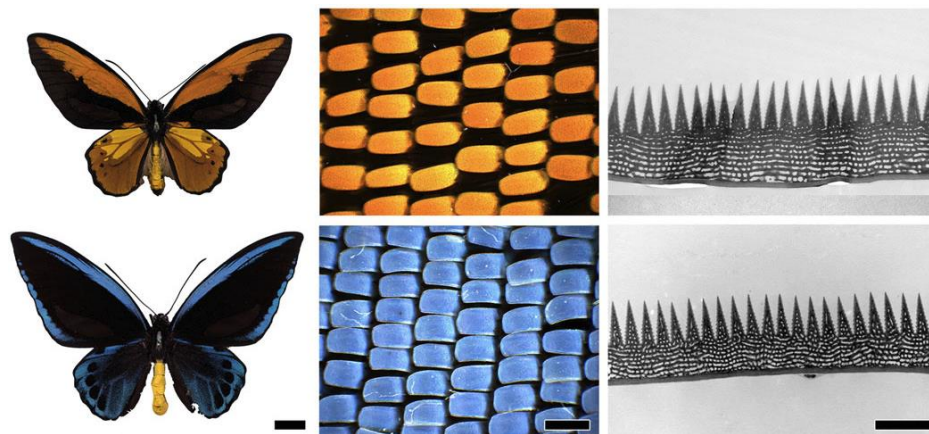


Figure 1.1: Butterfly wings exhibiting structural colour due to the dimensions of the chitinous ridges on the wing surface. For species (a) *Ornithoptera Croesus*, and (b) *Ornithoptera priamus*.

Structural colour is a phenomenon that utilises resonances produced by the physical dimensions of a structure to generate colour. It has been demonstrated as a feasible method for colour generation, with increased interest over traditional colouring methods, such as molecular dyes and pigments. Dyes and pigments generate colour

by light absorption in the molecular bonds for certain bands of the visible region, as seen in Figure 1.2. Structural colour allows for the printing of colour at and below the optical diffraction limit[5–7], without the use of dyes/pigments.

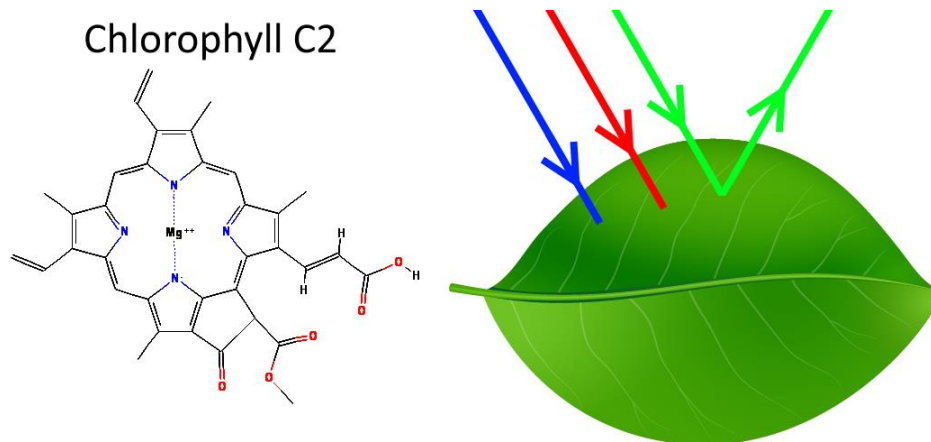


Figure 1.2: (a) Chlorophyll C2 molecule commonly found in plants. (b) Leaf absorbing red and blue wavelength regions, reflecting green light.

This technology is becoming more attractive commercially, as improvements to lithographic processes[8,9] become more widely available and scalable. Structural colour has been demonstrated in randomly distributed nanoparticle[10], and lithographically patterned nanostructures[6,11,12]. These metallic nanostructures have a number of advantages over dielectric structures, such as narrow spectral features, and smaller geometry requirements. The primary advantages of metallic structural colour technologies over traditional dye-based colour generation methods are that these nanostructure architectures are resistant to photo-bleaching[4], exhibit high robustness to physical stresses[13], the colour response of the structure can be generated at sub-diffraction dimensions[5–7]. Sub-diffraction limit nanostructures can generate structural colour by manipulating light on the nano-scale.

More recently, there has been interest in developing methods to tune their properties after fabrication by altering geometric parameters[14,15], and in this thesis the use of phase change materials (PCMs) to alter the refractive index of media surrounding plasmonic components is explored. PCMs can be altered by thermal[16,17] or electrostatic means[18,19], with potential for device applications.

These aspects indicate that metal nanostructures can be a viable technology to be used in future devices, in areas such as colour printing[11,20], holograms[21,22], display technology[23], as well as surface enhanced Raman scattering (SERS)[24], and anti-counterfeit measures[25] due to the difficulty in recreating nanostructured devices, and the particular spectral response they generate.

Thin film structures are applied across the field of optics for anti-reflection coatings, high reflection mirrors and optical filters. These structures can be as simple as a couple of layers of different materials or complex multi-layer aperiodic stacks. There are many examples of thin film structures producing vibrant structural colour across the visible wavelength range[26,27]. These structures exploit the interference of electromagnetic waves reflected at the interfaces. Traditionally, structures have been fabricated using lossless materials[28] to exploit the interference effect, though investigations have been carried out with highly absorbing materials[27,29]. Designs for high reflectance structures often incorporate a back metallic film[26]. More recently, very simple structures formed using a few nanometre thick highly absorbing layer of Ge deposited on an optically thick Au layer have been considered for coloured optical coatings[26]. It was shown that for a sufficiently thin Ge film interference effects could persist, and the desired reflected colour can be selected by varying the thickness of the ultrathin Ge layer, as shown in Figure 1.3.

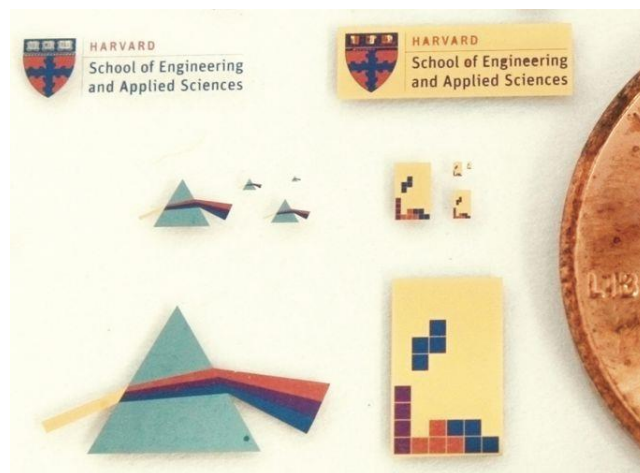


Figure 1.3: Nanometre optical coatings based on strong interference effects in highly absorbing media[26]. Structural colour, with variation achieved by changing Ge thickness.

Thin film stack structures capable of structural colour have been demonstrated by the formation of optical cavities in metal-insulator-metal (MIM) thin film stacks[30], with strong interference effects causing particular wavelengths to be constructively and destructively interfered, resulting in portions of the visible region being selectively reflected back to the observer. Other structures have utilised highly absorbing materials[26] to absorb certain wavelength ranges of the visible region, and produce coloured films with much thinner materials. However, these structures are material limited, and colours palettes are often incomplete as a product of restricted variables available that determine the colour produced. As illustrated in Figure 1.4, randomly distributed nanoparticle arrays have been demonstrated as strong colour filters[10], while maintaining ease of fabrication due to simple techniques of deposition. However, these materials are limited by the random distribution of nanoparticles resulting in broad resonance features, and so colour clarity of the structures is low.

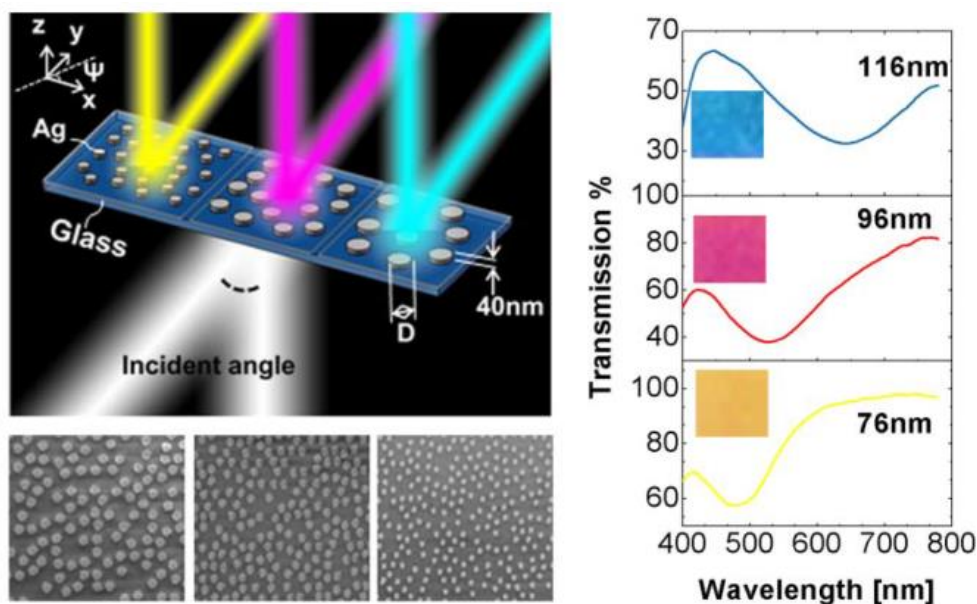


Figure 1.4: Angle-insensitive plasmonic color filters with randomly distributed silver nanodiscs[10]. This structure consists of randomly distributed Ag nanodiscs of different sizes on a SiO₂ substrate.

Patterned nanostructures hold particular interest in colour generation, as they can produce strong, sharp spectral features, due to narrow LSPR features formed by uniform shaped and spaced nanoparticles in an array configuration. This is

particularly apparent with noble metals, which produce strong plasmon responses[31,32]. Though it is important when utilising materials such as Ag, that encapsulation occurs immediately after Ag deposition to prevent tarnishing[33]. MIM nanoparticle arrays have been extensively studied in the Near-IR[34,35], though they consist of a single metal composition in both the nanoparticle array and backreflector components. Such structures have also been shown produced varied colour palettes, with uniform arrays of nanoparticles[6,20], mixed unit cells[11] to improve control over the colours produced, and non-circular particles to induce polarisation dependencies[12,36,37]. Though these structures hold difficulties in scalability to a mass production, progress has been made in recent years in nanoimprint lithography (NIL)[38,39], and in extreme ultraviolet lithography (EUV)[8], with wavelengths in the range of 10-14 nm facilitating the production of sub-diffraction limited geometries optically.

While many plasmonic nanostructures have focused on the use of noble metals such as Ag and Au, recent efforts in the use of aluminium have been attention of more intensive research efforts[40]. Aluminium is a low cost alternative to noble metals, and exhibits plasmon resonance responses in the UV-visible[41]. Al also maintains a 3 nm thick self-terminating oxide layer[42], which is due to the low ionic and electronic conductivity of Al, and stops further oxidation deeper into the layer[43]. This was included in the simulations of the structure. The layer can further be modified with an anodizing procedure, to generate thicker layers of oxide material[44]. This oxide layer has been the highlighted for its influence on the LSPR[42,45,46], and studies have been carried out into Al nanoparticle geometries[47], including spheroidal[41], triangular[48], disks[4] and rods[49,50]. It has also been utilised as a backreflector material in colour generation studies[11,12,51,52]. Aluminium plasmonic metasurfaces are used on the cutting edge in the control of light phase and polarization to generate holograms[53], colour filtering[51,54], directional couplers[55], polarizers[56], and sensor[57] technology, among others. Regarding angular dependence of colour generation in Al plasmonic

arrays, there has been some investigation. In the work by Clausen *et al.*[58], the plasmon resonance hybridization resulting of disk/hole coupled plasmonic modes has a major impact in the reflectance spectra. In the work by Duempelmann *et al.*[59], Al nanowires in a grating substrate generate plasmonic modes, that interact with surface plasmons to generate angular dependent colour.

The ability to electrically tune the response of a thin film stack is of interest for a wide range of applications such as dynamic optical components and colour tuning for displays. This has driven interest in the incorporation of phase change materials (PCMs)[60,61] within thin film stacks, and dynamic spectral tuning of the reflectance or transmittance of thin film interference stacks has been demonstrated[62,63]. The complex refractive index of PCMs is modified as it transitions from one phase state to another[16,18,64,65]. Chalcogenide-based PCMs such as GeSbTe (GST)[18,66,67] and AgInSbTe (AIST)[68–71] are materials with two stable phases, and have been previously explored for colour switching devices[72,73], and phase change memory cells for computing[67,68,74]. PCMs have been widely used in re-writable memory applications[74] such as the DVD format[75]. GST and AIST exhibit bi-stability; a permanent state will persist until a stimulus is applied to reverse the phase change[72]. The materials also exhibit high switching rates[72], on the order of several nanoseconds. Few nanometre thick layers of AIST or GST layer have been sandwiched between two layers of indium tin oxide (ITO), a transparent electrode, for colour generation based on reflective or semi-transparent structures. Bi-stable colour switching in the visible wavelength range as the material changes from the amorphous to crystalline state has been demonstrated[72,73,76].

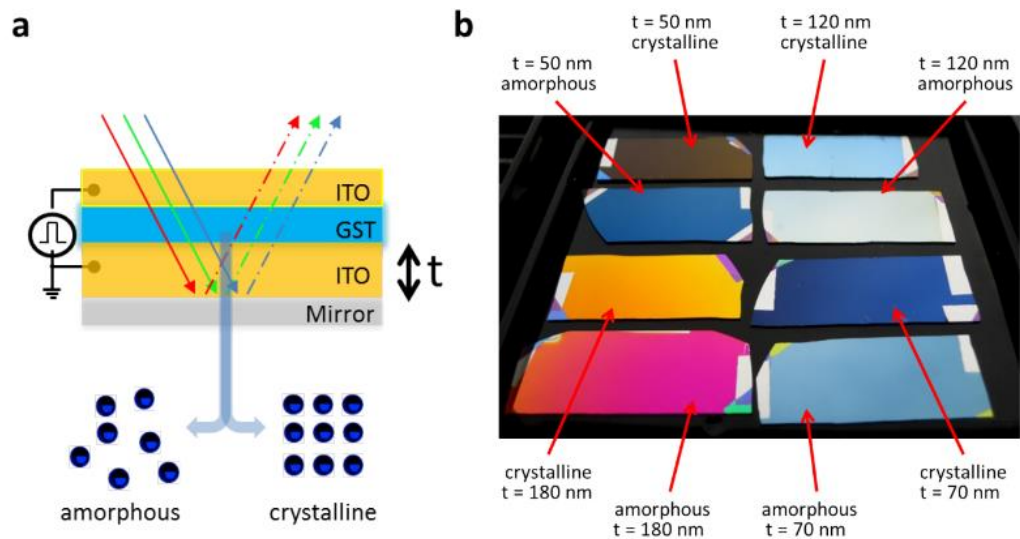


Figure 1.5: An optoelectronic framework enabled by low-dimensional phase-change films[72]. This structure consists a GST thin layer between two layers of ITO, with a Pt backreflector. Colour change is induced upon phase transition of the GST.

While these materials offer many advantages, they pose toxicity concerns[77] and, due to their high absorption, very thin layers are required. For example, in the case of GST layers as thin as 7 nm are required, introducing difficulties for the uniform fabrication of such ultra-thin layers[72].

VO₂ is another PCM which can be considered. VO₂ transitions from a low temperature semiconducting monoclinic phase to a high temperature rutile metallic phase at 68°C[17], significantly lower than the 170°C and 145°C required for AIST[62] and GST[67], respectively. This phase transition can be achieved by heating[16] or it can be electrically triggered[18] with lower power consumption than for AIST or GST. Studies have been carried out into the mechanism of electrically switching the VO₂ phase[78–80], with field thresholds on the order of 10⁷ V/m[79,81], and steady state switching has been demonstrated with an applied DC voltage[19]. Furthermore, its lower absorption allows for thicker layers, overcoming one of the fabrication difficulties associated with ultra-thin GST layers[72]. In summary, VO₂ can potentially offer lower toxicity[82], less stringent fabrication constraints[72] and lower power consumption[17], while providing stable, reversible and electrically activated tuning[83].

The refractive index change of VO₂ is greatest in the infra-red and microwave spectral ranges, which has motivated extensive studies using VO₂ for applications in IR waveguides[19,84,85], optical communications[83,86,87], IR sensing[88,89], and many THz applications[84,90,91]. It has also been widely studied for thermochromic windows[92] and, more recently, has been attracting renewed interest for tunable metasurfaces in the IR[93–95]. An ultra-thin layer of VO₂ on a sapphire substrate has been used to demonstrate a thermally tunable perfect absorber in the IR[96]. The material exhibits a smaller but still significant complex refractive index change in the range below 700 nm[17]. The phase transition produces a maximum change of 60% in n and of 20% in κ across the visible spectral range. While, this is lower than that of other PCMs, such as GST with a maximum change of 100% in n and 250% in κ over the same spectral range, the advantages of VO₂ described above warrant consideration of its potential for applications in the visible wavelength region. A previous study of VO₂ layers of varying thickness deposited on quartz showed that in the visible region the transmittance of the semiconductor phase is generally lower than that of the metallic phase for film thicknesses less than 35 nm but for thicker films the transmittance of the insulating phase is greater, arising from interference effects[97]. However, this study considered only a single layer of VO₂ on a substrate. Increased sensitivity to the refractive index change in a VO₂ layer over the visible range can potentially be increased by using multilayer structures comprised of transparent dielectric materials and VO₂ layers on a reflective back-reflector. In this thesis, the extent to which the tuning of the reflectance spectra can be exploited for colour switching is investigated.

Recently, developments have been made in the incorporation of nanoparticles to PCM structures in order to benefit from the strong interaction of plasmonic components to the incident field. The sensitivity of the LSPR in nanoparticles to the refractive index of the surrounding media[98,99] creates potential for large changes in reflectance between phases of the PCM. Chalcogenide based PCMs have been

utilised extensively in these nanoparticle systems[100], with significant alteration of the LSPR observed in the visible[101,102]. Applications of these structures in the visible region have focused on light harvesting[16,102] and sensing[18] applications. In the case of VO₂-nanoparticle systems, colour generation[103] and sensing in the visible[104] have been investigated. However, research has focused on the large refractive index change of VO₂ in the IR region[105–107], with often limited change observed in the visible when included. For this reason, many efforts with nanoparticle arrays have been in the IR[108]; in memory[109], optical switches[110–112], and sensing[113]. Patterning on-top of VO₂ with e-beam lithography[103,111] has been achieved without damage of the crystalline structure. In brief, this thesis investigates a number of nanostructures in the generation of structural colour, with an emphasis on dynamic colour in later chapters. The plasmonic architectures under consideration include a low-cost Aluminium-based nanodisc array structure, as well as a hybrid Au-Ag structure that constitutes a smaller footprint, both of which are capable of producing vibrant colour in reflection. VO₂ PCM structures are first introduced in a thin film stack design, with the goal of maximising the sensitivity of the VO₂ in the visible. Finally, nanoparticles are incorporated into the structure to avail of the sensitive LSPR phenomenon. In this way, dynamic structural colour is achievable after fabrication of the nanostructures.

Chapter 2 of the thesis will introduce the relevant topics of the research carried out. These include the concepts of thin film interference, and absorption, plasmons, as well as array effects, such as diffraction. The physics associated with both surface plasmon polaritons (SPP) and localised surface plasmon resonance (LSPR) are briefly explained, as well as a discussion of Fano resonance. The role of phase change materials (PCM) to the dynamic nature of the nanostructures are outlined. Finally, colour theory and colour models most often used by different industries are also introduced, with particular attention to the additive RGB colour model, as it is extensively utilised throughout the thesis.

The methods of simulation, fabrication, and characterisation will be the focus of **Chapter 3**. In particular, the introduction of the transfer matrix method (TMM), and finite-different time-domain (FDTD) simulations techniques are discussed. The methods of material deposition are presented, and the systems for electron beam lithography (EBL) are briefly reported. The in-house optical characterisation setup is outlined in this chapter, as well as the various other characterisation techniques utilised throughout the thesis.

A patterned plasmonic aluminium nanostructure is the first to be investigated for the generation of structural colour and is the focus of **Chapter 4**. This architecture is of a similar configuration to previous literature designs[11], and consists of an array of dielectric pillars, with Aluminium on the backreflector surface, and top of the discs. This creates a structure with a disc and hole component, separated by the dielectric pillar by tens of nanometres, allowing for strong interaction between the components. The primary goal of this chapter to validate the simulation techniques, and to be a proof of concept for fabrication of low costs patterned nanoparticle arrays in the facilities available.

In **Chapter 5** a hybrid metal nanostructure consisting of Au discs on a polymer thin film and Ag backreflector is investigated, due to the limitations associated with the structure investigated in Chapter 4. The structure benefits from the strong LSPR of Au nanodiscs, high reflectivity of Ag and the optical cavity produced by the transparent polymer layer, while maintaining a smaller unit cell footprint than the Aluminium structure. This minimises angular dependencies of the structure, with regards to diffractive effects, allowing for wide viewing angles.

Chapter 6 considers a simple thin film design, which incorporates a PCM in order to produce dynamic colour. VO₂ is selected, due to the comparatively low power requirements for phase transition, with the primary goal of the chapter to increase the sensitivity of VO₂ in the visible region.

Chapter 7 follows on from the thin film design proposed in Chapter 6, and incorporates Au nanoparticles of varying size and shape. The LSPR response and electric field distribution surrounding these particles are highly dependent on size, shape, and surrounding media; the nanoparticles act as sensitive components in the structure that further increase the colour change potential of the structure upon phase transition.

The major conclusions of the work will be summarised in **Chapter 8**, along with an outlook to future work. Appendices are also included, with supplementary information to some parameters presented for structures examined in chapter 7, as well as information on the sample recipes used in chapters 4 and 5. Finally, colour data is presented for all spectra presented in the thesis, with RGB values and colour swatches, as well as CIE xyY values listed.

Chapter 2

Background

Summary

This chapter will address the main background theory associated with the experimental sections of the thesis. As this thesis has focused on structural colour generated by a series of nanostructure designs, from thin film stacks to patterned nanoparticle arrays, these are the main topics addressed. Thin film stacks are one of the simplest forms of assemblies capable of structural colour. There are two primary mechanisms by which thin films selectively filter light of certain wavelength ranges to generate colour in reflectance; interference, and absorption. The basis for these mechanisms are first introduced. The concept and mechanism of Phase Change Materials are also presented briefly.

Nanoparticle arrays filter light via absorption and scattering by particles on the order of the wavelength incident on the structure, as well as interference mechanisms. Light incident on a dielectric-metallic surface or interface may induce oscillations of conduction band electrons in the metal if the momentum of the propagating wave and surface oscillation can be matched. These oscillations are known as a surface plasmons, and are in part, due to the dissociated electron cloud in the metal. The reflectance/transmittance spectra in plasmonic systems are highly wavelength dependent, with distinct absorption and scattering bands. As the wavelength range of visible light is in the 400-700 nm region, these structures can also result in angular diffraction effects due to their sub-micron scales, and are introduced here.

As structural colour is of interest throughout the thesis, colour theory must be addressed. Both subtractive and additive colour models are considered, as both have been utilised in the past for determining colour response in nanostructures.

2.1 Thin films

Thin films can be considered the simplest structure capable of generating structural colour. They consist of one or more layers of materials, coating the entire surface of a substrate. These layers can be dielectric or metallic, and can range from only a few nanometers thick, to several microns. Here, the primary mechanisms are described by which these stacks can selectively absorb incident light, and in doing so, appear coloured in reflection or transmission.

2.1.1 Interference

Propagating light is a transverse electromagnetic wave, with electric and magnetic fields oscillating orthogonal to each other and the propagation vector. Optical interference is a phenomenon in which propagating light waves interact with each other, as a superposition of the electromagnetic waves is formed. Depending on the phase difference between these waves, which may result in constructive or deconstructive interference. This phase difference can be induced in reflection from two interfaces of a layered structure, separated a distance d , with an example presented in Figure 2.1.

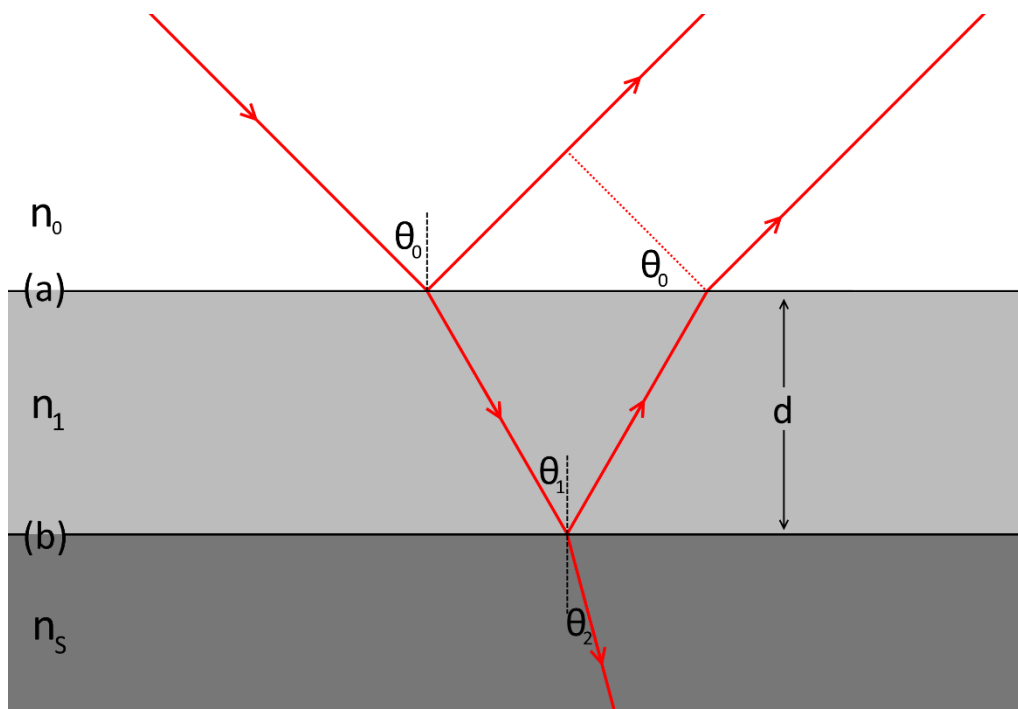


Figure 2.1: Schematic of a structure exhibiting thin film interference, with n_0 as the incident medium (usually air, $n = 1$), n_1 as the film, and n_s as the substrate.

The refractive index a material (n) is the measure of the difference in velocity that light propagates through the material (v), compared to that of propagation in free space (c), as $n = c/v$. In the case shown in Figure 2.1, assume that $n_0 = 1$, and that $n_0 < n_1 < n_s$. When light is reflected at a boundary in which the refractive index is higher, there is a 180° phase shift in the reflected light[114]. Here, this occurs at both boundaries, as n is higher at the far side of the boundary in both cases. Constructive interference will occur when the optical path length difference between the two waves is equal to a multiple of the wavelength of incident light, λ , as[114]:

$$2n_1d\cos(\theta_1) = m\lambda \quad (2.1)$$

where n_1 is the refractive index of the layer, θ_1 is the angle of the incident wave on the lower boundary, m is an integer multiple. This is only the case in the case if $n_1 < n_s$, as there will be a phase shift induced upon reflection at both interfaces. In the case of $n_1 > n_s$, the dependency follows:

$$2n_1d\cos(\theta_1) = (m - \frac{1}{2})\lambda \quad (2.2)$$

As no phase shift is induced at the lower boundary, a correction term of $-1/2$ is included. The relationship between the angle of the incident wave (θ_0), and the angle of incidence at the lower boundary (θ_1) is described by Snell's law as[115]:

$$n_0\sin(\theta_0) = n_1\sin(\theta_1) \quad (2.3)$$

where n_0 is the incident refractive index, usually air ($n = 1$), and n_1 is the refractive index of the layer. It is clear that the optical path length is highly dependent on the angle of incidence of the light, and so thin film interference is a phenomenon highly dependent on illumination and observation angle.

In this way, thin films of transparent materials can generate structural colour in reflectance, due to the optical path difference between reflected light from different layers. These can be stacked to form more complex structures known as distributed Bragg reflectors (DBRs)[29], capable of selectively reflecting wavelength regions. It should be noted that these layers must have thickness on the order of the

wavelength of light in order to satisfy the integer multiple condition in the optical path length.

This is the principle operation of the distributed Bragg reflector (DBR), a structure formed from multiple layers of alternating dielectric materials with thickness on the order of a quarter of the wavelength. Constructive interference will occur according to Equation 2.2, due to the alternating n values. Each layer in the stack partially reflects the light, with the optical path difference resulting in a first order ($m = 1$) constructive interference when $d = \lambda_m/4$, where λ_m is the wavelength of light in the material ($\lambda_m = n\lambda$). The region of high reflectance formed by this structure is called the photonic stopband, an example of which is presented in Figure 2.2.

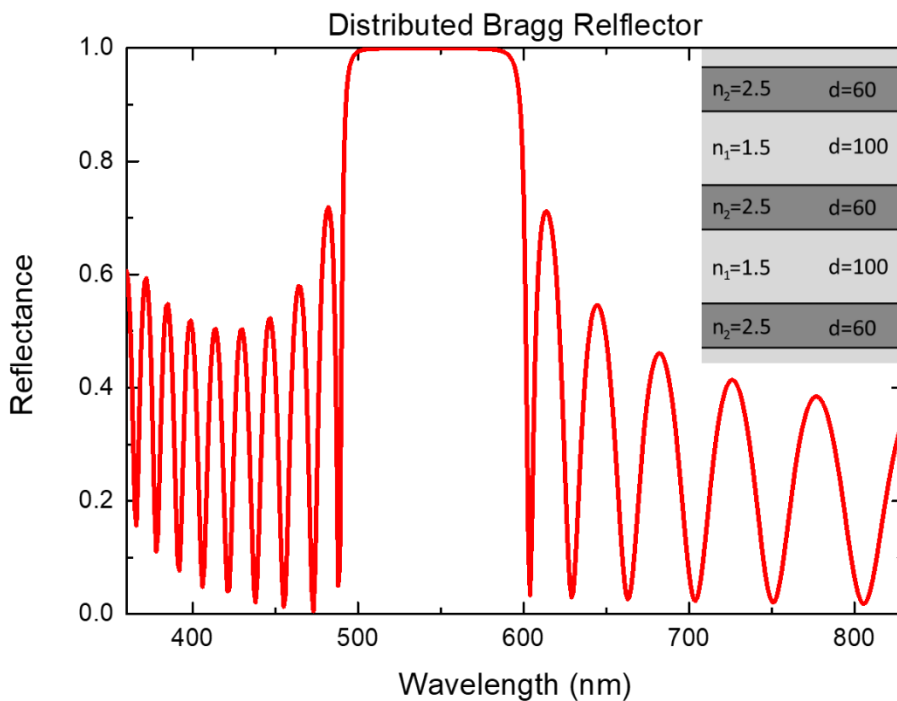


Figure 2.2: Reflectance spectrum of a 20-layer Distributed Bragg Reflector with 10 alternating layers of $n_1 = 1.5$ and $n_2 = 2.5$ on a Si substrate, with layer thickness (d) of 100 nm and 60 nm, respectively. This is calculated by the Transfer Matrix Method, with a stop band of approximately 100 nm in the 500-600 nm region of the visible spectrum.

(Inset) Schematic of layered structure.

2.1.2 Absorption

Optical absorption is the attenuation of a light wave as it propagates through a material, due to the inelastic interaction between the photons and electrons bound to atoms in the material. Energy is primarily lost through Joule heating, as inelastic

scattering in the material transfers energy to the ion cores, in the case of crystals, or to the vibration of bonds in molecules. Photons are absorbed when resonant with an electron energy level transition, or above the band gap of the material. This absorption of energy excites an electron to a higher energy level. The electron can then fall back to its ground state, in which case a photon is re-emitted, or the energy can be lost via non-radiative recombination of the electron to the ground state. This energy in the latter case is usually converted to heat. Studies into using thin metallic films for colour generation[27] have successfully generated vibrant colours from thin films of Ge on Au[26], with colour varied by changing the thickness of the Ge film.

The real part of the refractive index of a material (n) has been previously stated, though there also may be an imaginary component (κ), known as the extinction coefficient, responsible for describing the light attenuating characteristics of a material. In dispersive media with a complex refractive index, these values vary by frequency (ω), as the material responds to the electromagnetic wave differently depending of the frequency of oscillation. The larger the κ value, the more lossy the material is at that particular wavelength. Permittivity ($\bar{\epsilon}$) is the resistance to the formation of an electric field in a material, and related to the frequency dependent complex refractive index (\bar{n}) as[116,117]:

$$\bar{\epsilon} = \epsilon' + i\epsilon'' = \bar{n}^2 = (n + i\kappa)^2 \quad (2.4)$$

where

$$\epsilon' = n^2 - \kappa^2 \quad (2.5a)$$

$$\epsilon'' = 2n\kappa \quad (2.5b)$$

and

$$n = \sqrt{\frac{|\bar{\epsilon}| + \epsilon'}{2}} \quad (2.6a)$$

$$k = \sqrt{\frac{|\bar{\epsilon}| - \epsilon'}{2}} \quad (2.6b)$$

Transparent materials, such as glass or other dielectric materials, allow light below a certain frequency to pass through, as the first excited energy level of electrons in the material is larger than the energy of the incident photon below that frequency. The photon does not interact with the electrons in the material, and so light passes through without being attenuated. These materials are described by a refractive index which has a small extinction coefficient (κ).

Metals have a dissociated electron gas shared throughout the material. This is due to the position of the Fermi level in the conduction band in the material. The Fermi level is the highest energy level of an occupied electron orbital, and its position in the conduction band allows electrons to be removed from their ion cores easily by an applied electric field. This electron gas cloud is highly mobile, and can respond to the incident electromagnetic field below a certain frequency, known as the plasma frequency. The plasma frequency (ω_p) is described by[116]:

$$\omega_p = \sqrt{\frac{n_e e^2}{m^* \epsilon_0}} \quad (2.7)$$

where n_e is the electron density, e is electron charge, m^* is the effective mass of the electrons, and ϵ_0 is the permittivity of free space. From Equation 2.7, it can be seen that for different metals, the most important parameter when concerning the plasma frequency is electron density in the metal.

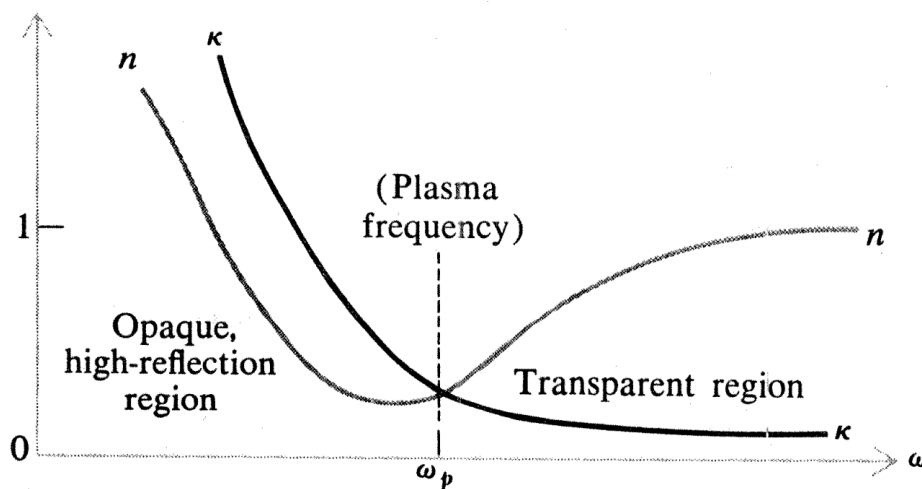


Figure 2.3: Real (n) and imaginary (κ) parts of the refractive index of a generic metal as a function of frequency, with plasma frequency (ω_p) shown.[118]

Above the plasma frequency, electrons are not able to respond to the driving oscillating field completely, due to inertia, resulting in a resistance of the material to the formation of an electric field. As a result, the material becomes transparent to light. Depending on the complex refractive index of the metal, it may absorb light according to the imaginary (κ) component. For most metals, this plasma frequency occurs in the ultra-violet region, and they appear to reflect the entire visible region. However, for some metals such as Cu, Ag, and Au, often referred to as “noble” metals, each have a filled $3d$, $4d$, and $5d$ electron orbital shell, but only a single electron in the $4s$, $5s$, and $6s$ shell, respectively[119]. This allows for inter-band transitions, where electrons are excited from the core electron orbitals, altering the refractive index significantly. In the case of Au and Cu, this leads to high reflectance at only the longer wavelengths of the visible, resulting in their red/orange hues. In the case of Ag this occurs at higher frequency leading high reflectance in the visible, with a near-UV transparency[120].

2.1.3 Phase Change Materials

A phase change material (PCM) is one in which a reversible physical change is observed in the structural configuration of the material under a stimulus, be it heat, electrical, or other. Of particular interest in this thesis are solid-solid PCMs, which maintain a solid phase of matter in both states, with a significant modification of the refractive index of the material as they transition from one phase state to another[16,18,64,65]. A number of chalcogenide-based solid-solid phase change materials have been widely utilised for memory applications, due to the change in refractive index exhibited by the material, while maintaining a solid state. In particular, the bi-stability[72] exhibited by GST have led to its use in re-writable optical disks such as the DVD format[74,75]. The significant refractive index change experienced is due to a change in the crystalline structure, from a low temperature amorphous state, which is insulating, to a high temperature crystalline state, that is metallic. This can be induced by heating the material conventionally above a certain

“transition” temperature, or as an electric field is applied to the material, to induce structural changes by Joule heating[18][121].

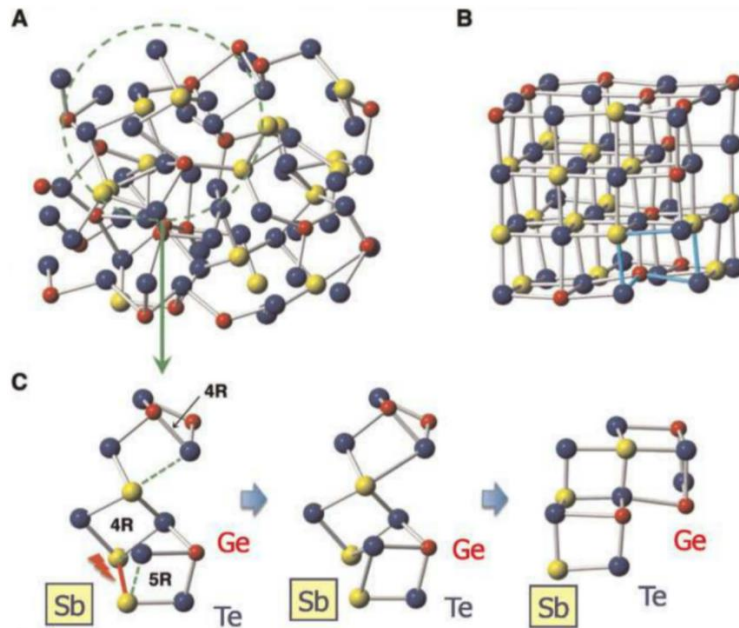


Figure 2.4: Crystalline structure of GeSbTe in the (A) low temperature amorphous insulating phase, and (B) high temperature crystalline metallic phase. (C) Cutout of the larger structure, illustrating the structural change[122].

VO₂ is a solid-solid PCM that transitions from a low temperature semiconducting monoclinic phase to a high temperature rutile metallic phase at 68°C[17], significantly lower than the 145°C required for GST[67].

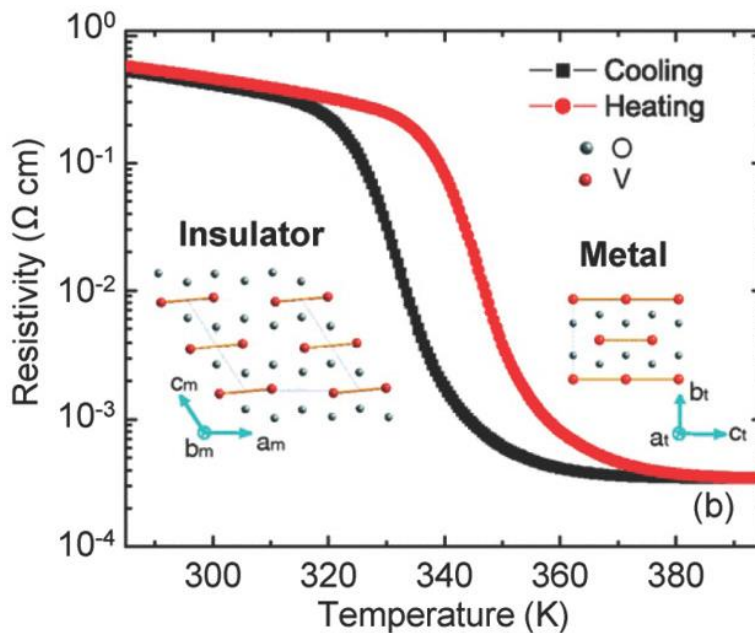


Figure 2.5: Temperature vs Resistivity plot for VO₂, with inset of VO₂ structure in the low temperature insulating phase, and high temperature metallic phase[123].

In the monoclinic phase, the crystalline unit cell of VO₂ contains a V⁴⁺-V⁴⁺ pair along the c-axis of the crystal[124]. Above the transition temperature, the c-axis pairs dissociate, closing the gap in the conduction band for vanadium in the 3d orbital[125], placing the Fermi level in the d orbital, and allowing for high conductivity, as shown in Figure 2.6.

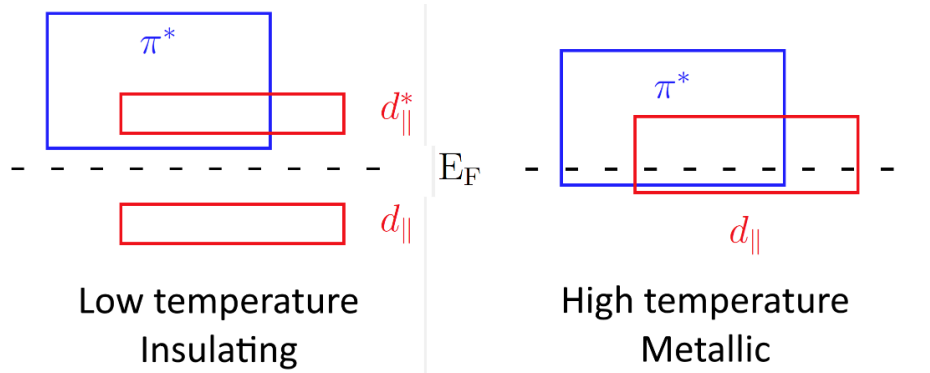


Figure 2.6: Band structure of VO₂ in the low temperature insulating phase, and high temperature metallic phase. [126,127]. The $d_{||}$ band is due to V-V pairs in the c-axis, as a result of the overlap of the dx^2-y^2 orbital in Vanadium.

The hysteresis effect observed in Figure 2.5 is due to the granular nature of the material and the alteration of the shape of the crystal lattice as phase transition takes place. As the material changes from the insulating to metallic phase, the crystal reorientation results in the dissociation of the V⁴⁺-V⁴⁺ pairs. This requires a change in the shape of the structure, in order for this change to occur, energy must be introduced, observed here as the extra heat required to induce the phase transition. Similarly, when the material cools below the transition temperature, and the pair reform, this also requires extra energy to facilitate the reorientation of the lattice. In this case, the temperature must drop below the transition temperature before phase transition will occur. The phase transition can be achieved by heating[16] or it can be electrically triggered[18]. Studies have been carried out into the mechanism of electrically switching the VO₂ phase[78–80], with field thresholds on the order of 10⁷ V/m[79,81], and steady state switching has been demonstrated with an applied DC voltage[19]. The switching mechanism in electrical actuation has been attributed to Joule heating as current is passed through it, inducing the phase transition to occur as the material heats above the threshold temperature[125]. However, the refractive

index change of VO₂ is greatest in the infra-red and microwave spectral ranges, which has motivated extensive studies using VO₂ for applications in IR waveguides [19,84,85], optical communications [83,86,87], IR sensing [88,89], and many THz applications[84,90,93]. The material exhibits a smaller but still significant complex refractive index change in the range below 700 nm[17], and with lower power consumption than for AIST or GST. This makes the material a viable alternative in the visible region, provided that the limited refractive index change can be utilised to its best potential.

2.2 Plasmons

Plasmons are oscillations of the conduction band electrons at the interface between materials in which there is a change in sign of the dielectric permittivity, ϵ . Metals exhibit negative relative permittivity at optical frequencies below the plasma frequency, where the electrons can respond completely to the induced field of the incident wave. The negative permittivity of metals below the plasma frequency is the origin of the high reflectivity observed in the visible, as most metals present plasma frequencies in the UV[116].

Plasmons can form at the boundary between a dielectric (d) and metal (m) material, though it can also occur at the boundary between a metal and air, or vacuum, due to their positive permittivity. However, as the plasmon has a higher energy than the propagating wave, it must be coupled to the interface. This can be done by utilising defect sites, or coupling into a material with higher refractive index to overcome the momentum mismatch. The plasmon has a shorter wavelength than the free-space or bulk propagating wave, it exhibits significant spatial confinement, and large field localisation.

Surface plasmons occur in two forms; surface plasmon polaritons (SPP), and localised surface plasmons (LSPR), which often have a strong resonance condition, due to the confinement of the oscillation to the particle boundaries.

2.2.2 Surface Plasmon Polaritons

Surface Plasmon Polaritons (SPPs) are propagating longitudinal surface waves that occur along the dielectric-metal interface. These present as evanescent fields perpendicular to the surface, that decay rapidly into the dielectric and metal, as illustrated in Figure 2.7.

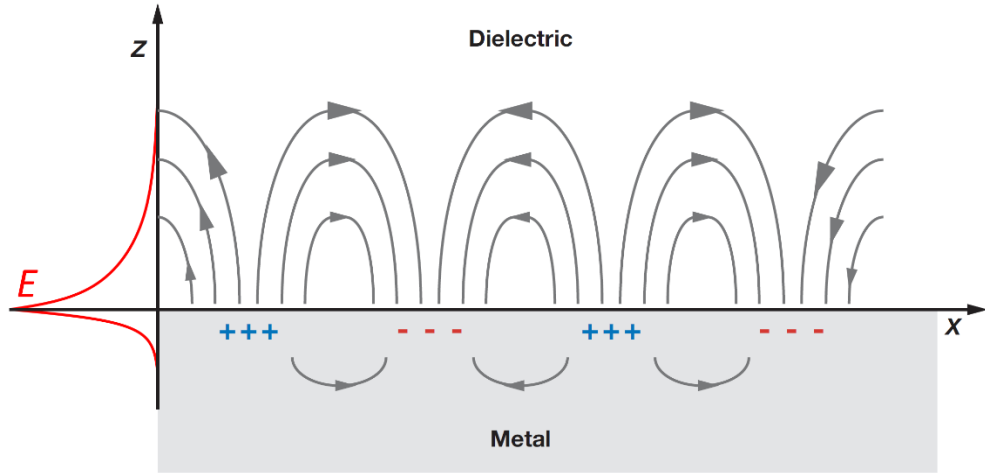


Figure 2.7: Surface plasmon polariton (SPP) oscillation at a dielectric-metal interface. A decaying evanescent field is observed normal to the surface[128].

The dispersion relation of a propagating oscillating light wave is the relationship between its frequency (ω) and wavevector (κ). The dispersion relation for a propagating wave in a non-dispersive dielectric medium is[116]:

$$\omega = \frac{ck}{\sqrt{\epsilon_d}} \quad (2.8)$$

where c is the speed of light, and the wavenumber is:

$$k = \frac{2\pi}{\lambda} \quad (2.9)$$

The dispersion relation for the bulk plasmon in a metal is:

$$\omega = \sqrt{\omega_p^2 + c^2 k^2} \quad (2.10)$$

Figure 2.8 illustrates the dispersion relation for SPPs, at both an air-metal ($a-m$) and dielectric-metal ($d-m$) interface.

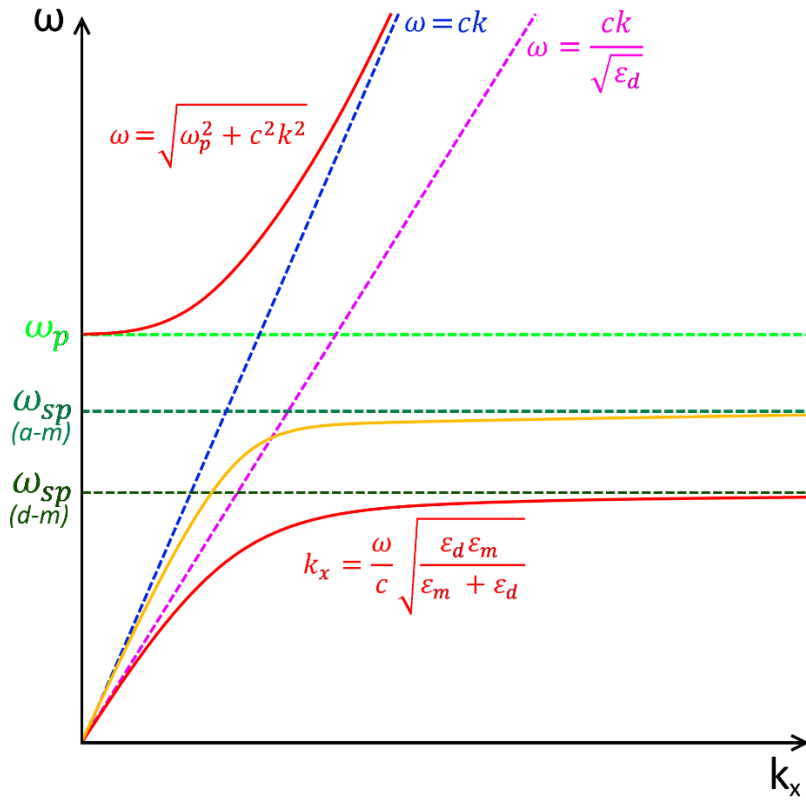


Figure 2.8: Dispersion relation of SPPs, at an air-metal (*a-m*) and dielectric-metal (*d-m*) interface. The blue and pink light lines are the relations for free space, and dielectric media, respectively.

Where ω_p is the plasma frequency of the metal, and is described in Equation 2.7. This relation is asymptotic, and tends towards the free space light line as k_x increases.

Surface plasmons can be excited at a dielectric-metal interface below the plasma frequency, in a regime where there is no propagation into the medium can occur, as ν values are imaginary. Only evanescent fields are supported at the interface between the dielectric and metal.

The wavevector along the propagation direction (k_x) is also asymptotic as it approaches the surface plasmon frequency (ω_{sp}), and is described by:

$$k_x = \frac{\omega}{c} \sqrt{\frac{\epsilon_d \epsilon_m}{\epsilon_m + \epsilon_d}} \quad (2.11)$$

From this, it can be determined that the maximum k_x occurs where $\epsilon_d = -\epsilon_m$. This relation assumes that the dielectric permittivity of the metal is given by:

$$\varepsilon_m = 1 - \frac{\omega_p^2}{\omega^2} \quad (2.12)$$

Therefore, the characteristic angular frequency of the plasmon that can be supported at the metal-dielectric interface is described by:

$$\omega_{sp} = \frac{\omega_p}{\sqrt{1 + \varepsilon_d}} \quad (2.13)$$

It is clear that the angular frequency is highly sensitive to the permittivity of the dielectric at the interface. In the case of a metal-air interface, where $\varepsilon_{air} = 1$, this relationship simplifies to:

$$\omega_{sp} = \frac{\omega_p}{\sqrt{2}} \quad (2.14)$$

For the wavevector in the z direction, perpendicular to the interface, in the metal and dielectric:

$$k_{zm}^2 = k_x^2 - \varepsilon_m \left(\frac{\omega}{c}\right)^2 \quad (2.15a)$$

$$k_{zd}^2 = k_x^2 - \varepsilon_d \left(\frac{\omega}{c}\right)^2 \quad (2.15b)$$

where

$$\frac{k_{zm}}{k_{zd}} = -\frac{\varepsilon_m}{\varepsilon_d} \quad (2.16)$$

SPPs can propagate for tens of microns depending on the losses at the interface[129]. As the SPP is an evanescent wave that decays quickly into both media, the SPP is not directly observed as the oscillation is confined to the surface interface, and far-field radiation of the light is often only measurable due to defect sites on the surface[130]. Surface near-field optical microscopy (SNOM) may be used to probe the near-field very close to the interface[129] to measure SPP characteristics.

However, in periodic arrays such as those used throughout this thesis, surface plasmons can be excited by the periodic array elements, such as the Al and Au discs in Chapters 4 and 5, respectively. These periodic surface plasmons (PSPs) propagate along the air-metal or dielectric-metal interfaces in the nanostructures, and are affected by the periodicity of the array. When the pitch of the array is half that of

the effective wavelength of the PSP, scattering can lead to the formation of standing waves, which results in a surface plasmon stop-band[131]. In the case of square arrays, where the periodicity is in both directions, this can lead to a full stop-band gap forming for surface plasmons[131,132]. This stop-band can affect the reflectance response of the nanostructure in the far-field in a narrow wavelength range. The wavelength (λ_{PSP}) of the PSP formed by the periodic array can be found by[51,133,134]:

$$\lambda_{PSP} = \frac{P}{\sqrt{i^2 + j^2}} \sqrt{\frac{\epsilon_d \epsilon_m}{\epsilon_m + \epsilon_d}} \quad (2.17)$$

where P is the pitch of the nanoparticle array, and the scattering orders are denoted by the integers i and j .

2.2.3 Localised Surface Plasmon Resonance

LSPR is a non-propagating form of plasmon excitation which occurs in conduction band electrons of metal nanoparticles. Incident electromagnetic radiation is coupled to these particles, often smaller than the wavelength, and induces the electrons in the conduction band to oscillate in response. As the electrons move across the surface, they are confined by the boundaries of the particle, as shown in Figure 2.9. These coherent plasmon oscillations are greatest at a resonant frequency defined by the size, shape, material and surrounding refractive index.

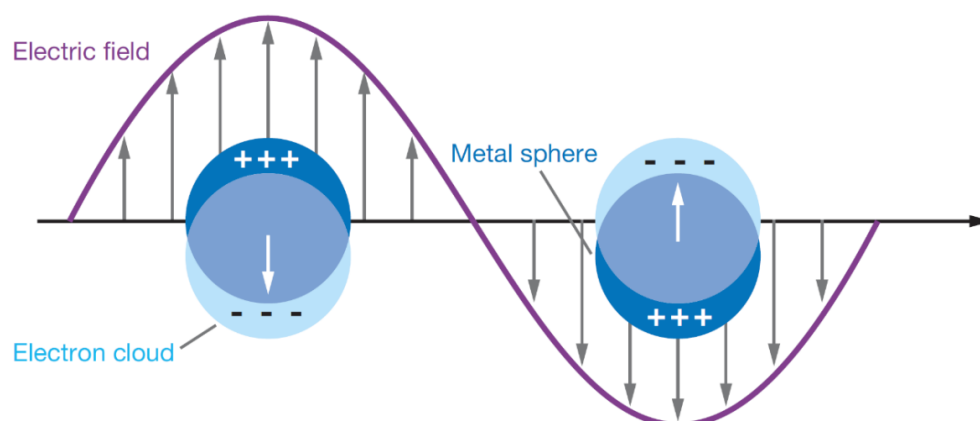


Figure 2.9: Localised Surface Plasmon Resonance (LSPR) oscillation in metal nanoparticles, induced by the incident oscillating field. Conduction band electrons react to the incident field by moving across the surface, producing strong field enhancement.[128]

The simplest particle can be examined; a sphere, using the quasi-static approximation provided that the size (d) is smaller than the wavelength (λ) of incident light. In this regime, the phase of the oscillating field across the particle can be assumed to be constant, and the field distribution can be calculated by simplifying to a particle in an electrostatic field. The dipole moment (P) of the nanoparticle induced by the external field (E_0) can be described by[116]:

$$P = \varepsilon_d \varepsilon_0 \alpha E_0 \quad (2.18)$$

where α is the polarizability of the particle. This is defined as[116]:

$$\alpha = 4\pi a^3 \frac{\varepsilon_m - \varepsilon_d}{\varepsilon_m + 2\varepsilon_d} \quad (2.19)$$

Here, a is the radius of the sphere. This follows the Clausius-Mossotti relation for molecular polarizability[135]. An interesting dependency is revealed there, in that the maximum polarizability of the particle occurs when $\varepsilon_m = -2\varepsilon_d$, known as the Fröhlich condition[136]. This is the maximum dipole excitation experienced by the metal nanoparticle, or the localised surface plasmon resonance (LSPR). Large field enhancement is experienced in close proximity to the particle in the frequency region of highest polarizability.

From this relation, the cross-section of extinction (C_{Ext}) can be determined. This is the effective area of collision in the interaction between the incident field and particle. The extinction is the combination of scattering (C_{Sca}) and absorption (C_{Abs}) cross-sections, due to the particle as:

$$C_{Ext} = C_{Abs} + C_{Sca} \quad (2.20)$$

The dependencies of C_{Abs} and C_{Sca} follow the form[116,137]:

$$C_{Abs} = k \operatorname{Im}[\alpha] = 4\pi k a^3 \operatorname{Im} \left[\frac{\varepsilon_m - \varepsilon_d}{\varepsilon_m + 2\varepsilon_d} \right] \quad (2.21a)$$

$$C_{Sca} = \frac{k^4}{6\pi} |\alpha|^2 = \frac{8\pi}{3} k^4 a^6 \left| \frac{\varepsilon_m - \varepsilon_d}{\varepsilon_m + 2\varepsilon_d} \right|^2 \quad (2.21b)$$

These can be used to determine the absorption and scattering cross-section for spherical, non-interacting particles where $d < \lambda$. An example, using a silver

nanoparticle in a refractive index material of $n = 1.33$ is shown in Figure 2.10 (a) for absorption cross-section and (b) for scattering cross-section.

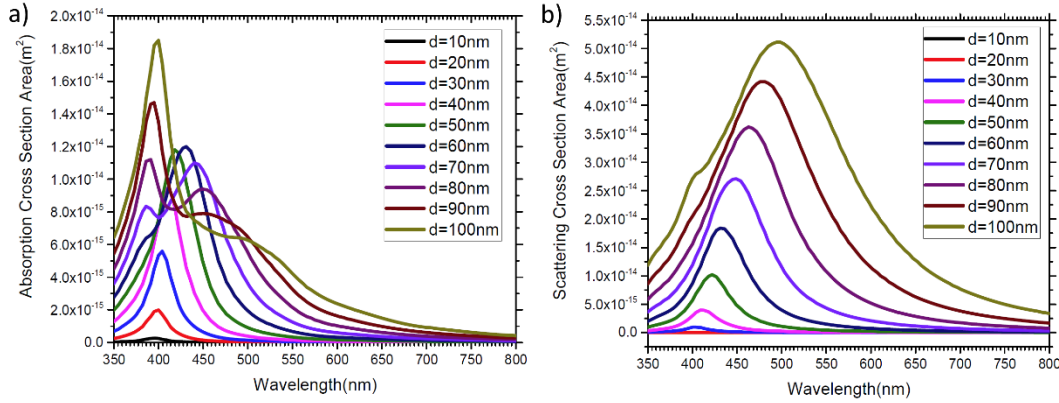


Figure 2.10: (a) Absorption and (b) Scattering cross-section spectra for Ag nanoparticles of 10-100 nm in 10 nm steps. Refractive index of the surrounding media is $n = 1.33$ [138].

It is important to note the scaling of absorption and scattering, where the a^3 dependency is dominant in small particles, but is quickly eclipsed by the scattering cross section, scaling with a^6 . As such, the measurement of scattering from small particles is difficult to examine in the presence of larger scattering particles, and so rely on absorption measurements, with a smaller scaling factor of a^3 [139], which is demonstrated in Figure 2.10 (a).

Using the relation in Equation 2.20, and the dependencies revealed in Equation 2.21a and 2.21b, the extinction cross-section for a sphere of volume (V), follows as[116]:

$$C_{Ext} = 9k\epsilon_d^2 V \operatorname{Im} \frac{\epsilon_m''}{[\epsilon_m' + 2\epsilon_d] + (\epsilon_m'')^2} \quad (2.22)$$

Extinction is a combination of the absorption and scattering cross-sections, and is illustrated in Figure 2.11 (a). Shown in Figure 2.11 (b) is the dependency of the peak extinction to the refractive index of the surrounding material.

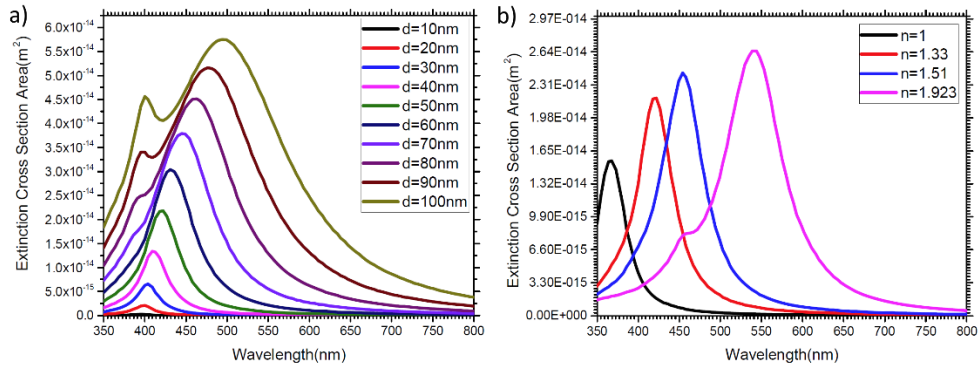


Figure 2.11: (a) Extinction cross-section spectra for Ag nanoparticles of 10-100 nm in 10 nm steps. Refractive index (n) of the surrounding media is 1.33. (b) Extinction cross-section of 50 nm particles in varying refractive index media, from $n = 1$ to 1.923[138].

Figure 2.11 (a) reveals that the extinction red-shifts, and increases in intensity as the diameter of the Ag nanoparticles are increased. Shown, in Figure 2.11 (b), is the extinction cross-section for 50 nm spherical Ag particles in varying refractive indices. This illustrates that the peak position is highly sensitive to the refractive index of the surrounding media, and red-shifts significantly as the refractive index increases. The extinction determines the total energy of the incident wave that is lost due to interaction with the particle, as:

$$1 = T + R + Ext = T + R + Abs + Sca \quad (2.23)$$

where transmission (T) and reflection (R) can be collected in the far field. Absorption (Abs) cannot be collected, and is lost in the material. Scattered (Sca) light can be collected, but has a large angular dependency.

The above Equations 2.21a, 2.21b, and 2.22 only hold true for non-interacting spherical metallic structures in nondispersive dielectric mediums. For more complex systems, such as those addressed in this thesis, which include particles of various shapes in array configurations, more complex numerical techniques are required[140]. The alteration of shape, size and surrounding media has a significant effect on the response of the nanostructure under examination, as well as the interaction between components and neighboring particles in array structures.

2.3 Fano resonance

While sharp spectral features in patterned nanostructures can be formed due to the relative uniformity in shape and periodicity of nanoparticles, another coupling mechanism for strong resonance responses in some patterned nanostructures is the formation of an interference effect known as Fano resonance[141–143]. This optical Fano resonance can be generated by the interference between components of a nanostructure, as the narrow discrete response generated by one component interacts with the broad continuum response from another, where the energy ranges of both components has an overlap. For example, where the evanescent field formed by the LSPR of a nanoparticle interacts directly with reflected light from another component[144,145], a Fano resonance can be formed. This is due to the LSPR forming a quantised oscillation of the conduction band electrons. These oscillations are confined by the boundaries of the material, and form an evanescent field in close proximity to the particle with a narrow frequency band. This evanescent field interacts with the broadband response formed by another component of the structure, such as the reflectance from a surface.

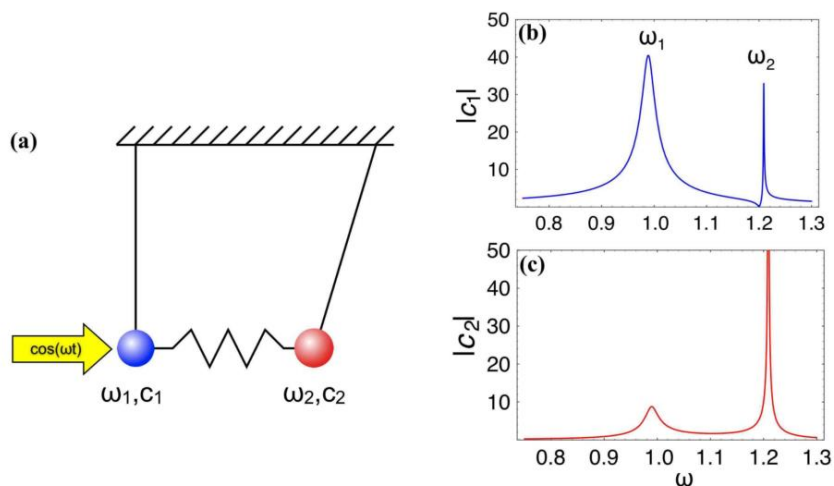


Figure 2.12: Coupled oscillator system that exhibits fano resonance lineshape as a result of the driven oscillation of one affecting the oscillation of the other.[142]

These Fano resonances can arise in coupled oscillator systems such as in Figure 2.12[142], where two components are linked, such that the driven swinging of one component affects the oscillation of the other. The resonance is dependent on the

separation in position of the peak amplitudes of the oscillators, and the driven amplitude. Critically, Fano resonance occurs in coupled oscillating systems in which the resonance is not identical in both oscillators and is observed where a broad resonance of one oscillator interacts with the narrow resonance of another, where the energy bands of the two systems are close or overlapping. This distinguishes Fano resonance from other coupled systems in which strong or weak coupled oscillation also occurs.

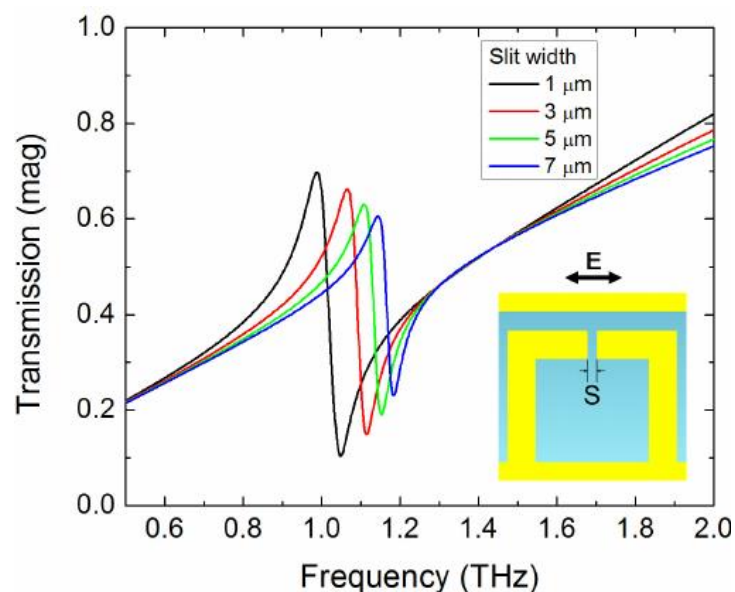


Figure 2.13: Fano resonance line shape in transmission as a function of slit width. Nanostructure of metallic slit array on a quartz substrate.[146] (Inset) unit cell of structure.

Depending on the phase of the reflected light, interaction between the fields will result in either destructive or constructive interference, and form sharp spectral features in far-field radiation from the nanostructure. The phase of the discrete oscillation varies more rapidly than that of the continuum, and so Fano resonance is often characterised by a particular asymmetric line-shape in the response of the system[147] as a result, as shown in Figure 2.13[146]. Here, the narrow slit provides a sharp resonance response, and the continuous wire acts as a broad resonator. These two components interact to form the Fano resonance response observed. This effect has been widely demonstrated[142] in even simple nanostructure configurations[116,142,148], such as that demonstrated by Shen et al.[143], in which

the LSPR from Al nanodiscs interacting with a dielectric substrate interact form a Fano resonance response.

In the Aluminium nanostructure discussed later, it is noted that the colour generation is not simply due to a combination of reflectance from the LSPR of the disc array combining with the high reflectivity of the backreflector, but is due to a strong Fano resonance between components of the structures. In this structure, the LSPR of the discs forms evanescent fields that decay quickly away from the nanoparticle boundaries and acts as a quantised energy oscillation. This then interacts with the hole component, which has a much broader spectral response that overlaps with the energy band of the disc LSPR. When these components interact, they exhibit a strong Fano resonance.

2.4 Array effects

Diffraction is an interference effect that arises from the superposition of waves originating from coherence sources. Diffraction is observed in the structure examined in Chapter 4, formed by the array periodicity producing a diffraction grating, as the pillars act as scattering sites. Here, diffraction from an array is described.

2.4.1 Diffraction

Diffraction from an array of particles occurs due to the interference caused by an optical path difference between propagating waves. Illumination of a periodic structure such as a grating or array of nanoparticles with separation (d), at an angle (θ), results in a difference in path length for the light in reflectance. This path difference, $d\sin\theta$, is a function of the angle and separation of the particles. The nanoparticles act as scattering sites, and are coherence sources for propagating waves in all directions, with a difference in their path length at a collection angle (φ) of $d\sin\varphi$. If the path length is an integer, m , of the wavelength, constructive interference occurs between the light waves originating from each scattering site,

resulting in a maximum intensity of light at that wavelength, at that angle, as demonstrated in Figure 2.14.

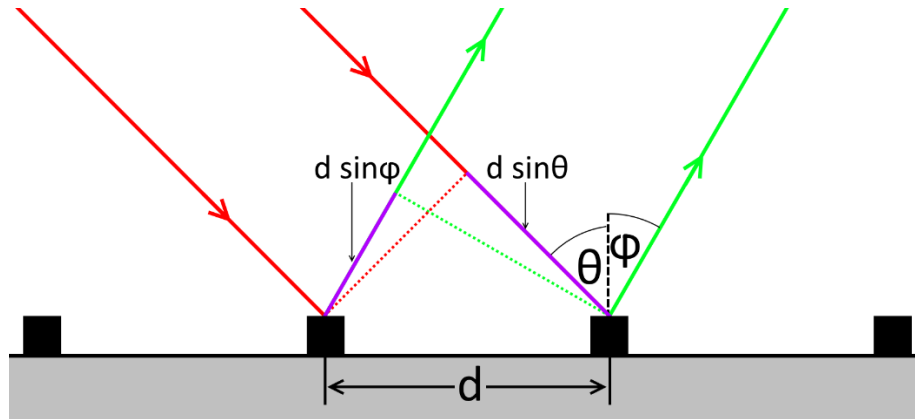


Figure 2.14: Schematic of a structure exhibiting diffraction interference, with incident light scattered at each site, the path length difference marked in purple. Constructive interference occurs where this path difference ($d \sin \theta - d \sin \varphi$) is equal to $m\lambda$.

As the diffraction is occurring in reflection, from a surface with scattering sites, the path length differences between each scattering site are subtracted from one another to determine the angles of constructive interference. Maxima for each wavelength occurs at different collection angles (φ), as the integer multiple depends on the wavelength. This relationship can be described by[149]:

$$\sin \theta - \sin \varphi = m \frac{\lambda}{d} \quad (2.24)$$

This allows for the formation of orders of diffraction, with $m=0, \pm 1, \pm 2, \pm 3\dots$ signifying the zeroth, first, second and third positive and negative orders, respectively. In the case of diffraction through a grating in transmission, the path length difference is determined by the addition of the terms.

Array structures have exhibited effects in normal reflectance, formed by diffraction parallel to the grating or array interface, known as a Wood's anomaly (WA)[51,150,151]. The wavelength at which these WAs occur at can be found by[51,150]:

$$\lambda_{WA} = \frac{P}{\sqrt{i^2 + j^2}} \sqrt{\epsilon_d} \quad (2.25)$$

where P is the pitch of the grating or nanoparticle array, and the diffraction orders are denoted by the integers i and j .

2.5 Colour theory

Human vision is determined by photosensitive receptors positioned at the back of the human eye, called the retina, onto which light is focused by the cornea. In low light conditions, the photoreceptor responsible for vision is the “rod” cell, which is extremely sensitive. At medium and high lighting conditions, rods are quickly desensitised, and vision is determined by “cone” cells. There are three types of cone cells, each responsible for light detection at different wavelengths. The colour cones responsible for human colour vision are the short (blue), middle (green) and long (red) wavelength photoreceptors, representing peak sensitivities at 400-420 nm, 530-540 nm and 560-580 nm respectively, though their sensitivity curves overlap significantly[152]. Signals from these cells are transmitted to the brain, where they are combined and are the basis for our sense of colour and vision.

When examining colours, two terms are often used to determine the characteristics of the response; luminance and chromaticity. Luminance is a measure of luminous spectral intensity, an indicator of the luminous power that is detected by an observer of an object or surface in reflection[152,153]. The larger the luminance value of the colour, the higher the visibility of that colour under the observation conditions. Methods for the determination of luminance will be described in Chapter 3, in Section 3.1.5.

Chromaticity is an objective quantitative measure of the quality of colour, and is independent of the luminance value of the object or surface being observed[152,153]. Chromaticity values denote every distinguishing colour that can be perceived by human vision. It can be subdivided into the classification of Hue and Saturation. Hue illustrates the “type” of distinguishable colour observed, such as green, blue, red, yellow etc. Saturation determines the proportion of pure colour in the total sensation of observation[153]. This is a qualitative description of the

“purity” of the colour observed, with white light considered the condition of lowest colour saturation, and the primary colours of red, green, and blue as the highest.

There are many colour models that have been developed to examine and allow devices to stimulate colour vision accurately. Here, two popular colour models will be introduced; CYMK and RGB, each of which have fundamental differences in the methods they employ. These colour models are presumed to use 8-bit per channel for the purpose of this thesis. This results in each component being represented by 8-bit numbers ranging from 0-255

2.5.1 CYMK

The CYMK (cyan, yellow, magenta, key/black) is a subtractive colour model, mainly used in the printing industry. It is widely used in printing due to the ease with which it can be applied when utilising dyes of these colours on a white substrate. The principle of the method is that the white background is obstructed by varying combinations of the dyes used. Combining any two primary dyes results in the secondary colours of red, green and blue, as seen in Figure 2.15. The combination of all three results in a limited black, and so a black (Key) component is also required to reduce luminance when necessary.

Key/Black is achromatic, and absorbs all wavelengths. The other three components serve to absorb selectively particular portions of the visible region, acting as an inverse of the RGB components used in additive methods. This results in each component appearing on the opposite side of the colour-space in Figure 2.15, to the wavelength region they absorb.

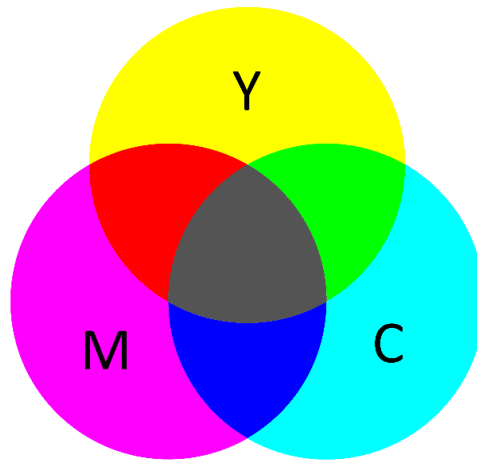


Figure 2.15: Cyan, Magenta, and Yellow colour components, overlapping to demonstrate the formation of secondary colours in the form of Red, Green and Blue. The central region of imperfect black indicates the need for a Key/Black component in CYMK.

Figure 2.15 reveals the cyan, magenta and yellow “primaries” of the CYMK model. In this subtractive colour model, cyan is responsible for the absorption of long wavelengths (red), yellow absorbs blue, and magenta absorbs green. In this way, the gamut of CYMK can be constructed to form colour on a white background material. The variation of colour in printing is achieved by the varied distribution of different sized (often microscopic) ink patches on a white background material.

In this model, chromaticity is indicated by the relative intensity of the CYM components, with luminance defined by that of Key/Black. In an 8-bit CYMK image, a vibrant red colour is achieved with a value of 0:255:255:0. To decrease the luminance of this red, the key/black component is increased, with a dark red achieved with a value of 0:255:255:255. Though this method has been widely used in colour printing technology, the requirement of a white substrate or equivalent surround material is a limiting factor in device design.

2.5.2 RGB

The RGB colour model is an additive model using values of three primary colours (red, green, and blue) in relative intensity, tristimulus values. This is an extremely widely utilised colour model in display technology. Three primary colours of the human eye are represented in this model, with the spectral intensity distribution for

each colour significantly overlapping with the wavelengths ranges of the three colour cones in the retina. Similar to the CYMK model, RGB values combine both luminance and chromaticity of a colour, with luminance represented by the magnitude of each component, and the chromaticity determined by the combination all values. Instead of each component being responsible for the absorption of a region of the visible spectrum, they are instead directly correlated each colour cone. The secondary colours generated by mixing two RGB components are that of Cyan, Magenta, and Yellow, corresponding to the CYMK values of the previously mentioned method. Mixing of all three components results in white light, as shown in Figure 2.16.

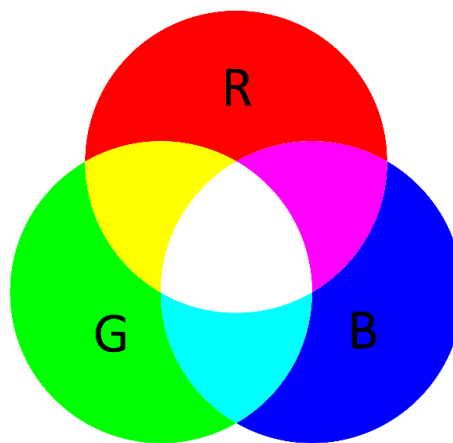


Figure 2.16: Red, Green and Blue colour components, overlapping to demonstrate the formation of secondary colours in the form of Cyan, Magenta, and Yellow, mirroring that of the CYMK colour space in Figure 2.15. The central region of white corresponds to the simulation of all three colour cones.

The 8-bit RGB colour space allows for over 16 million different combinations, and is used to comprehensively represent the full range of human colour vision. For example, an RGB of 255:0:0 indicates a predominantly red colour of maximum luminance, and so would be visible as a bright, pure red colour to human vision. A value of 63:0:0 also represents a red colour of the same chromaticity, hue, and saturation (as the relative weighting is the same) but at a quarter the luminance, and so would be visible as a darker red colour.

This model presents the best method for colour mapping of the structures considered in this thesis, as there is no requirement for a white background material, and there are less component colours needed to produce a full colour gamut. The key requirement of this model is that spectral features can be achieved in three broad, and easily defined regions of the visible region (red, green, and blue). These are more directly mapped to the values generated by the model, and require less interpretation than the CYMK model.

2.5.3 CIE

Colour clarity is a qualitative descriptor for the how a colour relates to the primary tristimulus values of red, green, and blue. The Commission Internationale de L'Eclairage (CIE) 1931 colour-map is used to determine trends and qualitatively analyse colour clarity, and is presented in Figure 2.17. The CIE colour-map is often presented as an xyY plot, with each xy coordinate representing a chromaticity value. The third axis is denoted Y , expressing the luminance of the colour, and is often included as a value ranging from 0-100 at the data point, to maintain a 2-dimensional graph.

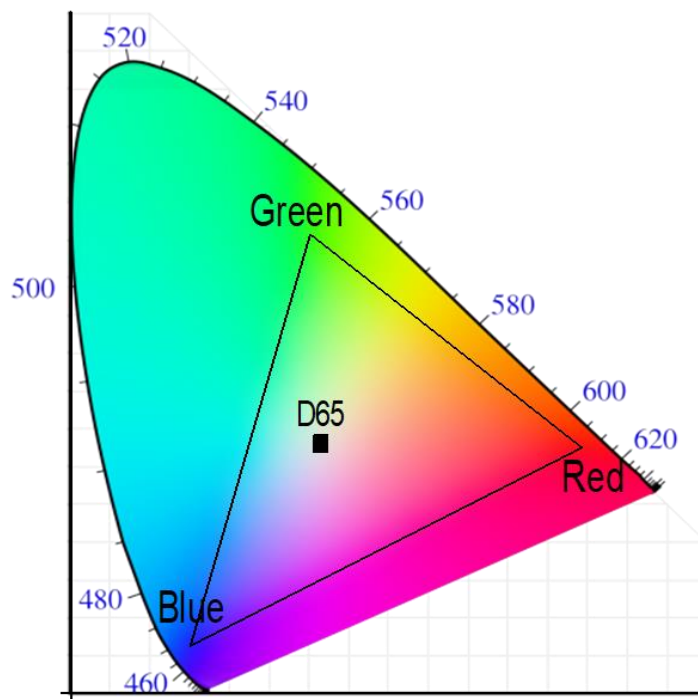


Figure 2.17: CIE colour-space map, indicating all chromaticity values at a luminance value. Wavelengths around the border of the shoehorn indicate the chromaticity representing individual wavelengths of light (such as that produced by a laser).

The centre point represents the area of lowest colour clarity, and indicates a spectrum that has equal stimulation of all three colour cone regions, in this case it is normalised to the D65 solar spectrum, a widely accepted standard for the RGB colour system[154,155]. This spectrum is presented later, in Figure 3.5.

Moving out from this centre point towards the border of the RGB region indicates an improvement in colour clarity, by increasing the saturation of the observed colour. As saturation is increased, the proportion of pure colour in the total sensation of observation[153] is increased. This means that the stimulation of a single colour cone is increasing, proportional to the other two, leading to more clear colours being observed. The red, green and blue tristimulus values represent the positions on the CIE colour-map that have the highest saturation in the RGB gamut, and so the highest colour clarity. In order for a colour to be positioned in close proximity to one of these positions, it must have a substantial reflectance intensity in only one of the three colour cone regions of the visible spectrum, while having significantly smaller reflectance in the other two. For example, an object with an observed colour near the blue primary with a large luminance has a high stimulation of the short (blue) colour cone receptors. This is due to a high reflectance intensity in the peak wavelength sensitivity range of 400-420 nm. The object also has a corresponding weak reflectance response at the middle (green) and long (red) wavelength ranges, and so appears a vibrant blue. This is similar for the positions near the red and green primaries, with stimulation of those particular wavelength ranges.

The luminance does not alter the position of the colour on the CIE 2-dimensional colour space map, as this is denoted by a 0-100 value. The central D65 position is the location capable of the largest luminance value, as it has intensity contributions from all three colour cones. The perimeter of the colour-map denotes a range of monochromatic light positions and is called the spectral focus[153].

2.6 Conclusion

In this chapter, the main background concepts associated with the various stages of the thesis has been addressed. The spectral response of thin films has been examined, both in terms of interference and absorption, with applications in single and multilayer stacks.

Electron oscillations at metal-dielectric boundaries have been introduced, with a focus on LSPR. The importance of LSPR is paramount in nanostructures, as field enhancement at nanoparticle boundaries has a strong impact on the far-field reflectance, as well as scattering, and resonant absorption peaks.

The phenomenon of Fano resonance has been introduced, as they have a direct influence on two of the structures presented in Chapters 4 and 5.

Colour theory has been introduced, with particular attention paid to the mechanism by which spectra are interpreted by human colour vision. This colour theory. Examples of two widely used colour models have been discussed, with the RGB additive colour model shown to be more suitable than CYMK for description of the structural colour generated by arrays of metallic nanoparticles. The CIE colour space map has been introduced, as this is an important tool for determining colour trends for the spectra later presented. The terminology for describing colour, and how it pertains to these models has also been introduced, with hue and saturation determining the colour observed, which together describe the chromaticity. Luminance has also been mentioned as an important parameter that determines the brightness of the observed colour.

Chapter 3

Methods

Summary

In this chapter, the methods employed throughout the thesis will be described in terms of their operation, and implementation later in the manuscript. The methods employed can be broken down into three main sections; Simulation, Fabrication, and Characterisation of the nanostructures under consideration.

The principle of the Transfer Matrix Method (TMM) is first described, as it is utilised in the simplest single, and multi-layer thin film structures. The TMM is capable of examining thin films comprised of materials with complex refractive indices, and is a fast simulation method over a wide wavelength range. Finite Difference Time Domain (FDTD) is introduced as a method for simulation of complex 3-dimensional structures. The commercial software Lumerical FDTD is used, with monitoring capability of the near, and far-field response of nanostructures. The description of a Python colour conversion script is also addressed, and is used wherever possible to determine colour response, and trends as geometries are varied.

Electron Beam Lithography (EBL), and other lithographic processes are introduced briefly, and the methods by which materials are deposited to form nanoscale structures are introduced.

Finally, the characterisation methods of the fabricated nanostructures are addressed, both in terms of the determination of structural dimensions, and the optical response under various lighting conditions and illumination angles. These measurements are used to determine the agreement between simulated structures and those fabricated.

3.1 Simulation

There are many configurations and parameters to consider when examining complex nanostructure architectures. Extensive simulation studies help to establish the structural parameters that are most sensitive to variation, and to achieve desired colours or switching capabilities of the structures. As fabrication is often costly and difficult at the nano-scale, these simulation studies are necessary in the development of a plasmonic nanostructure with the most optimal structure, that can then be fabricated. Due to the difficulty in fabrication of nanoscale devices, the results gained through simulation are important in saving time and narrowing the parameter space, and so must be robust and verifiable. In this thesis, several simulation techniques are used to determine the origin of the reflectance features, as well as the variation of certain spectral features as geometries are varied. Two primary simulation methods are used, Transfer Matrix for thin film structures, and Finite Difference Time Domain for more complex three-dimensional configurations.

3.1.1 Transfer Matrix Method

The Transfer Matrix Method (TMM) is a frequency domain numerical simulation technique that can be used to determine the transmittance, absorption, and reflectance spectra that result from a stack structure.

This method is based on a number of continuity conditions that occur with oscillating waves at the boundary of media with differing complex refractive indices, according to Maxwell's equations. The information used in a transfer matrix are the material's wavelength dependent complex refractive index (\bar{n}), and thickness (d) of each layer of material. As mentioned in Chapter 2, the complex refractive index is denoted as n for the real part and κ for the imaginary part, and follows the form of Equation 2.4. From this, the properties of a wave can be known at the start of a layer, and determined by a matrix operation at the end of the layer.

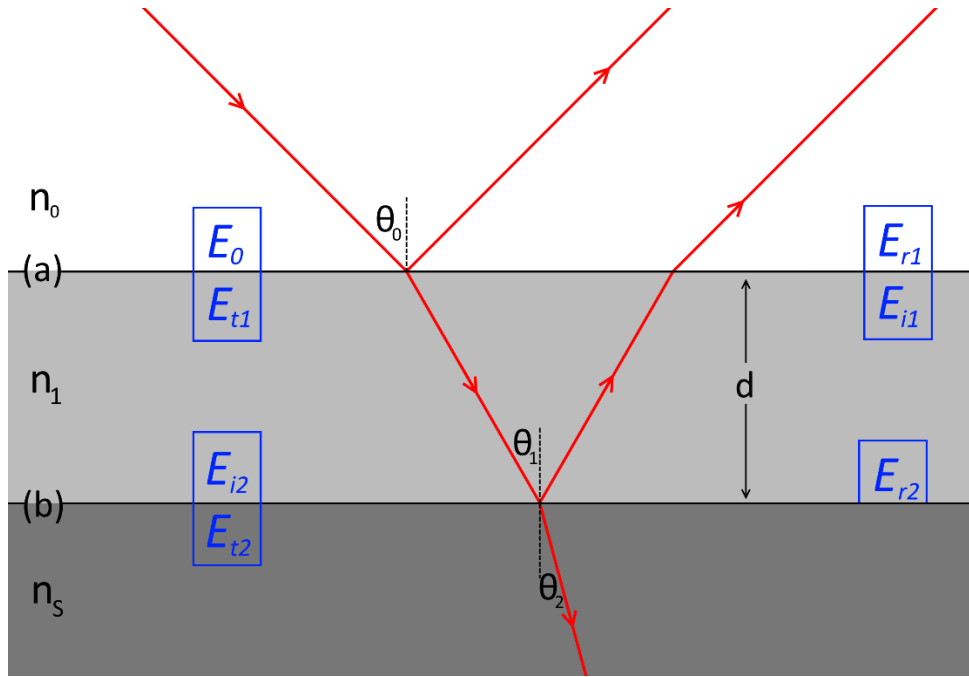


Figure 3.1: Diagram of beam with incident angle θ_0 , at a thin film interface, indicating the boundary conditions for the electric field at a and b .

Figure 3.1 reveals the boundary conditions of the wave incident on a thin film at angle, θ_0 . It is important to note that this considers an incident wave with transverse electric (TE) polarisation, where the electric field is perpendicular to the plain of incidence. From this, the E field at a and b interfaces can be determined as:

$$E_a = E_0 + E_{r1} = E_{t1} + E_{i1} \quad (3.1a)$$

$$E_b = E_{i2} + E_{r2} = E_{t2} \quad (3.1b)$$

The relation of the E and B fields can be described by:

$$B_a = \gamma_0(E_0 - E_{r1}) = \gamma_1(E_{t1} + E_{i1}) \quad (3.2a)$$

$$B_b = \gamma_1(E_{i2} + E_{r2}) = \gamma_s E_{t2} \quad (3.2b)$$

According to [156]:

$$B = \frac{n}{c} E = n \sqrt{\mu_0 \epsilon_0} E \quad (3.3)$$

where γ is:

$$\gamma_0 = n_0 \sqrt{\mu_0 \epsilon_0} \cos \theta_0 \quad (3.4a)$$

$$\gamma_1 = n_1 \sqrt{\mu_0 \epsilon_0} \cos \theta_1 \quad (3.4b)$$

$$\gamma_s = n_s \sqrt{\mu_0 \epsilon_0} \cos \theta_2 \quad (3.4c)$$

The phase difference that develops due to travelling through the layer, is described by[156]:

$$\sigma = \frac{2\pi}{\lambda_0} n_1 d \cos \theta_1 \quad (3.5)$$

where λ_0 is the wavelength of the incident light in layer n_0 . The formation of the transfer matrix from this, is described in detail by Pedrotti[156], with the matrix (M) for each layer described as:

$$M = \begin{bmatrix} \cos(\sigma) & \frac{i \sin(\sigma)}{\gamma} \\ i\gamma \sin(\sigma) & \cos(\sigma) \end{bmatrix} \quad (3.6a)$$

where

$$M = \begin{bmatrix} m_{11} & m_{12} \\ m_{21} & m_{22} \end{bmatrix} \quad (3.6b)$$

The matrix in Equation 3.6a is used to represent each layer, and by multiplication, determines the system matrix (M_T) of the entire stack, as:

$$M_T = M_1 M_2 M_3 \dots M_N \quad (3.7)$$

Here, M_N is the matrix for each layer in the stack of arbitrary layers. From this the transmission (t) and reflection (r) coefficients can be determined by[156]:

$$t = \frac{2\gamma_0}{\gamma_0 m_{11} + \gamma_0 \gamma_s m_{12} + m_{21} + \gamma_s m_{22}} \quad (3.8a)$$

$$r = \frac{\gamma_0 m_{11} + \gamma_0 \gamma_s m_{12} - m_{21} - \gamma_s m_{22}}{\gamma_0 m_{11} + \gamma_0 \gamma_s m_{12} + m_{21} + \gamma_s m_{22}} \quad (3.8b)$$

From these the Transmission (T) and Reflection (R) as a fraction of incident light intensity can be determined by:

$$T = |t|^2 \quad \text{and} \quad R = |r|^2 \quad (3.9)$$

Absorption can be measured as:

$$Absorption = 1 - T - R \quad (3.10)$$

For a *TE* polarised incident wave the γ_1 value is determined by Equation 3.4b. However, in transverse magnetic (*TM*) polarisation, the γ_1 value is determined by:

$$\gamma_1 = n_1 \frac{\sqrt{\mu_0 \epsilon_0}}{\cos \theta_1} \quad (3.11)$$

For unpolarised light at an angular incidence, an average of the reflectance can be taken, such that:

$$R = \frac{1}{2} (R_{TE} + R_{TM}) \quad (3.12)$$

All simulations in this thesis are carried out at normal incidence, with light incident perpendicular to the surface of the layer, and so the γ_1 values are the same for *TE* and *TM* polarisations.

This simulation method is suitable for thin film reflectance, transmission and absorption in single, or multi-layer stacks of materials. The technique is validated against literature in Chapter 6, used extensively in the thin film VO₂ study carried out in that Chapter.

3.1.2 Finite Difference Time Domain

Finite Difference Time Domain (FDTD) can be used to simulate the electrostatics of more complicated, three-dimensional nanoscale structures comprised of non-magnetic materials. Lumerical FDTD is a widely used commercial tool, in which simulations are generated in a Computer Aided Design (CAD) style visualisation tool that examines a simulation volume. This simulation volume is comprised of geometric components, where each object has the frequency-dependent complex refractive index information contained. A three-dimensional mesh permeates throughout the entire structure, in which the mesh intersections are the positions at which the electric and magnetic field are measured. This technique utilises the partial differential form of the time-dependent Maxwell's equations, and solves the electric field vector, followed by the magnetic field vector components sequentially and repeatedly until a steady-state field is resolved. These components are solved

at different locations within a mesh cell, known as the Yee cell, which is shown in Figure 3.2.

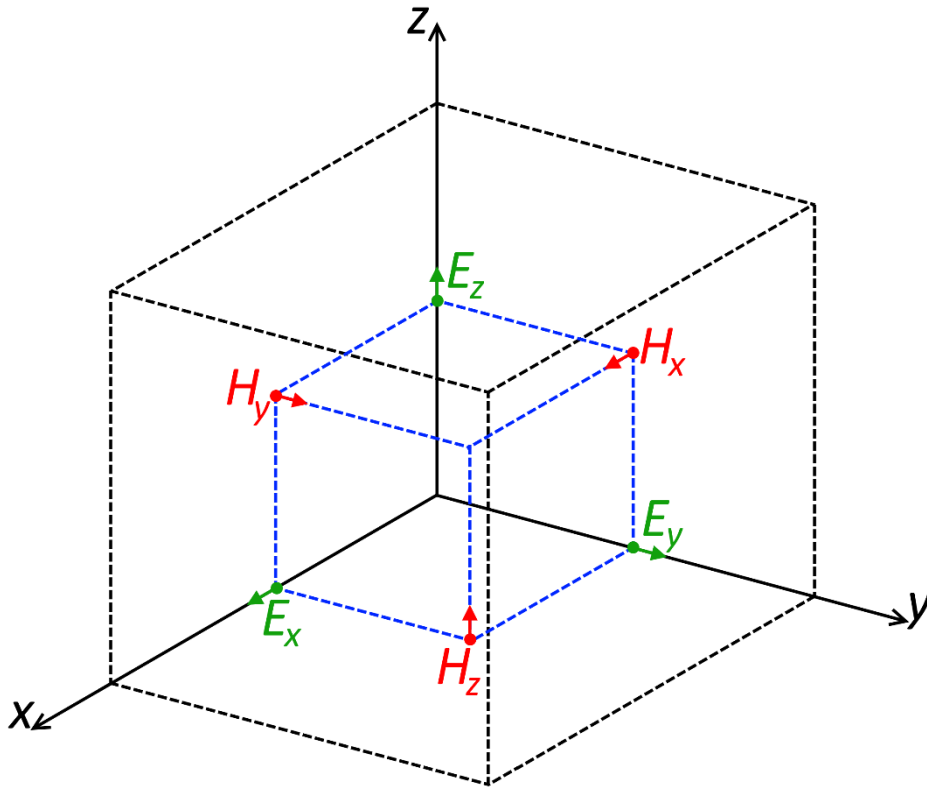


Figure 3.2: A Yee cell, used in FDTD to determine the electric and magnetic field components from the partial differential form of the time-dependent Maxwell's equations.

When the simulation has run for a sufficient time, the electric field strength reaches a steady state, falls below a set threshold value, or reaches a set time, at which point the simulation is cut off, and data is compiled. This simulation tool can be used to measure near-field and far-field information about the structures examined. The near-field refers to regions in close proximity to a polarisable component in the simulation, and is the region in which the evanescent wave of the LSPR can be measured. It is often proportional to the wavelength of the radiation emitted by an antenna or particle, known as the Fraunhofer distance (d_f), as[157]:

$$d_f = \frac{2D^2}{\lambda} \quad (3.13)$$

where D is the largest dimension of the particle. The far-field is outside this region, and concerns propagating electromagnetic waves, in which E and H are orthogonal to each other, and the propagation vector.

FDTD solver utilises the Maxwell's curl equations to find the time dependent E and H fields within the 3D mesh coordinates:

$$\nabla \times \mathbf{H} = \frac{\partial \mathbf{D}}{\partial t} \quad (3.14a)$$

$$\mathbf{D} = \varepsilon_0 \varepsilon_r \mathbf{E} \quad (3.14b)$$

$$\nabla \times \mathbf{E} = -\mu_0 \frac{\partial \mathbf{H}}{\partial t} \quad (3.14c)$$

where μ_0 is the permeability of free space. Here, D , H , and E are the Displacement, Magnetic and Electric fields. The commercial software Lumerical utilises an FDTD solver that is not capable of simulating magnetic materials. As such, the permeability of free space, μ_0 is used throughout. In a Cartesian coordinate system, Maxwell equations have six components, three for each of the Magnetic and Electric fields, according to H_x , H_y , H_z , E_x , E_y , and E_z . These fields are measured at specific positions in the Yee cell, as shown in Figure 3.2.

The curl measurements for the E and H fields are carried out sequentially in a leap-frog manner, where the time step incremented for a full sequence is Δt . It follows that the Electric field at time $t+\Delta t$ is:

$$E^{t+\Delta t} = E^t + \alpha(\nabla \times H^{t+\frac{1}{2}\Delta t}) \quad (3.15)$$

where α is a proportionality term. Similarly, the H field is measured as:

$$H^{t+\frac{3}{2}\Delta t} = H^{t+\frac{1}{2}\Delta t} + \beta(\nabla \times E^{t+\Delta t}) \quad (3.16)$$

where β is also a proportionality term. Both terms are a function of the simulation parameters, boundary conditions, stability factor, and materials. The time step function is then described as:

$$E^0 \rightarrow H^{\frac{1}{2}} \rightarrow E^1 \rightarrow H^{\frac{3}{2}} \rightarrow \dots \quad (3.17)$$

From the curl of the E field in Equation 3.14c, the partial differentials for find the derivative H can be described as:

$$\frac{\partial \mathbf{E}_z}{\partial y} - \frac{\partial \mathbf{E}_y}{\partial z} = -\mu_0 \frac{\partial \mathbf{H}_x}{\partial t} \quad (3.18a)$$

$$\frac{\partial \mathbf{E}_x}{\partial z} - \frac{\partial \mathbf{E}_z}{\partial x} = -\mu_0 \frac{\partial \mathbf{H}_y}{\partial t} \quad (3.18b)$$

$$\frac{\partial \mathbf{E}_y}{\partial x} - \frac{\partial \mathbf{E}_x}{\partial y} = -\mu_0 \frac{\partial \mathbf{H}_z}{\partial t} \quad (3.18c)$$

Similarly, the partial differentials for the derivative E are:

$$\frac{\partial \mathbf{H}_z}{\partial y} - \frac{\partial \mathbf{H}_y}{\partial z} = \varepsilon_0 \varepsilon_r \frac{\partial \mathbf{E}_x}{\partial t} \quad (3.19a)$$

$$\frac{\partial \mathbf{H}_x}{\partial z} - \frac{\partial \mathbf{H}_z}{\partial x} = \varepsilon_0 \varepsilon_r \frac{\partial \mathbf{E}_y}{\partial t} \quad (3.19b)$$

$$\frac{\partial \mathbf{H}_y}{\partial x} - \frac{\partial \mathbf{H}_x}{\partial y} = \varepsilon_0 \varepsilon_r \frac{\partial \mathbf{E}_z}{\partial t} \quad (3.19c)$$

Examining the Yee cell, for an example when calculating H_x , reveals the positions of interest in the cell, as illustrated in Figure 3.3.

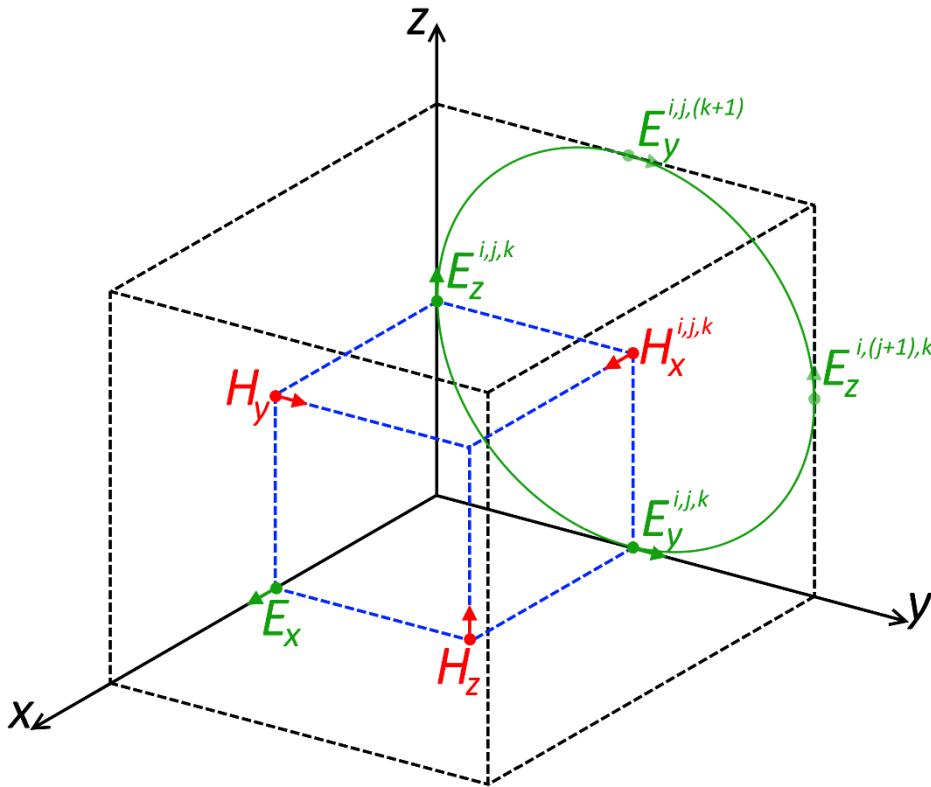


Figure 3.3: Yee cell, when measuring H_x . Measurement requires $E_y^{i,j,k}$, $E_z^{i,j,k}$, $E_y^{i,j,(k+1)}$, and $E_z^{i,(j+1),k}$ for determining $\nabla \times \mathbf{E}$.

From Figure 3.3, it is clear that this calculation requires information from neighbouring cells for the calculation of the various E and H fields, with the H_x field

requiring $E_y^{i,j,k}$, $E_z^{i,j,k}$, $E_y^{i,j,(k+1)}$, and $E_z^{i,(j+1),k}$. From this, finite difference equation required to measure H_x can be calculated as:

$$\frac{E_z^{i,(j+1),k} \Big|_t - E_z^{i,j,k} \Big|_t}{\Delta y} - \frac{E_y^{i,j,(k+1)} \Big|_t - E_y^{i,j,k} \Big|_t}{\Delta z} = -\mu_0 \frac{H_x^{i,j,k} \Big|_{t+\frac{1}{2}\Delta t} - H_x^{i,j,k} \Big|_{t-\frac{1}{2}\Delta t}}{\Delta t} \quad (3.20)$$

This calculation also occurs for H_y and H_z , with a different orientation of the E and H fields required, as described in Equations 3.18b and 3.18c, respectively. For measuring E_x , the Yee cell is again examined, and is shown in Figure 3.4.

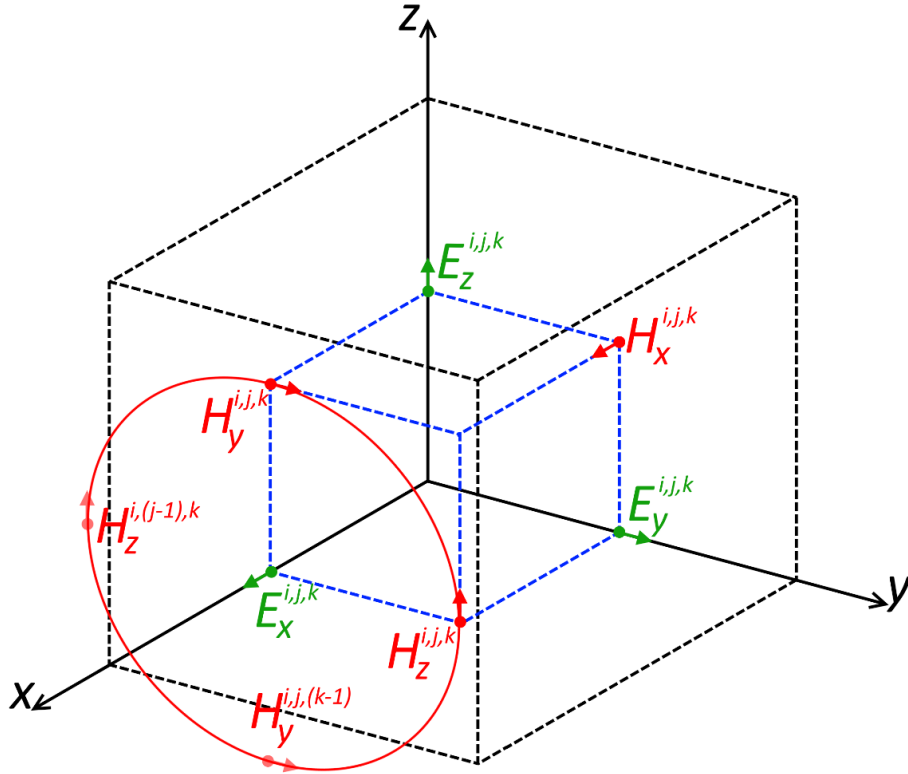


Figure 3.4: Yee cell, when measuring E_x . Measurement requires $H_y^{i,j,k}$, $H_z^{i,j,k}$, $H_y^{i,j,(k-1)}$, and $H_z^{i,(j-1),k}$ for determining $\nabla \times \mathbf{H}$. The x , y , and z co-ordinates of the cell are denoted with i , j , and k , respectively.

From Figure 3.4, the finite difference equation required to measure E_x can be calculated as:

$$\frac{H_z^{i,j,k} \Big|_{t+\frac{1}{2}\Delta t} - H_z^{i,(j-1),k} \Big|_{t+\frac{1}{2}\Delta t}}{\Delta y} - \frac{H_y^{i,j,k} \Big|_t - H_y^{i,j,(k-1)} \Big|_t}{\Delta z} = \epsilon_0 \epsilon_r \frac{E_x^{i,j,k} \Big|_{t+\Delta t} - E_x^{i,j,k} \Big|_t}{\Delta t} \quad (3.21)$$

Similar to the measurements of $H_{x,y,z}$, these calculation also occur for E_y and E_z , with a different orientation of the E and H fields required, as described in Equations 3.19b and 3.19c, respectively.

This simulation technique can be used to simulate arbitrary geometries of arbitrary materials over a broad spectral range in a single simulation. As the technique is in the time domain, all frequencies are simulated simultaneously. Nanoparticle arrays, as examined in this thesis, are simulated, utilising periodic boundary conditions, with a plane wave source. The direct measurements of the electric field (E), magnetic field (H), and Poynting vector (P) distribution are made possible using frequency dependent field profile monitors, that examine a 2-dimension cross-section of the structure being simulated, and recording the E and H fields for each mesh position. In the case of the Poynting vector, this indicates the energy flux of the EM wave, and is calculated as the cross product of the E and H fields, by[158]:

$$\mathbf{P} = \mathbf{E} \times \mathbf{H} \quad (3.22)$$

Both E and P monitors are normalised against the incident wave, which has an amplitude of 1 V/m in the electric field component. The electric field, magnetic field, and Poynting vector therefore have units of V/m, A/m, and W/m², respectively. Far-field radiation in reflectance from the structure is measured by frequency dependent monitor at 1 μm above the substrate. This monitor is a 2-dimensional plane spanning the entire simulation window, which is positioned to measure the electric and magnetic fields using the Yee cells across the plane. This measures the intensity and frequency of oscillations as the simulation is carried out and then proceeds to compile the data from the entire simulation time-frame upon completion of the simulation, to be used for determining far-field reflectance. This compiling normalises the response against the incident plane wave, and transforms the data to wavelength, in the range of 360-830 nm. A mesh size of 1 nm is used throughout, with a conformal mesh of 1. This is a technology utilised by the Lumerical software to reduce the impact of structural variations within a single Yee cell, by solving the Maxwell's integral equations near structure boundaries.

A disadvantage of the FDTD method is that the simulations must run long enough for the steady-state regime to be reached before completion and data compilation, to avoid pollution of the data by transient components of the nanostructure

response. The meshing density is also a major factor in simulations, as the domain is discretized with a rectangular mesh, and so staircasing effects are evident when simulating circular geometries, especially with large mesh step sizes. This is avoided in simulation here with a combination of mesh sizes that are significantly smaller than the geometric features, and the use of the conformal mesh in Lumerical. It should also be noted that simulation time scales with the 4th power of the mesh unit length, as time is also discretized proportional to the spatial dimensions. This can lead to an enormous increase in computational time and resources as mesh size is reduced.

3.1.3 Discrete Dipole

The discrete dipole method or approximation (DDA)[159,160] is an alternative technique to that of FDTD that follows the quasi-static dipole approximation described in Chapter 2. This method treats the system as a response of many individual electric dipoles; the individual dipoles are modelled with a particular polarizability, determined by the material parameters of the particle. The technique is used to determine the scattering and absorption properties of electromagnetic radiation in objects of arbitrary geometry.

An advantage of using this type of technique is that it immediately assumes a steady state approximation, as it works in the frequency domain, and so simulations do not need to run until transient oscillations die away.

As with TMM, DDA is a frequency domain simulation method, and so a simulation must be completed for each frequency. This is a disadvantage when simulating broad frequency or wavelength ranges compared to FDTD, as increasing the range has an impact on simulation time. The computational resources required for simulation also scale with the number of dipoles assumed in the structure, similar to the mesh density in the FDTD method. As the number of dipoles scales in three dimensions, a similar increase in computational time and resource requirements are noted as structure size and complexity are increased.

3.1.4 Refractive Index information

The frequency dependent complex refractive index information for all materials used in simulation (Ag, Al, Al₂O₃, Au, Cr, Pt, Si, and SiO₂) have been taken from Palik[161]. The Lumerical FDTD commercial software includes a library of refractive index information from Palik[161], which is fit with a polynomial in order to be used in the calculations of the E and H fields in the simulation. This polynomial fitted data is exported and also used in the Transfer Matrix simulations. Any data to be used in the Transfer Matrix that is not present in the Lumerical library, is first imported to Lumerical, fitted and then exported, to ensure that the data used in both simulation tools remains consistent. This is the case for the semiconducting and metallic states of VO₂, sourced from Cormier *et al*[17], as well as dielectric materials measured by ellipsometry, such as the polymer utilised in Chapter 5.

Multiple angle ellipsometry measurements are carried out on dielectric materials, such as the negative tone e-beam resist; ma-N and the propylene based polymer; Tafmer.

3.1.5 Colour conversion of spectra to sRGB and CIE xyY

The reflectance spectra calculated in FDTD and TMM simulation are formed by far-field propagating waves, which can be directly observed. In the case of visible wavelengths, in the region of 400-700 nm, these present as colours in human vision. A colour conversion script has been developed, to convert the spectra to a red, green and blue (RGB) colour space. The reflectance spectra throughout the manuscript are presented in their corresponding standard RGB (sRGB) value colour, unless otherwise stated.

The sRGB is a gamma corrected RGB colour model, widely used in digital display technology. Gamma correction is a non-linear transformation applied to the RGB values to allow for more increments at low luminance values, where the human eye is more sensitive to variation[162]. This results in more widely spaced values at high luminance, where colour vision is less sensitive to change. Pixels used in computer displays are in the vast majority of cases made up of three sub-pixels, each of which

is responsible for displaying one of the three primary colours. The spectral intensity distribution for each of these sub-pixels produces colour that significantly overlaps with the wavelengths ranges of the three colour cones in the retina of the human eye.

The conversion process is white-balanced against a D65 illuminant spectrum, $S(\lambda)$, which is shown in Figure 3.5, and is used throughout this thesis to simulate structures under daylight illumination. The D65 standard illuminant represents a noon daylight spectrum[163], and approximately follows the spectral emittance (M_λ) of a blackbody radiator at 6500 Kelvin, according to the Planck's law, as[156]:

$$M_\lambda = \frac{2\pi hc^2}{\lambda^5} \left(\frac{1}{e^{\frac{hc}{\lambda k_B T}} - 1} \right) \quad (3.23)$$

where h is the Planck constant, c is the speed of light, λ is the wavelength, k_B is the Boltzmann constant, and T is the temperature, in Kelvin.

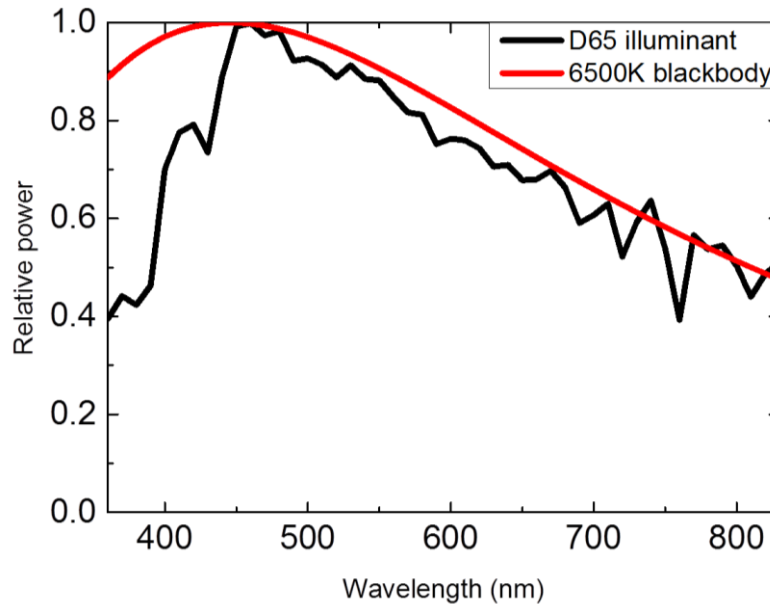


Figure 3.5: Relative spectral power distribution of the D65 solar spectrum[163], and normalised 6500 Kelvin blackbody radiator, according to Equation 3.23.

The colour conversion process takes the reflectance spectrum, $R(\lambda)$, and weights it against three functions; $x(\lambda)$, $y(\lambda)$, and $z(\lambda)$. These are the CIE 2° standard observer functions[153], whose distributions are shown in Figure 3.6.

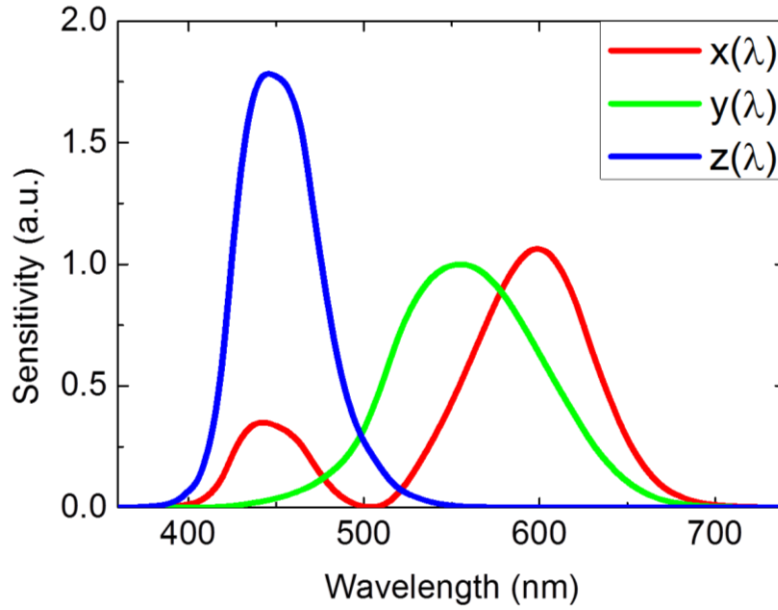


Figure 3.6: CIE 2° observer colour matching functions used to weight spectra, to obtain CIE XYZ values.

The $y(\lambda)$ curve describes the luminosity of a colour, and is analogous to the luminous efficiency function, which describes the average sensitivity over all three colour cones to the perception of brightness[153]. The $x(\lambda)$ and $z(\lambda)$ curves are used to determine colour chromaticity, with $x(\lambda)$ representing a mix of cone responses, and $z(\lambda)$ functioning to represent the short (blue) colour cone. All the curves have only non-zero values in the 400-700 nm region, and visible region is often described by this wavelength range. Simulations throughout the manuscript take place in the 360-830 nm wavelength range to gain some information to the near-UV and near-IR regions. These are used to find the CIE XYZ values for the spectrum, as[153]:

$$X = \frac{100}{K} \int_{360}^{830} R(\lambda) x(\lambda) S(\lambda) d\lambda \quad (3.24a)$$

$$Y = \frac{100}{K} \int_{360}^{830} R(\lambda) y(\lambda) S(\lambda) d\lambda \quad (3.24b)$$

$$Z = \frac{100}{K} \int_{360}^{830} R(\lambda) z(\lambda) S(\lambda) d\lambda \quad (3.24c)$$

where K is the luminosity function of a perfect reflectance diffuser, and acts as a normalising function. It is defined as:

$$K = \int_{360}^{830} (\lambda) S(\lambda) d\lambda \quad (3.25)$$

This weights the D65 illuminant spectrum against the $y(\lambda)$ curve, the luminous efficiency function, to determine the highest possible luminosity under the illumination conditions. This results in CIE XYZ values with a value range of 0-100.

To convert these XYZ values to RGB, they must first be set as decimals, by:

$$X_d = \frac{X}{100} \quad (3.26a)$$

$$Y_d = \frac{Y}{100} \quad (3.26b)$$

$$Z_d = \frac{Z}{100} \quad (3.26c)$$

As RGB values are a linear combination of CIE XYZ responses, a matrix operation can then be carried, as[164]:

$$\begin{bmatrix} R \\ G \\ B \end{bmatrix} = \begin{bmatrix} X_{R.max} & X_{G.max} & X_{B.max} \\ Y_{R.max} & Y_{G.max} & Y_{B.max} \\ Z_{R.max} & Z_{G.max} & Z_{B.max} \end{bmatrix}^{-1} \begin{bmatrix} X \\ Y \\ Z \end{bmatrix} \quad (3.27)$$

These take the form[165]:

$$\begin{bmatrix} R \\ G \\ B \end{bmatrix} = \begin{bmatrix} 3.2405 & -1.5371 & -0.4985 \\ -0.9693 & 1.8706 & 0.0416 \\ 0.0556 & -0.2040 & 1.0572 \end{bmatrix} \begin{bmatrix} X \\ Y \\ Z \end{bmatrix} \quad (3.28)$$

This outputs RGB values ranging from 0-1, which be gamma corrected and multiplied by 255 to form 8-bit sRGB values.

Gamma-correction applies a non-linear transform to the RGB values, to account for the non-linear response to luminance in human colour vision[162]. The gamma-correction function is applied to the linear R, G, and B values, and is described by[166]:

$$R_{sRGB} \begin{cases} 12.92R_{linear} & R_{linear} \leq 0.0031308 \\ \left(1.055R_{linear}^{\frac{1}{2.4}}\right) - 0.055 & R_{linear} > 0.0031308 \end{cases} \quad (3.29a)$$

$$G_{sRGB} \begin{cases} 12.92G_{linear} & G_{linear} \leq 0.0031308 \\ \left(1.055G_{linear}^{\frac{1}{2.4}}\right) - 0.055 & G_{linear} > 0.0031308 \end{cases} \quad (3.29b)$$

$$B_{sRGB} \begin{cases} 12.92B_{linear} & B_{linear} \leq 0.0031308 \\ \left(1.055B_{linear}^{\frac{1}{2.4}}\right) - 0.055 & B_{linear} > 0.0031308 \end{cases} \quad (3.29c)$$

The standard decoding gamma for sRGB is $\gamma = 2.2$. An exponent of 2.4 is used, to compensate for the linear threshold region below 0.0031308. This transform returns fractional (0-1) sRGB values, which must be multiplied by 255 and rounded to generate 8-bit sRGB values.

The XYZ primaries can also be mapped on to the CIE xyY plot, with the functions[167,168]:

$$x = \frac{X}{X + Y + Z} \quad (3.30a)$$

$$y = \frac{Y}{X + Y + Z} \quad (3.30b)$$

$$Y = Y \quad (3.30c)$$

Recall that the Y value in the xyY is the Y primary in the CIE standard observer functions, and denotes luminance. These values are plotted on the CIE xyY colour-space map, as seen in Figure 2.15. An example calculation of the XYZ to sRGB, and XYZ to xyY transforms are included in Appendix C for a sample XYZ input. Appendix C also includes sRGB and xyY colour value data for all spectra presented in the thesis.

3.2 Fabrication

The fabrication of even simple thin film structures can be challenging, due to the need for fabrication methods with reproducible geometries, that keep the variation of structural parameters at a minimum. When creating nanoscale arrays of particles, this complication is increased further, as fabrication is taking place on scales nearing the lower limit of resolution possible in state-of-the-art equipment[169]. Here, the methods employed to pattern nanostructure arrays of metal nanoparticles by lithography techniques, and the methods of deposition of the materials are presented. Also introduced are the techniques of verifying the dimensions and materials of the structures once fabricated. Finally, the optical characterisation techniques used to measure the fabricated samples are described.

3.2.1 Lithography

The primary method for fabrication of nanoscale array structures is by use of a lithography process. Many industries working in the nanoscale use photolithography to produce structures in large quantities with incredibly high accuracy, and it is a technology that is quickly improving to push the lower limit of resolution of manufacture, by using shorter and shorter wavelengths of light to reduce the diffraction limit of the features, and utilising other physical phenomenon such as photo interferometry to use interference patterns to further increase resolution[160].

Photolithography works by the process of coating a substrate with a photosensitive polymer material, known as a photo-resist. Deep-Ultraviolet (DUV) radiation is used to pattern the photo-resist, breaking or forming new bonds in the polymer chains, after which a developer solution removes the more soluble, short chain material. Though photolithography does have many applications in the manufacturing of nanoscale structures the resolution is limited, and surpassed by electron[170], and ion[171] beam lithography.

Ion beam lithography utilises charged particles, such as Helium or Neon ions which are accelerated to high velocity by a high voltage bias[172,173]. A typical Helium Ion Microscope column is shown in Figure 3.7. Similarly, electron beam lithography uses electrons. These are used in place of photons, and follow a similar principle to that of photolithography. A resist material is deposited to the surface in a thin layer (typically 100-400nm)[6,12,174] and a pattern is exposed, with the ions or electrons impacting the substrate and breaking polymer bonds this is then developed to selectively remove areas of resist, before further processing, such as deposition of metals.

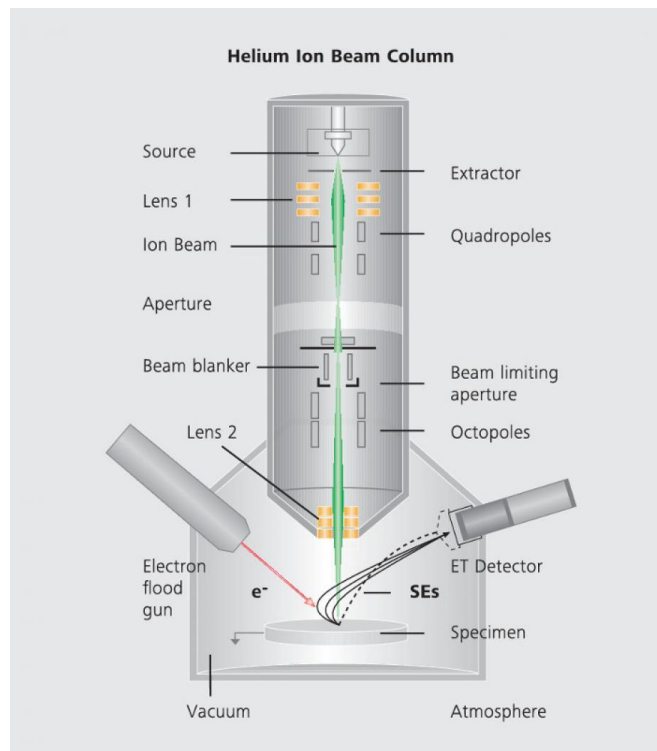


Figure 3.7: Schematic of a Zeiss Orion nano-fab column, used for Helium ion lithography[175].

In Electron Beam Lithography (EBL), electrons are accelerated at high vacuum by high voltage of typically 30kV. The electrons are focused and directed through magnetic lenses. This focused electron beam is then fired at the substrate and causes a change in the resist material deposited, making it more, or less soluble to a developer solution by changing the polymer length. Patterning is achieved through a combination of magnetic lenses that deflect the beam, so that it can be directed to specific parts of the target, and a beam blanker mechanism, that blocks the electron beam from striking the surface when engaged.

This combination of beam manipulation makes it possible to pattern separated structures on the target in a 2D plane. The advantage of using Helium ions, or similar ions such as Neon over electrons, is that they can impart more of their momentum to the resist layer, and are more massive, reducing the required dose. HIL is a powerful technique, that has been utilised to extremely high-fidelity structures[33,176–178], and has demonstrated a resolution on the order of 10 nm[179], with dense array structures possible due to the reduction in secondary

electrons from adjacent array cells. However, HIL is not utilised in this thesis, as structures were demonstrated to be within the resolution range of EBL.

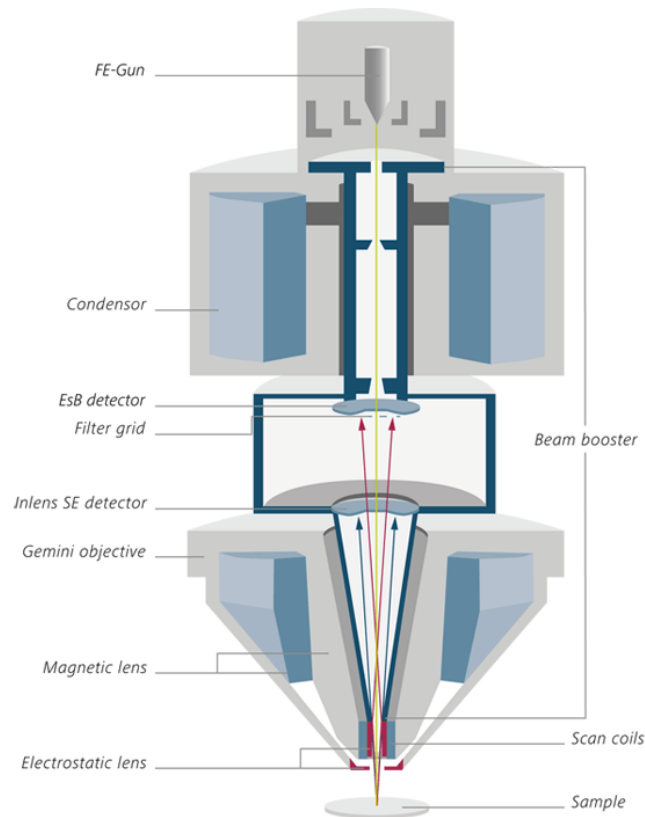


Figure 3.8: Schematic of a Zeiss Gemini column, as used in the Supra FE-SEM for electron lithography and imaging[180].

Field Emission Scanning Electron Microscopes (FE-SEMs) are often used for SEM imaging[181–183], and lithography of patterned nanostructures[20,58], as they provide high voltage electrons in a controlled stream that can maintain precise beam current[184]. The Carl Zeiss Supra FE-SEM is the primary lithography tool used for Chapter 5 in the Hybrid nanostructure, and a schematic is shown in Figure 3.8. The Field Emission source is a very sharp single crystal Zirconium tip that has a high bias voltage applied, with the tip acting as a cathode, and an anode located further down the column[184]. This voltage can vary from 1kV for imaging, to over 30kV for lithography. Electrons are ripped from the tip in a very controlled fashion, with very little stray electrons being produced. This results in a beam that is highly collimated, and capable of higher resolutions than that of the more common Tungsten filament thermal source method, particularly at low voltages. However,

these systems have been utilised at extremely high voltages (100kV) for nanoscale array fabrication[6,185,186].

Laser alignment stages are also available in some of the EBL tools. An Elionix 7700 is a thermal source SEM tool with a laser stage, used to fabricate larger samples by stitching small sub-sections together. These stages use laser interferometry to closely monitor the position of the position of the sample being processed. Detectors monitor the position of the stage, and correct any drift that occurs over the course of exposure. This leads to less misalignment in an exposed pattern over the course of exposure, and allows for much larger arrays to be produced with better stitching between smaller elements of the overall design. Though the resolution is not as sharp in thermal SEM systems, this tool is used in chapter 4 on the large scale 5 mm Aluminium nanostructure sample. This is done as the features and unit cell of the Aluminium structure are within the operating parameters of the Elionix system, and fabrication on this SEM allows for the creation of a very large sample.

3.2.2 Resists and Development

Patterning of the Aluminium nanostructure in Chapter 4 is carried out with Micro Resist ma-N 2401 negative tone electron-beam resist, which is sensitive to high energy electron and UV exposure. Negative tone resists remain on the substrate after exposure, with the developer solution removing all unexposed resist material. This resist is composed of novolac; phenolic resin which acts as a polymeric bonding agent, and bisazide; a photoactive compound that reacts to form an acid under exposure. The acid renders the resin component insoluble in an aqueous-alkaline developer solution after exposure. In the case of ma-N, this is the Micro Resist ma-D 525 developer solution.

Polymethyl Methacrylate (PMMA) is a common polymer based positive tone resist used in EBL that can also be applied to UV and X-Ray lithography processes. It is also sold under the commercial name of Plexiglas, Lucite or Perspex. Positive tone resists are exposed in the area that is intended to be removed. After exposure, the material becomes more soluble to the developer material, and is dissolved. The

PMMA utilised in Chapter 5 is Micro Chem PMMA 950 A3 with 950,000 average molecular weight in Anisole. On exposure to high energy particles, the bonds in the polymer break to form shorter chain polymers that are then more easily dissolved in a solvent. Methyl Isobutyl Ketone (MIBK) is used as a developer solution, often diluted with Isopropyl Alcohol (IPA) to vary the strength and speed of the developing process.

After the development process of a resist, the entire sample is coated with a thin metal film, by Physical Vapour Deposition (PVD). This is a line of sight technique, with normal incidence, and so only the tops of structures are coated in this process. In the case of a positive tone e-beam resist such as PMMA, Acetone can then be used to remove the resist material that remained after the patterning and development process, also resulting in the metal being removed from those areas. This leaves metal in the areas that the pattern had originally created in lithography. In structures where negative tone resists have been used, deposition results in the metal coating the top surface of the pattern, and the background, or backreflector. The resulting structure consists of metal supported on dielectric blocks, with a lower backreflector coated everywhere but the patterned areas.

3.2.3 Material Deposition

Deposition of thin films can be achieved by two methods, depending on the material in question. For dielectric materials; spin coating is used, and for metals; Electron Beam Physical Vapor Deposition (EB-PVD) is carried out.

For the deposition of dielectric materials, a spin coater is used to deposit the materials, with varying concentration, spin speed, time and ramp speed all affecting the thickness and uniformity of the final film. This method is capable of reproducibly depositing several nanometre thick layers of dielectrics onto a substrate. This is often followed by heating on a hot plate to drive off the remaining solvents and anneal the material to provide a more stable layer.

EB-PVD is carried out in a Temescal 7700 system. This system uses high energy electrons incident upon a target material, which evaporates the material from the

target and deposits it on the substrate under high vacuum[187]. This method is also capable of depositing several nanometre thick layers, with elemental metals such as Ag, Al, Au, and Cr available as target materials.

3.3 Characterisation

A comprehensive characterisation of the samples fabricated must be carried out, to measure the physical dimensions of the structure, and determine the optical response. This includes measurements of the structures components; the disc diameter, unit cell size, and material thicknesses, as well as the refractive index of all materials. Accurate optical characterisation is also important, as it is the means by which the response of the structure is assessed and compared to simulation. As some structures exhibit angular effects, notably that of the structure explored in Chapter 4, these are also characterised using an in-house system.

3.3.1 Structural parameters

The lateral dimensions of fabricated structures, such as diameter and unit cell size, are measured using the Carl Zeiss Supra FE-SEM, described above. A low accelerating voltage of <5kV is often used, in comparison to the >15kV used in lithography. This allows for the imaging of surface detail, such as the metal discs patterned in the structures of Chapters 4 and 5. Thickness measurements are carried out on a Dektak profilometer in the case of the metallic components of the structure. The hardness of metals allows for measurement by profilometer without deformation of the material. Dielectrics are measured on the Dektak and using multiple angle ellipsometry to verify results, as profilometry is a contacted measurement with potential to deform soft materials, leading to inaccurate results. Multiple angle ellipsometry is also used to determine the refractive index information of the ma-N resist material, and the Tafmer polymer used as a separating layer in Chapter 5. Refractive index information of the material before and after exposure to the lithography process is carried out, as the areas under the discs are exposed to the electron beam during the lithography process, and remain

after processing. The refractive index information of PMMA is not required, as it is not present in the final structure.

3.3.2 Normal incidence measurements

For normal incidence measurements of the structures, an in-house system is used for the measurement of reflection, and is shown in figure 3.10. A xenon lamp is used for illumination, to provide characterisation across a wide spectrum, including the visible region. The spectrum for the Xenon arc lamp as measured by the in-house optical characterisation system shown in Figure 3.9.

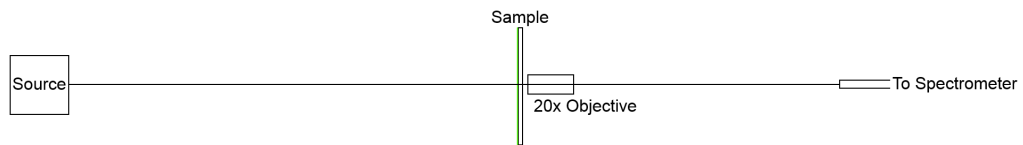


Figure 3.9: In-house optical characterisation setup for measuring transmission through samples. In the case of the Xenon lamp, there is no sample present.

The spectrum is shown in Figure 3.10, with the manufacturers reference also included.

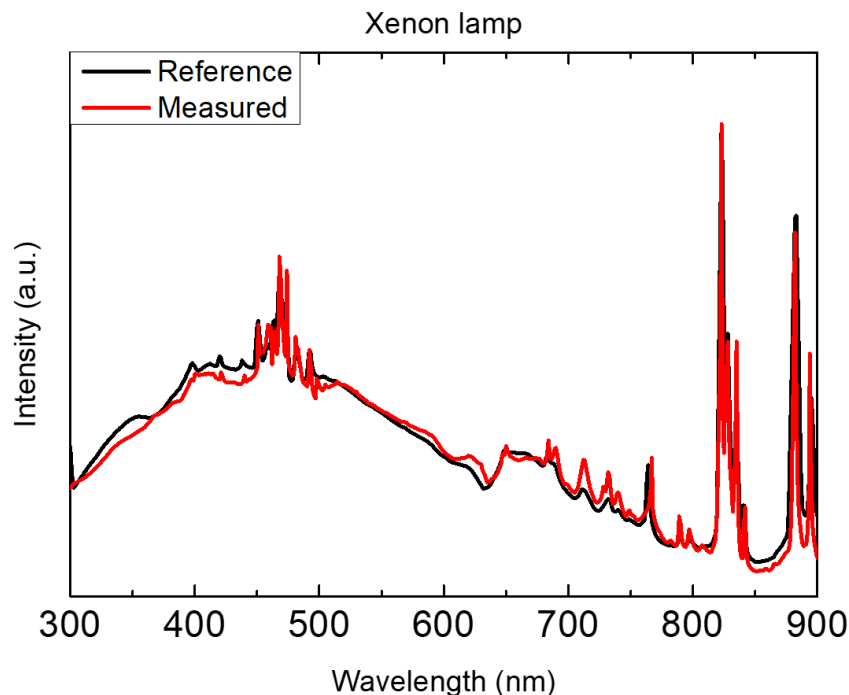


Figure 3.10: Spectrum of Xenon arc lamp source intensity, with reference spectrum from manufacturer. Spectra extended to 300-900 nm to illustrate thermal peaks.

Figure 3.10 illustrates the xenon arc lamp spectrum, extended to 300-900 nm in order to illustrate the sharp, narrow peaks present at longer wavelengths. This limits the

use of the xenon lamp to the visible, as the noise associated with measuring in regions of intense peaks is significant. As measurements throughout the thesis are focused on colour, the 360-830 nm region provided by the source is suitable for reflectance measurements with minimal noise. A liquid Nitrogen cooled synergJ CCD is used in conjunction with a Jobin Yvon Horiba triax 190 UV-Visible spectrometer to collect spectral data across this region.

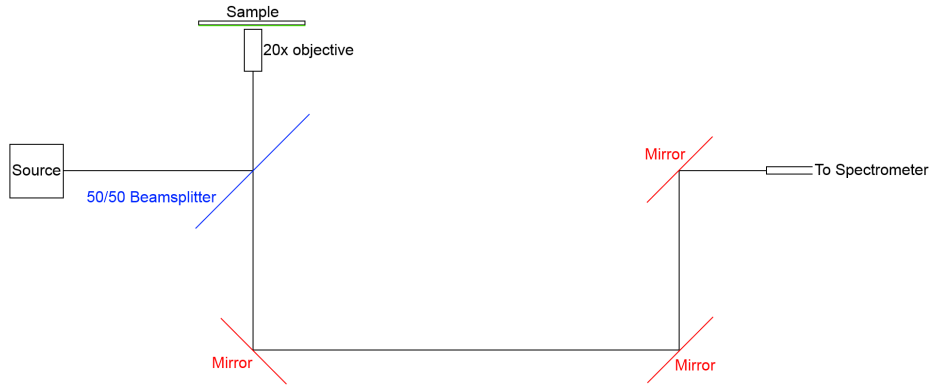


Figure 3.11: Schematic of the normal-incident characterisation setup, with a 50/50 beam splitter, 20x objective, and mirrors to direct the beam to the spectrometer. A Xenon arc lamp is the source used.

Using the apparatus in Figure 3.11, the reflectance of a reference mirror (R_{Mirror}) is measured, and noise (R_0) is subtracted by measuring the system with no sample present. This is weighted against the theoretical reflectance of the mirror, as stated by the manufacturer (R_{Ref}), to find the reflectance intensity of a perfect reflector (R_p) in the system, as:

$$R_p = \frac{R_{Mirror} - R_0}{R_{Ref}} \quad (3.31)$$

From this, reflectance spectra of samples (R_s) can be measured in the system, by:

$$R_s = \frac{R_{measured} - R_0}{R_p} \quad (3.32)$$

The spectra collected in simulation and characterisation are a function of an intensity ratio. As a result, all values are treated as a maximum of 1 for 100% reflectance. Reflectance measurements for a 10 nm Ag film is shown, as measured by the reflectance setup in Figure 3.12, with data from TMM and FDTD simulation

also included. Samples were fabricated by Temescal EB-PVD, with a deposition rate of 0.5 \AA/s .

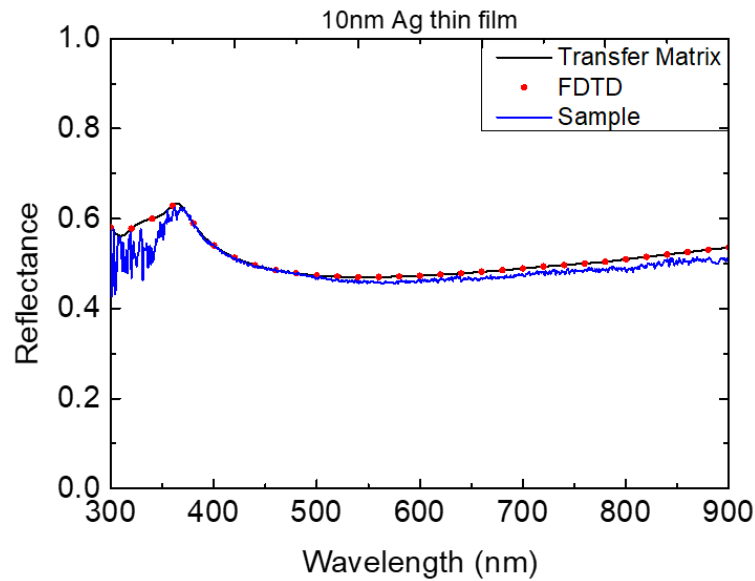


Figure 3.12: Normal incidence reflectance spectrum of 10 nm Ag thin film on Si, fabricated by EBPVD. Comparison by simulation, with Transfer Matrix and FDTD, for a 10 nm Ag film on Si.

3.3.3 Angular measurements

For the measurements of the diffractive effects exhibited by the structure in Chapter 4, an angular measurement apparatus is used, and is shown in Figure 3.13.

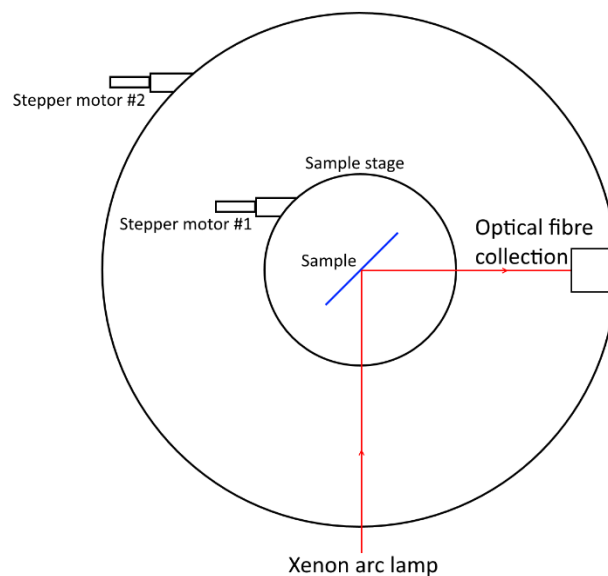


Figure 3.13: Angular characterisation apparatus, with white light from the Xenon arc lamp incident on the sample. The sample stage is raised above stage supporting the spectrometer collection. Stepper motor #1 is used to vary incident angle, and stepper motor #2 used to vary collection angle of the optical fibre.

Stepper motor resolutions for both #1 and #2 is approximately 1° , for measurement of both incident and collection angles, to fully characterise the angular and spectral dependence of the structure. Illumination in this setup is with the Xenon arc lamp, collimated with a lens, and an iris used to reduce spot size to the array dimensions. Spectral data is collected using a single-mode optical fibre, and measured by liquid Nitrogen cooled synergJ CCD and Jobin Yvon Horiba triax 190 UV-Visible spectrometer.

3.4 Conclusion

This chapter has introduced the methods of simulation, fabrication and characterisation of nanostructures examined in this manuscript.

The principle of operation of the TMM and FDTD have been described, and their use in the simulation of thin film, and more complex plasmonic structures. In particular, the Lumerical commercial simulation software has been introduced, and is the primary simulation tool for structures in Chapters 4, 5 and 7, due to the ability to examine complex three-dimensional structures. The method of colour conversion is described, through the use of the 1931 CIE 2^o standard observer functions, which is converted to the xyY and sRGB colour-spaces, to help determine colour response, and trends as geometries are varied.

The Carl Zeiss FE-SEM has been chosen as the primary EBL and characterisation tool for measurement of lateral dimensions of finished structures. Material deposition methods have been shown, in dielectric materials; by spin coating, and in metals; by EB-PVD.

Finally, the optical characterisation methods have been described, with xenon lamp excitation, and a UV-Vis spectrometer used to examine the structure across the visible region. Angular optical characterisation has shown using the same systems, but also utilising two stepper motors to rotate the sample and collection fiber.

Chapter 4

Aluminium Nanostructure

Summary

In this chapter, a plasmonic nanostructure is introduced, capable of generating structural colour by the interaction of an array of nanodiscs with nanoholes. The structure consists of an array of Aluminium nanodiscs positioned directly above an array of holes of the same dimension and separated by a dielectric pillar. The interaction between these components results in a strong resonance condition, known as Fano resonance, which directly alters the colour observed in the far-field.

Structures are first simulated using a finite-difference time-domain (FDTD) simulation method, which is validated against literature results which use a similar structure. The structure is simulated under white light illumination, and record the electric field (E) and Poynting vector (P) profiles in a cross section, as well as the far-field reflectance to be observed. These spectra are then converted to a sRGB value, to better determine colour trends as the geometries of the structure are varied.

Structures are fabricated on a glass quartz substrate, using Electron Beam Lithography (EBL), and the structural parameters are determined by SEM and Dektak measurements. Normal incidence spectral characterisation is carried out, and reflectance spectra are fitted against corresponding simulated structures, with good agreement. Angular characterisation shows first order diffraction effects, resulting from the relatively large 400nm pitch of the array acting as a diffraction grating.

4.1 Simulation

A commercial FDTD simulation tool, as mentioned in Chapter 2, is used to determine the far-field reflection, as well as visualise the electric field (E) and

Poynting vector (P) profiles throughout the structure in the xz plane. A plane wave at normal incidence to the substrate is used in all simulations, with propagation direction in the z -axis, polarised along the x -axis, as shown in Figure 4.1.

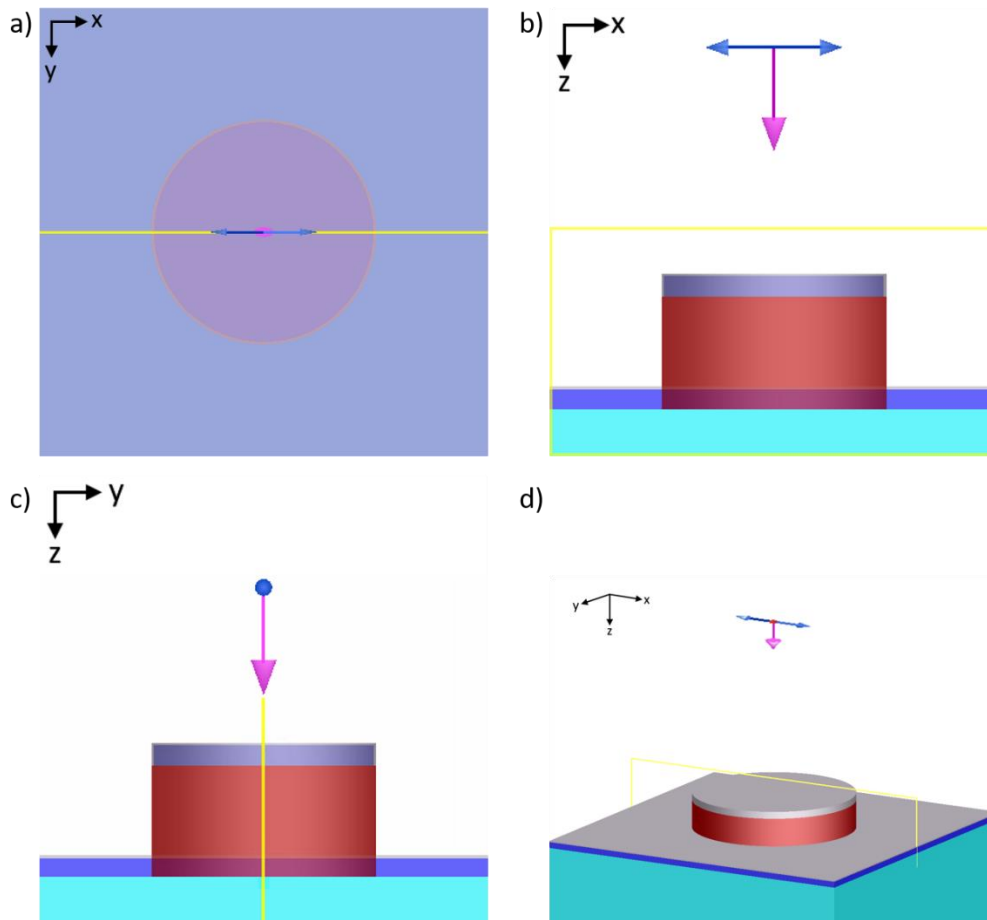


Figure 4.1: FDTD simulation space, illustrating the x , y , and z axes. (a) Top down (xy plane) (b) side view (xz plane), (c) side view (yz plane), and (d) perspective view. Polarisation and direction of plane wave source shown in all figures, as well as E and P field monitor.

Analysis of this data is used to determine the spectral response of the nanostructure, as well as to analyse the origin of the features presented. The simulation tool was first validated against a literature report, using a similar nanostructure[6] to those used in this study. This study provided simulation and experimental spectral data in the visible region for a range of disc diameters, allowing for robust validation of the simulation technique.

Once validated, the Aluminium structure under consideration in this chapter was then simulated. Firstly, structural components were examined, to determine their

role in generating spectral features, with particular attention paid to the E and P profiles at several points in the fully assembled structure. Finally, a range of geometries were tested to determine the sensitivity of reflectance features to variation, with colour conversion used to more easily follow trends.

4.1.1 Validation

FDTD is a simulation method used widely to examine complex plasmonic nanostructures. The FDTD simulation tool was validated against Kumar *et al.* "Printing at the optical diffraction limit"[6], due to the data presented consisting of both FDTD simulation and experimental data, over a range of diameters. This allowed for the simulation tool to be tested against another FDTD simulation results, as well as experimental data. Due to simulations being carried out over a range of diameters, it also allowed for trends to be matched, resulting in further validation of the simulation method.

A schematic of the structure is shown in Figure 4.2, which consists of a Si substrate, with hydrogen silsesquioxane (HSQ) pillars of 95 nm height in a square array, patterned onto the substrate[6]. After patterning, metals are then deposited, consisting of a Cr adhesion layer of 1 nm thickness, Ag layer of 15nm, and a capping Au layer of 5 nm to protect the structure from tarnishing[33]. This metal layer configuration is present on both the backreflector and top of the HSQ pillars, resulting in disc-hole nanostructure, with a fixed gap between pillars of 120 nm. The disc diameter is varied from 50-140 nm, in 10 nm steps. As a result, the pitch of the array increases with the increasing diameter.

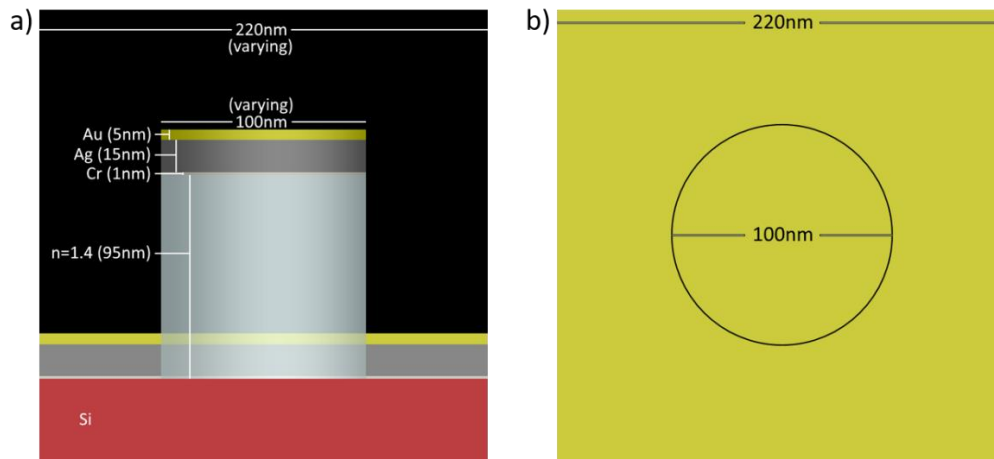


Figure 4.2: Example schematic of Kumar *et al.*[6] structure, consisting of CrAgAu with (1-15-5) nm thickness respectively. HSQ height of 95 nm, and 100 nm diameter with gap of 120 nm (220 pitch). From (a) side view (xz plane) and (b) top view (xy plane).

The refractive indices of Si, Cr, Ag, and Au were taken from Palik[161]. HSQ index was $n=1.4$, and periodic boundary conditions were used, as used in the simulations carried out by Kumar *et al.*[6]. Good agreement was established over the diameter range, with results presented in Figure 4.3.

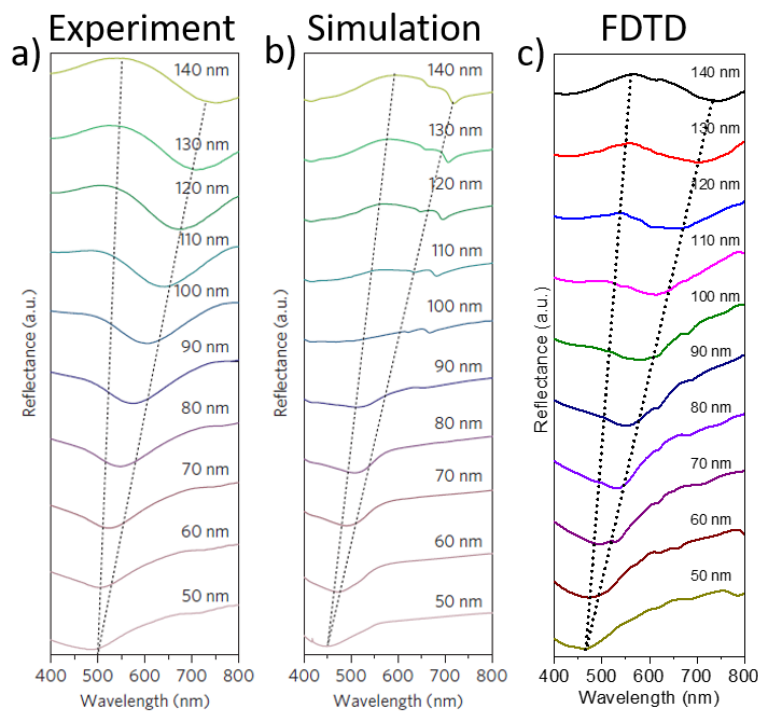


Figure 4.3: Reflectance spectra from Kumar *et al.* (a) Fabricated samples (b) Simulations, and (c) our FDTD reflectance spectra for CrAgAu structure with fixed 120 nm gap, and diameter variation 50-140 nm in 10nm steps[6].

Literature values of (a) experimental[6], (b) simulation[6], and the results of our FDTD simulation labelled (c), FDTD match well together over the full diameter range, with a particularly close match between the experimental results, and our FDTD spectra. To further examine this, the peak and dip positions for each diameter test were determined, and plotted, and are shown in Figure 4.3, comparing the simulation, experimental and our FDTD results.

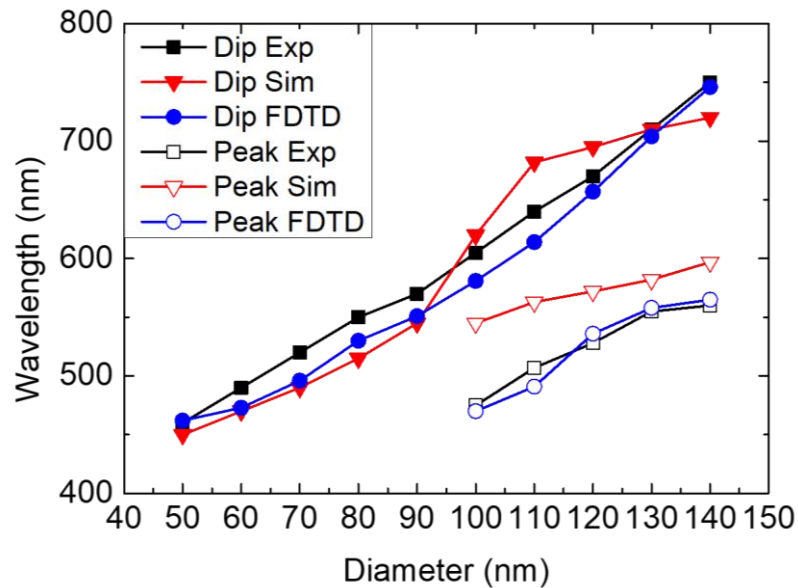


Figure 4.4: Peak and dip positions as a function of diameter for, comparing fabricated samples (Dip Exp, Peak Exp), paper simulation (Dip Sim, Peak Sim), and our FDTD simulation (Dip FDTD, Peak FDTD) undertaken to validate tool.

From Figure 4.4, a near-linear trend of both peak and dip position can be seen in the experimental results, with peaks only present in 100-150 nm disc diameter cases, as revealed in Figure 4.3. The paper results show good agreement between simulation and experiment, though the dip trend presents a sharp red-shift in dip position in the 90-100 nm diameters, and a reduced peak movement in the 110-140 nm diameters. Peak positions of the report simulation are also offset in wavelength by approximately 30-50 nm in all cases.

In the case of our FDTD simulations, a closer agreement with experimental results from Kumar *et al.*[6] are noted overall. In all but one case (100 nm diameter), the dips are closer in wavelength than the report simulations for every diameter simulated, and peak positions are particularly closer to the experimental results.

The position of these peaks is key to establish when converting to an additive colour model such as sRGB, as they are the primary feature used to determine the colour generated.

From this test, the FDTD simulation method was validated as a tool for determining accurate reflectance spectra in nanoscale metallic disc arrays. From here, simulation a novel Aluminium nanostructured array begins, with confidence that the results will accurately reflect experimental structures.

4.1.2 Al nanostructured array

The typical aluminium nanostructure under consideration consists of a SiO₂ substrate, Micro Resist ma-N 2401 nanopillars in a square array, and an aluminium coating, forming both the backreflector, and on top of the pillar. Similar Al-based nanodisc-nanohole arrayed structures have been demonstrated previously[11,37], as well as simple Al nanoparticle[12,42,51,53], and nanohole[188] arrays. This is a similar configuration to the structure described in the previous section[6], and is shown in Figure 4.5. However, the dimensions of this structure are larger than that considered by Kumar *et al.* due to Al nanoparticles having a strong LSPR in the visible with larger particles than with Ag and Au[40,42,46].

Figure 4.5 illustrates that the discs are 200 nm in diameter with a pillar height of 100 nm, and Al thickness of 20 nm. The array has a unit cell dimension of 400 nm. A self-terminating oxide layer of 3 nm is observed for aluminium under atmospheric laboratory conditions[42]. As such, structures are simulated with the top surface of the backreflector covered in 30 nm of Al₂O₃, and a 17 nm Al layer. This is also the case for the disc. The side walls of the discs are also exposed to atmosphere, and so they also have a 3 nm coating of Al₂O₃. The pillar is assumed to be non-porous to oxygen, and so the bottom of the disc, and sides of the hole walls do not have an oxide layer. This describes the “typical” structure under consideration, with all simulations based on these dimensions.

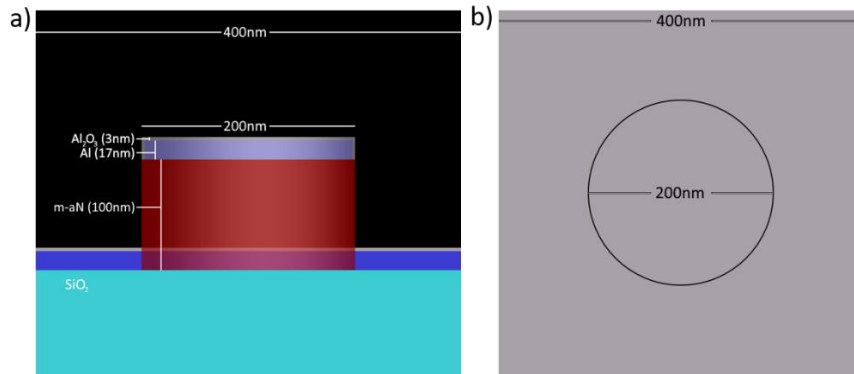


Figure 4.5: Schematic of “typical” structure parameters; 17 nm thick Al with 3 nm oxide layer, 200 nm diameter Al disc on 100 nm thick ma-N pillar, and pitch of 400 nm. From (a) side view (xz plane) and (b) top view (xy plane).

The structure may be broken into two main components, the discs and the holes (including the pillar). These two components are simulated separately, to determine their spectral characteristics, and develop a structure with the strongest spectral response, by engineering the strongest interaction of these components. Discs in free space are first simulated, with a square array pitch of 400nm and varying disc diameter, with the 200 nm disc diameter case shown in Figure 4.6 (a). An oxide layer is not included below the disc, to reduce variables when comparing to the full structure. Disc diameters of 100, 150, and 200 nm are simulated in this test, to determine the strength of the LSPR peak with this geometry and material composition. The spectra for these are included in Figure 4.6 (b).

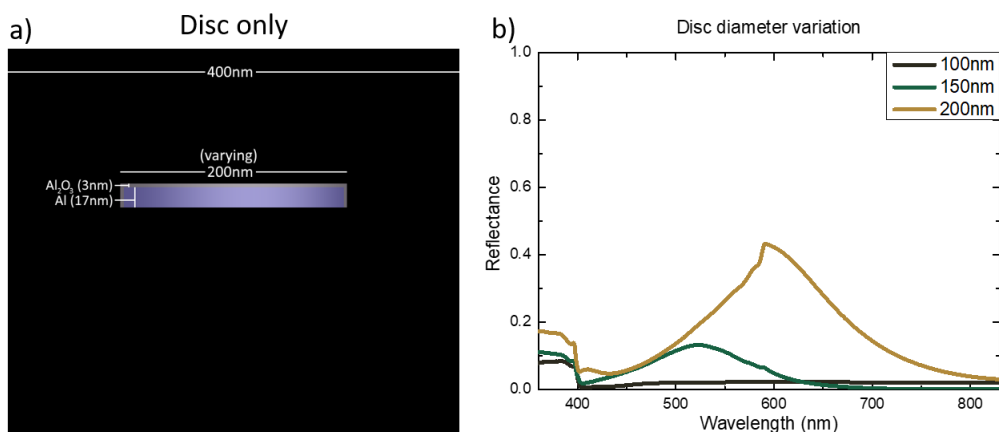


Figure 4.6: (a) Schematic of Al disc component, 17 nm Al with 3 nm oxide layer, diameter of 200 nm and pitch of 400 nm. (b) Simulation spectra of discs with 100, 150, and 200 nm diameter (fixed pitch of 400 nm).

There is a common shoulder feature present at wavelengths below 400 nm in Figure 4.6 (b), a feature that is present in many of the simulations of this chapter, with a sharp change in reflectance noted from high to low above this threshold. This occurs in all simulations featuring a 400 nm unit cell size. This is linked to the size of the unit cell, and is discussed further in section 4.1.3, as increasing the cell size results in a red-shift of this feature. For the 100 nm diameter case, there appears to be no discernible peak, with a maximum reflectance of approximately 2% across the visible region. Low reflectance is to be expected, as a 100 nm disc in a 400 nm square array has a unit cell fill factor of approximately 5%. The LSPR resonance peak for a disc of this diameter is also expected to lie in the ultra-violet region[46], and so no strong interaction between the incident light and disc is anticipated in the simulated spectral range. The LSPR peak for the 150 nm diameter case is noted at a wavelength of 520 nm, with maximum reflectance of 13%. The fill factor of the disc in this case is 11%, as well as having the LSPR occur in the visible region, resulting in a larger reflectance peak. A sharp peak is noted in the 200 nm diameter case at 590 nm, with a LSPR peak reflectance of 43%. In this case the fill factor of the disc in the unit cell is 20%, with a large reflectance attributed to the strong interaction between the disc and a large portion of the visible region.

The hole component may be considered as including the ma-N pillar for determining the response of the nanohole array component, as illustrated in Figure 4.7 (a). Simulation reflectance spectra from structures with Aluminium layers of 17 nm thickness, with a 3 nm thick oxide layer are shown in Figure 4.7 (b). The reflectance response of hole diameters of 100, 150, and 200 nm are shown. Also included is the response of a continuous Aluminium layer, with no hole. Finally, the response of a hole with a refractive index of $n = 1$, replacing the ma-N material is included, to illustrate the effect of the pillar on the spectral response.

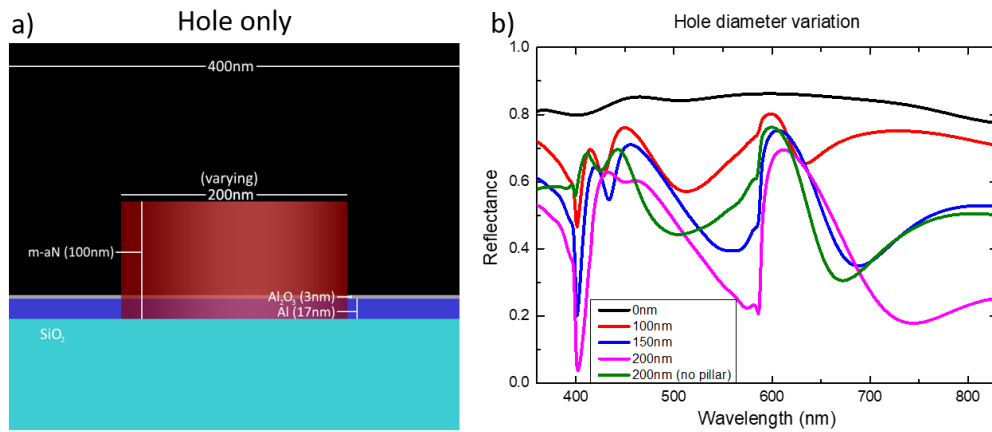


Figure 4.7: (a) Schematic of Al hole component, 17 nm Al with 3 nm oxide layer, 200 nm diameter ma-N pillar and pitch of 400 nm. (b) Simulation spectra of holes with planar Al (no hole), 100, 150, and 200nm diameter hole (fixed pitch of 400 nm), and 200nm hole with $n=1$ (no pillar).

From Figure 4.7 (b) it can be seen that the reflectance is reduced as the hole diameter increases. This contrasts with the trend that is noted in Figure 4.6 (b), with increasing disc diameter. This reduction in reflectance is due to the loss of metallic material as the hole size increases. The larger the fill factor in this case, the lower the reflectance, as the hole allows for light to pass through the component and to be lost in transmission. The peak positions do not significantly red-shift in this case compared with the observations for the disc component. Instead, the peak values stay largely unchanged, with a reduction and a redshift in the dip positions both in the 470-500 nm, and 610-660 nm regions. This is due to the increase in the hole diameter allowing for a combination of more light to be directed through the hole, subsequently to be lost in transmission, and the LSPR condition of the hole shifting such that more incident light can be coupled into the excitation of the localised plasmon around the hole.

A significant reduction and redshift of the dip at 500 nm in the 100 nm diameter case is noted as the diameter is increased, with a reduction and redshift from 60% at 500 nm to 20% at 580 nm. This reduction in reflectance, that shifts significantly as the hole increase in diameter, indicates that the energy is not lost in transmission, but in the excitation of the LSPR. A sharp spectral dip is also noted at 400 nm, that tends towards lower reflectance as the diameter is increased. The wavelength of this

dip does not change with diameter, indicating that this is a mode that is coupled by the dielectric pillar into the substrate and transmitted. This is further validated by examining the 200 nm structure that does not have a ma-N pillar present, in which case the dip noted is very small. A higher reflectance is noted across the spectrum in the case of no pillar, indicating that the presence of this component acts to more efficiently couple energy into the hole and substrate.

The fully assembled structure is presented in Figure 4.8 (a), with the disc centred above the hole by the ma-N pillar. Disc diameter (and subsequently ma-N pillar, and hole diameter) are examined for 100, 150, and 200 nm cases[143], as was done for the component simulations. The reflectance spectra for these are shown in Figure 4.8 (b).

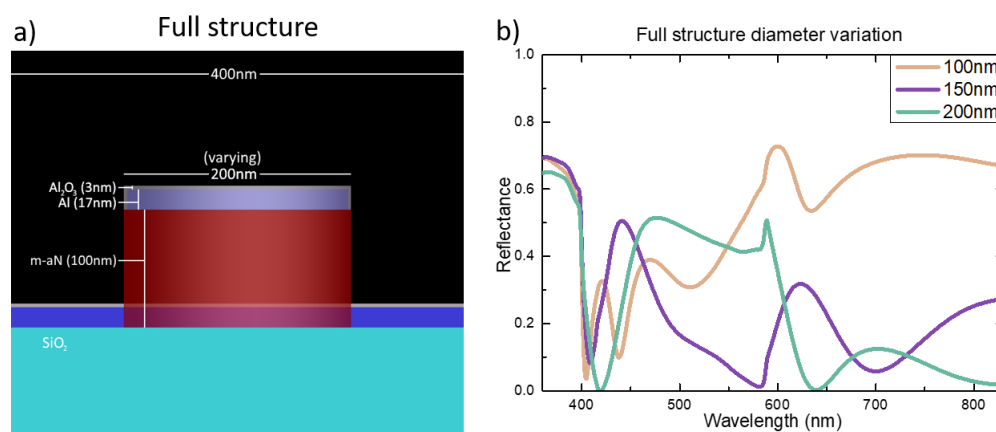


Figure 4.8: (a) Schematic of fully assembled structure, 17 nm Al with 3 nm oxide layer, 200 nm diameter Al disc on ma-N pillar, and pitch of 400 nm. (b) Simulation spectra of structure with 100, 150, and 200nm diameter hole (fixed pitch of 400 nm). The spectra are plotted in the corresponding sRGB colour.

The spectra presented in Figure 4.8 (b) are plotted with a line colour corresponding to the sRGB colour observed. sRGB and CIE values for these plots, as well as colour swatches, are included in Appendix C for all structures. From Figure 4.8 (b), it is clear that this is a nanostructure capable of generating strong structural colour with distinct colour saturation, due to the sharp spectral features in the visible. Large luminance is also observed, due to the high reflectance of the peaks. Also noted is that, by changing the diameter of the disc/hole, the chromaticity is changed significantly. The 100 nm case shows a reflectance spectrum with a predominantly

orange colour, 150 nm diameter presents a purple/indigo colour, and 200 nm shows as a bright green colour.

Examining the 100 nm diameter structure it is observed that, due to the weak LSPR and small fill factor of the disc/hole in the unit cell, the reflectance is largely dominated by the spectral response of the hole, as the response of this component was much stronger than that of the disc. The reflectance dip at 400 nm is also present in the spectrum for the hole component alone. This dip is noted for all three diameters tested here, further demonstrating that this feature arises from the pillar hole coupling light into the hole and substrate efficiently at this wavelength.

The 150 nm disc diameter array presents a lower reflectance at long wavelengths, with the peak at 600 nm shifting to 630 nm and dropping by more than 50% compared to the 100 nm diameter case. An increase in the reflectance at 450 nm can be attributed to the increased reflectance in the disc, and a stronger interaction between the disc and hole.

The 200 nm diameter is an interesting case, as the two features present in the 100 and 150 nm diameter structures appear not to be present. Instead, a single broad feature ranging from 400-600 nm is seen, with a particularly sharp peak in reflectance noted at 589 nm. This peak is due to the strong interaction between the LSPR of the disc, and the reflectance peak at 600 nm from the hole component, and has an asymmetric shape typical of Fano resonance[147]. Both features are centred around 600 nm, and the reflectance quickly falls off on both sides of the resonance peak. *E* and *P* profiles of the structure are examined at this wavelength, as well as the wavelengths of other key features, to examine the interaction of the components, particularly the Fano resonance[141]. Size dependency and trends will be further discussed in section 4.1.3.

The *E* and *P* profiles are presented for the 200 nm diameter structure, along the *xz* plane. This is along the plane of polarisation of the incident EM field, and is chosen to determine the excitation along the polarisation axis, which is expected to provide

the maximum electric field displacement. Figure 4.9 introduces both the E and P profiles for the two main dip features, at 420 and 639 nm. Figure 4.10 shows the E and P maps for the main peak features at 475 and 589 nm.

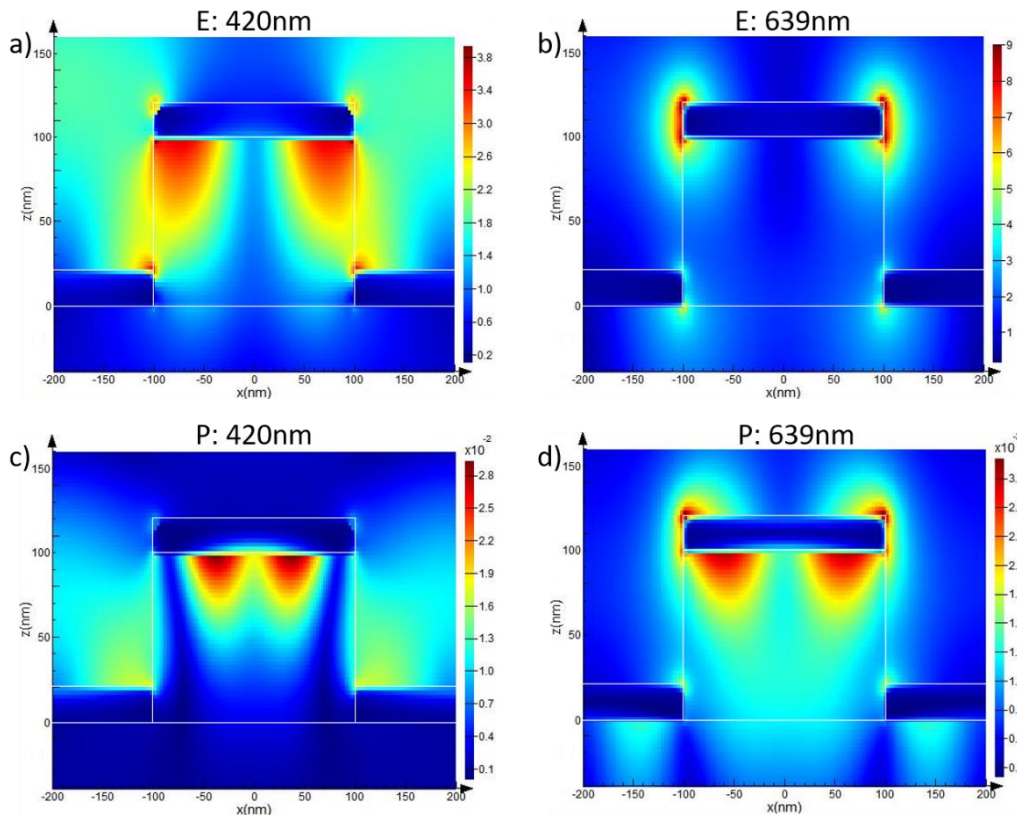


Figure 4.9: (a,b) Electric field and (c,d) Poynting vector magnitude xz plane (side) profiles at reflectance dips in the full structure at (a,c) 420 nm and (b,d) 639 nm. The monitor is positioned through the centre of the disc in all cases.

The field maps for the dips at 420 and 639 nm are shown in Figure 4.9. The electric field maps show a distinct difference in field localisation in the structure at each wavelength. The highest E-field intensities are noted at the top corners of the disc and hole in (a), with a peak intensity of 3.6 V/m localised at the bottom corners of the disc. In (b), there is a larger maximum field (9.0 V/m) that is located almost entirely around the perimeter wall of the disc. This is expected at 639.9 nm, as the disc LSPR peak at 600 nm is located close to this wavelength, and there is still an efficient coupling of incident light into the discs, resulting in large E-field intensity as conduction band electrons are oscillated in the metal, but are confined by the boundaries of the disc. A maximum Poynting vector magnitude of approximately 3.1×10^{-2} W/m² is noted in both cases, and is located predominantly below the disc

surface, indicating this to be the highest region of electromagnetic energy flux in the nanostructure at this wavelength. This suggests that the primary mechanism by which light is lost by the nanostructure at this wavelength to be by an obscuring of light from being scattered to the far field for where it could be detected in reflection.

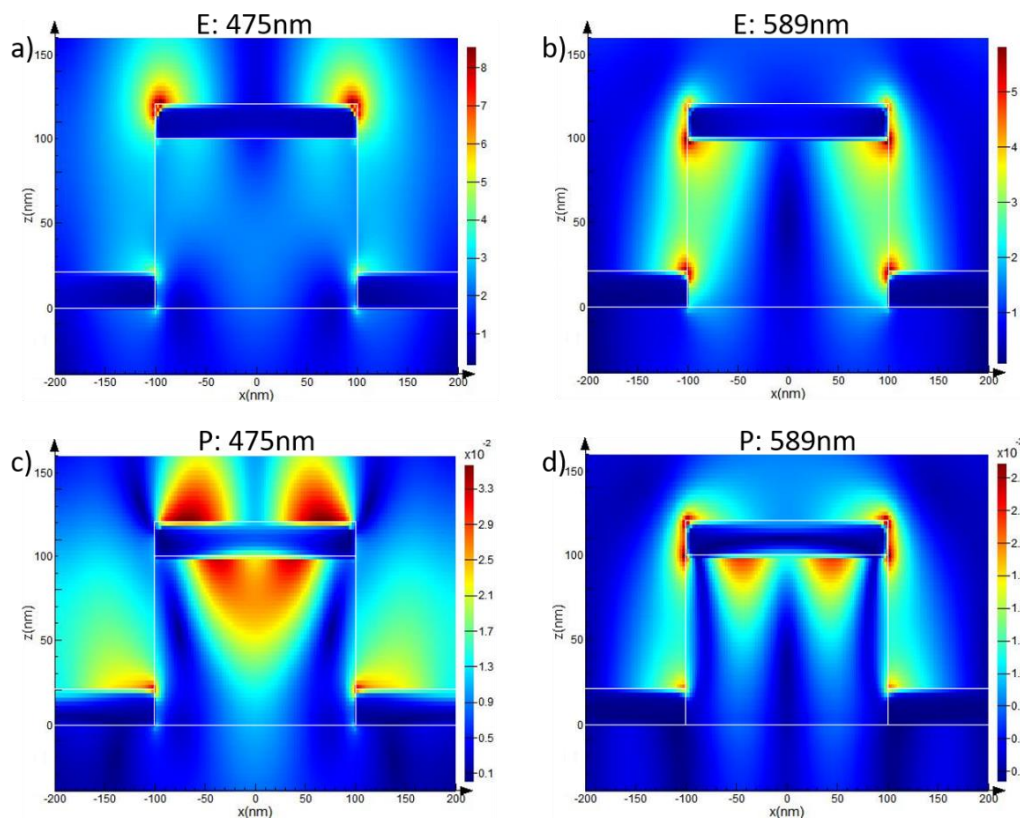


Figure 4.10: (a,b) Electric field and (c,d) Poynting vector magnitude xz plane (side) maps at the reflectance peaks in full structure at (a,c) 475 nm and (b,d) 589 nm.

The field profiles of the peaks at wavelengths of 475 and 589 nm are examined in Figure 4.10. The largest E-field intensity, for the 475 nm case (a), is located at the top corners of the discs, with a maximum of almost 10 V/m, and low field strength is noted elsewhere in the structure. As seen in Figure 4.6, the reflectance of the disc at this wavelength is low, though Figure 4.7 shows a high reflectance in the hole component. This indicates that losses at this wavelength is due to the coupling of incident light to the disc where it is lost in absorption and trapped below the disc lower surface (c), while the primary high reflectivity mechanism is reflectance from the backreflector. This occurs with no strong interaction between the disc and hole. Conversely, in (b), the field strength is smaller, with a maximum of approximately 6.6 V/m, though is it located at the lower corners of the disc walls, and top surface

of the hole corners, with a large field also observed along the pillar-air boundary between the components. This suggests a strong interaction between the disc and hole at this wavelength, as the field strength is nearly constant along the length of the pillar height.

It is clear that the cause of the very sharp peak in reflectance at 589 nm is due to a strong interaction between the disc and hole components over a short wavelength range. Analysis of the Poynting vector profile in (c) reveals the energy flux of the EM wave located around the centre of the bottom surface of disc, and a maximum of 3.8×10^{-2} W/m² above the outer 50 nm of the top surface of the disc. As mentioned previously, this indicates that the primary losses at this wavelength are due to trapping of light under the disc. While part (d) of Figure 4.10 has a similar distribution to the E-field in (b), with a maximum vector magnitude of 3.0×10^{-2} W/m² located along the side walls of the disc. The largest P is noted at the bottom of the discs, and the top corners of the hole surface also, though it is lower in magnitude than the maximum observed at the side walls of the disc.

The maximum E-field and Poynting vector magnitude measured in this structure across the wavelength range simulated occurs at 620 nm, with 10.0 V/m and 5.5×10^{-2} W/m², respectively. This indicates that the wavelength region of 589-639 nm, bordered by the disc and hole features, is formed by the Fano resonance between the disc and hole components, which is often characterised by the distinct asymmetric line shape observed in this region. This asymmetry reveals itself here in the form of an extremely sharp spectral peak at 589 nm, followed by a dip to near-zero reflection at 639 nm, on the other side of the central resonance (620 nm) position.

Finally, xy *E* and *P* maps at 589 nm for the disc and hole are presented in Figure 4.11. This is taken at a representative wavelength of 589 nm, due to the large reflectance at this peak. However, the shape of the *E* and *P* distribution is almost identical at all wavelengths, typical of dipole excitation, varying only in magnitude and range over which the field decays.

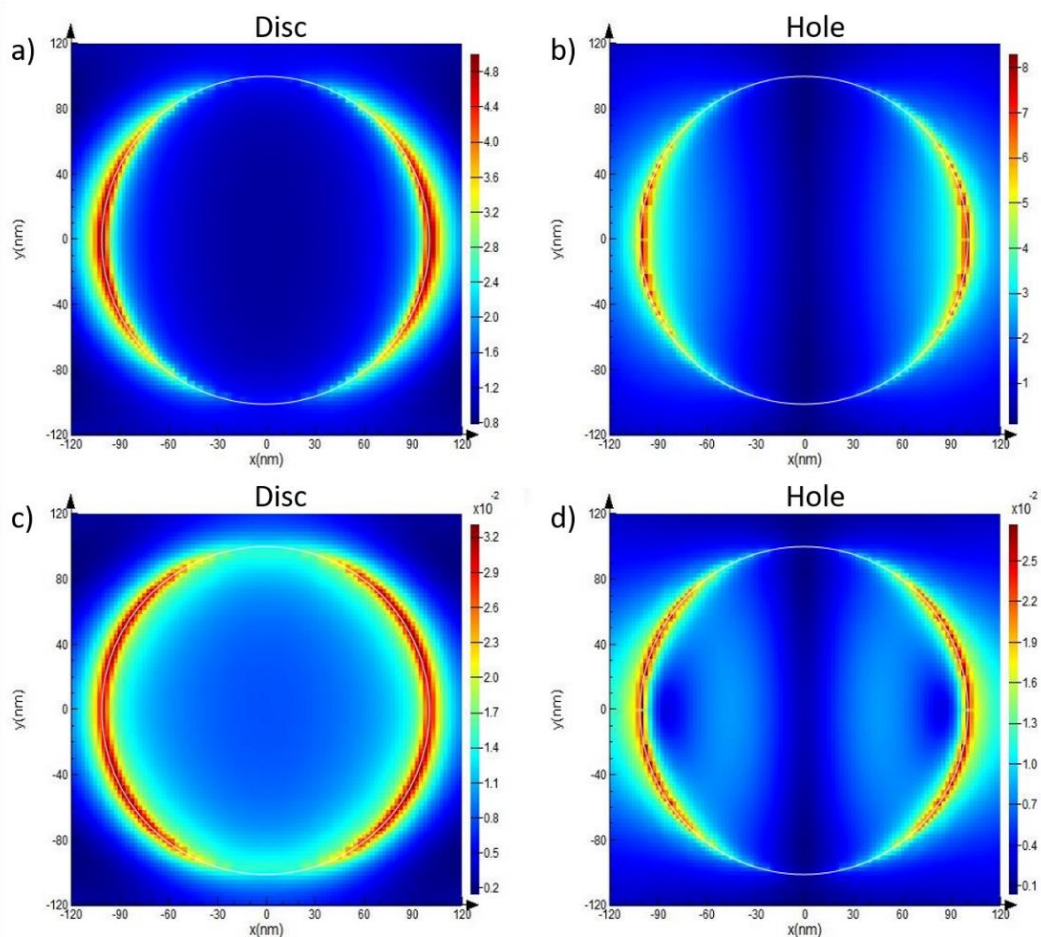


Figure 4.11: (a,b) Electric field and (c,d) Poynting vector magnitude xy plane (top down) profiles for 589 nm wavelength at the (a,c) disc and (b,d) hole.

4.1.3 Geometries

Though the disc diameter is one parameter that was tested to a degree in section 4.1.2, there are many parameters that can be assessed in this structure to determine the sensitivity of the LSPR conditions and Fano resonance, and hence reflected colour, to structural variation. This section addresses the variation of several key geometric parameters, and the spectral trends that are associated with these variations. CIE xyY colour-space maps and colour swatches are used throughout to illustrate trends and determine chromaticity and luminance more easily.

For each of the figures in this section, five representative spectra from the simulations are presented, with variation of one structural parameter. In each case, the third (central) simulation is that of the “typical” configuration parameters, with a 17 nm thick Al, 3 nm thick Al₂O₃, 100 nm thick ma-N pillar, 200 nm diameter and 400 nm unit cell size (pitch). This “typical” configuration is shown in Figure 4.5.

Variation of parameters is considered in this way to determine the change in the reflectance response of the structure as the “typical” parameters are deviated from. The variation of four structural parameters are examined, to determine colour sensitivity and further understand light-matter interactions in the structure. These are: Diameter (fixed gap), diameter (fixed pitch), gap (fixed diameter, and pillar height).

Firstly, the diameter of the disc is varied with a fixed gap. This is done to determine the effect of changing the disc/hole LSPR on the response of the nanostructure, while maintaining the same interaction distance between discs. All other material parameters are fixed, as stated previously.

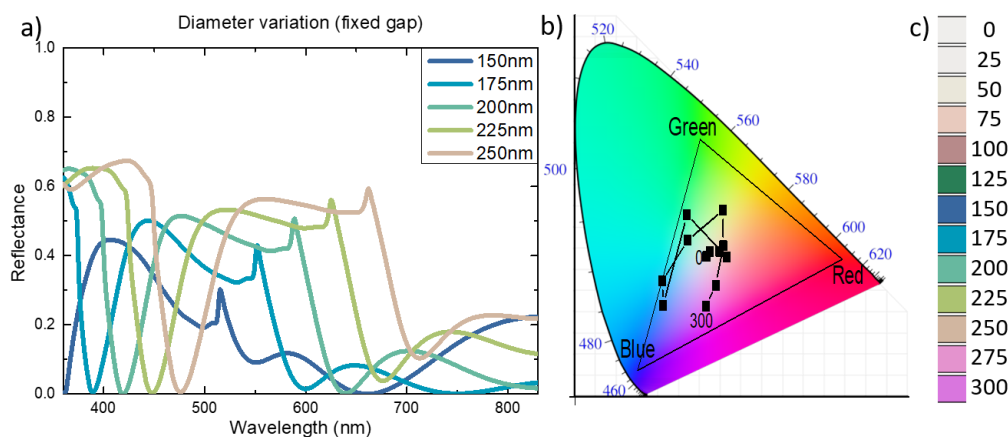


Figure 4.12: (a) Reflectance spectra with varying disc/hole/pillar diameter and a fixed gap of 200 nm between discs, showing spectra for 150-250 nm diameters. (b) CIE map for the full range of 0-300 nm in 25 nm steps. (c) sRGB colour swatches at the corresponding diameter.

Results for this test are presented in Figure 4.12. A representative range of 150-250 nm diameters are selected, and the spectra are shown in (a). A similar spectral shape is present in all spectra shown for this range, including the sharp asymmetric peak noted at 589 nm for the 200 nm disc diameter case. This peak shifts from 510 to 760 nm as the disc diameter is varied between 150 and 250 nm, with an increase in the peak reflectance value as diameter is increased. The dip noted at longer wavelengths has the lowest reflectance in the 200 nm diameter case at 639 nm. The combination of the high reflectance peak, and near-zero reflection at this diameter indicates that this disc size allows for the strongest interaction between the disc and

hole, forming the strongest Fano resonance condition and associated spectral features. Lower reflectance at smaller disc diameters is due to the inefficient excitation of the plasmon in the visible spectral range for smaller discs, leading to a weak interaction between the disc and hole, reducing the feature definition. Figure 4.12 (b) further illustrates the colour trend noted in this structure over a larger diameter range (0-300 nm in 25 nm steps) plotted on a CIE xyY map. The individual colours are more clearly illustrated in Figure 4.12 (c), with the colour swatches. At 0 nm, there is no disc, and so simply planar reflectance from the Aluminium thin film is noted. As the disc/hole is introduced, a weak disc/hole interaction is formed. As diameter is increased, chromaticity change is noted towards discernible colours as the LSPR of the disc is formed in the visible, spectral features move into the visible and the disc/hole interaction is strengthened. As the diameter is increased past 250 nm, chromaticity changes towards a “pink” hue, as the plateau of reflectance shifts towards the red (long) colour cone receptor, and the feature associated with the unit cell size moves further into the visible, shifting by approximately 25 nm for each diameter step (a one-to-one ratio). This causes a high reflectance overall, but stimulates multiple colour cones and causes the colour clarity to be reduced, as one cone is no longer predominantly being stimulated. A pink hue is noted when the red (long) cone is highly stimulated, while both the blue (short), green (middle) cones are stimulated to a lesser extent.

To investigate the degree of inter-disc interaction, the spectral response of the nanostructure can be examined as diameter is increased with a fixed unit cell size (pitch).

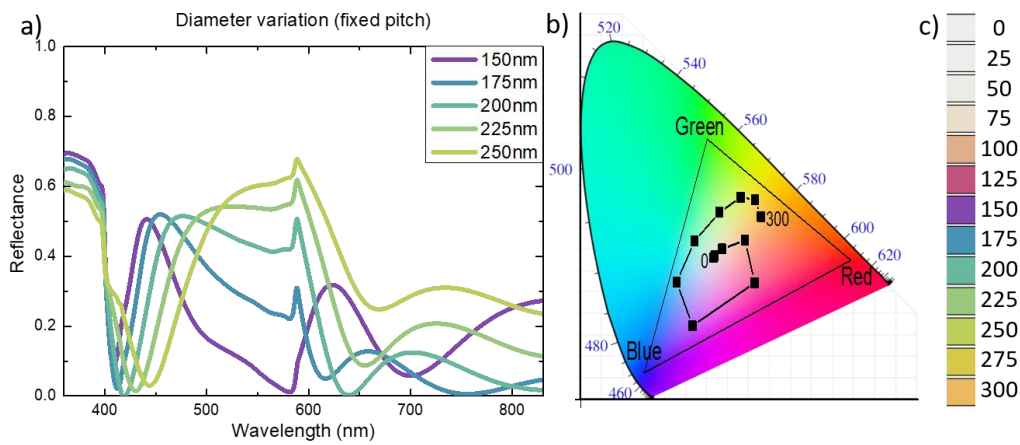


Figure 4.13: (a) Reflectance spectra with varying disc/hole/pillar diameter and a fixed unit cell size of 400 nm, showing spectra for 150-250 nm diameters. (b) CIE map for the full range of 0-300 nm in 25 nm steps. (c) sRGB colour swatches at the corresponding diameter.

This is demonstrated in Figure 4.13, where disc diameter is varied from 0-300 nm in 25 nm steps, while maintaining a pitch of 400 nm, with part (a) examining the range of 150-250 nm. The 150 nm diameter structure is the only one presented that does not exhibit the sharp spectral peak feature at approximately 589 nm, that was previously attributed to Fano resonance. This feature is not observed for any disc diameter below 175 nm. This is because the disc LSPR is weak at smaller disc diameters, as illustrated in Figure 4.6 (b) for the 100 nm and 150 nm discs. As the LSPR is weak, there is no strong interaction between the evanescent field around the disc and the hole, and so a Fano resonance is not observed. Instead, the reflectance consists of two broad peaks at 440 and 625 nm, which is primarily the response of the hole component, as shown in Figure 4.7 (b).

As the disc diameter is increased, the sharp Fano resonance peak formed at 589 nm increases in intensity, and does not shift in wavelength position. A similar phenomenon has been reported by Kumar *et al.*[6], using the structure illustrated in Figure 4.2. In that study, as diameter was varied with a fixed pitch, a peak attributed to Fano resonance was observed and did not vary with diameter of the disc/hole components with a fixed pitch. This indicates that the peak is highly dependent on the unit cell size, and not only the diameter of the discs/holes. However, an increased diameter also causes an increase in the dip value noted at 639 nm in cases

above 200 nm, and red-shifts by approximately 10 nm with each step. This indicates that, in order to maintain the most distinguishable spectral features, the best diameter and gap between particles is 200 nm.

Figure 4.13 (b) illustrates the colour trend for the entire simulation range, and presents CIE xyY results for 0-300 nm diameter in a fixed 400 nm unit cell. At small diameters, the fill factor of the discs is small, with weak interaction with the incident field. This results in a response that is dominated by the reflectance of planar Aluminium until the fill factor is significantly increased. In the range of 150-250 nm, as shown in (a), a colour range of high clarity purples and blue-greens is noted as the short and middle colour cones are stimulated.

At diameters above 250 nm, the LSPR of the disc shifts towards the IR and coupling between the nanodiscs in the array becomes stronger. Reflectance at longer wavelengths increases, and the sharp dip observed in the 400-450 nm region in Figure 4.13 (a) continues to red-shift with near-zero reflection. This results in high reflectance in only the 500-700 nm region, responsible for green, and red colour sensitivity, respectively. This leads to the yellow/orange colour observed as the disc diameter tends towards 300 nm.

To further investigate the degree of inter-disc interaction, the spectral response of the nanostructure can be examined as the gap is varied with a fixed diameter. This allows the plasmon response of the disc to remain unchanged, while varying the distance between neighbouring cells. If the interaction between the cells is negligible, one would expect that the response of the structure would remain largely unchanged. An increase in reflectance would be expected as the gap is increased, due to the increase of planar Al present in each unit cell. The spectra for varying gap with a fixed diameter are shown in Figure 4.14 (a).

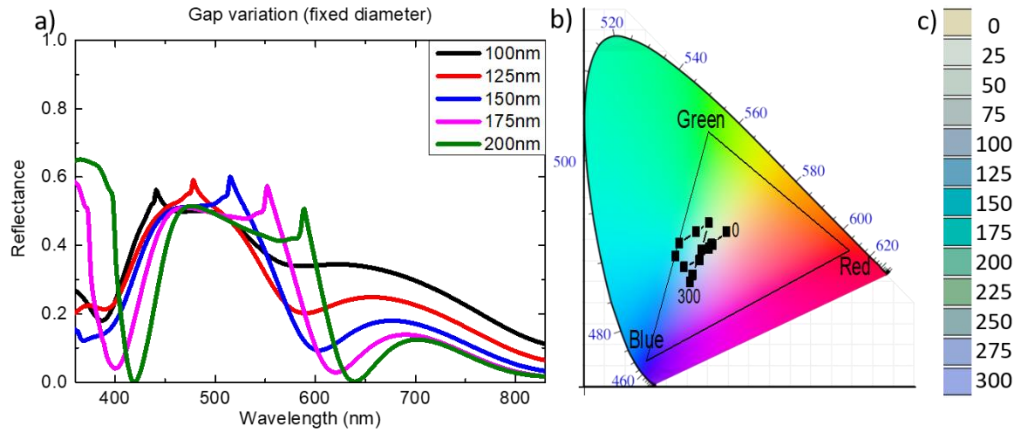


Figure 4.14: (a) Reflectance spectra with varying disc gap, and a fixed diameter of 300 nm, showing spectra for 100-200 nm gap in 25 nm steps. (b) CIE map for the full range of 0-300 nm in 25 nm steps. (c) sRGB colour swatches at the corresponding diameter.

Figure 4.14 (a) illustrates the reflectance spectra for a varying gap between discs of a fixed diameter of 200 nm. All spectra demonstrate a broad peak in the 400-600 nm region. The sharp dip observed at short wavelengths is also shown to be dependent on the gap between the discs, as was observed in Figure 4.12 (a). Reflectance across the visible decreases with increasing gap, a trend that indicates interaction between the discs, that is sensitive to their proximity to each other.

The sharp Fano resonance peak seen in other parameter tests is also seen here, and red-shifts approximately 25 nm with every gap increase of 25 nm. This indicates a strong dependence of the Fano resonance with disc separation[143], and illustrates strong inter-disc interaction.

Array effects such as the array periodic surface plasmon (PSP) and Wood's anomaly (WA) were introduced in Sections 2.2.2 and Section 2.2.4 of Chapter 2, respectively. The potential impact of these phenomena can be examined in this structure, using Equation 2.17 for the SPP, and Equation 2.25 for the WA.

Periodicity (nm)	Al - pillar interface		Al - air interface		Al - effective medium	
	λ_{PSP} (nm)	λ_{WA} (nm)	λ_{PSP} (nm)	λ_{WA} (nm)	λ_{PSP} (nm)	λ_{WA} (nm)
300 nm	399	384	312	300	345	332
400 nm	522	512	409	400	433	425

Table 4.1: Expected wavelengths for the periodic surface plasmon (PSP) and Wood's anomaly (WA) for the Aluminium structure at 300 nm and 400 nm periodicity. At the Al-pillar, and Al-air interfaces, as well as the calculations for an effective medium in the unit cell.

Table 4.1 shows the calculated values for the PSP and WA in this structure for 300 nm and 400 nm periodicity. These periodic effects are considered at both the Al-air interface with refractive index $n = 1$, as well as the Al-pillar interface, with refractive index $n = 1.64$ for the ma-N. Also calculated are the values with an effective medium formed, where the percentage volume of the pillar in the unit cell is measured. In the case of the 300 nm periodicity, the effective medium is $n = 1.223$. For the 400 nm periodicity, the effective medium is $n = 1.125$.

For array pitches of 300 nm and 400 nm with a fixed disc diameter, such as those shown in the Figure 4.14, the 300 nm pitch corresponding to the 100 nm gap, and 400 nm pitch corresponding to the 200 nm gap.

For the 300 nm periodicity, values presented in Figure 4.1 fall outside the wavelength range examined in the case of the Al-air interface, and effective medium calculations. The calculations for the Air-pillar interface for the SPP and WA return values of 339 nm and 384 nm, respectively. These values do correspond to a dip in reflectance in the 100 nm gap (300 nm periodicity) case in Figure 4.14. However, the results for the 400 nm pitch for the Al-pillar interface do not appear to correspond to any spectral features observed for the 200 nm gap (400 nm periodicity) in Figure 4.14. Similarly, results for the Al-air and effective medium calculations at 400 nm periodicity do not appear to resemble any features that may have red-shifted from the 300 nm periodicity case. These calculations indicate that the phenomena of PSP and WA do not have a significant impact on the reflectance from the array structure.

In Figure 4.15, the height of the ma-N pillar is varied from 0-200 nm in 20 nm steps. This test is used to determine the effect the disc/hole separation has on the spectral response of the nanostructure.

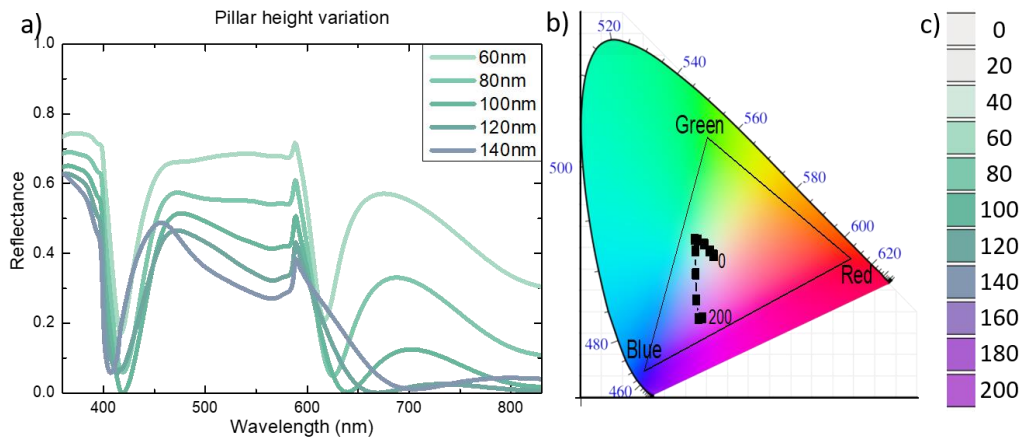


Figure 4.15: (a) Reflectance spectra of simulation with varying pillar height, showing spectra for 60-140 nm diameter simulations. (b) sRGB colour values of varying pillar from 0-200 nm in 20 nm steps.

Figure 4.15 (a) shows the reflectance spectra from simulations with a height variation of 60-140 nm in 20 nm steps. As the thickness of the ma-N pillar is increased, the spectral shape remains largely unchanged, with no significant shifting of features in the centre of the visible region. However, the peak at approximately 650 nm quickly drops and shifts to the IR as height is increased. It does not have a strong effect on the colour change noted, however, as colour cone sensitivity is not particular strong at these wavelengths.

Reflectance in the visible is also reduced with each height increase. In part, this can be attributed to light being coupled through the hole/pillar, and into the substrate as the pillar height is increased, as more of the pillar is exposed with each height increase. This corresponds to an increase in transmission. The rate of reduction in reflectance is smaller with each height increase, and in the 140 nm case actually leads to an increase in reflectance in the 400-480 nm region. This occurs as the interaction between the disc and hole components weakens as the distance between them increases, and this region trends towards the reflectance response of the hole component observed in Figure 4.7 (b).

The dips in reflectance are the most significantly affected feature as a function of height. The dip at approximately 410 nm is fully formed by a height 60 nm, though it is noted that at small heights, this dip is not as strongly developed. The dip of

near-zero reflection at 100 nm height, at 639 nm, is the feature most significantly changed in the visible region as a function of height. The 100 nm height case demonstrates the lowest reflectance of near-zero reflection in this feature of any height tested. This further indicates, as with other tests, that the “typical” configuration is ideal for presenting the highest contrast of spectral features, and subsequently most vibrant colours in reflection.

4.2 Experimental

This section details the fabrication and characterisation of the Aluminium nanostructure samples. Diffraction effects were observed during characterisation, and are also examined.

4.2.1 Fabrication

10x12 mm SiO₂ substrates were cut from a 1 mm thick microscope slide, sonicated in solutions of Acetone, Methanol and Isopropyl Alcohol (IPA), respectively, for 20 minutes each before being dried with a Nitrogen gun to ensure no residue was on the surface.

Spin profile tests were carried out on ma-N, with the aim of depositing a uniform 100 nm layer of the material. Micro Resist ma-N 2401 was used as a negative tone resist to fabricate nanostructure arrays, spin coated for 60 seconds at 3000 rpm, before being placed on a hotplate at 90°C for 60 seconds. E-Spacer was deposited by spin coating for 60 seconds at 3000rpm, to prevent excess charge build up, improving resolution of finished arrays. This was vital, as structures were fabricated on SiO₂, a highly electrically insulating material. The nanodisc array patterns were then fabricated by e-beam lithography (EBL)[189], using an Elionix 7700 Thermal Field Emission Scanning Electron Microscope (TFE-SEM). An accelerating voltage of 15 kV was used at a working distance of 5 mm, with a beam current of 50.9 pA and aperture of 10 µm delivering an area dose of 140 µC/cm² over an array area of 50 µm cells. The patterns consisted of discs of 200 nm diameter, with a pitch of 400 nm. These cells were stitched together in a 100x100 array, to form a large, 5 mm

square array of nanodiscs. After exposure, E-Spacer was removed with a rinse in de-ionised water for 10 seconds. Patterns were developed by submerging the sample in ma-D 525 developer for 10 seconds. Immediately after this, samples were rinsed with deionised water for 60 seconds, then IPA for 10 seconds, before an air gun was used to remove the IPA.

Thin film Aluminium was deposited on the substrates using a Temescal FC-2000 Electron-Beam Physical Vapour Deposition (EBPVD) system, with a 20nm layer at a deposition rate of 0.5 \AA/s . This structure fabrication process is illustrated in Figure 4.16.

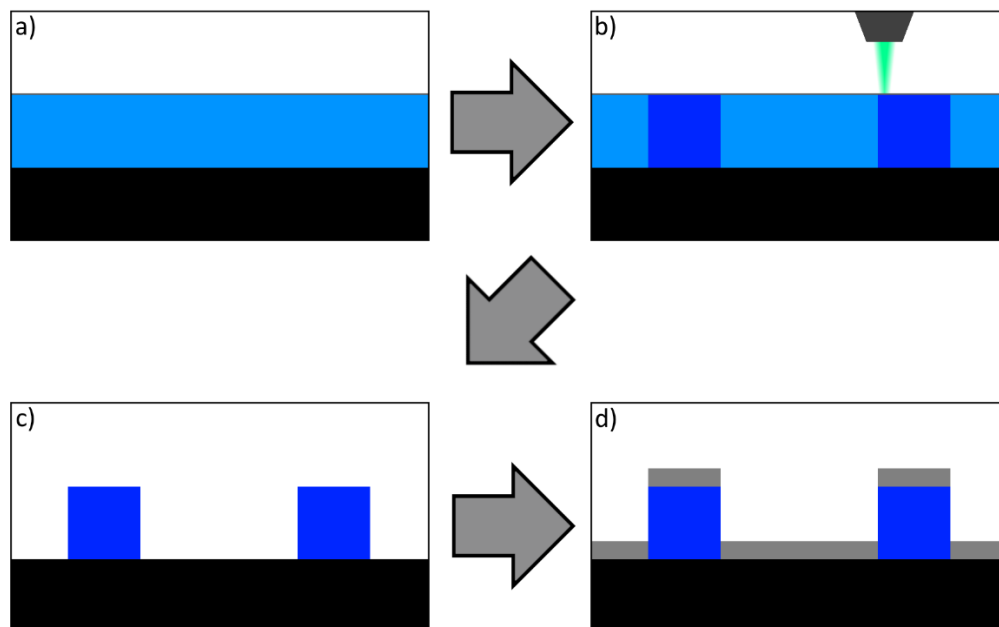


Figure 4.16: Fabrication process for array structure. (a) ma-N deposition, (b) EBL patterning, (c) development, (d) Al deposition to form final structure.

4.2.2 Characterisation

The completed array was first viewed under an optical microscope to determine structure defects and colour uniformity across the sample, shown in Figure 4.17. Also included is a camera image of the sample, with the array clearly visible as a green square, and surrounding reflective Aluminium on the substrate.

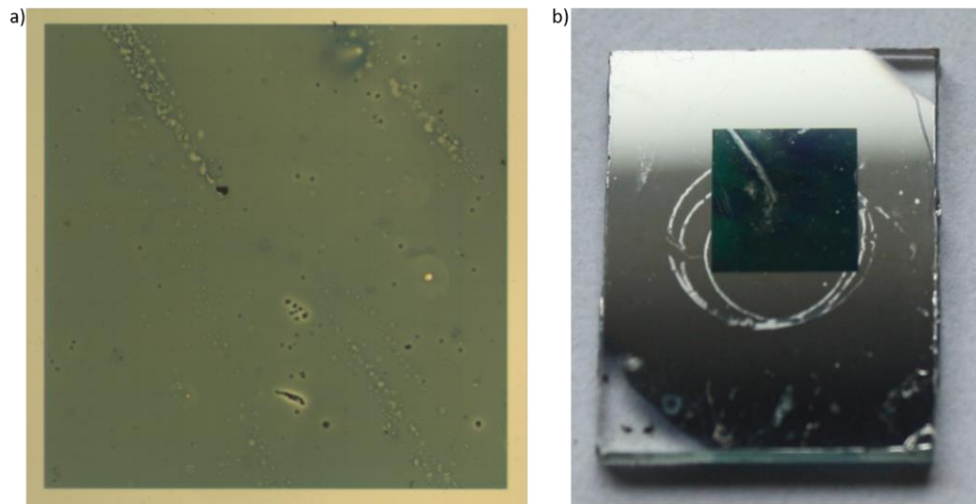


Figure 4.17: (a) Optical microscope image of the array at 5 times magnification, showing some large-scale defects in the surface due to dirt or other contaminants, but overall good colour uniformity across the array. (b) Camera image of full sample substrate, showing square patch of green, denoting the array. Rings present are water marks left by the development process.

Layer thicknesses were measured on a Dektak profilometer, with annealed ma-N, and Al measured on clean SiO₂ substrates. Thicknesses were determined to be (102 ± 5) nm, and Al thickness of (20 ± 2) nm, with results shown in Figure 4.18. Measurements were taken by scratching a line in the material, and measuring a 300 μ m section perpendicular to the line at five points on the substrates, which were averaged and a standard deviation determined. The profilometer had a probe stylus radius of 12.5 μ m, at a Force of 3 mg.

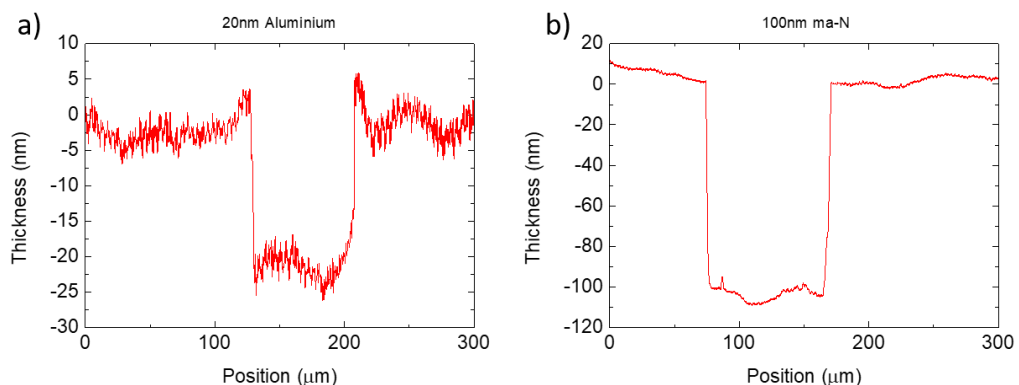


Figure 4.18: Profilometer measurements of (a) ma-N and (b) Al layer thickness, showing a thickness of (102 ± 5) nm, and (20 ± 2) nm, respectively.

The SEM imaging was carried out on fabricated structures using a Carl Zeiss Ultra FE-SEM. An accelerating voltage of 5 kV was used, at a working distance of 8.4 mm and aperture of 10 μm . A micrograph of the sample is presented in Figure 4.19.

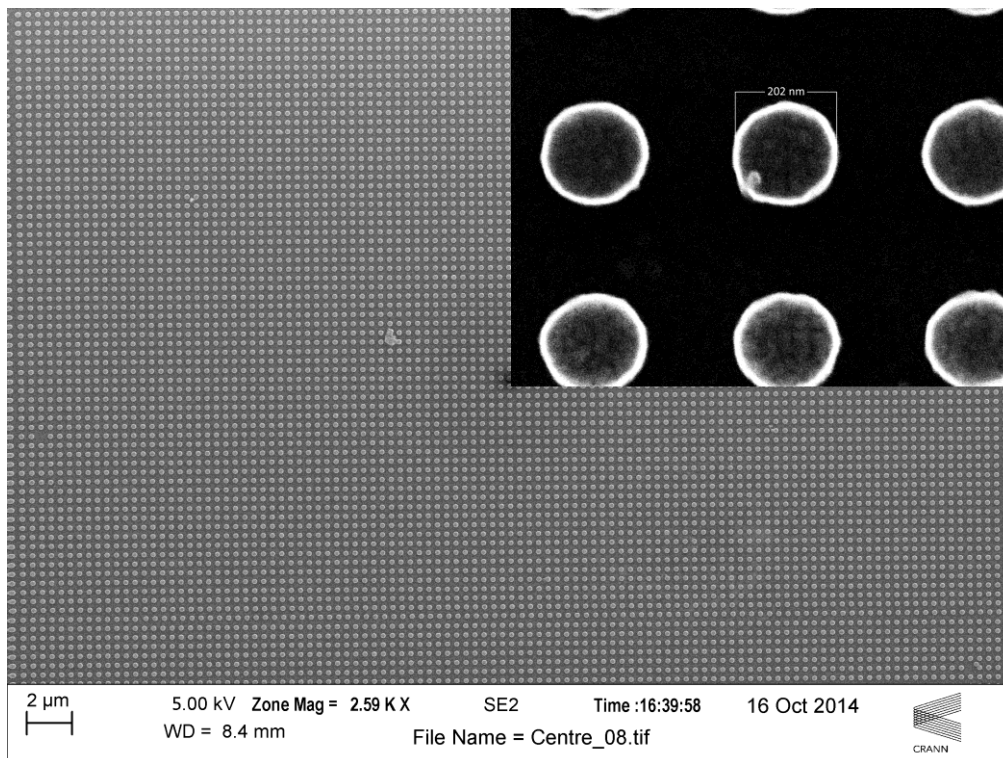


Figure 4.19: SEM micrograph of Aluminium nanodisc array, showing good array periodicity. (Inset) Magnified image, with disk diameter measurement. Mean disc diameter of (200 ± 2) nm is determined over 10 measurements.

The nanodiscs are seen to be arranged in a square array with (400 ± 1) nm pitch, with minimal defects in the structure seen in Figure 4.19. The inset illustrates an example measurement of disc diameter, showing disc shape to be uniform, and circular. The fabricated nanodiscs are found to have good definition and mean diameter of (200 ± 2) nm.

Optical characterisation was carried out by measuring the reflectance spectrum under normal incidence, as described in Chapter 3, Section 3.3.2. Figure 4.20 reveals the reflectance spectrum for the sample, and compares it to that of the “typical” structure, mentioned earlier.

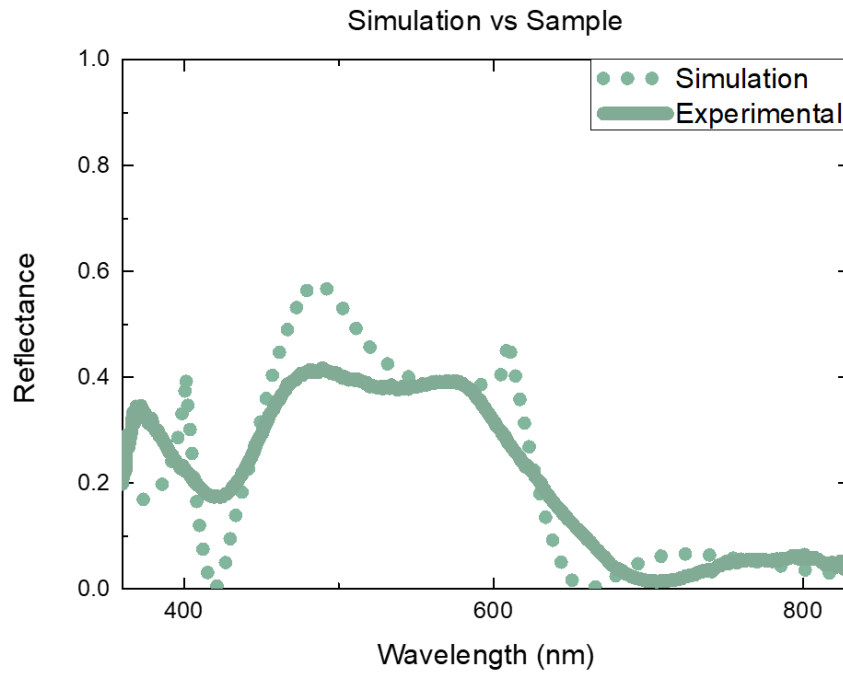


Figure 4.20: Reflectance spectrum of simulation with 200 nm pillar height, 200 nm disc diameter, and 400 nm pitch (simulation). Spectrum from optical characterisation of the sample fabricated.

Examination of Figure 4.20 reveals good agreement of the spectral position of the main features with the simulation of the structure. The dips and peaks present in the simulation also occur in the sample, with close proximity to the wavelengths that indicating a good agreement with the model. The dip noted at 420 nm in the simulation does not reach near-zero reflection in the fabricated sample, and the peak values are not of the exact same magnitude or sharpness.

There are two factors that may contribute to the minor discrepancies between the simulated and measured results, those being variation in the geometry in the sample over the measured area, and the angular incidence and collection over which the reflectance is measured. In the case of the variations in the geometry, this can be attributed to small imperfections and variations in the structure[11], that leads to an averaging over the surface of the array of the spectral response, resulting in peaks that are not as sharp as in the simulation, as the optical signal is collected over an approximately 50 μm spot side, where the simulation examines a semi-infinite array of perfectly identical unit cells. As the measurement system used a 20x objective, the illumination and collection is taken over an approximately 23.6° angle.

This also potentially has an impact on the spectral response of the sample in the system, as these structures are known to be sensitive to angular effects.

Overcoming these discrepancies would be challenging, as simulation would be require a combination of many disc diameters and pillar heights, but would still represent “perfect” structures, with stronger resonances than that of the fabricated sample. Simulations would also be required with varying incident angles of light.

4.2.3 Diffraction effects

During the fabrication process, before metal deposition, it was noted that the structure exhibited a diffractive effect in reflection, due to the ma-N pillars alone. This effect persisted after metal deposition, and was examined further to understand the dependencies of the diffractive effect. The in-house optical setup for angular characterisation as mentioned in chapter 3, was utilised in this case. A fixed incident angle (θ) of 45° was used, and the detector was swept across a range of angles (φ) from normal to the surface (0°), to parallel (90°), on the incident side of the normal, as shown in Figure 4.21.

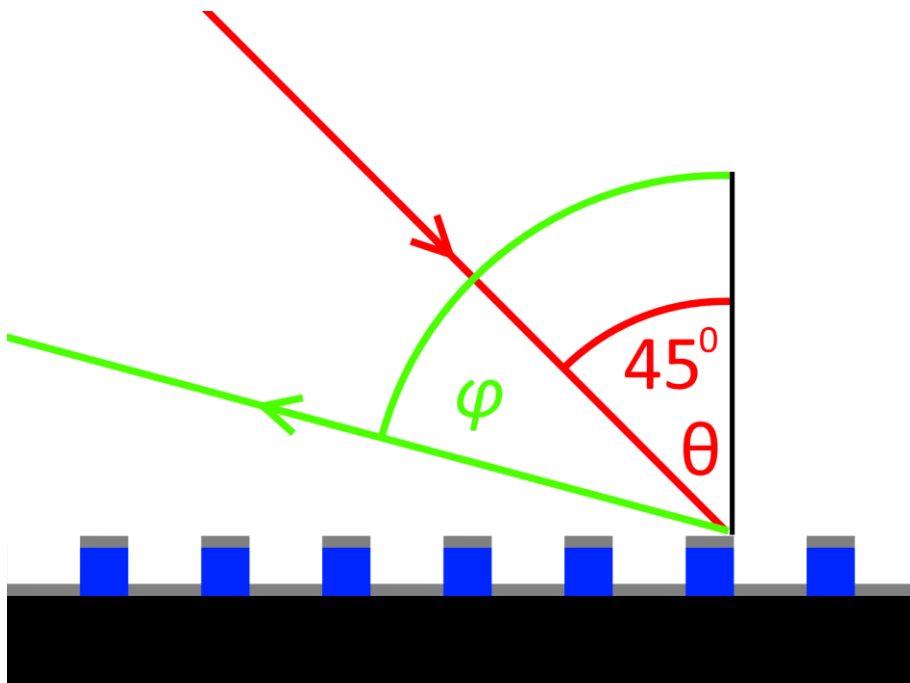


Figure 4.21: Angular reflectance measurement, with incident angle (θ) of 45° , and detector angle (φ) from normal to the surface (0°), to parallel (90°).

This was done as the diffractive effect occurred on this side of the normal. The far side of the normal under these illumination conditions does not exhibit a splitting of wavelength by colour, and has only a single spot of specularly reflected light at 45° . Figure 4.22 (a) illustrates the diffraction effect as taken by a camera, with the blue (left) area at angle φ of 0° , and the red (right) area at 90° . The corresponding spectra collected by the characterisation setup is shown in (b) at $20\text{-}80^\circ$, in 4° steps.

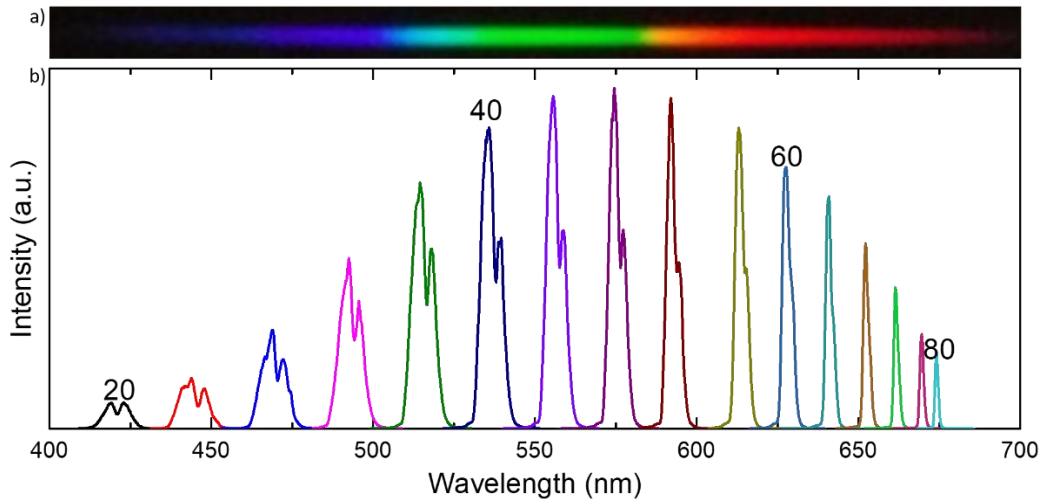


Figure 4.22: (a) Camera image of diffraction effect with 45° incident angle (θ). (b) Reflectance spectra of from angular optical characterisation of the sample, with fixed incident angle of 45° , and measurement angles (φ) of $20\text{-}80^\circ$ in 4° steps. These measurements were performed in collaboration with Dr. E. Pedreuz.

The intensity distribution of the diffracted light is at a maximum at the 48° , with intensity falling off gradually as the angle of collection is scanned out from this position, following a gaussian distribution. Two distinct peaks are present at angles close to the normal, with the features converging as the angle is increased, until they are indistinguishable from each other above an angle φ of 60° . The position peaks (at shorter wavelengths in the case of double peak line shapes) are plotted, and compared to a first order diffraction grating, with the equation[156]:

$$\sin\theta + \sin\varphi = m \frac{\lambda}{d} \quad (2.24)$$

where θ is the angle of incidence (45°), $m = 1$ is the order of diffraction, λ is the wavelength of the diffracted light at an angle of φ , and a grating constant (unit cell

side) d . The fitting of this equation to the experimental results of the peaks is shown in Figure 4.23.

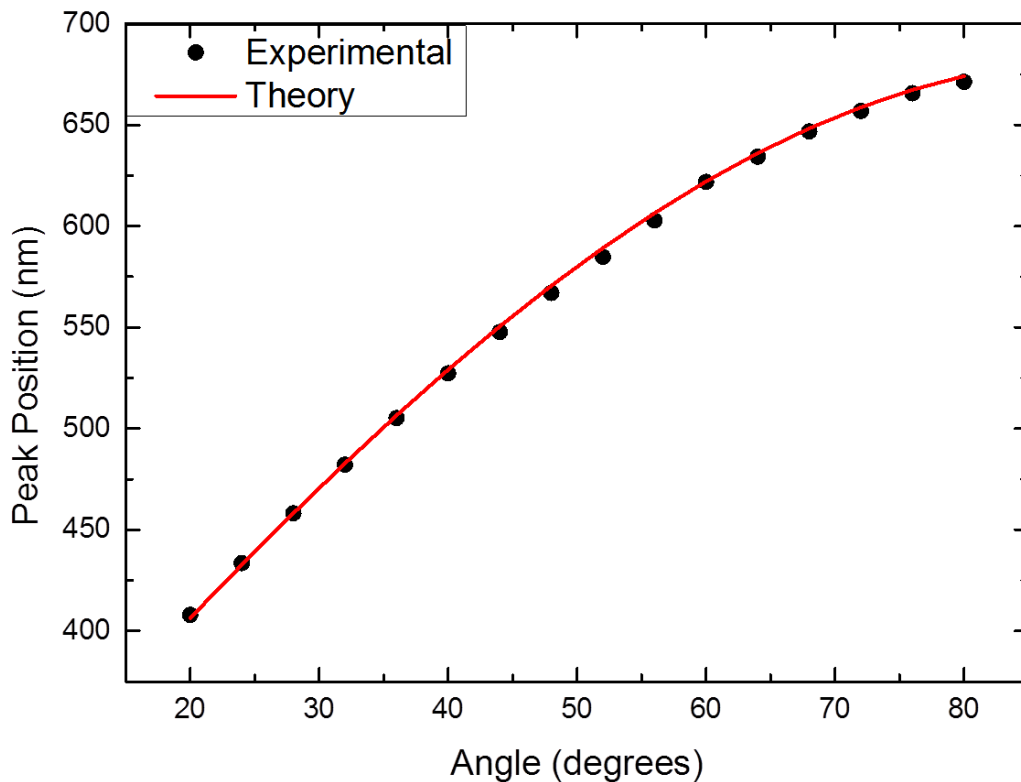


Figure 4.23: Fitting of the short-wavelength peak values in diffraction to a first order diffraction grating as described in Equation 2.8.

Figure 4.23 shows good agreement between the peaks, and a first order diffraction grating equation, indicating that the structure is acting as a diffraction grating with grating constant of 400 nm.

The double peak observed does not apply to two separate grating constants, as a first order diffraction grating with a larger unit cell does not correlate with the second peak. At an angle of 20° , peak 1 occurs at 420 nm, and peak 2 occurs at 423 nm. If it is assumed that peak 2 follows a first order diffraction grating, it would have a grating constant of 403 nm, according to Equation 2.8. However, as the angle increases, this would not have a trend that would converge with peak 1, and would have a wavelength of 681 nm at 80° . This is not in agreement with the value of 675 nm in Figure 4.23 for peak 1, and indicates a different phenomenon is occurring to generate a second peak. If one was to assume that the second peak was formed due to an increase in the effective grating constant due to the higher refractive index of

the disc material, one would assume this effective constant would be 532 nm, as the disc is 200 nm, with a refractive index of approximately $n = 1.66$. With this grating constant, according to equation 2.8 at an angle of 20° the peak would occur at 558 nm, and at 80° at 900 nm.

This double peak may be due to either a subtractive or additive effect that is angularly dependent in the structure. A subtractive effect assumes that there is one broad spectral feature, which is the result one mechanism, and a second mechanism causes the dampening of response over a short wavelength range, leading to the formation of two peaks. An additive effect assumes that the peaks are formed separately, and are offset by a small energy difference, resulting in the separation of the peaks. In the case of a subtractive effect, it is assumed that this double peak is actually the result of a broader, single peak that is being selectively subtracted over a short wavelength range. This could occur due to a scattering effect in the structure, which is highly angularly dependent. However, the structure has a diffraction trend with peak 1 following a first order grating with grating constant of 400 nm, with the trend matching for all angles. If one was to assume a larger peak centred at approximately 421.5 nm at 20° , this would result in a trend with a peak wavelength of 678 nm at 80° , according to Equation 2.17, which is not observed. This indicates that the peaks are the result of separate phenomenon, and not the result of a subtractive effect of a single, broader diffraction peak.

An additive effect remains as the most plausible cause of the double peak. More specifically, this is the combination of a regular diffraction pattern in the trend noted in peak 1, and a second separate but similar effect that forms peak 2. As this effect follows a similar trend with close dependencies to peak 1, it is clear that it is also based on diffraction. Efforts have been made to simulate the structure in the Lumerical far-field projection tool, to determine the origin of this double peak. Progress has been made in developing a model and the double peak has been observed in limited circumstances. However, these peak positions do not correlate with observed effects completely. Importantly, the double peak effect has not been

noted in component simulations, where the structure is incomplete, indicating that it is indeed caused by an interaction between components. This suggests that the effect is the result of an interaction between the disc and hole components, with the most likely origin being the Fano resonance, that is also the origin of the strong colour noted in the structure. As this effect is an interference interaction similar to that of the diffraction phenomenon, it follows that this may interact with the propagating light formed by diffraction in the structure. This interaction shifts the wavelength position at angles closer to the normal, while having less effect as the angle is increased. Ultimately, the origin of this effect is not completely understood, and would require significant effort in simulation to develop a model that completely describes its cause.

4.3 Conclusion

In this chapter, an aluminium nanostructure capable of strong structural colour has been demonstrated by simulation in a FDTD simulation tool. Strong resonance interactions between the disc and hole component, as well as the interaction between the discs in neighbouring cells, have been shown to have a significant impact on the spectrum of reflected light from the array. The colour sensitivity dependencies on the size of the unit cell, diameter of the disc/hole, and the height of the ma-N pillar have been examined, and the interaction between the disc and hole component has been shown to exhibit a Fano resonance condition that directly affects reflection in the far field.

Samples have been fabricated using EBL, with a laser stage used to stitch ten thousand 50 μm square arrays together to form an array large enough to be easily visible to the human eye. SEM imaging and Dektak profilometry was used to determine the physical parameters of the structure. The sample was optically characterised, and good agreement was found between the position of the spectral features in the fabricated array, and a simulated structure of the same material properties and dimensions.

A strong first order diffraction effect was observed in the structure, due to the 400 nm pitch of the array, which could be explained by diffraction theory. A two-peak feature was noted at short wavelengths. This could not be successfully simulated but is suspected to be due to the separation of the disc and hole by a dielectric material forming a scattering site for the incident light as it is diffracted.

The diffraction effect formed by this structure is a limiting factor in the implementation of the structure to display applications, requiring large viewing angles, over which the reflectance spectrum of the structure remains largely unchanged. However, this does allow for the structure to be used in other device applications, such as holographic displays.

Chapter 5

Hybrid Nanostructure

Summary

In this chapter, a hybrid metal nanostructure consisting of Au discs on a polymer thin film and Ag backreflector has been investigated for vibrant structural colour in reflection. The structure benefits from the strong LSPR generated in the Au nanodiscs, high reflectivity of Ag and the optical cavity produced in the transparent polymer layer by interactions between the disc and film. This structure generates a near-zero reflection in a narrow wavelength range. The sharp spectral dips with near-zero reflection are examined, and are shown to be due to a magnetic plasmon resonance below the Au discs, which is highly sensitive to the thin film interference from the polymer and Ag film.

FDTD simulations reveal a cyclical colour trend as the polymer layer thickness is varied. The dependence of colour on several geometric parameters is examined, including the optical path length in the polymer, unit cell size, disc diameter, as well as composition of metal components in the structure. Colour variation sensitivity is not as strong for these parameters as for polymer thickness.

100 μm x 100 μm arrays of Au nanodiscs are fabricated on Si substrates, with 150 nm diameter discs and 300 nm pitch using electron beam lithography (EBL). Assessment of the polymer film by ellipsometry reveals that the fabrication process causes minimal damage to the polymer film properties. The small changes in refractive index are taken into consideration in the simulations. Good agreement is found between arrays simulated by FDTD and those fabricated with the same structural parameters. Diffraction effects are not observed in samples, due to the smaller unit cell than that used in the structure examined in Chapter 4.

5.1 Simulation

Lumerical FDTD was used to simulate far-field reflectance throughout this chapter, with material refractive index data gathered from Palik[161]. Light propagating from above, along the z-axis is normally incident on the structure, with polarization along the x-axis, as shown in Figure 5.1.

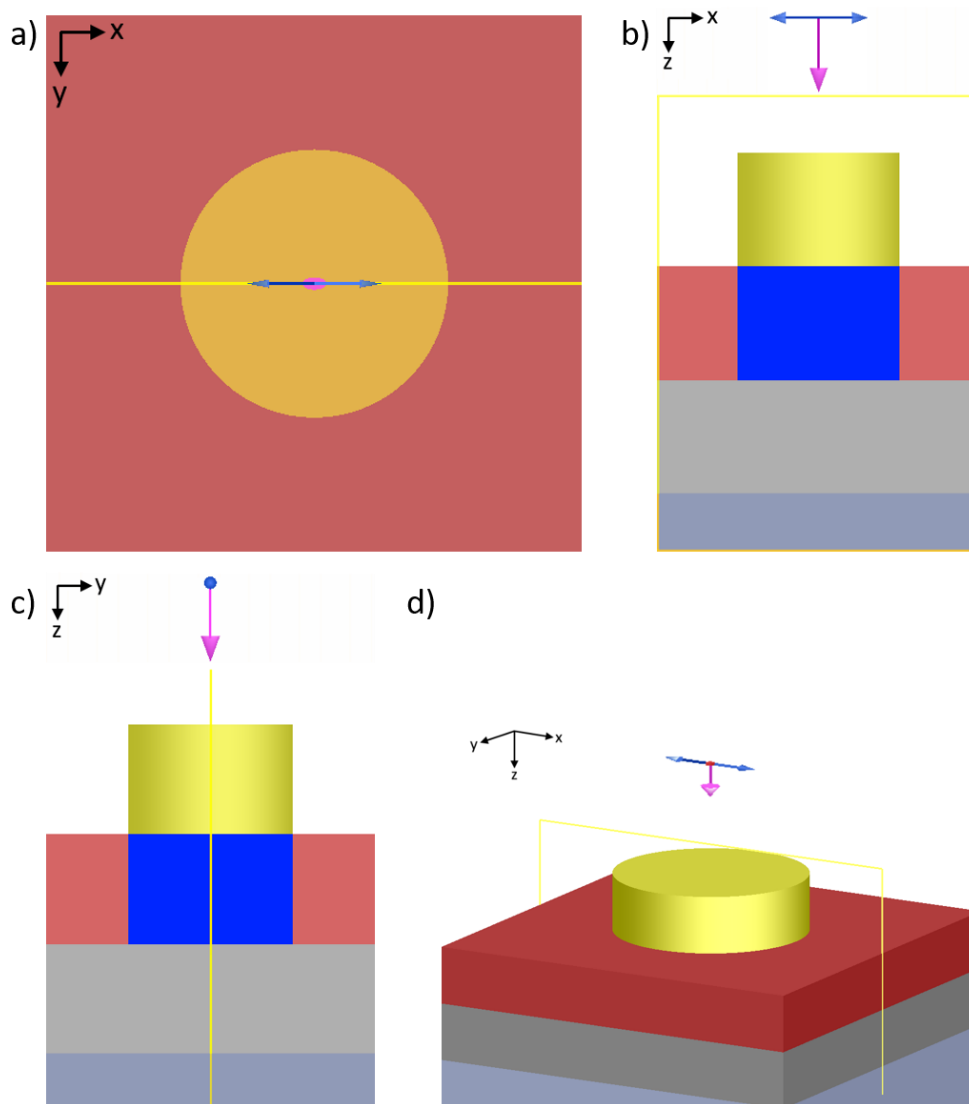


Figure 5.1: FDTD simulation space, illustrating the x , y , and z axes. (a) Top down (xy plane) (b) side view (xz plane), (c) side view (yz plane), and (d) perspective view. Polarisation and direction of plane wave source shown in all figures, as well as E and P field monitor.

In a similar progression to Chapter 4, the structure is broken down to two separate sub-assemblies, and simulated to determine the origin of spectral features. The Au discs were considered as one component, with the polymer film, Ag film and

substrate considered as the other. From this, interactions between these components in the hybrid structure were more easily examined. Geometry variation was then tested to determine colour sensitivity to several structural parameters. A RGB colour conversion script has also been used throughout to aid in determining trends and colour response of the nanostructure array.

5.1.1 Hybrid nanostructure array

The Localised Surface Plasmon Resonance (LSPR) of plasmonic resonators in nanostructures is extremely sensitive to the composition of the surrounding media, and proximity of other resonators. Many studies focus on the use of a single metal nanoparticle-insulator-metal structures[11,12,190–196]. This chapter investigates a hybrid metal nanostructure, consisting of a Au and Ag component, separated by a dielectric layer. Later, alternative metal configurations are proposed that have cost saving implications with this architecture.

LSPR is a collective oscillation of the conduction band electrons in a metal. In this case, the oscillations of the electrons in the Au nanodiscs are confined by the boundaries of the disc. The LSPR frequency is determined by the geometry of the disc, the material composition, the proximity of the nanoparticles to each other, and the refractive indices of the surrounding media. At the resonance frequency, the electron oscillator strength in a nanoparticle is greatest, and generates the largest electric field at the boundaries of the particle. This is the frequency with the highest scattering cross-section, and results in a strong reflectance peak, with intensity falling off from the central resonance wavelength. The LSPR has a decaying evanescent electric field in the immediate vicinity of the disc, with intensity falling away rapidly from the surface interface.

Mitsu Chem Tafmer PN 2070 is the propylene-based polymer utilised as the dielectric layer in this structure. As discussed later, the fabrication process only slightly modifies the polymer. This is taken into account throughout the chapter, with all simulations having a disc, with corresponding Tafmer layer below with refractive index of the “irradiated” polymer. As the Ag layer is optically thick no

light reaches the substrate. There is no impact from the optical properties of the substrate, and no transmission characterisation is required. Si is selected, as it is a relatively cheap, high quality substrate with low surface roughness and excellent adhesion properties, and less charging complications in fabrication using EBL.

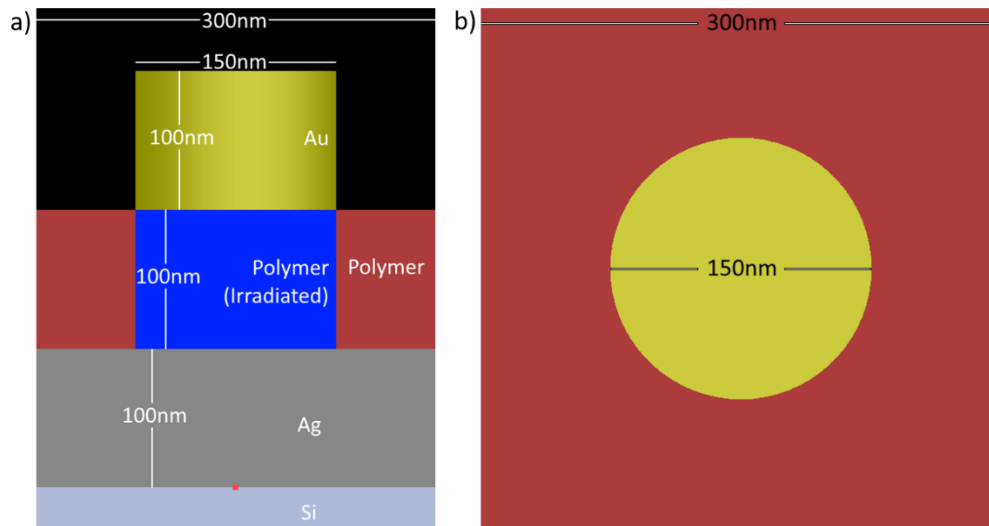


Figure 5.2: Schematic of “typical” structure parameters; 100 nm thick Ag, polymer, and Au nanodisc, with 150 nm diameter, and pitch of 400 nm. Disc of irradiated polymer directly below Au disc. From (a) side view (xz plane) and (b) top view (xy plane).

The “typical” structure considered for this chapter is that shown in Figure 5.2, which consists of a Si substrate, 100 nm thick Ag layer, 100 nm thick polymer layer with irradiated disc cylinder of 150 nm diameter, Au disc of 100 nm thickness and 150 nm diameter, and a cell pitch of 300 nm. All simulations consider a square array of the unit cells under normal incidence plane wave excitation. From this the colour generation mechanism is examined, and its origin determined.

In this section, the components of the nanostructure are examined, in order to determine the origin of the spectral features observed in the assembled structure. Firstly, the far-field reflectance of the disc component is examined, shown in Figure 5.3 as a square array of discs in free space with diameters of 100, 150, and 200 nm. In each case the unit cell size is 300 nm.

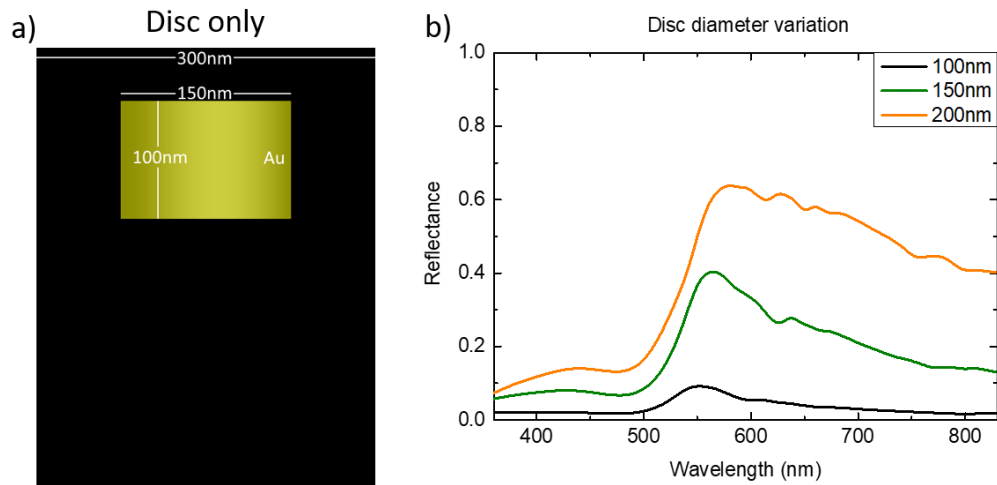


Figure 5.3: (a) Cross section schematic of the Au disc component, 100 nm thickness, diameter of 150 nm, and pitch of 300 nm, in free space. (b) FDTD simulation reflectance spectra of discs with 100, 150, and 200 nm diameter (fixed pitch of 300 nm).

In the disc arrays illustrated in Figure 5.3 (a), an incident plane wave on a periodic sub-wavelength Au nanodisc array excites a LSPR. A reflectance peak is formed at a wavelength of 550 nm, 565 nm, and 580 nm for the 100 nm, 150 nm, and 200 nm disc diameters, respectively. This is due to the shape, size, material composition and surrounding refractive index of the material.

A disc diameter of 100 nm leads to a peak at 550 nm with a weak LSPR reflectance response. The low reflectance intensity is partially due to the small fill factor of the particle in the unit cell, and more significantly due to the weak LSPR response of the disc at this diameter. The 150 nm case presents an LSPR peak at 565 nm, with a higher peak intensity. The 200 nm case has higher reflectance still, and a peak position of 580 nm. In this case, the reflectance quickly falls away from the resonance position at shorter wavelengths, but at longer wavelengths remains high. This is due to increasing the reflectance as the fill factor of the discs in the unit cell increases and tends towards a planar film of Au.

As there is no substrate present in these simulations, the energy of the incident field is either scattered, lost in absorption in the nanoparticle, or lost in transmission between the gaps in the array lattice. Only a portion of the scattered light is radiated back to the far-field observer located above the particle array.

The impact of the polymer layer on the LSPR of the disc can be examined by simulating a structure with only the polymer layer and disc array present, as shown in Figure 5.4 (a). Here, discs with diameter 150 nm, and thickness 100 nm are placed in a square array with 300 nm pitch on a polymer layer. This component simulation takes into account the “irradiated” polymer material directly below the disc, resulting from EBL exposure, which is the same shape as the disc. Polymer thicknesses of 100 nm, and 2000 μm are examined.

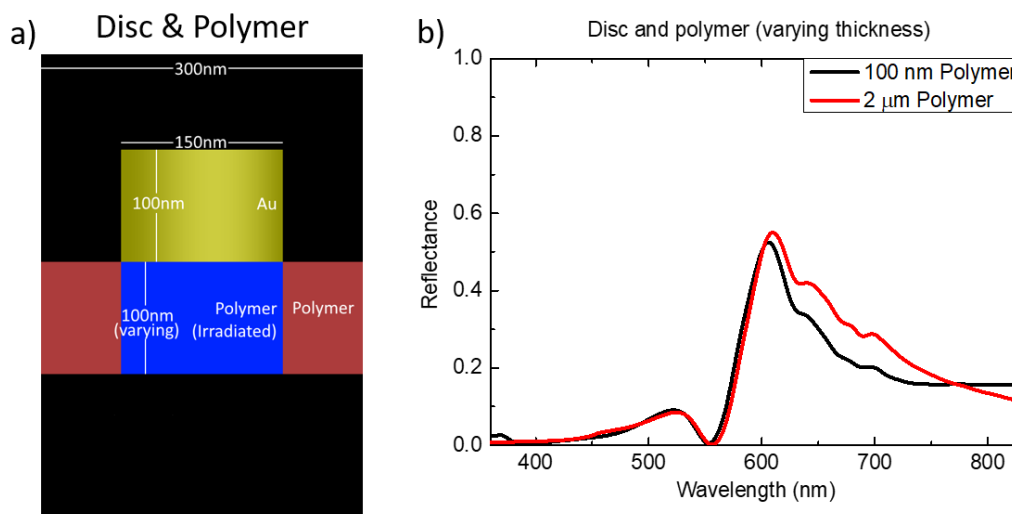


Figure 5.4: (a) Cross section schematic of the backreflector component, with Si 100 nm thickness of Ag, and polymer thickness of 100 nm and 2 μm. An irradiated polymer of diameter 150 nm, and pitch of 300 nm is also included. (b) FDTD simulation reflectance spectra of disc and polymer component, with 100, 150, and 200 nm diameter of disc and irradiated polymer (fixed pitch of 300 nm).

Figure 5.4 (b) shows the reflectance spectra for the disc-polymer structure with polymer thicknesses of 100 nm and 2 μm. The 100 nm thickness is typical of the structure under examination, and the 2 μm thickness is used to illustrate the negligible variation in reflectance from the structure as the thickness is varied a significant amount. For both thicknesses, the reflectance responses significantly overlap below 600 nm, with only a small increase in reflectance for the 2 μm thickness in the 600-750 nm region. The LSPR peak for the disc, observed at 565 nm for the disc with no polymer in Figure 5.3 (b), red-shifts to 600 nm in Figure 5.4 (b), with the polymer layer present. This red-shift in LSPR peak is expected for a

nanoparticle in close proximity to a dielectric with refractive index above that of free-space.

Also noted in Figure 5.4 (b) for both thicknesses, is the formation of a near-zero reflection at 550 nm. This absorption band is the result of the interaction between the disc and polymer at the interface, as the dip is not observed in the Au nanodisc arrays in free space when there is no polymer present, as shown in Figure 5.3. It is also clear from Figure 5.4 (b) that this near-zero reflection is not dependent on the thickness of the polymer, as the response is very similar in both the 100 nm and 2 μm cases. This further demonstrates that the phenomenon is the result of an interaction between the disc and polymer close to the interfaces. This disc-polymer interaction can be examined by studying the E and H fields of the structure at 550 nm.

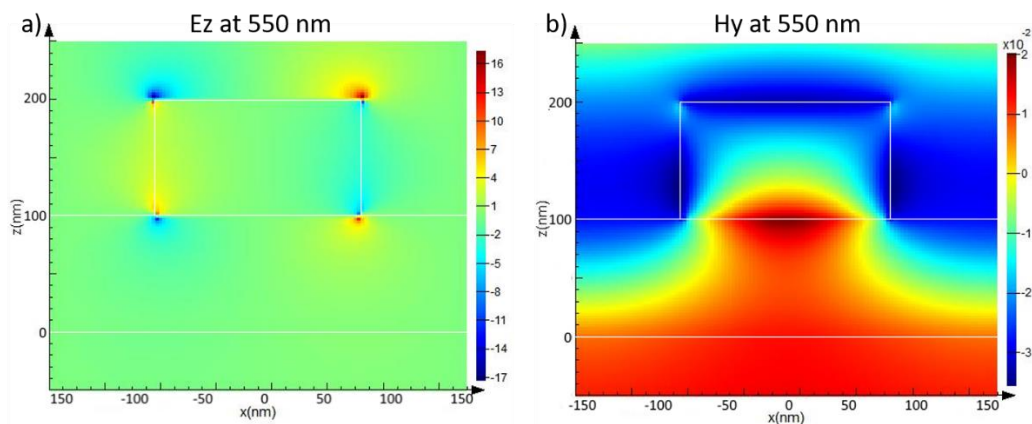


Figure 5.5: Two-dimensional field profiles of (a) z component of electric field (E_z), and (b) y component of magnetic field (H_y) at 550 nm.

Figure 5.5 (a) is field map of the z component of the E field in a cross-section of the structure in the xz plane. The polarisation of the incident field is along the x -axis, and propagates from above, along the z -axis. The E_z field map illustrates the formation of multipoles, localised at the corners of the disc at the top and bottom surfaces. These have alternating polarities, and the multipoles form a large curl in the E field at the disc-air and disc-polymer interfaces. Figure 5.5 (b) shows the y -component of the H field (H_y), which the largest magnitude observed in the structure at this wavelength, and localised directly below the disc surface. This

localisation illustrates the formation of a magnetic dipole along the y-axis at the bottom surface of the disc, at the disc-polymer interface.

Magnetic dipole resonance is the formation of a strong magnetic dipole, formed by a multipole electric resonance in a nanostructure when illuminated. The incident wave creates a multipole, which in turn generates a strong curl in the electric field. This leads to the formation of the magnetic dipole orthogonal to the curl of the electric field and the propagation vector of the incident wave. In this case, the multipole nodes have a large field in the z-axis, and so a magnetic dipole is formed in the y-axis.

This is the primary mechanism for the near-zero reflection observed at 550 nm in the disc-polymer component. In this case, incident light is coupled to the disc close to the peak of the LSPR of the disc alone, as shown in Figure 5.3 (b). This creates an electric multipole in the z-axis, at the disc-polymer interface, and excites the magnetic dipole in the y-axis, directly below the disc. Energy is trapped below the disc, where it cannot be re-radiated back to the observer. This magnetic dipole is the magnetic plasmon resonance, and has been observed previously at metal nanoparticle-dielectric interfaces, resulting in bands of near-zero reflection[190,191,196].

Shown in Figure 5.6 is the backreflector component, considered here to be the Si substrate, 100 nm Ag layer, and 100 nm Taferm polymer layer. The disc of irradiated polymer is included here in a 300 nm pitch square array, with disc varying disc diameter corresponding to the diameter of the Au disc examined in Figure 5.3, of diameter 100 nm, 150 nm, and 200 nm. Also included is a simulation with no irradiated material.

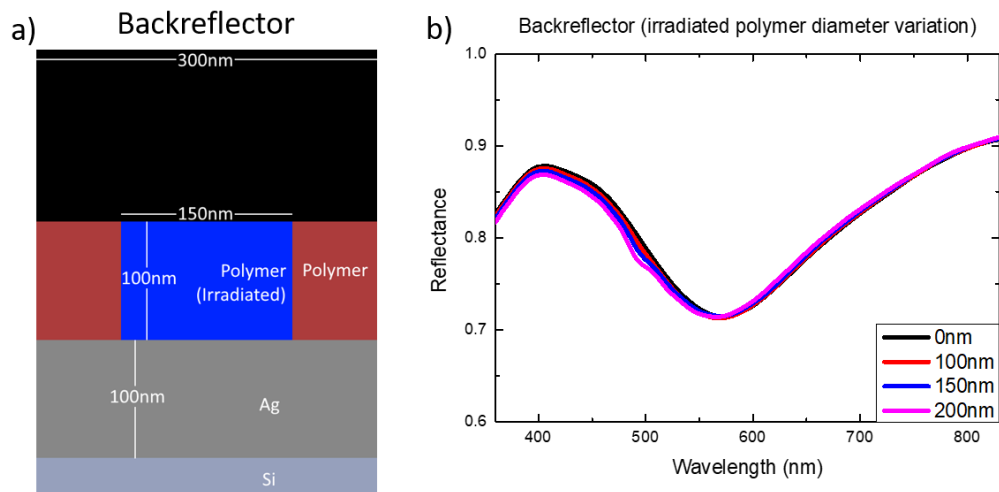


Figure 5.6: (a) Cross section schematic of the backreflector component, with Si substrate, 100 nm thickness of Ag and polymer, and irradiated polymer diameter 150 nm, and pitch of 300 nm. (b) FDTD simulation reflectance spectra of backreflector with 100, 150, and 200 nm diameter of irradiated polymer (fixed pitch of 300 nm).

The primary function of the polymer material is to prevent tarnishing of the Ag layer, and provide a robust platform on which the Au nanodisc array can be patterned. As light is incident on this component, it propagates through the polymer with negligible attenuation and is reflected by the Ag layer. This results in reflectance that is spectrally dependent on the thin film interference effect resulting from the refractive index change at the Ag interface, and the optical path length (nd) of the polymer layer. A polymer thickness of 100 nm is chosen, as it results in a thin film interference effect with a local minimum at approximately 565 nm, corresponding to the peak of the LSPR in the 150 nm disc. This can be observed in the 0 nm case in Figure 5.6, which corresponds to a film of polymer with no “irradiated” polymer cylinder. However, the change is small, and has negligible effect on the response of the component. It can be seen from this Figure that there is no considerable change in reflectance caused by introducing this irradiated polymer cylinder.

Introducing the Ag layer to the disc-polymer structure shown in Figure 5.4 (a), the full structure can be realised. The primary function of the Ag layer is to recycle energy that would be lost in transmission back to the disc component for further interaction with the disc component, increasing reflectance. Due to the strong

overlap of spectral features of the disc-polymer, and Ag-polymer sub-assemblies, a strong interaction is expected in the complete structure presented in Figure 5.7 (a), with the parameters shown.

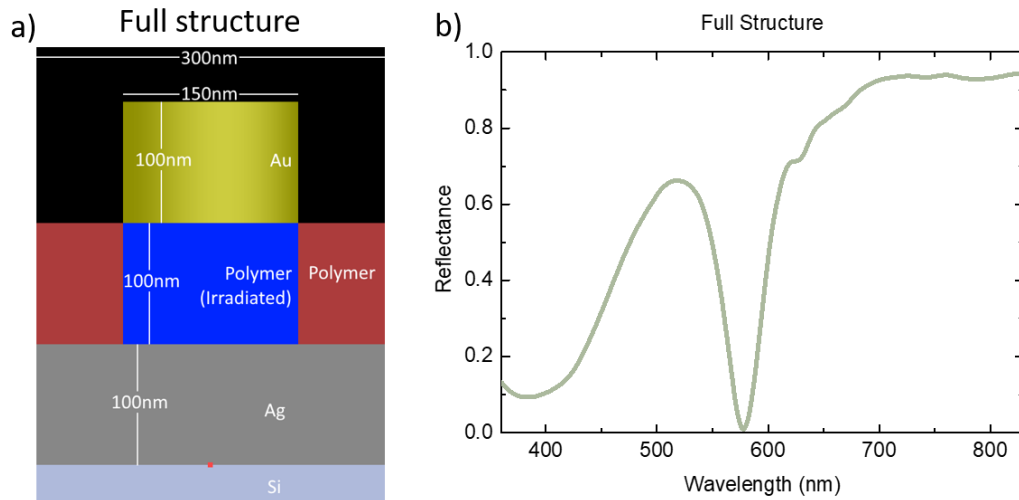


Figure 5.7: (a) Schematic of the Hybrid nanostructure unit cell on Si substrate, with layer thicknesses of 100nm Ag, Polymer and Au, a 300 nm pitch, and 150 nm diameter discs. (b) FDTD simulation reflectance spectra of full structure, combining backreflector and Au nanodisc array. RGB colour displayed as line colour.

This is the case, as demonstrated in Figure 5.7 (b), with the full structure reflectance containing near-zero reflection in a narrow band, centred at 580 nm. The sharp spectral dip is formed due to the magnetic plasmon resonance below the disc, at disc-polymer interface[190,191,196], as observed at 550 nm in the disc-polymer component in Figure 5.4 (b). The introduction of the Ag layer does not result in an increase in reflectance across the entire spectrum, indicating an interaction between the disc-polymer component and the Ag layer that maintains a near-zero reflection feature at 580 nm.

Incident light that is non-interacting with the disc component propagates into the polymer layer, where it is reflected by the Ag backreflector. The 30 nm red-shift in the dip position is due to the introduction of the Ag layer forming a thin film stack. This component causes a strong thin film interference effect to form in the structure, with standing waves formed in the polymer layer. The nodes formed at the polymer-air and polymer-disc interface result in an alteration of the conditions of the dip position, red-shifting it to 580 nm.

To confirm that near-zero reflection in the complete structure is due to the formation of a magnetic dipole resonance, the E_z and H_y field maps can be examined at the peak position at 520 nm, as well as the dip position at 580 nm.

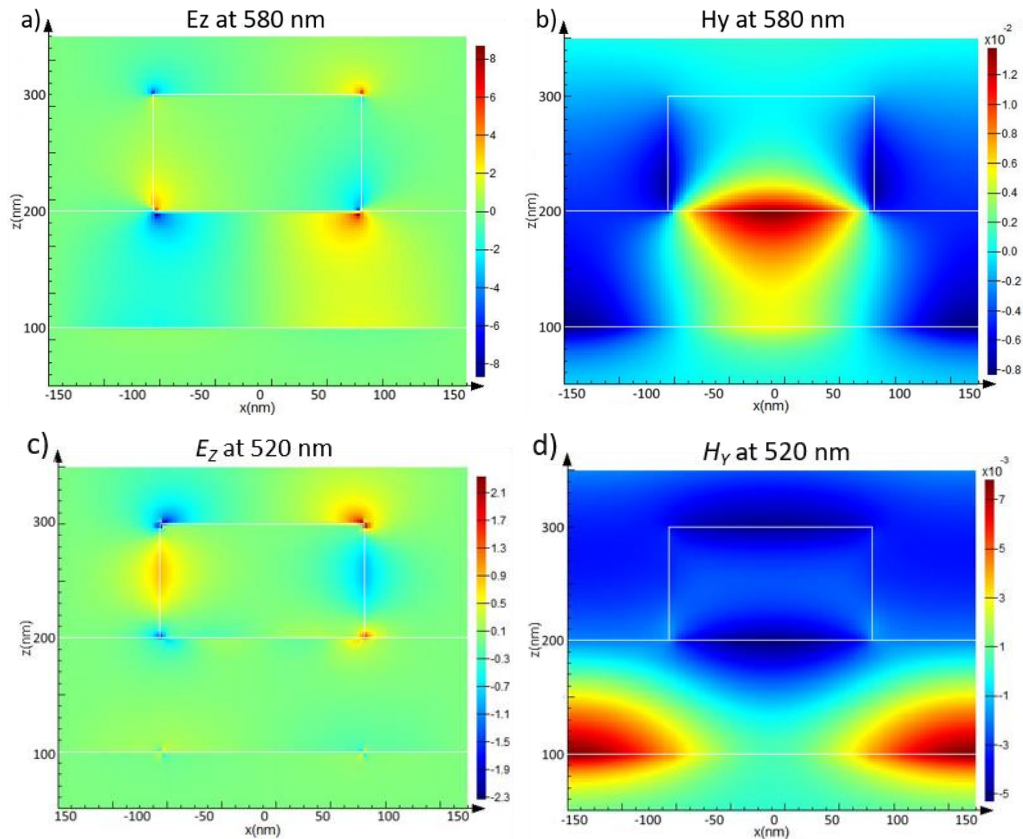


Figure 5.8: Two-dimensional field profiles of (a-c) z component of electric field (E_z), and (b-d) y component of magnetic field (H_y) at (a,b) 580 nm, and (c,d) 520 nm.

Figure 5.8 (a) reveals for the dip at 580 nm, a similar multipole formation at the top and bottom surfaces of the disc, at the disc-air and disc-polymer interfaces, as was observed for the dip feature at 550 nm in the disc-polymer component E_z map in Figure 5.5 (a). Also noted is a significant E_z magnitude in the region between Au disc and Ag layer, directly below the disc corners. This was not observed in Figure 5.5 (a), and is due to the presence of the Ag layer forming a thin film stack, which interacts with the disc. Figure 5.8 (b) shows the H_y field map, demonstrating the formation of the magnetic dipole directly below the disc, at the disc-polymer interface. The field extends to the Ag backreflector, illustrating a lensing effect as incident light is coupled below the disc surface. Figure 5.8 (c) reveals that there is a similar multipole formation in E_z , around the disc at 520 nm. However, the largest

field magnitudes are at the top corners of the discs, rather than at the polymer-disc interface seen for the 580 nm case. Also noted is that the magnitude is approximately a quarter of that seen for the 580 nm case, indicating a much weaker excitation at this wavelength. This is to be expected, as the disc LSPR at this wavelength is shown to be weak at 520 nm in Figure 5.3 (b). Also revealed in Figure 5.8 (d) is the H_y plot at 520 nm, indicating that there is not localisation of the magnetic field at the disc-polymer interface at this wavelength. The large magnetic field localisation in the y -axis is only observed in a narrow wavelength range around the 580 nm dip, indicating that it is the mechanism by which the near-zero reflection occurs.

These field maps illustrate that the near-zero reflection is due to the formation of a magnetic plasmon resonance below the disc, that efficiently couples light into the structure, and traps it below the disc, where it is obstructed from being re-radiated back to the observer.

There is a notable increase in reflectance for the complete structure, particularly in the region of 450-550 nm. There is also a significant increase in reflectance above 600 nm, and towards the boundary of the IR, at 700 nm. At short wavelengths, there is inefficient coupling of incident light to the disc LSPR, as observed in the disc component in Figure 5.3 (b). The Ag component has high reflectivity across the visible, and is non-interacting with the disc in this wavelength region. Subsequently, the predominant re-radiation mechanism for light at this wavelength is planar reflectance. Losses in reflectance can be attributed to scattering of light at the corners of the disc, absorption into the Au due to the low reflectance of Au at this wavelength, as well as some weak coupling of light into the structure. In the near-IR, the region of 700-830 nm in the spectrum shown in Figure 5.7 (a), the structural dimensions are much smaller than that of the wavelength of incident light, as a result an effective medium is perceived, and there are no resonance conditions being met in the disc, due to in-efficient coupling to the particle far from the resonance wavelength. Both Au and Ag have high reflectivity in the IR, as such,

high reflectance is expected as one tends towards the red and into the Near-IR region above 700 nm.

5.1.2 Geometries

Structural parameters were varied in a similar fashion to that of the Al structure in Chapter 4, though the number of example spectra selected for examination is reduced. This is due to the nature of the change in spectral shape of the reflectance from this nanostructure as parameters are varied when compared to the Al structure. The spectra in this case are harder to read when overlaid, and so less are shown but the same variation range of 0-300 nm was examined in most cases.

The first parameter to be varied in the structure was that of polymer layer thickness, to determine the sensitivity of colour on the optical path length, nd , of the separation between the discs and backreflector components. The typical structural parameters were maintained, with a Si substrate, 100 nm Ag layer, 100 nm thick Au nanoparticles, with 150 nm diameter, and 300 nm pitch simulated on a polymer with varying thicknesses of 0-300 nm with a step size of 25 nm. A 150 nm pillar of irradiated polymer was also included and varied in thickness to match the surrounding polymer layer.

Two representative spectra with polymer thicknesses of 100, and 200 nm, are displayed in Figure 5.9 (a). In this case, only two spectra were selected for examination, due to difficulty in resolving the features from each individual spectrum when several spectra are overlaid.

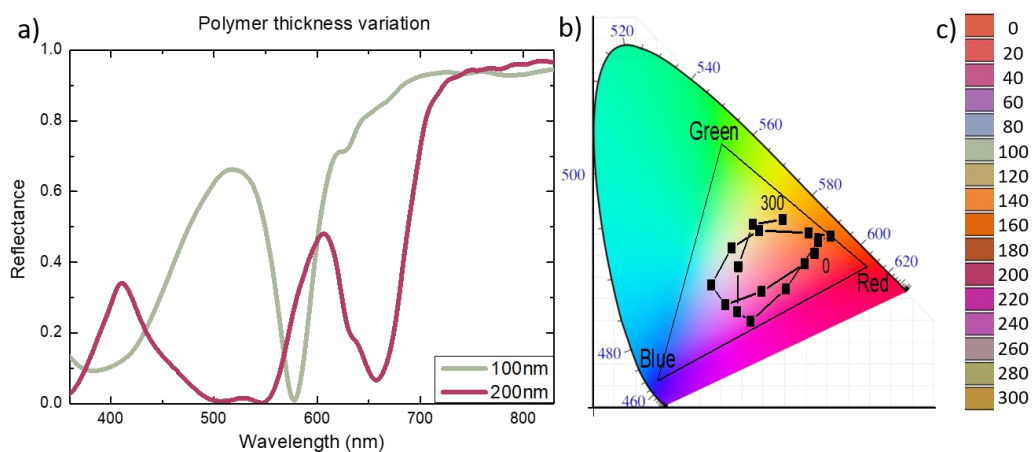


Figure 5.9: (a) Reflectance spectra of nanostructure with 100 nm and 200 nm polymer layer thicknesses. (b) CIE xyY colour-space map from reflectance spectra, for polymer layer thickness of 0-300 nm, with 20 nm step size. (c) sRGB colour swatches at each thickness.

The 100 nm simulation has a high reflectance peak of 66% at 520 nm, and a near-zero reflection at 580 nm. The shape and distribution of the spectral features results in strong overlap with the middle (green) cone, and a relatively weak overlap of short (blue) and long (red) cones. This results in a green colour response with good colour clarity. When polymer thickness is increased to 200 nm as shown in pink/red in Figure 5.9, the thin film interference effect results in a red-shift of spectral features, with the 520 nm peak shifting to 606 nm. A reduction in reflectance from 66% to 48% is also noted at this peak. The near-zero reflection noted at 580 nm is red-shifted to 657 nm, with a minimum reflectance at this position increasing to 6%. An area of low reflectance is introduced between approximately 500-550 nm, due to the red-shifting of spectral features from the UV. These factors combine to weakly stimulate the short (blue) cone, while having relatively large spectral intensity overlap with the long (red) cone, producing a pink-red colour.

Figure 5.9 (b) shows a CIE xyY map from the spectra, that allows for a determination of colour trends as the thickness was varied. A roughly cyclical colour trend is noted, with a periodicity of approximately 180 nm of polymer thickness change.

Figure 5.9 (c) reveals the sRGB colour swatches, that further illustrates the cyclical chromaticity change as thickness is varied. A wide chromaticity range is

demonstrated, with red, blue and green colours generated at 0 nm, 80 nm, and 100 nm of polymer, respectively. This is important for display applications, in which these primary tristimulus colours are a requirement to generate red, green, and blue sub-pixels

Polymer thickness was further increased to 1000 nm, to determine the extent to which thickness can be increased, while maintaining colour clarity and distinct chromaticity change. Simulations of the typical structural parameters were maintained, while polymer thickness was varied from 0-1000 nm, with 25nm step size.

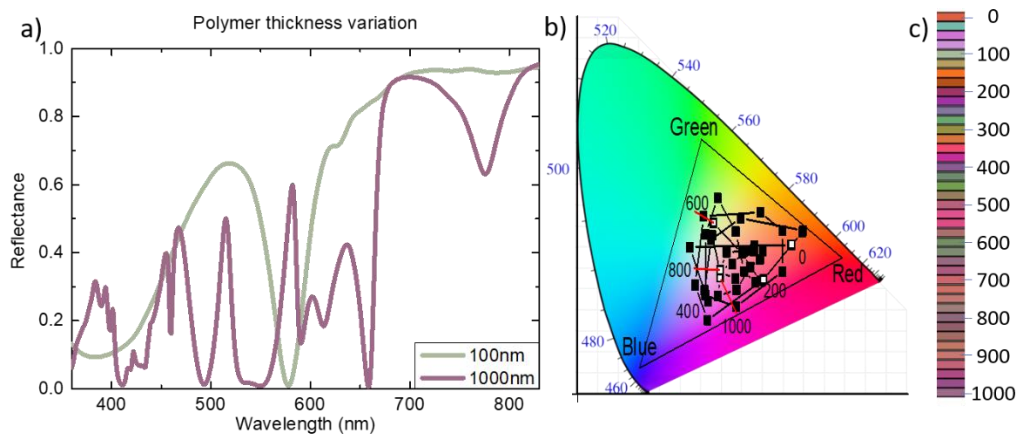


Figure 5.10: (a) Reflectance spectra of nanostructure with 100 and 1000 nm polymer layer thickness. (b) CIE xyY colour-space map from reflectance spectra, for polymer layer thickness of 0-1000 nm, with 25 nm step size. White dots indicate every 200 nm step. (c) sRGB colour swatches at each thickness.

Figure 5.10 (a) examines the 100 nm and 1000 nm thickness cases, to illustrate the narrowing of spectral shapes as the thickness is increased from the “typical” structure with 100 nm, to that of 1000 nm. There is a notable reduction in colour saturation and clarity for thicker layers. In the 1000 nm thickness case, many more sharp spectral features in the visible region are noted, with reflectance peaks of 40-50% and spectral dips with near-zero reflection at a number of positions. The thin film interference effect at this optical path length results in many spectral features in reflectance, and produce the reflectance spectrum shown in Figure 5.10 (a). No significant overlap occurs with only one cone, and so colour clarity is reduced.

The trend of this reduction in clarity is further demonstrated in Figure 5.10 (b), with CIE xyY positions plotted, and (c) sRGB colour swatches for each simulation. The approximately cyclical colour trend noted in Figure 5.9 (b) is present here. However, the saturation of colours and the chromaticity change is significantly reduced with each increment above approximately 400 nm of polymer thickness. Though there is clearly a cyclical periodicity to the colour change with thickness variation, the optical path length must be sufficiently small in order for single spectral features to form, and good colour clarity to be produced in reflectance.

5.2.1.1 Diameter variation (fixed pitch)

The diameter of the disc is the second parameter to be examined, maintaining a fixed unit cell size (pitch) of 300 nm throughout. Representative spectra for 100 nm, 150 nm, and 200 nm cases are shown in Figure 5.11 (a).

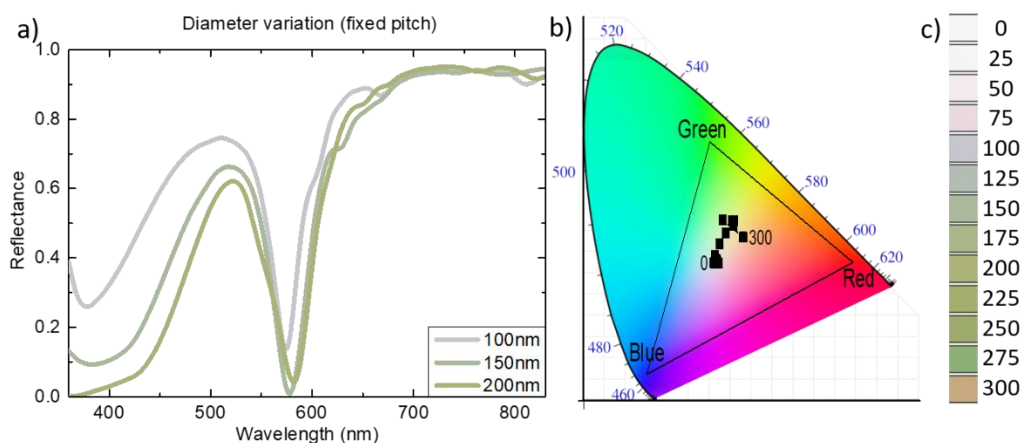


Figure 5.11: (a) Reflectance spectra for varying disc diameter of 100 nm, 150 nm, and 200 nm, and a fixed unit cell size (pitch) of 300 nm. (b) CIE xyY colour-space map from reflectance spectra of varying disc diameters (fixed pitch) from 0-300 nm in 25 nm steps. (c) sRGB colour swatches at each diameter.

The spectral shape remains largely unchanged. A decrease in reflectance at shorter wavelengths is noted as the diameter is increased. This can be attributed to the increase of the fill factor of the disc in the unit cell as diameter is increased. At small diameters the disc constitutes a small portion of the unit cell, as illustrated in Figure 5.3, and also leads to this component only contributing a small amount to the reflectance. This, combined with the weak LSPR of the Au disc component, leads to a high reflectivity at short wavelengths, as silver dominates the reflectance response

of the structure. As the diameter increases, the disc fills more of the unit cell, and the LSPR of the disc increases in strength. As the disc fill factor increases the backreflector fill factor reduces, and so the disc response has more impact on the reflectance, despite the disc reflectance being weak in this region. This leads to a reduction in reflectance of the peak at 520 nm.

The strong dip noted at 580 nm does not change position as the diameter is varied. However, in the 100 nm case the dip does not experience near-zero reflection, with a minimum of approximately 15% reflectance. This is due to the LSPR of the disc at this diameter being weak, as mentioned previously. As the LSPR is weak, the intensity of the magnetic plasmon resonance below the disc is reduced. As the diameter is increased, the LSPR strengthens, and so does the magnetic plasmon resonance, and its interaction with the thin film interference interaction between the components, leading to a near-zero reflection formed. As seen in Figure 5.3, the Au LSPR peak position does not change significantly as the diameter is increased, only shifting from 550 nm to approximately 580 nm as the diameter is varied from 100 nm to 200 nm. This also leads to the dip position not shifting significantly.

Figure 5.11 (b) illustrates the CIE xyY plot, and (b) sRGB colour swatches for the full range of diameter variation of 0-300 nm in 25 nm steps, further illustrating the colour change as the diameter is increased. Starting with the absence of the disc, and increasing in diameter, the trend noted previously of the disc fill factor affecting the colour is clear, with the response moving from white towards the green colour noted at 150 nm diameter. Increasing the disc diameter further increases the fill factor of the Au disc until it eventually dominates the reflectance as the response is primarily due to the reflectance of planar Au, appearing as a gold/orange.

5.2.1.2 Diameter variation (fixed gap)

The third parameter to be varied is that of the diameter with a fixed gap between discs. Three example spectra are examined in Figure 5.12 (a).

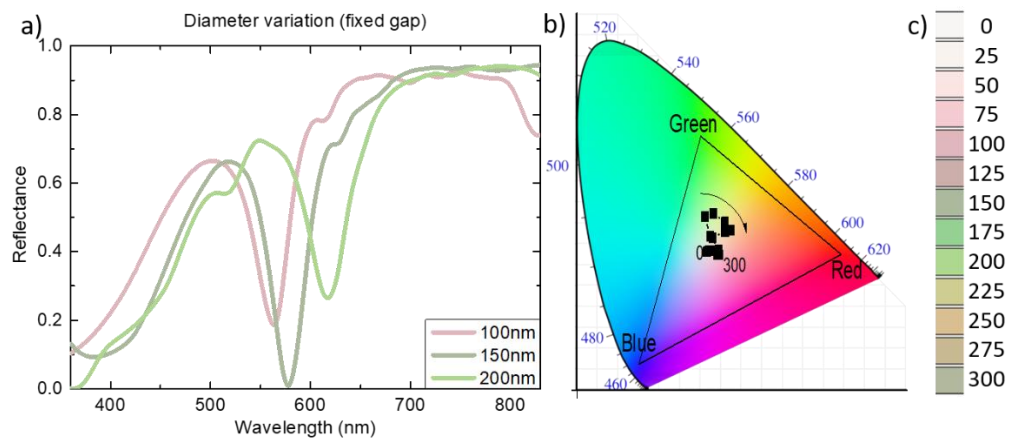


Figure 5.12: (a) Reflectance spectra for varying disc diameter of 100, 150, and 200 nm, and a fixed gap of 150 nm between discs. (b) CIE xyY colour-space map from reflectance spectra of varying disc diameters (fixed gap) from 0-300 nm in 25 nm steps. (c) sRGB colour swatches at each diameter.

From these spectra in Figure 5.12 (a), it is clear that the variation of the unit cell size (pitch) of the array leads to a red-shift of the peak and trough features in the visible region. In the case of the 100 nm diameter disc and corresponding 250 nm unit cell size, the peak is noted at approximately 500 nm. This shifts to 550 nm as the diameter increases to 200 nm, where the pitch is 350 nm. This red-shift in dip position of 50 nm for a 100 nm diameter increase is a significantly larger shift than that observed with a fixed pitch of 400 nm in Figure 5.11, where the dip red-shifts by only 5 nm. This indicates that there is weak inter-disc interaction, as maintaining a fixed gap between them allows for a larger shifting of spectral features than if the pitch is fixed.

The 150 nm diameter case in Figure 5.12 is the only one presented with a near-zero reflection in the dip. This is due to the sensitivity of the disc LSPR position to disc diameter, which shifts significantly more than in Figure 5.11. As the interaction with the backreflector is highly sensitive to the position of the LSPR peak, the offset between the disc component peak and backreflector component dip leads to a weaker interaction between them, and so near-zero reflection is not observed in the 100 nm and 200 nm diameter cases. In Figure 5.11, this is not as severe, as the disc LSPR position does not significantly red-shift with diameter, and so the disc and backreflector interaction remains largely unchanged.

Figure 5.12 (b) illustrates the CIE xyY plot from the reflectance spectra in the full range. Also included in Figure 5.12 (c) is the sRGB colour swatches. The variation leads to a similar trend to that noted in Figure 5.11 (b), as the disc diameter is similarly increased in that study. However, as the disc separation is maintained, the fill factor of the disc in the unit cell does not significantly change in the range above 150 nm, and so the reflectance of the structure does not tend towards a planar Au reflectance. Instead, as the diameter is increased the colour tends towards a single green colour as the increase in diameter does not significantly affect the resonance conditions in the structure.

5.2.1.3 Varying gap (fixed diameter)

The fourth, and final parameter to be examined is that of varying gap with a fixed diameter of 150 nm, to further examine inter-disc interaction. Representative spectra for the 50-150 nm range are shown in Figure 5.13 (a).

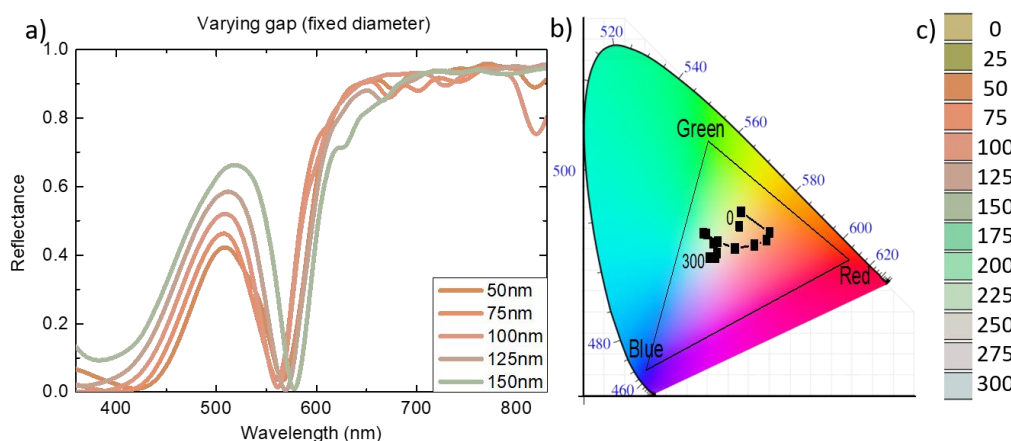


Figure 5.13: (a) Reflectance spectra for varying gap between discs of 50-150, in 25 nm steps, with a fixed diameter of 150 nm. (b) CIE xyY colour-space map from reflectance spectra of varying gap (fixed diameter) from 0-300 nm in 25 nm steps. (c) sRGB colour swatches at each gap.

Figure 5.13 shows the spectra for disc gaps of 50-150 nm in 25 nm steps, with a fixed diameter of 150 nm. There is a clear trend towards higher reflectance across the visible, with exception of the dip feature, which maintains near-zero reflection throughout. The increase in reflectance is expected, as the fill factor of the discs in the unit cell is reduced as the gap increases. This leads to a larger contribution to the reflectance from the Ag backreflector. The features appear to red-shift with

increasing gap by a small amount, with the dip shifting by approximately 15 nm over the gap range shown. This indicates that the inter-disc interaction is weak, as observed previously in Figures 5.11 and 5.12. The strongest evidence of inter-disc interaction is in the comparison of Figure 5.11 and 5.12, where the fixing of the pitch in Figure 5.11 appears to impede the red-shifting of the dip feature, which is not observed in Figure 5.12.

Though this variation of disc gap with a fixed diameter has been utilised to determine inter-disc interactions, it can also be used to determine impact of the array periodic surface plasmon (PSP) and Wood's anomaly (WA) in this structure, using Equation 2.17 for the PSP, and Equation 2.25 for the WA. Figure 5.14 shows the reflectance spectra for structure with a fixed diameter of 150 nm, and a varying periodicity of 300 nm, 350 nm, and 400 nm. The 300 nm periodicity case corresponds to the "typical" structure parameters of 150 nm diameter, 150 nm gap.

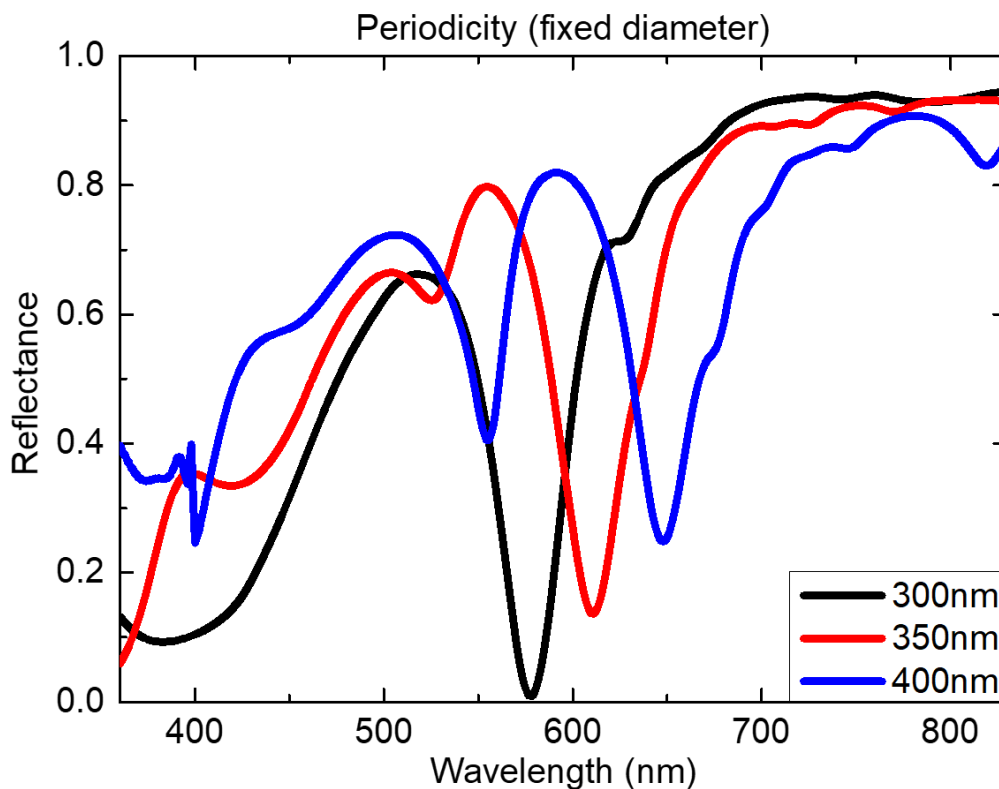


Figure 5.14: Reflectance spectra for array periodicity of 300 nm, 350 nm, and 400 nm, with a fixed diameter of 150 nm. Line colour is not shown in representative sRGB colour value, to aid in observation of each line-shape.

For array pitches of 300 nm, 350 nm, and 400 nm with a fixed disc diameter, such as those shown in the Figure 5.14, the wavelengths of the PSP and WA can be determined. The wavelengths for the first-order PSP with a 300 nm, 350 nm, and 400 nm pitch are 503 nm, 565 nm, and 632 nm, respectively. The wavelengths for the first-order WA for the same pitches are 444 nm, 518 nm, and 592 nm.

In the case of the PSP wavelengths, there is no correlation noted with spectral features observed in Figure 5.14 at the corresponding periodicities. For the WA wavelengths, there is a dip feature noted at approximately 525 nm that is close to the 512 nm value presented for the WA with a 350 nm periodicity. However, this dip is not observed in the 300 nm periodicity case, and does not agree with the 400 nm periodicity dip feature that appears to be this feature red-shifted to 550 nm, where it is expected to occur at 592 nm for a WA. As no features are observed at the expected wavelengths for all periodicities, for either the PSP or WA, these phenomena are determined to not have a significant impact on the reflectance from the array structure.

5.1.3 Material Composition

Material composition is one area of particular interest in structural colour, as noble metals have been extensively studied for their strong resonance effects, and the resistance to tarnishing of platinum group metals. However, structures utilising these materials exhibit high costs for production in devices, as raw materials are highly expensive. Alternative materials, such as Al have been examined in recent years[11], due to the high reflectance of the material, and the formation of a self-terminating 3 nm oxide layer, that protects the material from tarnishing[42]. Indeed, this was a motivation of the investigation of the Al nanostructures in Chapter 4.

Figure 5.15 consists of the colour swatches from FDTD simulation of typical structural parameters, but with varying metal composition. The dependency of the colour response is examined as the polymer thickness is varied in structures consisting of various metal combinations.

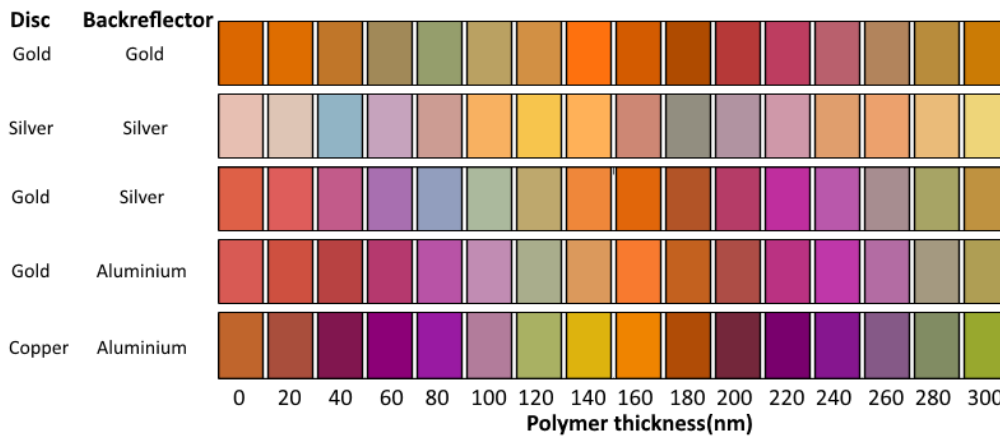


Figure 5.15: Colour swatches of material simulations with differing metals in disc and backreflector as polymer thickness is varied.

The CIE xyY plots for these colour trends are also presented in Figure 5.16 for each composition, with most structures following a general cyclical colour trend, similar to the hybrid structure presented previously in the chapter.

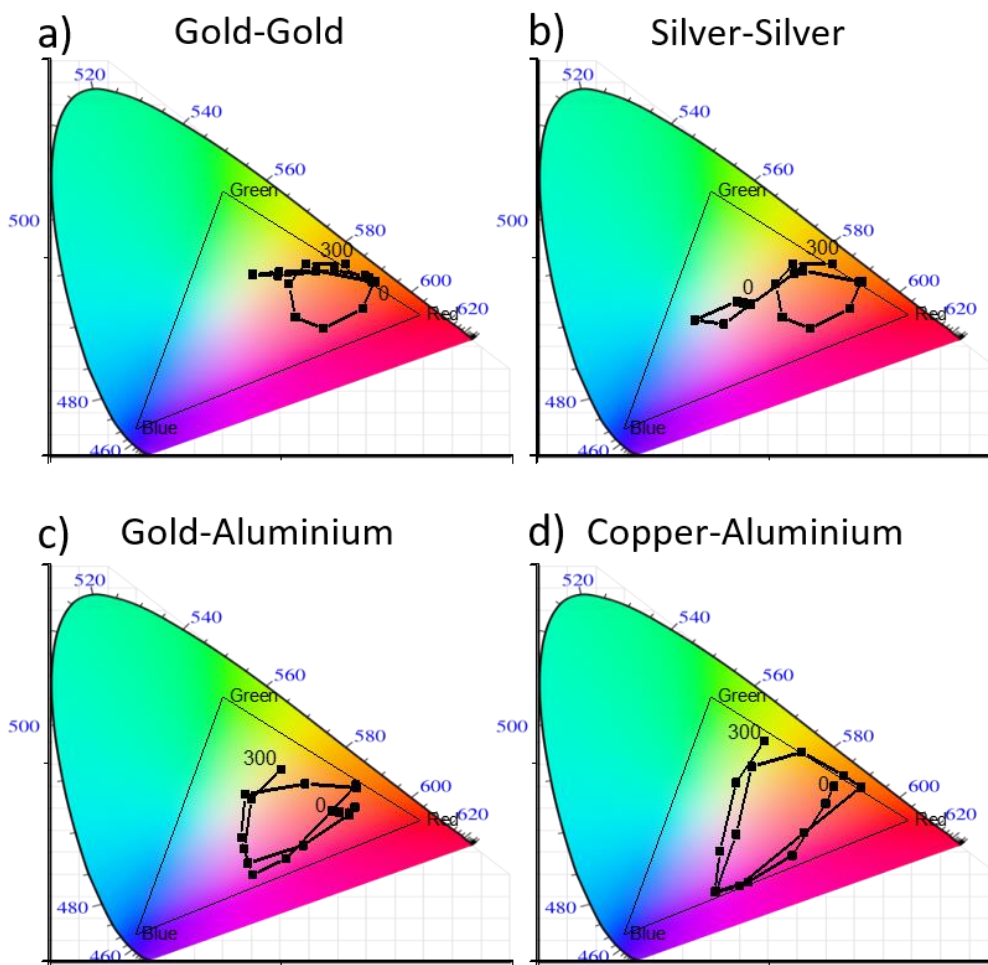


Figure 5.16: CIE colour-space maps of each material combination tested, indicating chromaticity performance in colour generation at varying polymer layer thickness.

Structures often use Au as a plasmonic resonator component due to the strong LSPR of Au nanoparticles in the visible, as well as its resistance to tarnishing. However, the use of Au as a backreflector material has limitations, as it has low reflectance below 500 nm. It is evident in Figure 5.15, that by using Au for both metallic components has a significant effect on the colour response of the system at all polymer thickness, resulting colour palette that is predominantly orange and red tones. This is further demonstrated by the CIE plot in Figure 5.16 (a), which shows a distinct localisation of chromaticity values in close proximity to the red tristimulus value.

Conversely, with an Ag-Ag system shown in Figure 5.16 (b), the colour palette consists entirely of pastel colours, due to the high reflectivity of the silver backreflector and the top surface of the Ag disc in the structure. The resulting spectra contain high reflectivity across the visible spectrum, due to high reflectivity at off-peak positions and so a washed out pastel palette is the result. It is also important to note that by altering the disc metal properties, the resonance properties of the LSPR are also altered, with a peak resonance position of 450 nm for an Ag disc with 150 nm diameter and 100 nm thickness.

By utilising Al as a backreflector material in Figure 5.16 (c), and Au disc, a colour palette is produced with very similar properties to the Au-Ag hybrid metallic structure, though the colour cycle is offset by approximately 20 nm in polymer thickness. This is attributed to the difference in refractive indices between Ag and Al resulting in a red-shift of the thin film interference feature position at the same thickness of polymer. While the Ag-polymer backreflector stack produced a spectral dip at 520 nm with 100 nm polymer, the spectral dip for an Al-polymer is located at 590 nm for the same polymer thickness.

A suitable substitute for Au can be found in Cu, as Cu exhibits a strong LSPR condition in the visible, with similar structural dimensions as Au. The LSPR resonance peak of a 150 nm diameter, 100 nm thickness Cu disc is 600 nm. When incorporated into the nanostructure as the disc material in Figure 5.16 (d), it

produces sharp spectral features with high intensity, corresponding to sRGB values with high colour saturation. In practical terms, a structure incorporating this material would need protection from tarnishing, as Cu oxidises quickly. This could be achieved by encapsulation in a top polymer layer, though this would change the refractive index around the disc, and would result in a shift in the LSPR position for particles of the same size and shape.

5.2 Experimental

This section details the fabrication of the Hybrid nanostructure samples, the determination of structural properties and dimensions, and the optical characterisation. Two samples were considered for fabrication, and are shown here for comparison with simulation results.

5.2.1 Fabrication

Substrates were cut from plane (100) 10 cm diameter Si wafers, to 10x12 mm sample substrates. These were sonicated in solutions of Acetone, Methanol and Isopropyl Alcohol (IPA), respectively, for 20 minutes each. They were then dried with a Nitrogen gun to ensure no residue remained on the surface. Thin film metallic layers were deposited on the substrates using a Temescal FC-2000 Electron-Beam Physical Vapour Deposition (EB-PVD) system, beginning with a 100 nm Ag layer at a deposition rate of 0.5 Å/s. Immediately after completion, a propylene based polymer layer was deposited using a simple spin coating process at 3000 rpm for 30 seconds. The polymer layer acted as a sealant, preventing tarnishing of the Ag. It was also the material onto which the Au nanodisc arrays were fabricated.

In order to pattern the Au discs, a layer of PMMA was spin-coated, followed by 2 minutes at 180°C on a hotplate. The PMMA was used as positive tone resist. PMMA layer thickness was measured using a Dektak profilometer and was found to have a thickness of 250 ± 5 nm. E-Spacer was spin coated at 3000 rpm for 30 seconds, and was used to prevent excess charge build up, improving the resolution of finished arrays. The nanodisc arrays were patterned by EBL on a Carl Zeiss Supra Field

Emission Scanning Electron Microscope (FE-SEM). An accelerating voltage of 15 kV was used at a working distance of 5 mm, with a beam current of 35.6 pA and aperture of 10 μm delivering an area dose of 250 $\mu\text{C}/\text{cm}^2$ over an array area of 100 μm . After EBL patterning of the arrays, the E-Spacer was removed by immersion and rinsing in de-ionised water for 10 seconds. The patterns were developed using a 1:3 solution of Methyl Isobutyl Ketone (MIBK) to IPA for 45 seconds. Samples were immediately submerged in IPA for 10 seconds to stop the development of the resist, followed by drying with a Nitrogen gun. Subsequently, a 100nm thick Au layer was deposited by EB-PVD, at a deposition rate of 0.5 $\text{\AA}/\text{s}$. Lift-off was carried out by submersion of the samples in Acetone solution heated to approximately 40 $^{\circ}\text{C}$ on a hot plate for 10 minutes. This removed the remaining PMMA and unwanted Au from the samples. This process is illustrated in Figure 5.17.

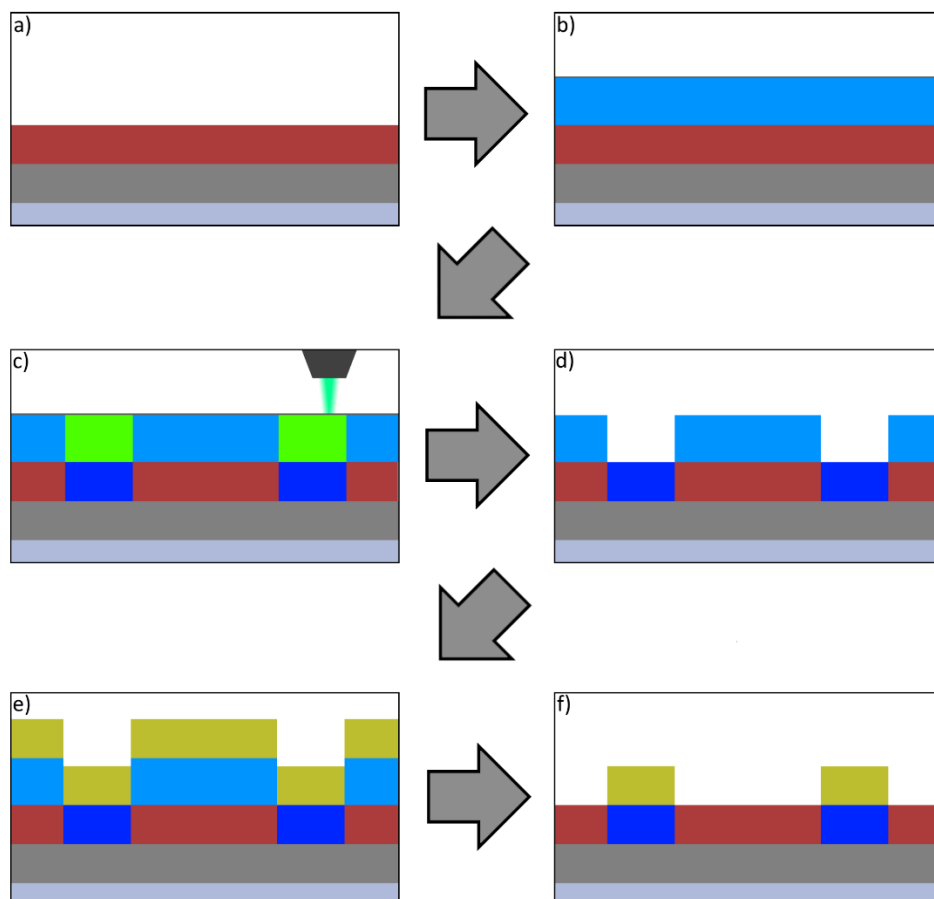


Figure 5.17: Fabrication process for array structure. (a) Ag and Polymer deposition, (b) PMMA deposition, (c) EBL patterning, (d) development, (e) Au deposition, and (f) lift-off to form final structure.

5.2.2 Characterisation

The dielectric material used throughout was a propylene based transparent polymer with commercial name Tafmer. This was used as the supporting layer for the Au nanodisc arrays, and was selected due to the resistance of the material to the development process after EBL patterning.

The structural properties of the samples were characterised. Multiple angle scan micro-spot ellipsometry was carried out on a SOPRA GESP 5 Variable Angle Spectroscopic Ellipsometer. This was used to determine the polymer thickness in the fabricated structures, with a lateral spot size of 300 μm , as well as the measurement of the polymer refractive index. Two samples were fabricated with varying polymer thicknesses. This was done to determine the viability of the structure for fabrication, and sensitivity to structural variation in thin and thick polymer layers. Two samples also allowed for the matching of experiment to simulation at two polymer thicknesses.

Multiple angle ellipsometry measurements returned values of (70 ± 5) nm for Sample A and (196 ± 5) nm for Sample B, for the thickness of the polymer layer in an area near the patterned array on each substrate. Due to the relatively low Young's modulus of 14 MPa for Tafmer PN 2070, Dektak measurements could not be carried out to verify these thicknesses. Fabrication on such a thin polymer film is challenging, and it is important to determine if the fabrication process modifies the properties of the polymer layer. In particular, to determine if the molecular structure of the polymer, and, consequently, its optical properties are altered by exposure to high energy electrons during the EBL process, or if changes have been induced chemically by the development or lift-off procedures. As ellipsometry measurements could not be performed on the area directly below the Au nanodiscs, a test sample was prepared to determine damage caused by the fabrication process. This sample consisted of a Si substrate, 100 nm Ag layer, 300 nm polymer layer and PMMA layer. EBL exposure was then carried out on a 3 x 3 mm area, with a dose of 250 $\mu\text{C}/\text{cm}^2$, followed by the same chemical treatment undergone by the full

patterned samples for development and lift-off. The complex refractive index and thickness of the polymer in the test sample were then analysed using ellipsometry, both on the area of exposure and at a position near the exposed area. The spectral dependences of n and κ for the polymer are shown in Figure 5.18 (a) and (b), respectively.

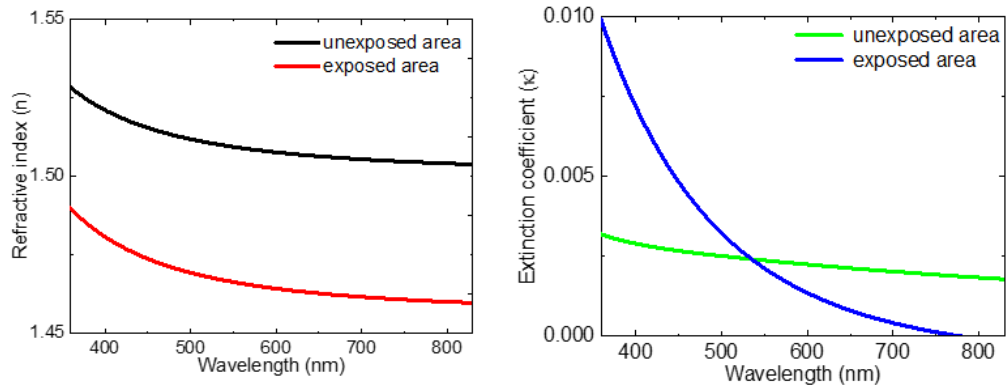


Figure 5.18: (a) Real (n) and (b) Imaginary (κ) components of complex refractive index of propylene-based polymer used in nanostructure fabrication measured by ellipsometry for both the area exposed EBL and, and the area unexposed. Both areas were treated chemically according to the fabrication procedure.

The thickness of the exposed polymer area was found to be (292 ± 5) nm, which corresponds well to that of (288 ± 5) nm measured on a close-by unexposed area. This indicates there is no significant change in the polymer thickness due to the EBL process. This also means that difference in thickness of the polymer is expected below the discs in the array samples, and the measurement taken off the array is suitable.

The real component, n , of the refractive index reduced by approximately 3.5% after exposure to EBL and chemical treatment. This is potentially due to the breaking of polymer bonds by high energy electrons, reducing the polymer chain lengths in the layer. Changes in the imaginary component, k , of the refractive index were found to significantly increase on the exposed area of polymer, particularly at shorter wavelengths in the visible spectrum. This indicates an increase in scattering due to an increase in surface roughness after e-beam irradiation, though the scattering is relatively low in both cases. This is illustrated in Figure 5.18 (b), with the exposed

area averaging an extinction across the visible region of 4.71% and the unexposed area averaging 2.71%.

Electron microscopy imaging was carried out on fabricated structures using a Carl Zeiss Supra FE-SEM. An accelerating voltage of 5 kV was used, at a working distance of 4.9 mm and aperture of 10 μm . A micrograph of sample B, with polymer layer thickness of (196 ± 5) nm is shown in Figure 5.19.

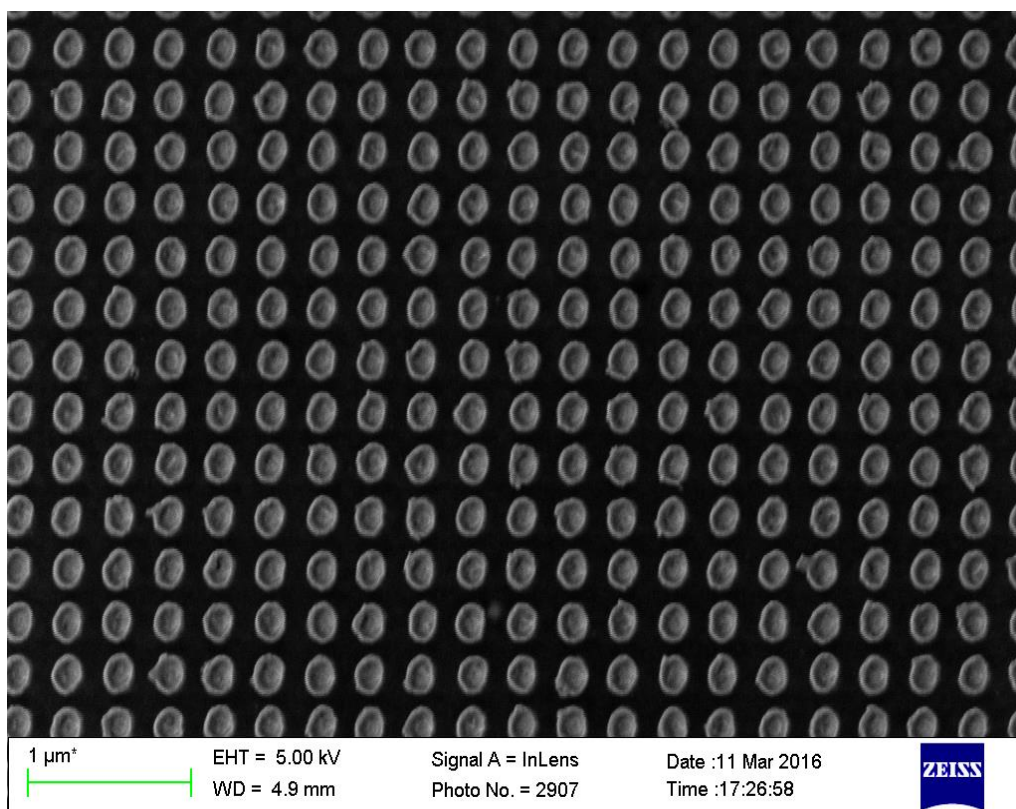


Figure 5.19: Carl Seiss Ultra FE-SEM image of fabricated array (Sample B) with Au disc diameter measured of (200 ± 10) nm and good nanoparticle shape uniformity noted.

The fabricated nanodiscs are found to have a mean diameter of (200 ± 10) nm over 10 measurements. Disc shape appears slightly oblong in the vertical axis, potentially due to charging in the material as the design was patterned by EBL. Also observed is a slight dip in the centre of the discs, as seen in Figure 5.19. The nanodiscs are arranged in a square array with 300 nm pitch, with minimal defects observed across the array.

Having successfully fabricated the structures, the arrays were optically characterised. Optical microscope images for each of the samples are presented as

insets in Figure 5.20 (a) and (b) for sample A and B, respectively, along with the measured spectra of the arrays. Distinct purple and red colours are observed for the polymer thicknesses of 70 nm and 196 nm, respectively. The microscope image shows uniform colour response across the array area, indicating good structural uniformity across both arrays. The corresponding reflectance spectra are also presented in Figure 5.20 and were measured using a custom-built setup. A Xenon lamp is used as a source. The custom-built setup allows for normal incidence reflectance measurements, with a spot size of approximately 50 μm . Sample A shows higher reflectance tending towards the blue (<500nm) region of the visible spectrum and lower reflectance in the red than sample B.

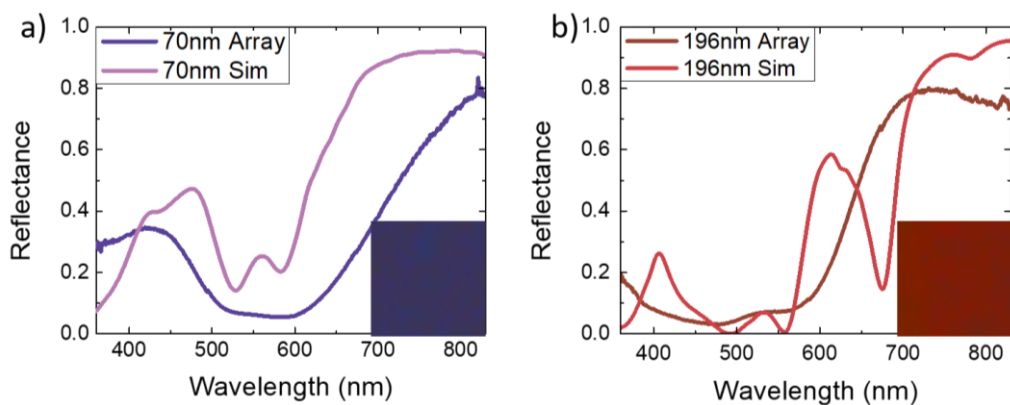


Figure 5.20: (a) Reflectance spectra of sample A, with 70 nm polymer thickness, measured by in-house characterisation system (70nm Array) and simulated by FDTD (70nm Sim). (b) Reflectance spectra of sample B, with 196 nm polymer thickness, measured by in-house characterisation system (196nm Array) and simulated by FDTD (196nm Sim). Microscope image of 40 μm square section of each array (insets).

Discrepancies noted between simulation and fabricated arrays can be attributed primarily to two distinct causes; variation in geometry of the structure, such as disc shape, and polymer layer thickness, and key differences between the FDTD simulation and measurement methodologies. Figure 5.11 has shown that with a fixed pitch, the disc diameter does not significantly impact the colour produced by the structure, indicating the variation in diameter noted in the SEM image in Figure 5.19 is not a contributing factor. However, variation in polymer layer thickness and the dips observed in the top surface of the Au discs, are two parameters which may have significant impact on reflectance. As the structure has been shown in Figure

5.9 to be particularly sensitive to polymer thickness, even slight variation in this parameter over the array would lead to significant changes in reflectance. Though disc diameter has been shown to have little impact on the response of the nanostructure, the shape of the disc may still be a contributing factor in other dimensions. The variation in the top surface of the discs, as observed in the SEM image in Figure 5.19 is shown to be significant and may be a contributing factor to the discrepancy observed. Unit cells in the simulation are perfectly symmetrical and repeating, resulting in responses that are more narrow than those that would be observed in a system with a number of subtly varying parameters.

There are a number of key differences between the simulation, and measurement by the in-house optical characterisation system. In the FDTD simulation, a femtosecond pulse plane wave excitation is used, with a perfectly parallel wave incident on the surface. However, in the optical characterisation system, a 20x objective is used to illuminate the array, and collect light to be analysed by the spectrometer. This introduced angular effects both in illumination and observation angle that may also contribute to the discrepancy observed between simulated and measured structures.

Ultimately, it may be a combination of a number of these factors, both caused by the variation in the structure in parameters not examined, and the contribution from angular effects brought on by the collection angle in measuring the samples.

The structure unit cell of 300 nm has been selected to place the structure as close to the optical diffraction limit[6] as possible, and minimise the diffractive effects noted in the Aluminium structure examined in Chapter 4. Angular effects in the structure have been examined, with limited angular dependence of incident or viewing angle observed with these samples. Samples have not exhibited diffractive effects using the angular characterisation apparatus. However, due to the size of the arrays fabricated, there is difficulty in fully measuring angular dependence, as the incident spot size utilised in the setup is larger than the arrays.

5.3 Conclusion

A novel metallic hybrid nanostructure has been demonstrated, capable of producing vibrant colour in reflection under white light illumination, while avoiding angular and diffractive effects by maintaining at the diffraction limit. FDTD simulations have been carried out to determine the dependencies of the colour on the optical path length, nd , between the disc and backreflector. Optimisation of the structural components has been carried out to determine the most suitable geometries for maximum luminance, tunability and colour clarity. The primary mechanism for colour generation has been discussed, and a sharp near-zero reflection across a narrow band centred at 580 nm has been attributed to a magnetic plasmon resonance, which is highly sensitive to the thin film interference interaction between the disc and backreflector.

An approximately cyclical colour trend has been illustrated, with a repeating trend observed after every 180 nm of polymer thickness change. Variation of other geometries has been examined, with a lower sensitivity of colour generation to these parameters, compared to the polymer thickness. Alternative metal compositions to the noble metals used have also been discussed as a means to reduce fabrication costs. This has also shown to potentially improve the performance of the nanostructure in some configurations, such as the Cu-Al combination.

Fabrication of two samples has been carried out by EBL directly onto ultrathin propylene polymer layers. Physical parameters of these samples have been verified, with ellipsometry used to determine thin film thickness and refractive index, and electron beam imaging used to verify Au nanodisc dimensions and array periodicity.

Modification to the polymer layer by fabrication has been assessed by ellipsometry, and is shown to be negligible, though these parameters have been considered in simulation. Optical characterisation has been carried out, first under optical microscope, and by spectral measurement under Xenon lamp illumination, with

good agreement between fabricated arrays, and simulation, verifying the model that has been developed.

Chapter 6

VO₂ thin films

Summary

A thin film stack consisting of layers of Indium Tin Oxide (ITO) with an intermediate Vanadium Oxide (VO₂) layer on an optically thick Ag film is investigated in this chapter for dynamic structural colour. The structure benefits from the phase change properties of VO₂ allowing for colour actuation by electrical or temperature switching.

This material is compared with other phase change materials (PCMs), such as Silver Indium Antimony Telluride (AIST), and Germanium Antimony Telluride (GST), in similar structural configurations. VO₂ can be offered as a lower power consumption alternative to these materials. It has been overlooked in the visible spectral range due to a smaller refractive index change below 700 nm compared to AIST and GST.

Simulations were carried out using the Transfer Matrix Method (TMM) described previously in Chapter 3. The sensitivity of the visible reflectance spectrum to the change in phase of a 30 nm VO₂ layer is shown to increase after it is incorporated in a thin film stack, with comparable performance to other phase change materials investigated. Variation of material thickness is carried out to determine colour trends and performance, and the inclusion of a top ITO layer is also shown to improve the chromaticity change on phase transition.

6.1 Simulation

All data provided in this chapter is from simulations carried out using TMM. Refractive index information for AIST and GST were taken from the data presented by Ríos *et al.*[73], VO₂ from Joushaghani[17,197], for ITO from König *et al.*[198], with Ag, Pt, SiO₂ and Si from Palik[161].

In the case of AIST and GST structures, TMM simulations were carried out using the same parameters as [73] and [72], respectively, to validate the simulation technique. Results obtained are in agreement with published spectra. VO₂-ITO stack structures of a similar configuration were then simulated, varying structural parameters. Performance of the structures in terms of dynamic colour generation and tuning were determined by the change in reflectance (ΔR), and chromaticity change, examined by conversion to sRGB and CIE xyY colour-space plots.

6.1.1 AIST and GST structures

ITO is a commonly used transparent conductive oxide[199,200] that can act as the contact material in electrically activated thin film PCM structures[72]. With a relatively constant real (n) and low imaginary (κ) component across the visible, ITO has low absorption, making it suitable for thin film interference structures and for maximising the light interaction with a PCM layer. Studies examining ITO-PCM-ITO stacks have been recently published, utilising Sb-Te based PCMs, as such as AIST[73], and GST[72]. These materials are often selected, as they have significant change in both components of the complex refractive index in the visible spectral range upon phase transition, as shown in Figure 6.1.

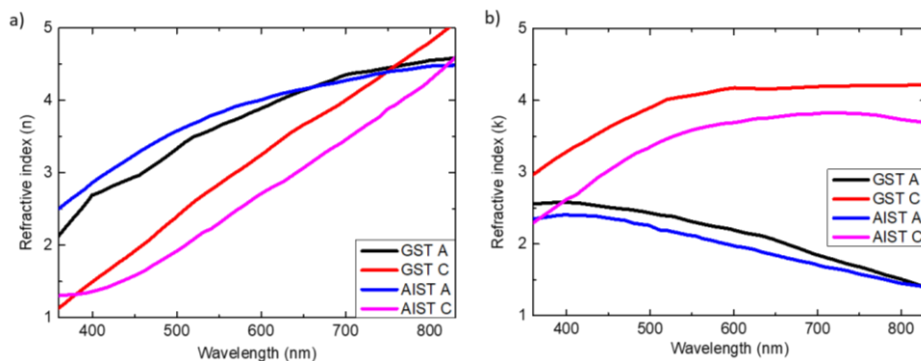


Figure 6.1: (a) Real (n), and (b) Imaginary (κ) component of the refractive index of AIST and GST in the Amorphous (A) and Crystalline (C) phases[73].

Figure 6.1 shows that the refractive index of AIST and GST are similar for n and κ in both phases, due to their similar structural and elemental composition[73]. AIST and GST both transition from a low temperature amorphous insulating phase, to a high temperature crystalline metallic phase at 170°C[62] and 145°C[67], respectively. The maximum change of n in the visible is approximately 170% for AIST, and 116% for GST. The κ change for both materials increase for wavelengths towards the IR, with the largest at the border of the visible (700 nm) of 210% and 236% for AIST and GST, respectively.

The thin film stack structure studied in both papers is shown in Figure 6.2 (a). This configuration is used throughout this section, for both the AIST, and GST structures.

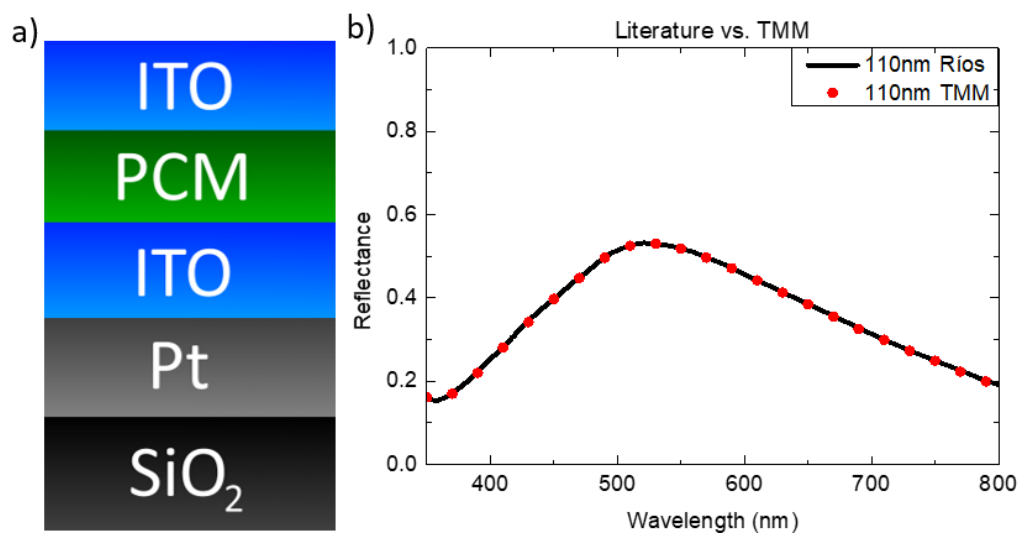


Figure 6.2: (a) Typical structure reported in the literature[72,73], with ITO, Phase Change Material (PCM) stack, an Pt layer and SiO₂ substrate. (b) Reflectance spectrum from Ríos *et al.*[73], compared with TMM spectrum for a structure with 10 nm top ITO, 7 nm AIST, and 110 nm bottom ITO layer.

Ríos *et al.*[73] considered this stack structure with a configuration of a 10 nm ITO top layer, 7 nm AIST layer, bottom layer with 70, 110, and 160 nm ITO, and a Pt layer of 100 nm to act as a mirror. An example reflectance spectrum, shown in Figure 6.2 (b), for the structure with 10 nm top ITO, 7 nm AIST, and 110 nm bottom ITO layer. This figure compares the reflectance from Ríos *et al.*[73] and a TMM simulation for the same parameters, with good agreement demonstrated.

The reflectance spectra with corresponding sRGB line colour are displayed in Figure 6.3 (a) for Amorphous and (b) for Crystalline AIST, simulated by TMM. As the spectra reported by Ríos *et al.*[73] considered the 350-830 nm wavelength range, the refractive index data was extrapolated over 800-830 nm, region, in order to cover the 360-830 nm wavelength range for colour conversion.

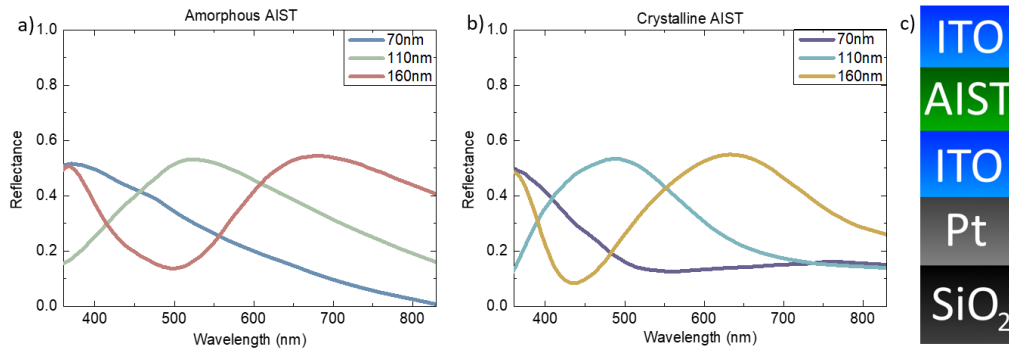


Figure 6.3: Reflectance spectra of the (a) Amorphous and (b) Crystalline phases of AIST of 7 nm, with top ITO layer of 10 nm, and bottom ITO layer in thicknesses of 70, 110, and 160 nm, respectively. The line for each spectrum is shown in the sRGB value colour.

The spectra for the structure with the amorphous AIST phase in Figure 6.3 (a) shows colours of blue, green, and red for ITO thicknesses of 70, 110, and 160 nm, respectively. There is a significant colour change observed after phase transition, presented in the spectra of Figure 6.3 (b), with a blue-shift noted in all cases. A blue with lower luminance, cyan, and yellow, are noted as the reflectance intensity of the spectra reduce at longer wavelengths. This apparent reduction of reflectance at longer wavelengths is due to the significant increase of the κ component of the complex refractive index upon transition to the crystalline phase, as seen in Figure 6.1 (a). This increase is larger at longer wavelengths, leading to a reduction in the reflectance noted towards the IR. The change in reflectance is further demonstrated in Figure 6.4 (a), which plots ΔR , $\Delta R = R_A - R_C$, where R_A and R_C are the reflectance of the amorphous and crystalline phases, respectively.

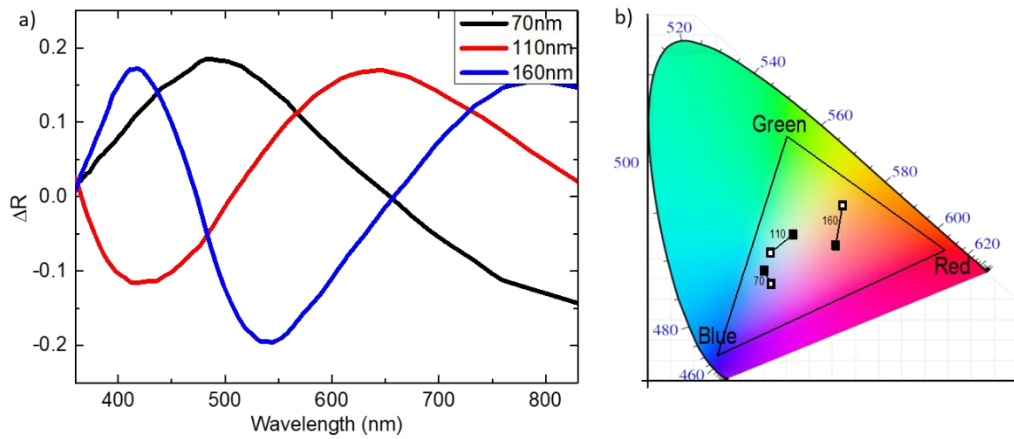


Figure 6.4: (a) ΔR values ($\Delta R = R_A - R_C$) for each thickness of ITO. (b) CIE colour-space plot of each thickness, for the AIST Amorphous (black dot) to Crystalline (white dot) phase transition.

Figure 6.4 (a) illustrates that the maximum ΔR value exhibited by this configuration in the visible occurs in the 160 nm ITO thickness structure, with a maximum of 19% at approximately 540 nm. A CIE colour-space plot is also demonstrated in Figure 6.4 (b), with phase transition from amorphous to crystalline leading to a counter-clockwise transition across the CIE colour-space. The distance between the CIE coordinates indicates the chromaticity change due to the phase change of the AIST. These results present values with proximity to the blue, green, and red primaries for 70, 110, and 160 nm ITO thicknesses, respectively.

A similar study by Hosseini *et al.*[72] using GST as the PCM in an ITO stack structure has also been investigated to determine the performance, in terms of the change in reflectance spectra, and change in chromaticity. The structure also used a 10 nm top layer of ITO, 7 nm PCM (in this case GST), and had bottom ITO of varying thicknesses, with a mirror of 100 nm of Pt on an SiO_2 substrate. The reflectance spectra are displayed in Figure 6.5 (a) for Amorphous, and (b) for Crystalline GST in the structure.

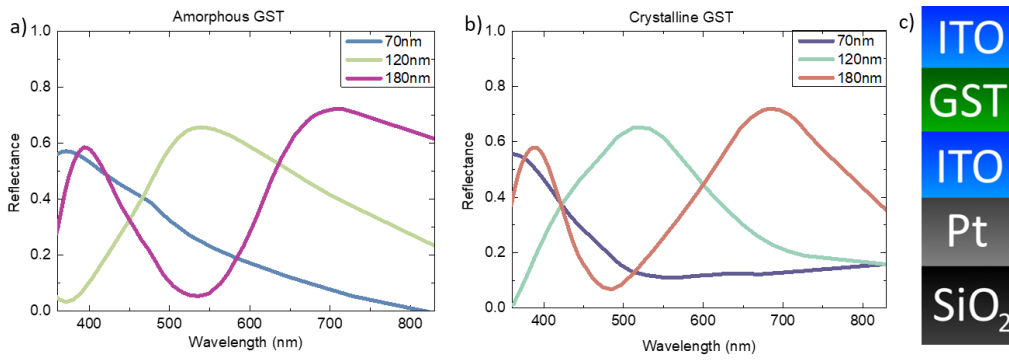


Figure 6.5: Reflectance spectra of the (a) Amorphous and (b) Crystalline phases of GST of 7 nm, with top ITO layer of 10 nm, and bottom ITO layer in thicknesses of 70, 120, and 180 nm respectively. The line for each spectrum is shown in the sRGB value colour.

The amorphous state, shown in Figure 6.5 (a), shows that colours of blue, green and pink have been generated for bottom ITO thicknesses of 70, 120, and 180, respectively. Upon phase transition to the crystalline state, shown in Figure 6.5 (b), these colours blue-shift in a similar fashion to that shown in Figure 6.3, with a darker blue, cyan and orange colour noted for 70, 120, and 180 nm of ITO for GST in the crystalline phase as features blue-shift. This similar transition is due to the similar refractive indices of the AIST and GST in their respective states, leading to similar spectral changes occurring upon transition between phases. The performance of this structure is examined in Figure 6.6, by examining ΔR and CIE.

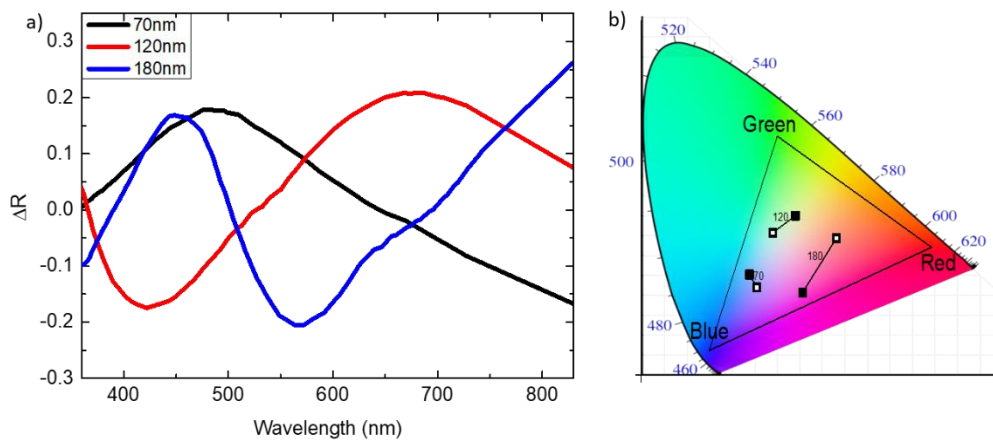


Figure 6.6: (a) ΔR values ($\Delta R = R_A - R_C$) for each thickness of ITO. (b) CIE colour-space plot of each thickness, for the GST Amorphous (black dot) to Crystalline (white dot) phase transition.

Figure 6.6 (a) shows the ΔR values for each structure presented across the visible. Similarly to Figure 6.4 (a), the ΔR values increase towards the IR, as the change in

the κ value of the complex refractive index is more significant in this region. The maximum ΔR value noted in the visible is a 21% change at approximately 560 nm, and occurs in the 180 nm thick ITO structure. The CIE colour-space map shown in Figure 6.6 (b) also illustrates the chromaticity change in the structure after transitioning from the amorphous to crystalline state, for each thickness of ITO. A counter-clockwise trend is noted with phase transition of the GST, similar to that shown for AIST in Figure 6.4 (b). The proximity of the thickest ITO structure is shown to have the greatest chromaticity change, though this occurs from an area of low colour saturation (along the bottom border of the sRGB region in the CIE plot). It is clear from the data presented, that these structures perform similarly due to the similarities in the refractive indices of the PCMs utilised, and the structural parameters of the studies.

6.1.2 Vanadium Oxide thin films

VO_2 is another PCM which can be considered for colour switching applications. VO_2 transitions from a room-temperature semiconducting monoclinic phase to a high temperature rutile metallic phase at 68°C[17], significantly lower than the 170°C and 145°C required for AIST[62] and GST[67], respectively. Furthermore, its lower absorption allows for thicker layers, overcoming one of the fabrication difficulties associated with ultra-thin GST layers[72]. As VO_2 can potentially offer lower toxicity[77], less stringent fabrication constraints[72] and lower power consumption[17], it offers a viable alternative to these Sb-Te based PCM structures, while providing stable, reversible and electrically activated tuning[83].

The reflective structures incorporate an optically thick layer of Ag (100 nm) on a Si substrate which provides high reflectance (>95%) across the visible spectral range. The Ag layer also exhibits high conductance and can be used as a bottom contact for device applications. Ag is often difficult to incorporate into structures due to tarnishing, but in this case, it is sealed from the atmosphere at the bottom of the structure, similar to the structure in Chapter 5. Si is selected as it is considered a typical substrate in devices, and is compatible with silicon and CMOS technologies.

As the Ag is optically thick, and transmission characteristics are not of interest, transparent materials such as glass, quartz or sapphire may be used if desired. Also shown in Figure 6.7 (a) and (b) shows the n and κ values for both the semiconducting monoclinic and metallic rutile states of VO₂.

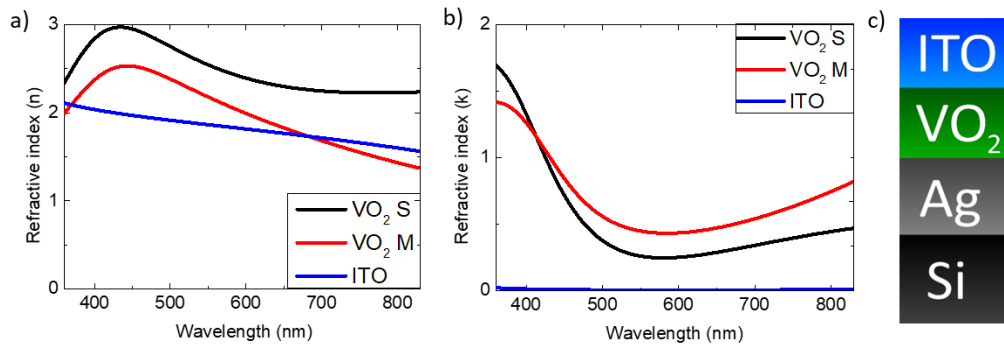


Figure 6.7: (a) Real component of the refractive index (n) of monoclinic semiconducting (cold) phase and rutile metallic (hot) phase of VO₂, and of ITO material used as transparent contact. (b) Imaginary component of the refractive index (κ). (c) Schematic of the three-layer thin film structure consisting of ITO as a transparent contact, VO₂ as a phase change material, silver as a back-reflector and second contact, on a silicon substrate.

The changes in the n and κ values of VO₂ for the semiconducting to metallic phase are illustrated in Figure 6.7 (a) and (b). It is clear from this figure that both the Δn and Δk of VO₂ are much smaller than for AIST and GST in the visible, with a maximum Δn of 18% at 560 nm, and Δk of 75% at 700 nm, the border of the IR. It is also clear that the κ values for both states are smaller than that of AIST/GST, allowing for thicker layers to be utilised, while maintaining the same absorption, permitting greater control in fabrication.

Electrically actuated phase switching has been previously demonstrated on a timescale of approximately 2 ns[19], with a threshold field (V_T) of 1.8×10^7 V/m[19,79,81]. This is particularly of interest for device implementation over thermal switching, as fast response times with low power consumption are required in device applications, and thermal actuation is generally not desirable. An electrically actuated setup, such as that presented by Sánchez *et al.*[201], with an external resistor used in series to reduce power consumption[202], would be

possible with this structure. With a VO₂ thickness of 30 nm, in the configuration in Figure 6.2 or 6.7 (c), a threshold voltage of 0.54 V would be required, assuming a threshold voltage of 1.8x10⁷ V/m[19,79,81]. Electrical actuation can be considered in this structural configuration utilising either the bottom layer of ITO or Ag as a bottom contact.

The power consumption is application dependent, and varies with pixel size and the circuitry for implementation. It can be minimized by having the device in series with an external resistor with a resistance close to that of the VO₂ device in the insulating phase[201,202].

The resistivity (ρ) of VO₂ in the semiconducting phase is $\sim 2 \Omega \cdot \text{cm}$ when sputtered, as reported by Joushaghani *et al.*[202]. The resistance (R) is then:

$$R_{VO_2} = \rho \frac{l}{A} \quad (6.1)$$

From this, VO₂ resistance in the semiconducting phase for a pixel of area (A) of 10x10 μm^2 , and thickness ($l=30 \text{ nm}$) is 6 Ω . The power consumption (P) can be minimized when the VO₂ device is in series with an external resistor, R_{ext} as[201]:

$$P = \frac{V_{S \rightarrow M}^2}{R_{ext}} \quad (6.2)$$

where the switching voltage is[201]:

$$V_{S \rightarrow M} = V_T \left[1 + \frac{R_{ext}}{R_{VO_2}} \right] \quad (6.3)$$

The power consumption can be further reduced by increasing the external voltage but this causes an increase in the switching voltage. The resistance to minimise power consumption corresponds to $R_{ext} \approx R_{VO_2}$. From this, a power consumption of 50 mW is obtained for a 10 μm pixel.

Figure 6.8 displays the reflectance spectra for (a) semiconducting and (b) metallic phases of VO₂, in the structure illustrated in Figure 6.7 (c). This is a simple

electrically contactable thin film structure that can be constructed with VO₂, and utilises the Ag as a bottom contact, and ITO layer as a top contact.

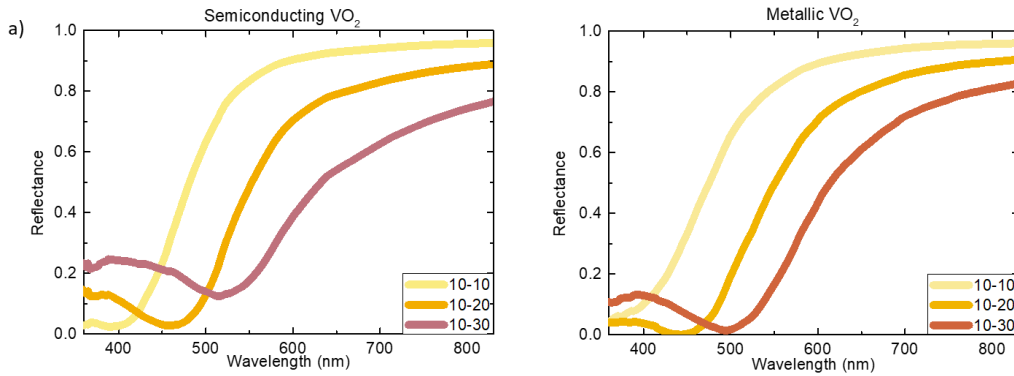


Figure 6.8: Reflectance spectra of three structures consisting of 10 nm of ITO, and varying VO₂ thickness of 10 nm, 20 nm and 30 nm in the (a) Semiconducting (S) and (b) Metallic (M) phases. The line for each spectrum is shown in the sRGB value colour.

VO₂ layer thicknesses of 10 nm, 20 nm and 30 nm are considered in Figure 6.8, with a fixed 10 nm thick top ITO layer. The visible colour in reflection varies from yellow toward red as the VO₂ thickness increases in both phases. The change in colour is predominantly due to the increased absorption with thicker VO₂ layers. Only limited spectral changes are evident after the phase transition, with a maximum ΔR value of 16% at 465 nm observed for the 30 nm VO₂ structure. The change in κ and, consequently, the size of the change in reflectance, $\Delta R = R_S - R_M$, induced by the phase transition is low, where R_S and R_M are the reflectance of the semiconductor and metallic phase structures, respectively. At thicker VO₂ layers, absorption is increased, resulting in a lower reflectivity across the visible region. As a result, any changes in spectral shape will be less evident for thicker layers, as the low reflectivity produces colours with low luminance which are hard to distinguish from each other. Such a simple structure does not allow for full exploitation of thin film interference effects.

6.1.3 ITO-VO₂-ITO stacks

The change in complex refractive index of the VO₂ layer can be better exploited when it is incorporated into an ITO stack, on an Ag back reflector, similar to the literature structure[72,73] introduced in Figure 6.2. This structure is shown in Figure 6.9 for clarity.

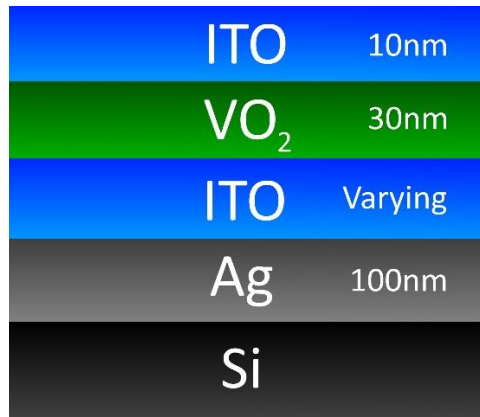


Figure 6.9: VO₂ structure with ITO top layer of 10 nm, 30 nm VO₂ layer, and a bottom layer of ITO with varying thickness. A 100 nm layer of silver is below this stack, on a Si substrate.

As shown in Figure 6.9, the thickness of the top ITO layer is fixed at 10 nm, as is that of the VO₂ layer at 30 nm. The thickness of the bottom ITO layer is varied from 0 nm to 40 nm. The reflectance spectra are displayed in Figure 6.10 (a) for the semiconducting and (b) for metallic phases.

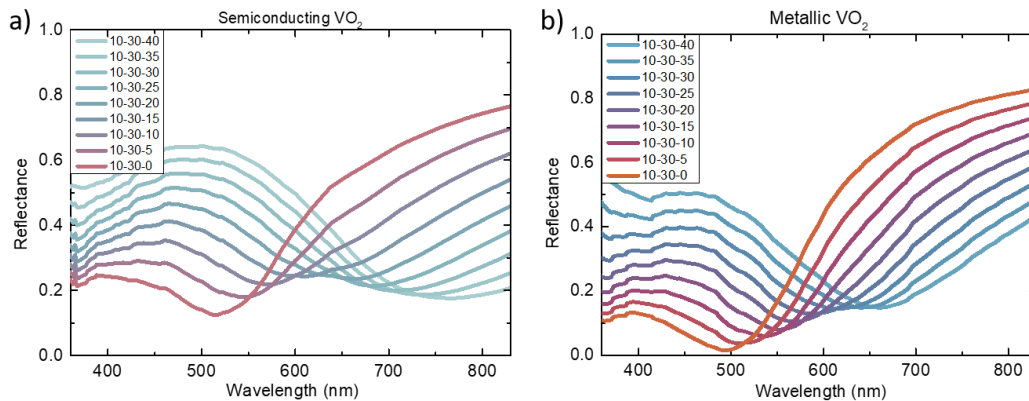


Figure 6.10: Reflectance spectra for the structure of VO₂ in the (a) semiconducting and (b) metallic phase, for varying thickness of the bottom ITO layer from 0 nm to 40 nm.

Firstly, the colour tuning as a function of the ITO layer thickness can be observed. For VO₂ in the semiconducting phase, Figure 6.10 (a), the peak at approximately 400 nm and the dip in reflectance at 500 nm redshift as the ITO layer thickness increases. The redshift of the dip is almost twice that of the peak, which causes a broadening of the spectral feature, and the peak reflectance values increase as the ITO thickness increases. The higher reflectance at longer wavelengths shifts towards the IR, causing a reduction in the stimulation of red cone receptors. Reflectance intensity across the green and blue cones increases as ITO thickness increases and due to the

increase in the width of spectral features, there is an overall reduction in colour saturation. There is also an increase in luminance, as the peak reflectance is higher. This indicates that using thinner layers of ITO produces structures with better colour saturation due to narrower spectral features, a topic that is discussed further in Section 6.1.5. Comparing the semiconducting phase with the metallic phase in Figure 6.11 (b), reveals that the redshift of the spectral features is much larger for the semiconducting phase, and higher minimum reflectance results in lower luminance than for the metallic phase.

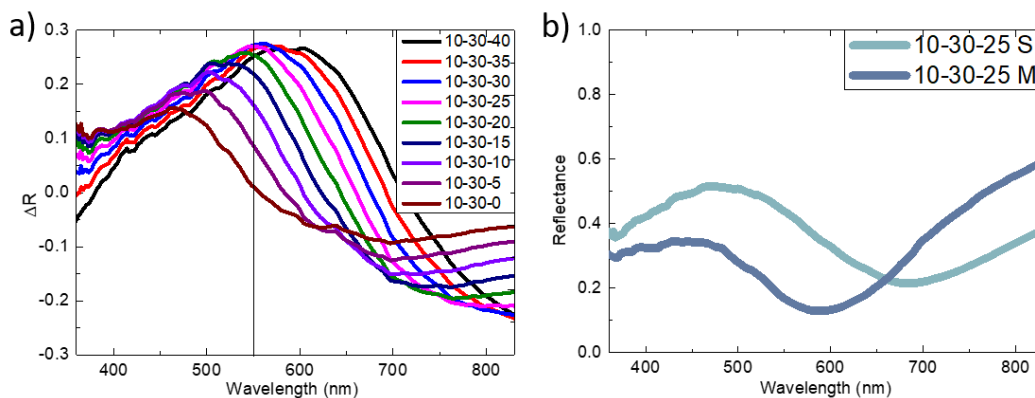


Figure 6.11: (a) ΔR ($=R_S-R_M$) spectral dependence, where R_S is the reflectance for the semiconducting phase and R_M is the reflectance for the metallic phase. (b) The reflectance spectra for the structure showing the largest ΔR after the transition from the semiconducting to metallic phase.

Figure 6.11 (a) clearly demonstrates that the introduction of the bottom ITO layer provides for much larger changes in reflectance, ΔR , reaching values of over 27% for a bottom ITO layer of 25 nm or more in thickness. This can be compared with 16% in the absence of the bottom ITO layer for the same thickness of VO_2 discussed in Section 6.1.2. The peak position of ΔR redshifts by approximately 15 nm for each 5 nm increase in ITO thickness. The cavity structure has greatly increased the sensitivity of the visible reflectance spectra to the phase of the VO_2 layer. These ΔR values are comparable to those reported in the literature for AIST[72] and GST[73] structures discussed in Section 6.1.1, with maximum ΔR values of 19% and 21% for the 160 nm thick AIST structure, and 180 nm thick GST structure, respectively.

However, structures exhibiting the large ΔR values do not necessarily lead to significant changes in colour. Example spectra for the semiconducting and metallic phases of VO₂ with a 25 nm thick ITO structure is shown in Figure 6.11 (b), and correspond to the largest ΔR observed at 550nm, in the centre of the visible region. The structure has a 10 nm top ITO layer, 30 nm VO₂ layer and 25 nm bottom ITO layer. In the semiconducting phase, a broad intense spectral feature overlaps with all three colour cones significantly, and in particular with the blue and green cones with high intensity.

In the metallic phase, there is a reduction in luminance across the visible region, with a markedly lower minimum reflectance at the dip at 580 nm. This causes a reduction in stimulation of the red colour cone and a shift in chromaticity is noted towards the blue primary.

6.1.4 VO₂ Thickness

To further optimise the ITO cavity structure the impact of the thickness of the VO₂ layer is examined, where the combined thickness of the VO₂ layer and bottom ITO layer is kept constant at 55 nm. In this way, the spectral peaks and troughs are maintained at approximately the same positions as the VO₂ thickness is changed. This variation can be used to identify the structure that has the greatest sensitivity to the phase change of the VO₂ layer, without shifting spectral features. The spectra for the semiconducting and metallic phases are shown in Figure 6.12 (a) and (b), respectively.

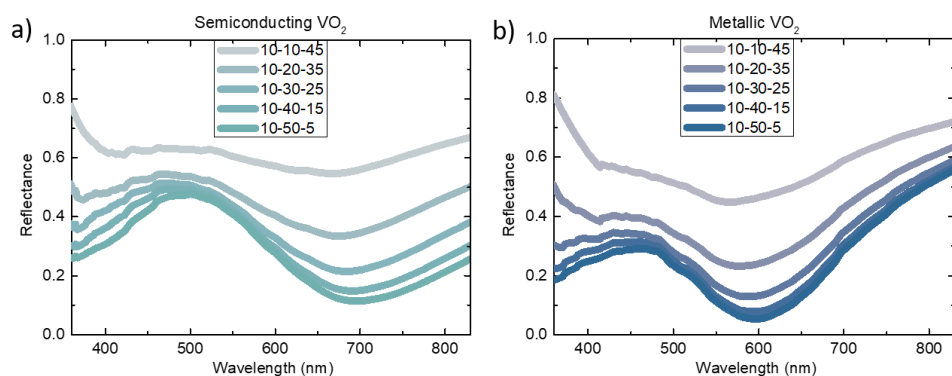


Figure 6.12: Reflectance spectra of ITO/VO₂/ITO/Ag/Si stack structure with total VO₂ layer and bottom ITO layer thickness of 55 nm with varying thickness of VO₂ from 10-50nm in 10nm steps, for the (a) semiconducting and (b) metallic phase, respectively.

As expected, increasing the thickness of the absorbing VO₂ layer results in an increase in absorption and reduced luminance. The difference in reflectance values at the peak and trough increases with increasing VO₂ thickness, with spectral features becoming more defined. This leads to a reduction in the simultaneous stimulation of multiple colour cones, producing a trend away from pastel colours to values closer to the red, green, and blue primaries, as saturation increases. Little change in the colour produced for each phase or the ΔR values across the visible part of the spectrum is observed for thicknesses greater than 30 nm, with a maximum ΔR of approximately 30% at 550 nm.

Figure 6.13 (a) demonstrates that the ΔR values are independent of any spectral shifts, as the stack thickness, and so optical path length remains largely unchanged. Figure 6.13 (b) and (c) illustrate the thickest, and thinnest VO₂ cases, respectively.

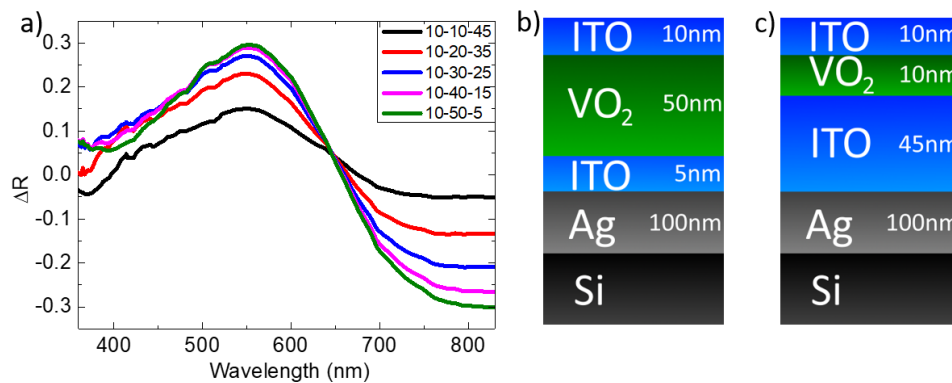


Figure 6.13: (a) ΔR values for phase change, showing a maximum ΔR at 30% at 550 nm for 50 nm of VO₂. Schematic for the thickest VO₂ (b) and ITO (c) layers.

It should be noted that if the bottom ITO layer thickness is fixed at 25 nm then the positions of the peaks also shift as the VO₂ thickness is increased. This is demonstrated in Figure 6.14. Here, the positions of spectral features red-shift, as the optical path length of the stack increases with increased VO₂ thickness.

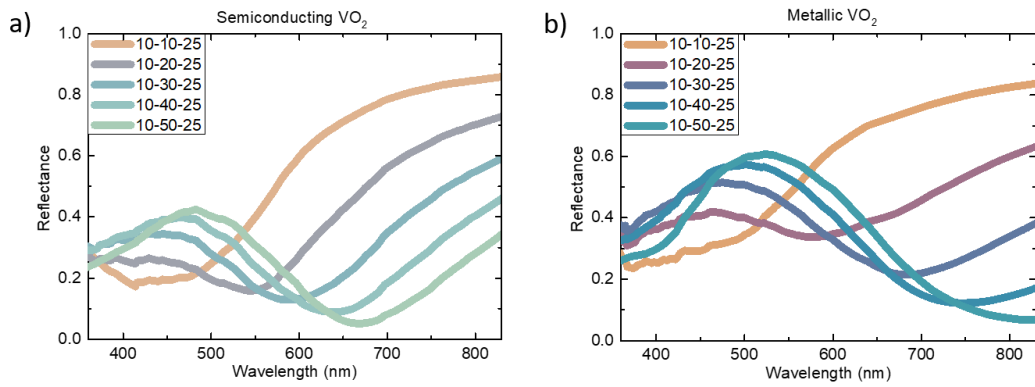


Figure 6.14: Reflectance spectra of ITO/VO₂/ITO/Ag/Si stack structure with varying VO₂ layer thickness of 10-50nm in 10nm steps, and static ITO layer thickness of 25 nm for the (a) semiconducting and (b) metallic phase, respectively.

The impact on the performance of the structure can be determined by examining the ΔR of the phase transition in this case, as in Figure 6.15 (a). The schematic of the structure is also included in Figure 6.15 (b) and (c) for the thickest and thinnest VO₂ cases, respectively.

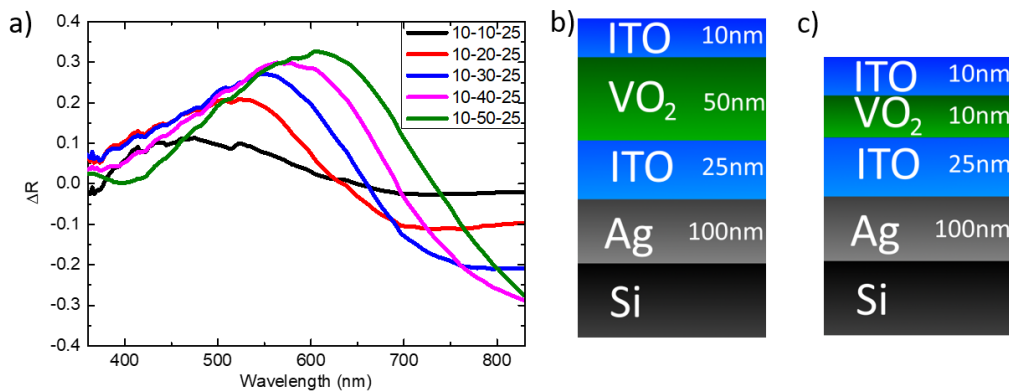


Figure 6.15: (a) ΔR values for phase change of the material, showing a maximum ΔR for this stack configuration also at 30% for 50 nm of VO₂, but at 600 nm. Schematics showing the structures for the (b) thickest and (c) thinnest VO₂ layer.

The ΔR values displayed in Figure 6.15 (a) demonstrate that there is no effect on the maximum value obtained on phase transition, when compared to Figure 6.13 (a). This indicates that the maximum ΔR values is determined by VO₂ thickness only, while the thickness of ITO controls the thin film interference condition that affects the position of spectral features.

6.1.5 Impact of the ITO top contact

The impact of the top ITO layer on the performance is discussed, with Figure 6.16 revealing the reflectance spectra for structures with a 10 nm layer, and with no ITO layer above the VO₂.

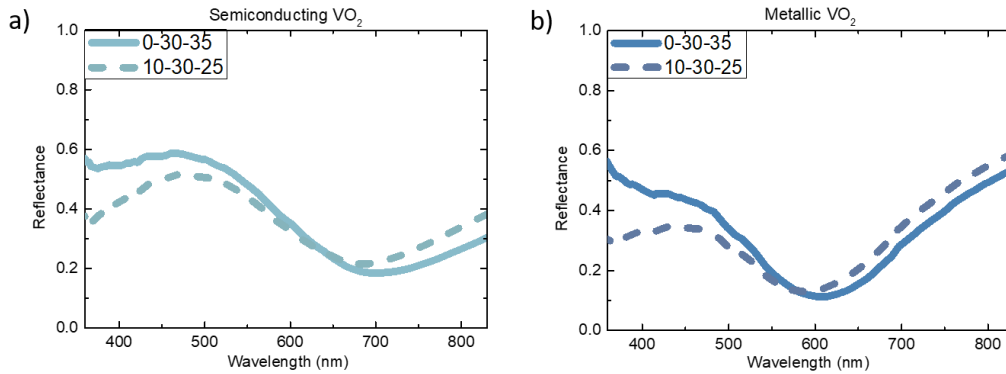


Figure 6.16: Reflectance spectra of (a) ITO-VO₂-ITO and (b) VO₂-ITO structures on 100 nm Ag and Si substrate. 10 nm (dashed) and 0 nm (solid) top ITO contact, 30nm VO₂ and 25 nm bottom ITO thickness.

The top ITO contact is vital for the electrical contacting of the VO₂ layer in this configuration, while the bottom ITO layer can be substituted with Ag as the bottom contact. However, it has been demonstrated throughout section 6.1.2 that the presence of the bottom ITO layer is required to maximise the impact of the phase change of VO₂ on colour change, using the thin film the interference effect. From Figure 6.16 (a) the inclusion of the top ITO layer is shown to reduce the reflectance across the visible for the semiconducting state of VO₂. This is shown to have little effect on the chromaticity, as the largest changes in reflectance occur at the border to the UV region, resulting in only a small change in the overlap with the blue colour cone. This effect is also observed in Figure 6.16 (b) for VO₂ in the metallic state, with a similar negligible impact on chromaticity. This reduction in reflectance can be attributed to the change from an air-VO₂ to air-ITO top interface for the structure, resulting in a difference in the transmission and reflectance coefficients for the structure.

While ΔR is a measure of the sensitivity of the reflectance of a structure to the phase change material, its use is limited for determining structures for optimal spectral tuning. The use of ΔR as a means to determine performance does not differentiate

between changes in the reflectance values and spectral shifts, where the former has a stronger impact on luminance and the latter on chromaticity. In Figure 6.17, the range of colours that can be achieved, the impact of the top ITO contact layer and the change in chromaticity of the reflected colour induced by the semiconductor to metal transition are examined by plotting the sRGB data generated for the variety of structures simulated on a CIE xyY colour-space map.

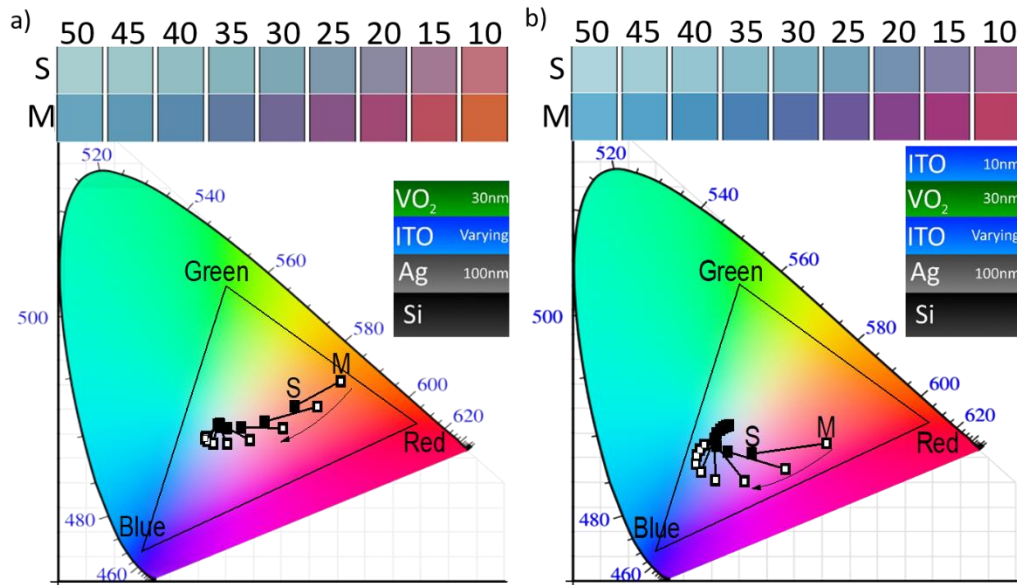


Figure 6.17: CIE map (a) with no top ITO layer and (b) with a 10 nm top contact ITO layer. Both cases have a 30 nm thick VO₂ and varying thickness of ITO below the VO₂ layer. For VO₂ in the Semiconducting (back dot) and Metallic (white dot) phases.

Figure 6.17 (a) shows the data for varying bottom ITO layer thickness and no top ITO layer. For the thinnest ITO layer of 10 nm the CIE colour point, labelled S for the semiconductor phase, the position on the CIE map is near the midpoint of the red and green primaries. After transition to the metal phase the spectral features narrow and reduce in intensity, resulting in a shift towards the border of the sRGB gamut, labelled M, as colour saturation increases. As the ITO layer thickness increases the colour for the semiconducting phase moves closer to the blue primary, and spirals towards the centre. The change in position on the colourmap after the transition to the metallic phase decreases with increasing ITO layer thickness. In all cases the change is towards a more defined single colour, with lower luminance, and greater colour saturation after semiconductor to metal transition. This indicates

that ITO thickness must be kept low in order to maintain chromaticity values closer to the sRGB borders.

Figure 6.17 (b) shows the colour dependence on the bottom ITO layer thickness in a structure including a top ITO layer. Again, the increasing bottom ITO layer thickness results in a spiralling of the S and M positions towards the centre of the CIE map, and a reduction in the colour change after phase transition. As for the previous structure, there is little change for structures with intermediate ITO layers thicker than 30 nm. Comparing Figure 6.17 (a) and 6.17 (b), the colour-space positions for the S and M phases for the thinnest ITO layer are closer to the blue primary when a top layer of ITO is incorporated. It is noteworthy that the positions for all structures shown in Figure 6.17 (b) are further from the centre position than those in Figure 6.17 (a). This is a consequence of the narrower spectral features. The presence of the top ITO layer improves the performance of the structure upon phase transition, as chromaticity changes more significantly. It is of interest to note that, while the 10-30-25 structure demonstrated the largest ΔR value of all structures tested, the CIE plot shows that the 10-30-10 structure demonstrates the most significant change in chromaticity as seen in the largest movement across the CIE colour-space from one primary to another. This signifies that the ΔR parameter alone does not provide sufficient insight as a method to determine the optimal structure for colour change and utilising the CIE colour map is a more comprehensive method for analysing the colour tuning properties. Trends are more difficult to follow when chromaticity and luminance values are desired, though luminance values can be shown for each position as a numerical label. It is noted that the range of structures investigated could not provide access to the full CIE colour-space, with the green spectral range in particular, unsupported.

6.2 Conclusion

A simple planar ITO-VO₂-ITO-Ag structure has been investigated, and the extent to which VO₂ can be exploited for modulated reflectance and colour change has been explored. Incorporation of a thin film of VO₂ in a multilayer ITO-VO₂-ITO-Ag stack has been shown to offer a greater change in reflectance and larger spectral tuning than a simpler ITO-VO₂-Ag structure. The intermediate ITO layer plays an important role in fully exploiting thin film interference effects. Structures with 10 nm of ITO under a 30 nm VO₂ layer were found to offer the largest dynamic colour tuning range as the phase state transitions from semiconductor to metal. This structure had the largest movement across the CIE colour-map of any structure examined, though the ΔR value was 22% at 500nm, smaller than the 10-30-25 ITO-VO₂-ITO structure that exhibited a maximum change of 25% at 550nm.

The VO₂/ITO structure does not provide access to the full CIE colour-space, with the green spectral range unsupported. Further investigation of nanostructured VO₂-metal structures could extend the colour space. VO₂ has the advantage of lower temperature or voltage requirements for tuning between phase states, and lower absorption than other PCMs allows for finer control of reflectance and colour by layer thickness. However, switching performance, in terms of the change in reflectance ΔR , is found to be comparable with other PCM-based thin film stacks, with potential for device applications in displays, optical memory switches and dynamic optical components.

Chapter 7

Metal nanoparticle-VO₂ structures

Summary

This chapter investigates the incorporation of Au nanoparticles into the VO₂ thin film structure. The phase change properties of VO₂, in combination with the high scattering cross section and sensitive LSPR of Au nanoparticles allow dynamic colour switching, potentially with a larger gamut than the thin film structure.

First, the hybrid metal nanostructure examined in Chapter 5, is combined with a 30 nm VO₂ layer to determine the colour change potential of the structure, consisting of a 100 nm thick Ag backreflector, polymer layer, and Au nanodisc of 150 nm diameter in a square array of 300 nm pitch. This is considered to determine the colour change potential of the hybrid nanostructure when combined with VO₂, in a configuration with the least amount of alteration to the original structure.

The VO₂ thin film stack structure studied in Chapter 6 was optimised using a thin film interference effect, to sensitise the VO₂ in the visible. This thin film stack is combined with an Au nanoparticle array, with varying diameter discs. Different particle shapes are also examined, with an Au box, hexagon, star, and triangle of fixed volume considered in the structure, in place of the disc component. These particles are chosen to investigate increased field enhancement, due to the sharpness of the particle corners.

Imbedding of the Au particles into the VO₂ layer has also been carried out, to maximise the interaction between the large field enhancement in the nanoparticles, and the VO₂ layer. Nanoparticles of various shapes are also investigated in this section.

7.1 Simulation

All data provided in this chapter is from simulations carried out using the Finite Difference Time Domain (FDTD) method. Refractive index information for VO₂ was digitised from the data presented by Joushaghani[17,197], and Ag, Pt, SiO₂ and Si from Palik[161]. Refractive index information for the exposed and unexposed Tafmer polymer material was determined by ellipsometry, as presented in Figure 5.12 in Chapter 5.

A number of nanostructure configurations are considered, all of which combine Au nanoparticle arrays, with a thin films stacks of the phase change material (PCM) VO₂, SiO₂, and Ag on a Si substrate. Au particles of varying shape and size were investigated, to determine the effect on the field enhancement around the particles, and the resulting reflectance spectra. Metal nanoparticles are well documented to exhibit LSPR that is highly sensitive to the refractive index of the surround media[98,99], chalcogenide-based PCM-nanoparticle structures have been examined in the visible[100–102]. While the focus of VO₂ has been most predominantly in the IR[105–107], nanoparticle systems in the visible for colour[103] and sensing[104] have been demonstrated. Patterning on-top of VO₂ using e-beam lithography[103,111] has been achieved, without damage of the crystalline structure.

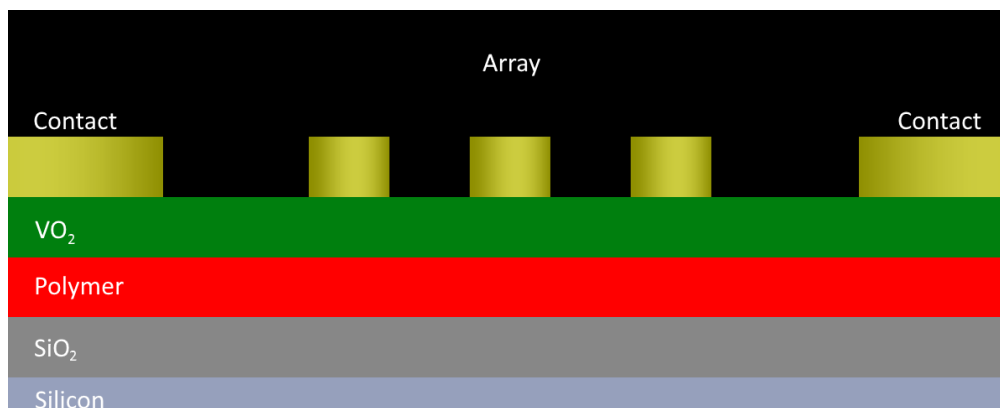


Figure 7.1: (a) Schematic profile of the contacting method used in nanostructures with nanodisc array. Array is deposited with contacts on either side, in order to electrically trigger phase transition.

Due to the inclusion of Au metal nanoparticles in the structures examined throughout this chapter, vertical contacting of the structure, as implemented in Chapter 6, is not feasible. Instead, the structures are assumed to be contacted from contacting pads on each side of the array, as shown in Figure 7.1. This was also implemented by Markov *et al.*[110] with structures of a similar configuration. Spectra were analysed using sRGB and CIE xyY conversion to compare performance of the structure on VO₂ phase transition.

7.1.1 Hybrid structure with VO₂ layer

The first structural configuration under consideration is that of the hybrid structure examined in Chapter 5, with a VO₂ layer of 30 nm included above the polymer layer. This presumes a fabrication procedure following those in Chapter 5, followed by the deposition of a 30 nm thick VO₂ layer. The result is a structure with a partially imbedded Au disc. For simplicity of design, VO₂ is not present at the top of the Au discs, achievable by the deposition of an intermediate lift-off material before deposition of the VO₂. Figure 7.2 demonstrates the schematic of this configuration.

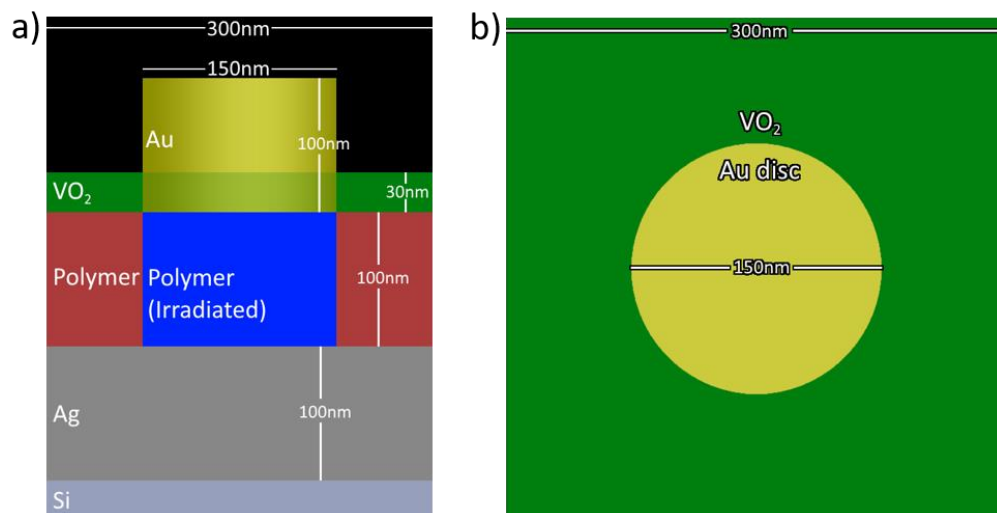


Figure 7.2: (a) Schematic profile of the Hybrid nanostructure unit cell on Si substrate, with layer thicknesses of 100 nm Ag, Polymer and Au, 30 nm VO₂ layer. (b) Top-down schematic of the structure unit cell, with 150 nm diameter Au disc, and 300 nm pitch.

Similar to the polymer in Chapter 5, an “irradiated” polymer refractive index is used below the Au particle with the same diameter, to represent exposure to the layer as a result of the Electron Beam Lithography (EBL) process. A non-irradiated polymer

refractive index is used elsewhere. The reflectance spectra of this structure in the low-temperature monoclinic semiconducting phase, and high-temperature rutile metallic phase of VO₂ are shown in Figure 7.3.

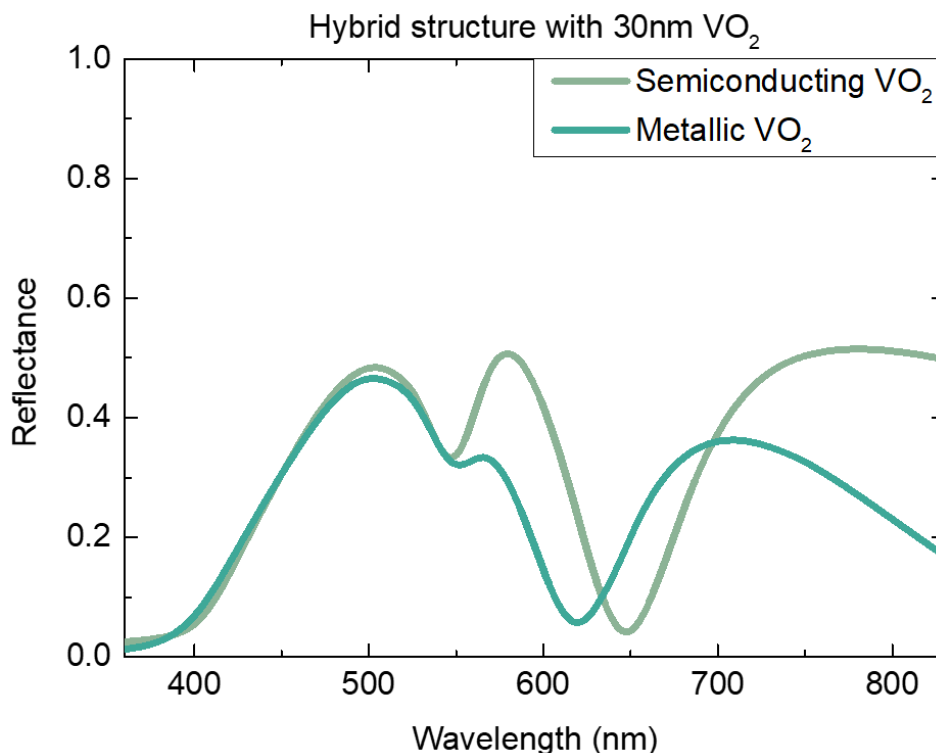


Figure 7.3: Reflectance spectra of the structure with VO₂ in the semiconducting and metallic phase. The line for each spectrum is shown in the sRGB value colour.

Figure 7.3 demonstrates a negligible change in the reflectance upon phase transition below 550 nm. The peak noted at approximately 580 nm in the semiconducting phase notably blue-shifts to 565 nm, due to the decrease in the real, n component of the refractive index in the metallic phase. The peak also reduces in intensity, consistent with the increase in the imaginary, κ component of the refractive index. The dip at 650 nm also blue-shifts to 620 nm on phase change, due to the decrease in the n component. This is a trend noted throughout the chapter, upon phase change from the semiconducting to metallic phase of VO₂. These changes in spectral shape are further demonstrated in Figure 7.4 (a).

The changes in spectral shape result in an overall reduction in the stimulation of the middle colour cone, responsible for green colours, and so the colour shifts towards

are more blue hue (the change of colour from one discernible tone to another) in the metallic phase.

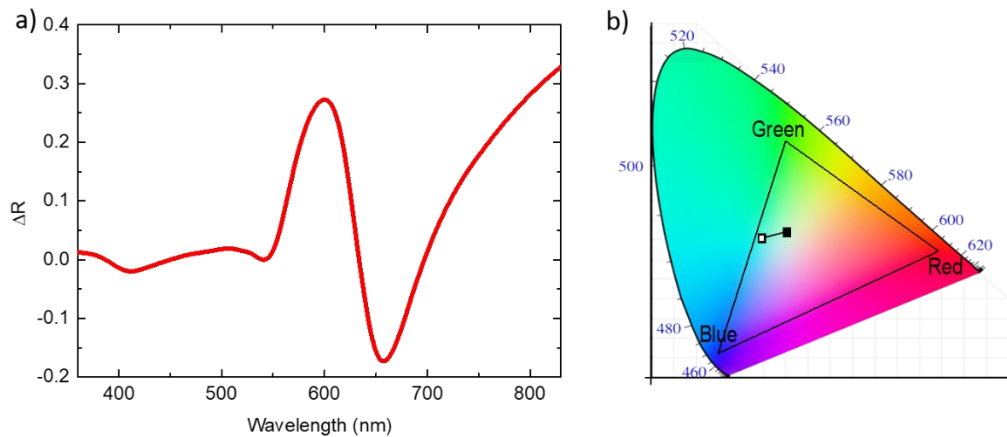


Figure 7.4: (a) ΔR ($=R_S-R_M$) spectral dependence, where R_S is the reflectance for the semiconducting phase and R_M is the reflectance for the metallic phase. (b) CIE colour-map positions of the colour presented by the structure with VO_2 transitioning from semiconductor (black dot) to metallic (white dot) phase.

Figure 7.3 (b) illustrates the CIE colour-map positions of this structure as the VO_2 changes phase. It is clear from this that the change in colour hue is small, particularly when compared to that presented by the thin film structure in Figure 6.17 (b), at smaller thickness of ITO. The positions in the CIE in Figure 6.18 (b), and change in position at phase change in this structure is consistent with that of positions noted in Figure 6.17 (b) for the thickest layers of ITO. This indicates that this structural configuration does not present any advantages in performance over that of the thin film design presented in Chapter 6.

Figure 7.5 reveals the (a,b) Electric field and (c,d) Poynting vector profiles for the structure under consideration. These profiles are taken at (a,c) 580 nm for the semiconducting phase of VO_2 , the peak position of reflectance mentioned earlier for this phase. The profiles (b,d) are measured at 565 nm, and are for the metallic phase of VO_2 , the peak position of this structure in this phase.

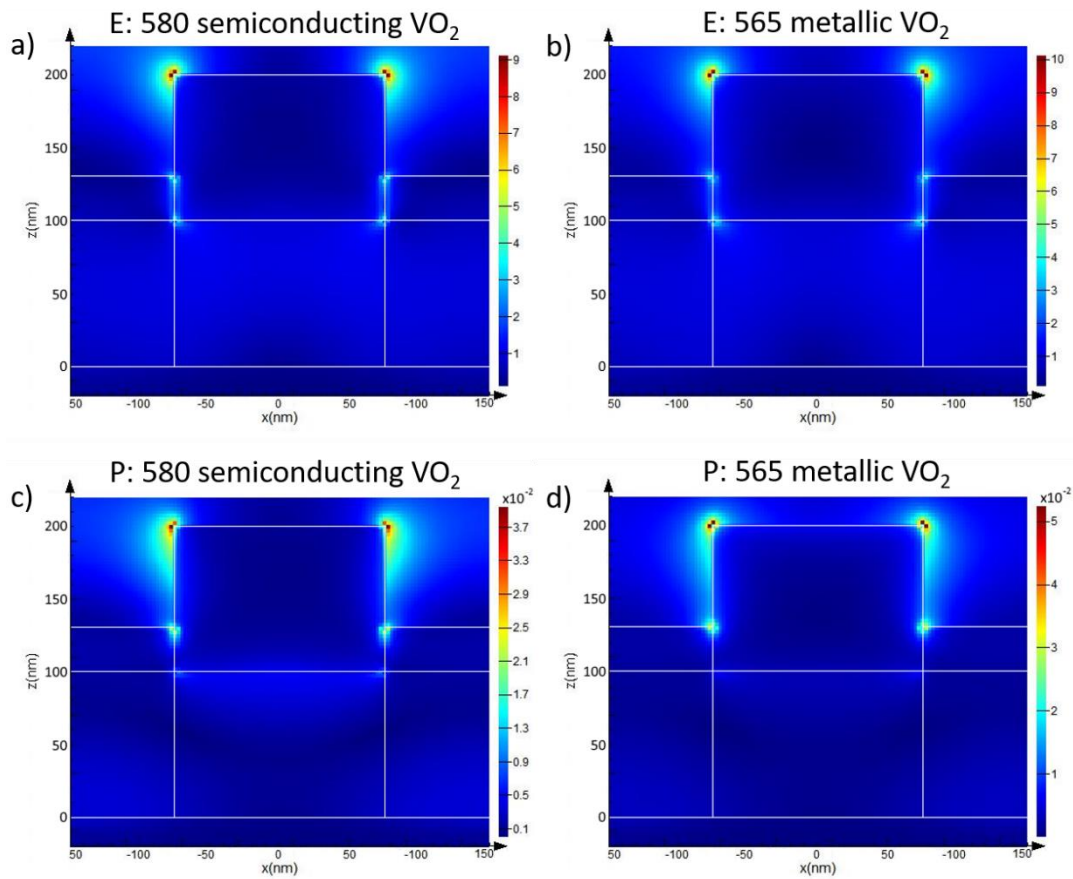


Figure 7.5: (a,b) Electric field, and (c,d) Poynting vector profiles of the structure at (a,c) 580 nm for the semiconducting phase, and (b,d) 565 nm for the metallic phase of VO₂.

Figure 7.5 (a,b) shows the electric field profiles at 580 nm and 656 nm, which is the peak position for each phase. A large electric field localisation is observed at the top corners of the disc in both, with no discernible changes in the field profiles at the disc-VO₂ boundary. The largest field strength at both wavelengths is observed at the top corners of the disc, with lesser “hotspots” also observed at the top and bottom corners of the VO₂ layer that contact the disc. As the largest E fields are observed a considerable distance from the Au-VO₂ interfaces, the interaction between these components is relatively small, and so the LSPR of the disc is not significantly altered by the phase change of the VO₂. The change in spectral shape is largely attributed to the VO₂ thin film, and not the disc interaction with the film. In the Poynting vector profiles in Figure 7.5 (c,d), there largest magnitudes are also observed outside of the VO₂ layer at the top disc corners, further demonstrating weak disc-VO₂ interaction.

Figure 7.6 reveals the E and P profiles for the semiconducting and metallic phases at the same wavelength of 580 nm. From this, the impact of the phase change on the disc LSPR, and energy flux in the structure can be examined.

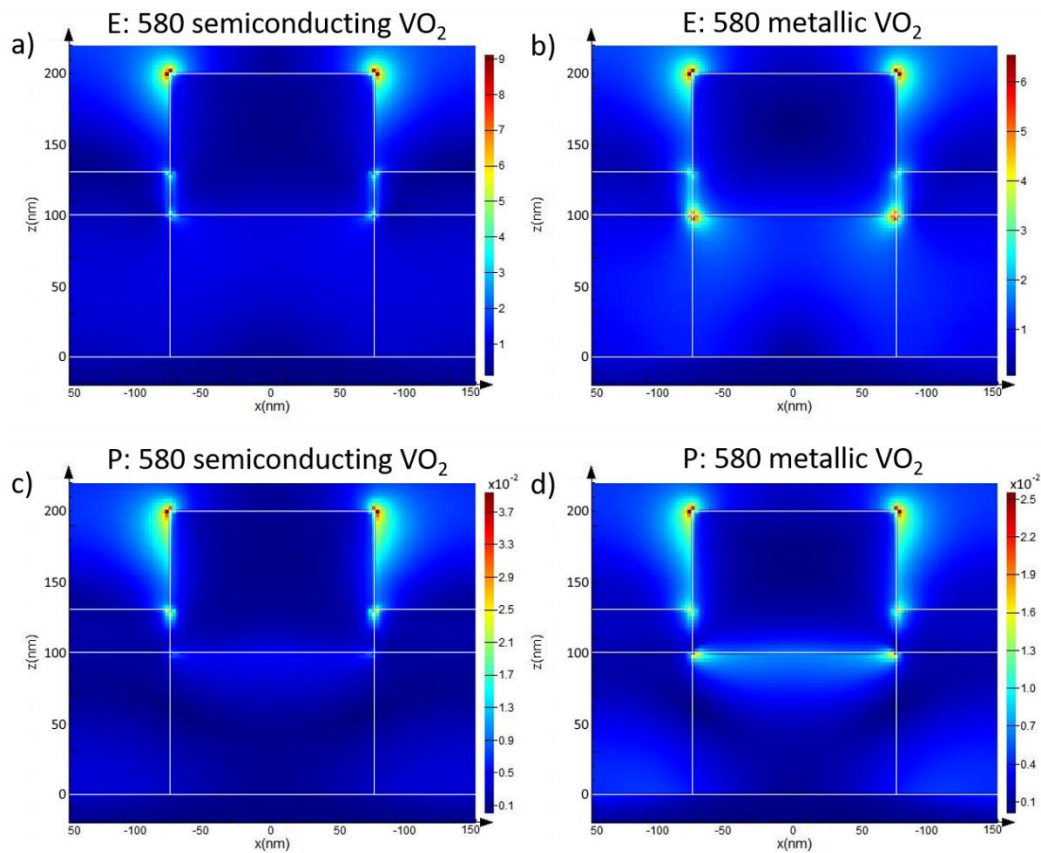


Figure 7.6: (a,b) Electric field, and (c,d) Poynting vector profiles of the structure at 580 nm for the (a,c) semiconducting, and (b,d) metallic phase of VO_2 .

Again, the largest E field magnitudes in the structure in both phases of VO_2 are located at the top corners of the disc in Figure 7.6 (a,b). However, there is a notable increase in the E field at the bottom corners of the disc, and along the wall that interfaces with the VO_2 layer. Poynting vector magnitudes in these locations are also increased, indicating that this region has an increase in energy flux as a result of the increased absorption of the metallic phase of VO_2 . There is also an increase in P at the lower disc surface, indicating an increase in energy flow to this region of the structure, which may also cause a reduction in reflectance at this wavelength.

There are several design parameters that can be improved to maximise the interaction between the disc and VO_2 , and subsequently increase the colour change as the VO_2 switches phase. By reducing the dielectric layer thickness, the CIE

positions noted in Figure 7.3 (b) may trend towards larger separation, as seen in Figure 6.17 (b) with thinner ITO layers in the thin film structure. Changing the shape of the Au particle may also serve to increase field enhancement presented by the particles to have a stronger interaction with the VO₂, and improve colour change potential. Finally, imbedding the Au disc array into the VO₂ layer may place the areas of high field enhancement in the layer, increasing the interaction between the particles and the VO₂. The following sections investigate these parameter and geometry changes, first investigating thinner layers of dielectric below the VO₂ layer, followed by an examination of Au nanoparticle shape. The incorporation of the nanoparticle into the VO₂ layer is also explored, for both discs and nanoparticles of varying shapes.

7.1.2 Discs on VO₂

The second architecture under consideration more closely resembles the parameters of the thin film stack explored in Chapter 6, with a VO₂ thickness of 30 nm, and SiO₂ thickness of 30 nm. A 100 nm thick Au disc array is positioned on-top of the VO₂ layer. SiO₂ is used as the dielectric material, as it has low absorption in the visible. Deposition of VO₂ requires heating the substrate to several hundred degrees [203–205]. This is possible on-top of SiO₂, as the material has a high melting point. SiO₂ has an average n component across the visible of approximately $n = 1.5$, lower than that of ITO, with an average of approximately $n = 1.8$, as shown in Figure 6.7 (a). This leads to the optical path length (nd) of the SiO₂ being shorter with a comparable layer thickness. Due to this material change, thin films explored with this architecture are considered with a SiO₂ thickness of 30 nm, instead of the 25 nm of ITO utilised in Chapter 6, to represent a layer of the same nd when utilising SiO₂.

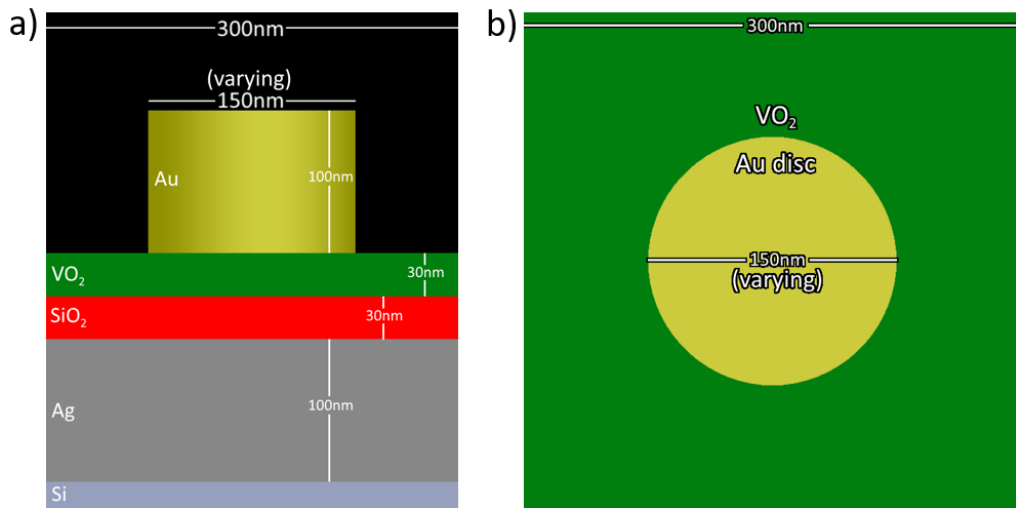


Figure 7.7: (a) Schematic profile of the nanostructure unit cell on Si substrate, with Ag and Au thicknesses of 100 nm, SiO₂ and VO₂ thicknesses of 30 nm. (b) Top-down schematic of the structure unit cell, with 150 nm diameter Au disc and 300 nm pitch.

Figure 7.7 reveals the schematic for this structural configuration, with a Si substrate, 100 nm Ag and Au thickness, 30 nm SiO₂ and VO₂ thickness. A disc diameter of 50-250 nm is considered for examination, with a fixed unit cell of 300 nm. The reflectance spectra for these structures are shown in Figure 7.8 for the (a) semiconducting and (b) metallic phase.

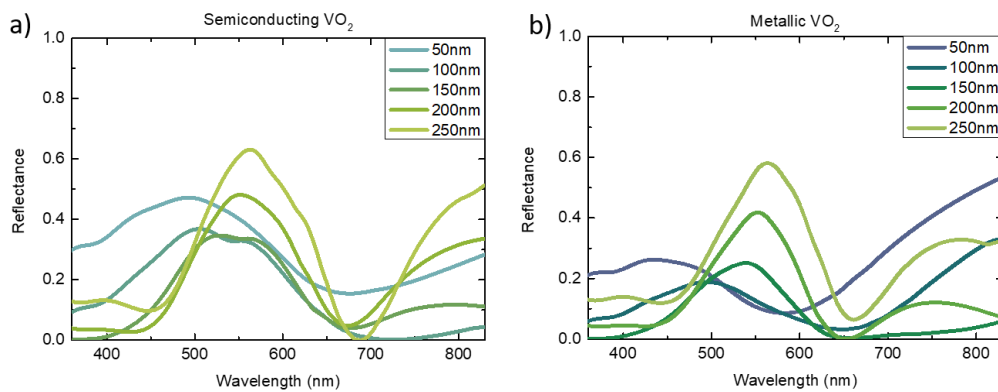


Figure 7.8: Reflectance spectra of five structures with varying disc diameter 50-250 nm in 50 nm steps, for the (a) Semiconducting and (b) Metallic phases. The line for each spectrum is shown in the sRGB value colour.

Figure 7.8 shows the trend of reflectance spectra for the structure with VO₂ in the low-temperature (a) semiconducting and (b) metallic phase, with disc diameter varying from 50 to 250 nm. With an Au disc diameter of 50 nm, the reflectance spectra for both phases is similar in shape to that of the thin film structure with 25 nm of ITO, shown in Figure 6.11 (b). This indicates that the reflectance response

originates primarily from the thin film structural components, and not the disc component. This is expected, as the scattering cross-section for a 50 nm Au disc is negligible. A 100 nm diameter disc is considered in Figure 5.3 (b), which has a reflectance peak of only approximately 9% at 550 nm. One would expect a 50 nm diameter disc to have considerably lower reflectance.

As disc diameter increases, the reflectance at shorter wavelengths is reduced, as the Au disc fill factor in the unit cell increases. The reduction in reflectance at the shorter wavelengths is due to the low reflectance intensity caused by the disc LSPR in this region at all diameters. As the fill factor of the disc in the unit cell increases, it obscures the VO₂ layer, and reduces reflectance for the structure at short wavelengths. The peak noted in the structure reduces as diameter is increased, until 200 nm diameter, where the peak reflectance begins to increase again. This is due to the trade-off between the fill factor and reflectance of the Au disc component as diameter increases.

The trend is clarified when considering the Au disc component as a function of diameter, as presented in Figure 5.3 (b), for 100 nm thick discs of varying diameter in free space. At small diameters, the disc LSPR response in reflectance is weak, and the fill factor is low, and so the thin film component in the complete structure dominates the reflectance spectrum. As diameter is increased towards 150 nm, the fill factor increases, but reflectance from the disc component is low, and so the reflectance from the structure is reduced. At approximately 200 nm diameter, the reflectance spectrum from the disc, seen in Figure 5.3 (b) is shown to have a high intensity peak, contributing to the reflectance of the structure. The red-shift in the peak can also be attributed to the disc component, with the LSPR position red-shifting as the diameter is increased.

The 150 nm disc diameter case presents the spectra in both phases with the most colour saturation observed in Figure 7.8. This is due to the relatively narrow spectral peak, and positions of near-zero reflection on either side of the peak positions.

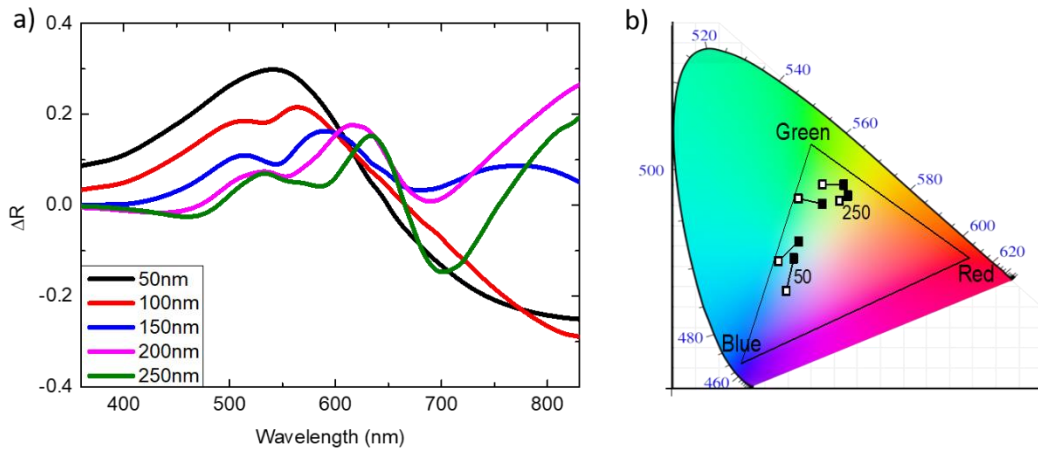


Figure 7.9: (a) ΔR values for phase change of the VO₂ layer from the semiconducting to metallic phase as a function of disc diameter. (b) CIE colour-map for each diameter of 50-250 nm, with phase change of VO₂ from semiconducting (black dot) to metallic (white dot) phase.

Figure 7.9 (a) illustrates the ΔR values for this structure as the disc diameter varies from 50-250 nm. The maximum ΔR value noted is in that of the 50 nm structure, with a maximum of 30% at 530 nm. The maxima trend towards lower values as disc diameter is increased, and red-shifts with the LSPR of the disc, as mentioned previously. This decrease in ΔR maxima is also mirrored in the CIE colour-map values shown in Figure 7.9 (b). The CIE point separation decreases with increased diameter, and tends towards the green primary.

The performance of the structure in terms of ΔR achieved and CIE map separation has not been improved, compared to that of the thin film structure, with ΔR and CIE colour-space shown in Figures 6.11 and 6.17, respectively. However, values in this area of the CIE colour-space had not been previously achieved when examining the structure in Chapter 6. This has shown that inclusion of nanoparticles to the structure allows for further expansion of the colour gamut.

7.1.3 Particle shapes on VO₂

The introduction of Au particles of various shapes has been considered in place of nanodiscs in the array. By altering the nanoparticle shape to those with increasingly sharp vertices, the field enhancement is increased in the vicinity of the particles[99]. This increase in field enhancement has the potential to increase the interaction

between particles and VO₂ layer, leading to more significant colour changes upon phase transition. Figure 7.10 illustrates the particles introduced to the nanostructure as alternatives to the circular discs used previously.

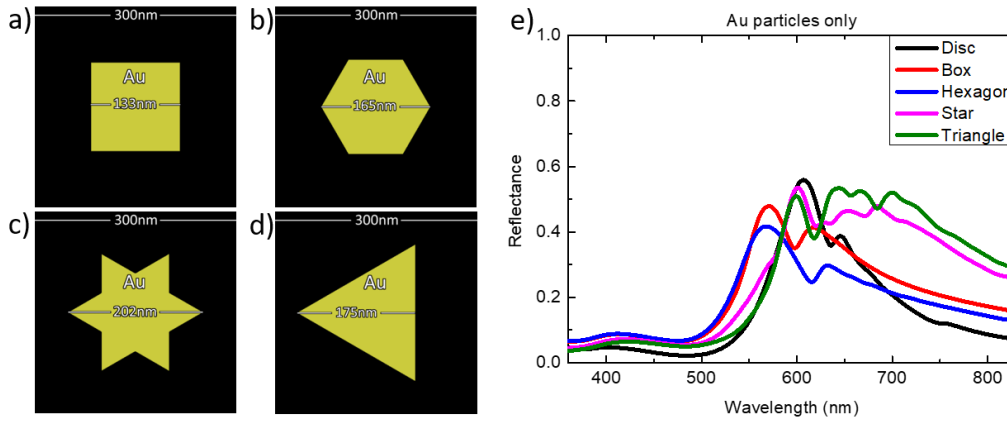


Figure 7.10: (a-d) unit cell for the simulated particles in free space ($n=1$). All particles are 100 nm thick, with a (a) box, (b) hexagon, (c) star, and (d) triangle of equal volume to that of the 150 nm diameter disc. (e) Reflectance spectra of each particle, including the disc for reference.

Figure 7.10 (a-d) illustrates the shapes of nanoparticle selected. Each particle was 100 nm thick, and so volume calculation was simplified to the area of the particles when viewed from above. Simple geometric shapes of varying sharpness were selected, with a (a) box, (b) hexagon, (c) star, and (d) triangle selected. Though (c) and (d) both have vertices of 60°, the asymmetry of the particles allows for excitation along a longer axis than that of the star, potentially allowing for larger charge build-up at the tip orientated along the polarisation axis, and greater field enhancement.

All particles were of the same volume, equivalent to the volume of the 150 nm disc used in Section 7.1.1. A fixed volume was selected, as the LSPR of nanoparticles are known to be sensitive to size, by maintaining a fixed volume this was minimised. As all particles were of the same height, the volume calculation simplified to area calculations of the geometric shapes, where the areas of the circle (A_C) box (A_B), hexagon (A_H), star (A_{ST}), and triangle (A_T) are as follows:

$$A_C = A_B = A_H = A_{ST} = A_T \quad (7.1)$$

$$\frac{\pi}{4} l_C^2 = l_S^2 = \frac{3\sqrt{3}}{8} l_H^2 = \frac{\sqrt{3}}{4} l_{ST}^2 = \frac{\sqrt{3}}{3} l_{ST}^2 \quad (7.2)$$

where l_x is the length shown for each shape in Figure 7.10 (a-d).

Figure 7.10 (e) shows the reflectance spectra for each particle shape, along with the disc reflectance. These simulations are carried out in free space, with a surrounding refractive index of $n = 1$, for the surrounding media. Polarisation of the incident light is along the x-axis, with the monitor in the xz plane, as with all previous FDTD simulations in the thesis.

The spectra show similar features throughout each shape examined, with the box and hexagon having a reflectance peak at shorter wavelengths than the other particles, at 570 nm. This peak is due to the short polarisation axis present in both shapes, allowing for plasmon resonances at shorter wavelengths than that of the disc. Reflectance spectra for the triangle and star shapes exhibit particularly strong overlap of the peak position to that of the disc. Higher reflectance at longer wavelengths can be credited to the longer axis present in these shapes.

These particles were introduced to the structure architecture presented in Figure 7.7 (a). The reflectance spectra for each of these shapes are presented in Figure 7.11, for VO₂ in the (a) semiconducting, and (b) metallic phase.

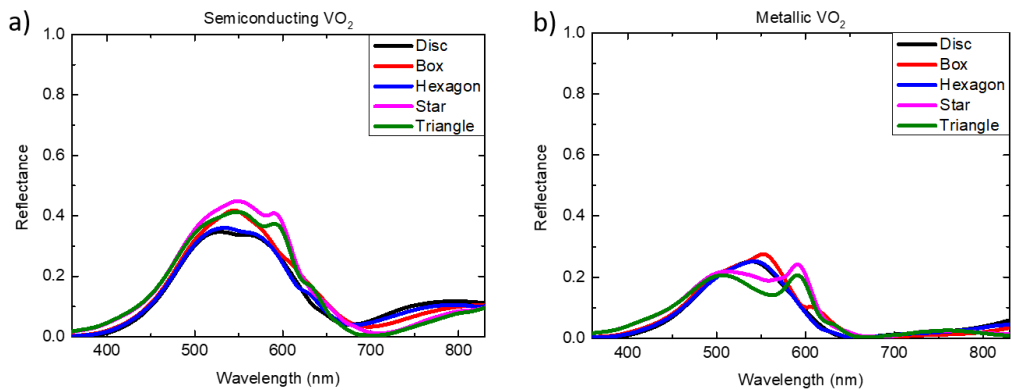


Figure 7.11: Reflectance spectra for the nanostructure with the disc, box, hexagon, star, and triangle shaped nanoparticles, with VO₂ in the (a) semiconducting, and (b) metallic phase. sRGB values are not shown, as the spectra significantly overlap and produce similar colour hues.

The reflectance spectra from Figure 7.11 includes the disc structure of 150 nm diameter, also shown in Figure 7.8. sRGB colour values are not used in this plot, as the spectral changes overlap across a wide range, making them hard to distinguish. The broad overlap across the visible also leads the sRGB values to be similar for all particle shapes, with a green hue of similar saturation and luminance throughout, for both phases of VO₂. A wide peak dominates most of the visible region for both phases in every shape examined, similar to the spectra examined in Section 7.1.2.

In the case of the box, star and triangle, there is a notable increase in reflectance in the 500-600 nm range compared with that of the disc, but no increase in reflectance in the hexagonal particle structure, which follows the disc spectral shape throughout the visible region. One would expect there to be a similar response for the box and hexagon, when examining the reflectance of the particle components in Figure 7.10 (e), due to their similar responses. This indicates that due to the shape of the box, there is a stronger interaction with the VO₂ layer than for the hexagonal particle. Further insight into this is revealed when examining the field profiles in Figure 7.14, later.

There is also an increase in reflectance noted in the star and triangle particles when compared to the disc in the semiconducting phase of VO₂, with a peak reflectance at 545 nm. As a similar peak is noted in the box shape, but not the disc or hexagon, indicating that the origin of the higher reflectance is the sharpness of the corners of the particles in which it is observed. Figure 7.12 (a) shows a field distribution at 545 nm in the star structure, with a large field enhancement along the side of the wall in proximity to the VO₂, where interaction with the layer occurs. This indicates that the shape allows for field enhancement near the VO₂ layer, increasing sensitivity of the structure to the phase change. This peak is drastically reduced in the metallic phase, with a local dip forming for both the star and triangle cases. This dip also appears to red-shift upon phase change, further indicating that the feature is sensitive to the phase transition.

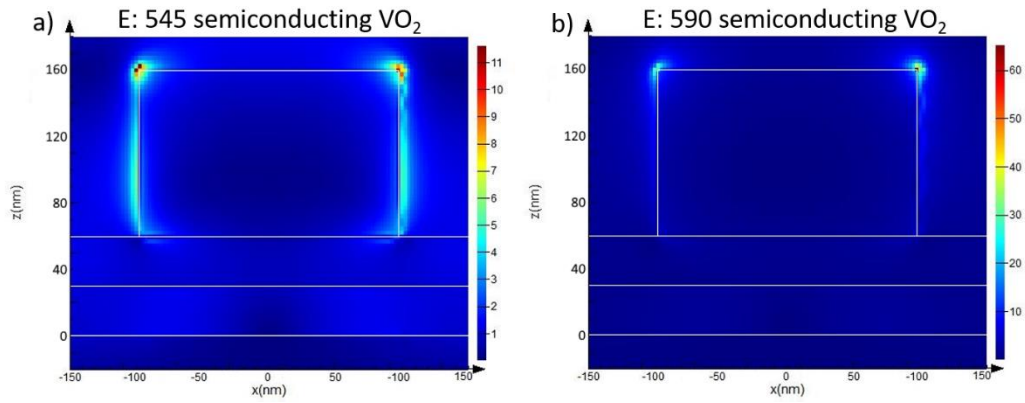


Figure 7.12: Electric field profile cross sections of star nanostructure unit cell at (a) 545 nm, and (b) 590 nm., with semiconducting VO₂.

A second peak is also noted in Figure 7.11 (a) at 590 nm, a feature not noted in the box or hexagon shapes. This feature is attributed to the acute angle of 60° for the vertices only present in these particles. These secondary peaks are also noted in the spectra of Figure 7.11 (b), for the metallic phase of VO₂ at approximately the same spectral position, having not been as strongly affected by the phase change as the peak noted at 545 nm. The peaks do not shift on phase change, and Figure 7.12 (b) indicates that the field is localised strongly at the top corners of the particle. These regions of largest field enhancement are positioned furthest from the VO₂, leading to the weakest interaction with the layer.

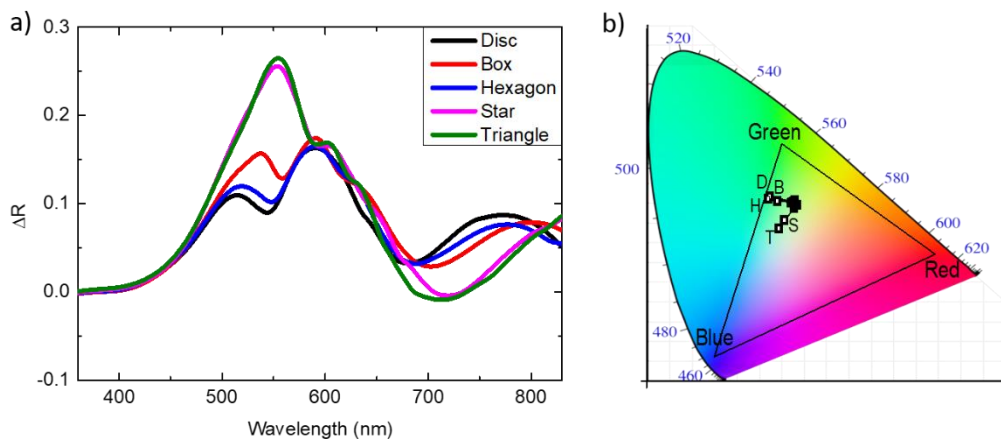


Figure 7.13: (a) ΔR values for phase change of the VO₂ layer from the semiconducting to metallic phase for each particle shape. (b) CIE colour-map for shape, with phase change of VO₂ from semiconducting (black dot) to metallic (white dot) phase.

Figure 7.13 (a) illustrates the change in the peak at 545 nm to a dip at 580 nm for the star and triangle particles, which are significant in comparison to the other particle shapes. The star and triangle particles demonstrate the largest ΔR , with a maximum

of 26% at 545 nm. The CIE plot is also shown for these structures in Figure 7.13 (b). For each case, the plot shows a small colour change compared to the values achieved in Figure 7.9 (b) for varying disc diameter. The values are also broadly overlapping, as is expected with spectra of such similar shape.

The top-down (xy plane) electric field profiles are shown in Figure 7.14 for the disc, box and hexagonal shapes, with Figure 7.15 demonstrating the field profiles for the star and triangle structures.

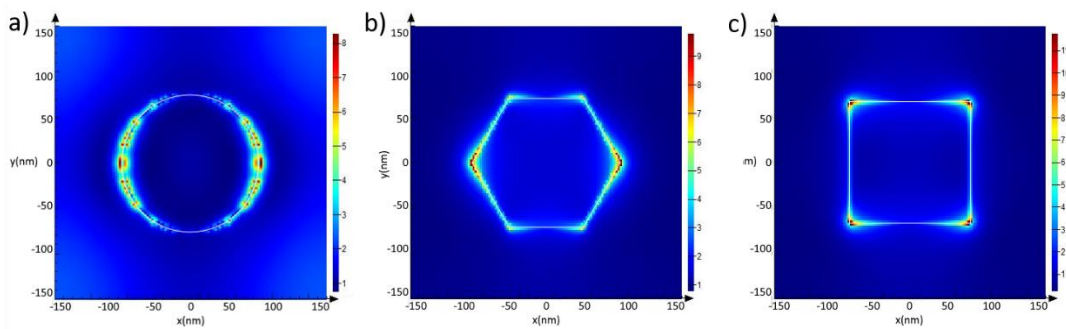


Figure 7.14: 2-dimensional top-down electric field profile, positioned at the top surface of the (a) disc, (b) hexagon, and (c) box particles at 545 nm. VO_2 in the semiconducting phase.

The electric field profiles in Figure 7.14 and 7.15 illustrate the maximum E field magnitudes measured for each particle structure, in the order of increasing maximum value noted. The structure exhibiting the smallest E field maximum is in that of the disc, with the largest field noted in the triangle. Figure 7.14 (a) shows the disc maximum field at 545 nm to be 8 V/m, the hexagon in (b) to have a larger enhancement of over 9 V/m, and (b) the box to have the largest of the three, at over 11 V/m. This gives insight to the increased reflectance noted at this wavelength in Figure 7.11 (a) for the box structure over that of the disc and hexagon.

A similar response is also noted in the star and triangular structures in Figure 7.15 (a) and (b), respectively.

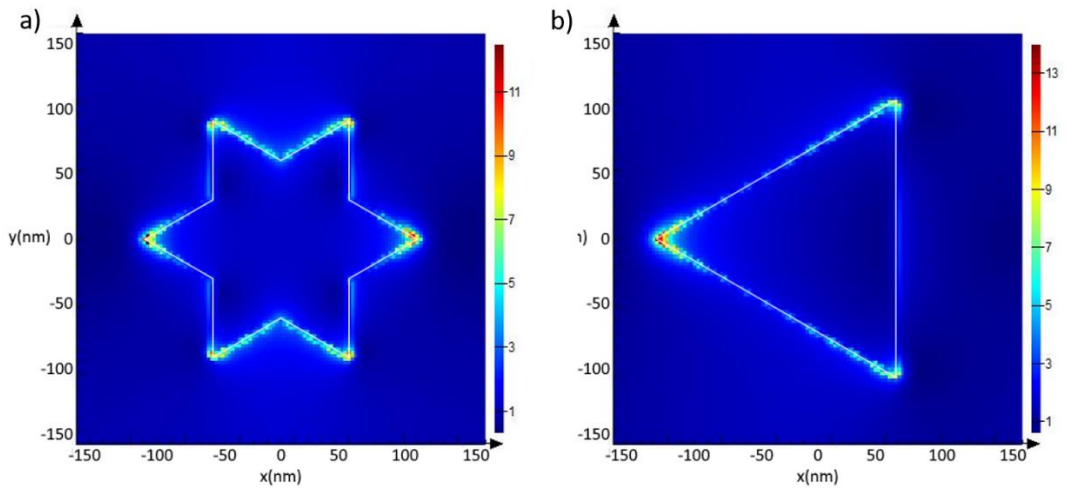


Figure 7.15: 2-dimensional wavelength dependent top-down electric field profile, positioned at the top surface of the (a) star, and (b) triangle particles at 545 nm. VO₂ in the semiconducting phase.

Figure 7.15 reveals E field maps for the (a) star structure, with maxima at the points of the star along the polarisation axis of approximately 12 V/m. A further increase is noted in the (b) triangle, with approximately 13 V/m observed at the point of the Au particle. A second position is also examined, at 590 nm for the star and triangle structures, where a second peak is noted in the spectra in Figure 7.11.

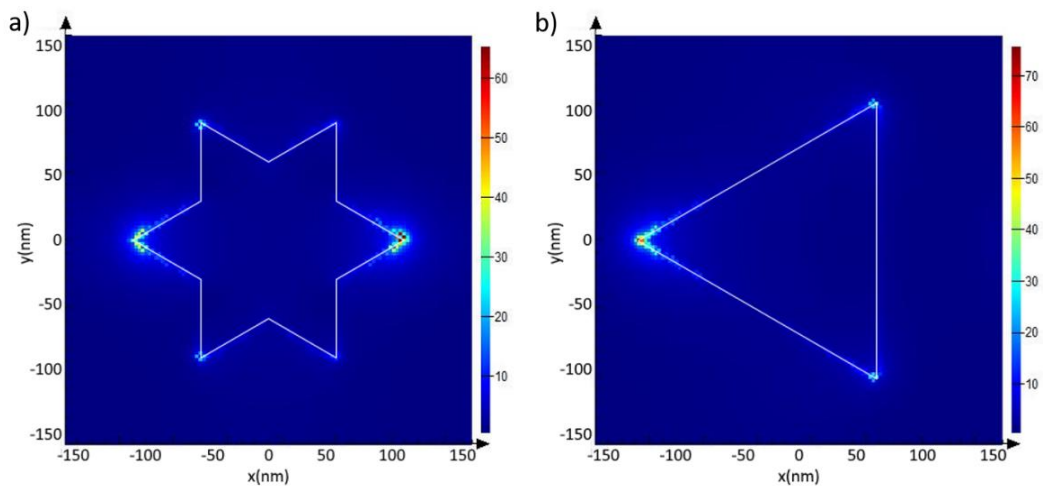


Figure 7.16: 2-dimensional wavelength dependent top-down electric field profile, positioned at the top surface of the (a) star, and (b) triangle particles at 590 nm.

Figure 7.16 reveals that the maximum E field at 590 nm for both structures also occurs at the tips of the structure along the polarisation axis. However, the field enhancement at this position is much larger than those noted previously, with a maximum for the (a) star of over 60 V/m, and (b) triangle of over 70 V/m. This is also observed in the side profile of the star structure in Figure 7.12 (b), which is also

measured at 590 nm. This feature is not significantly altered upon phase change of the VO₂, due to the position at the top corners of the particles, shown in Figure 7.12 (b), leading to a weak interaction with the layer.

Though an increase in E field magnitudes is observed for all particle shapes examined over that of the discs, there is negligible change in the reflectance spectra in Figure 7.11. A small increase in reflectance in the 400-500 nm wavelength range is observed in the box, star, and triangle structure, though this has little impact on the colour observed, other than a slight increase in luminance. In order to take advantage of the large E fields observed in these particle shapes, and increase particle-VO₂ interaction; imbedding is necessary to position the top corners inside the VO₂ layer.

7.1.4 Discs imbedded in VO₂

Section 7.1.1 has demonstrated that partially imbedded discs have minimal impact on the phase change potential of the structure. Nanodiscs on-top of the structure also yielded similar performance in Section 7.1.2. Previously, Figure 7.5 (a,b) revealed that for a partially imbedded disc, there is substantial field enhancement in the VO₂ layer at the boundaries of the Au particle walls.

By imbedding the particles fully in the VO₂ layer there may be potential to maximise the field interaction with the thin film, as the largest fields yet have been observed at the top corners of the particles. In this section, the impact of fully imbedding the Au nanoparticles is investigated for colour change potential. Disc thickness is changed to 30 nm throughout, in order to full imbed the discs in the 30 nm thick VO₂ layer.

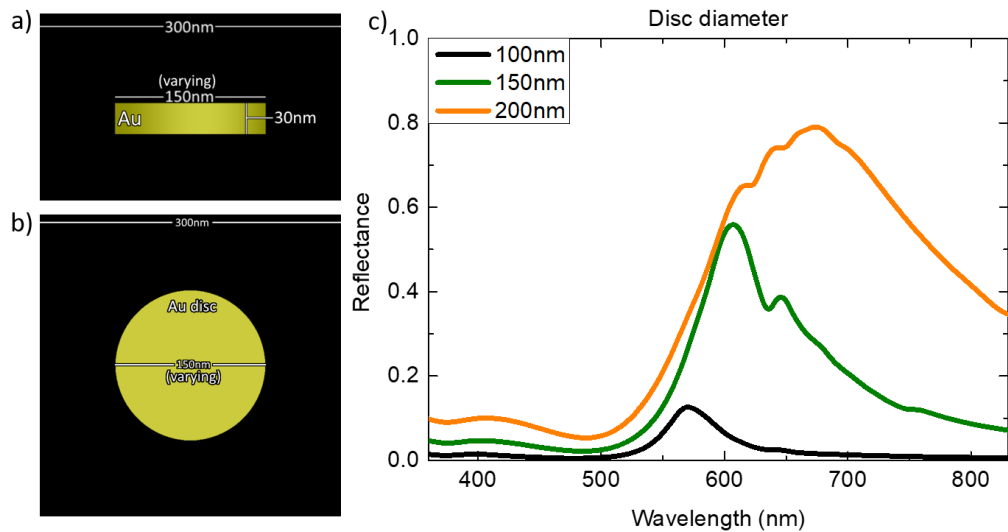


Figure 7.17: (a) Schematic profile of the disc in free space, with Au thicknesses of 30 nm. (b) Top-down schematic of the structure unit cell, with 150 nm diameter Au disc and 300 nm pitch. (c) Reflectance spectra of 100, 150, and 200 nm diameter discs.

The discs simulated in Figure 7.17 are 30 nm thick, with diameters of 100, 150, and 200 nm. A fixed pitch of 300 nm is maintained. This is a similar configuration to the disc simulated for the hybrid structure in Chapter 5, illustrated in Figure 5.3. However, discs of 100 nm thickness were examined in that case, with the reflectance spectra of which are shown in Figure 5.3 (c). When compared to Figure 7.17 (c), the reflectance response for each diameter is similar in shape, with a single LSPR peak noted in the visible region of each spectrum. A peak reflectance of 12% is noted at 570 nm for the 100 nm disc, 56% at 600 nm for the 150 nm diameter, and 80% at 670 nm for the 200 nm diameter disc. This is a larger wavelength range than for the 100 nm thick discs, which range from 550-580 nm for discs of 100-200 nm diameter.

This indicates that these 30 nm thick particles exhibit resonance positions with higher sensitivity to diameter than the 100 nm thick Au discs. Also, despite the volume of the 30 nm thick particles being only 30% of the equivalent diameter 100 nm thick Au discs; resonance positions for these discs occur at longer wavelengths in all cases, which has been observed previously[206].

The position of the LSPR peak position at longer wavelengths can be attributed to the oscillation of the electric charge at the metal-air interface along the top and bottom surfaces of the disc. In the case of the 30 nm thick particles, the dipolar

excitation occurs with the two surfaces in close proximity to each other, allowing for interaction between the two, which results in a red-shift in the resonance oscillation. As the thickness is increased, these dipole excitations separate, and interaction between the dipole systems is reduced, resulting in a blue-shift in the resonance position.

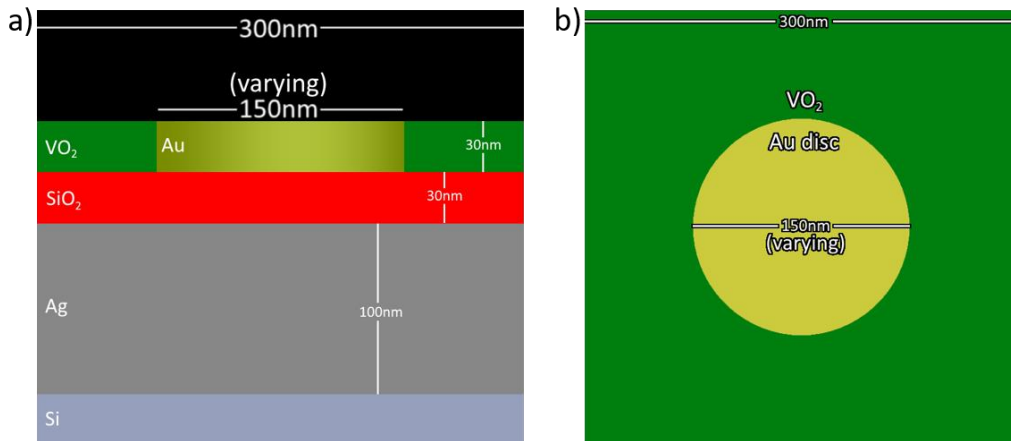


Figure 7.18: (a) Schematic profile of the nanostructure unit cell on Si substrate, with Ag thickness of 100 nm, Au, SiO₂ and VO₂ thicknesses of 30 nm. The Au disc is imbedded within the VO₂ layer. (b) Top-down schematic of the structure unit cell, with 150 nm diameter Au disc and 300 nm pitch.

Figure 7.18 illustrates the structure under consideration. In this configuration, the SiO₂ thickness remains at 30 nm thickness.

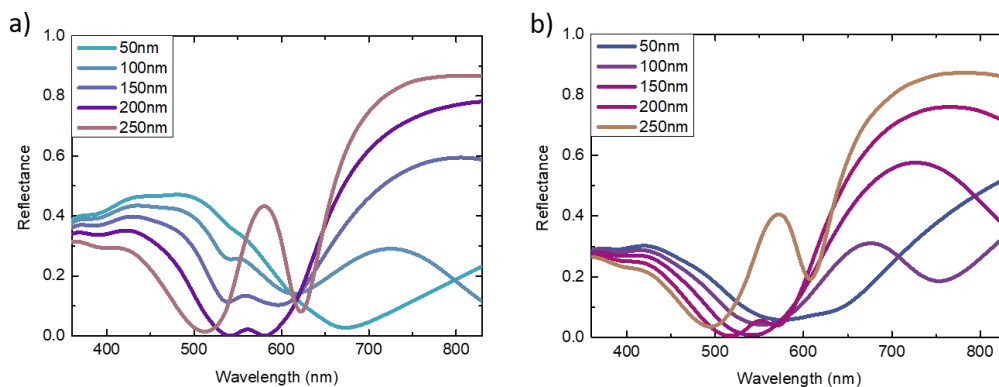


Figure 7.19: Reflectance spectra of five structures with varying disc diameter 50-250 nm in 50 nm steps, for the (a) Semiconducting and (b) Metallic phases. The line for each spectrum is shown in the sRGB value colour.

Figure 7.19 shows the spectra for the imbedded Au nanoparticle structure in both phases of VO₂. With an Au disc diameter of 50 nm, the structure resembles the thin film VO₂ reflectance noted in Figure 6.11 (b) in both phases, similar to that observed

in the 50 nm disc example in Figure 7.8. As disc diameter increases, the peak position and intensity at short wavelengths, below 500 nm, blue-shifts and is reduced. The dip noted at approximately 680 nm in the semiconducting phase also blue-shifts, with a small peak forming in the centre of the dip. This dip reaches a near-zero reflection at two points in the 200 nm diameter case, at 540 and 580 nm. This near-zero reflection is also observed at one position in the metallic phase, at 515 nm in the 200 nm diameter case, with the small peak also observed.

The 250 nm disc diameter is a specific case where an intense, narrow peak is noted in both phases of VO_2 spectra. This peak corresponds to an increase in electric field enhancement at the top corners of the disc, decaying quickly above the disc surface and into the VO_2 layer near the top of the disc, as shown in Figure 7.20. This indicates a strong LSPR condition being generated for this particle geometry when imbedded in the VO_2 , leading to the formation of a feature with high reflectance intensity over a narrow range.

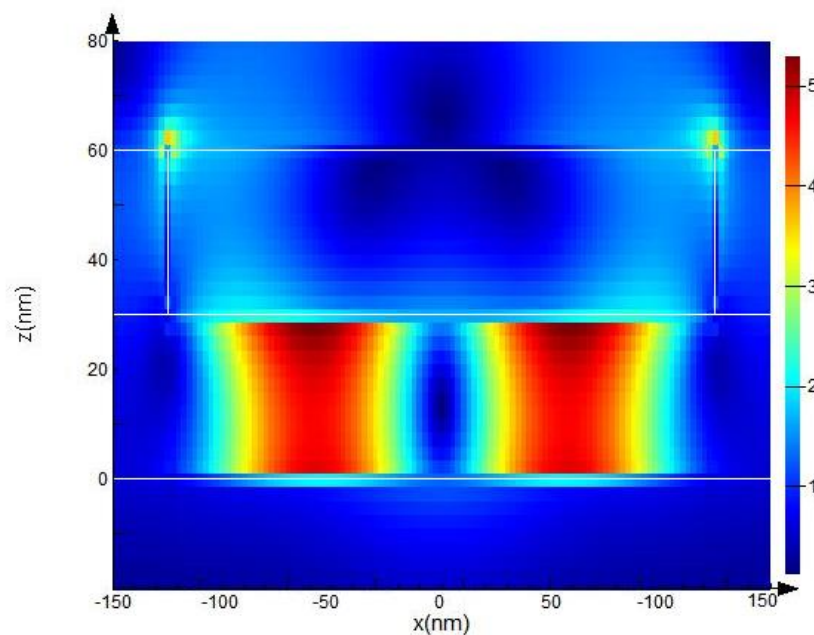


Figure 7.20: Electric field profile cross sections of 250 nm disc diameter unit cell at 580 nm., with semiconducting VO_2 .

The rising reflectance noted at longer wavelengths with increasing diameter is attributed to the disc high reflectivity. At longer wavelengths, the high reflectivity of Au has more impact as the fill factor of the disc in the unit cell increases.

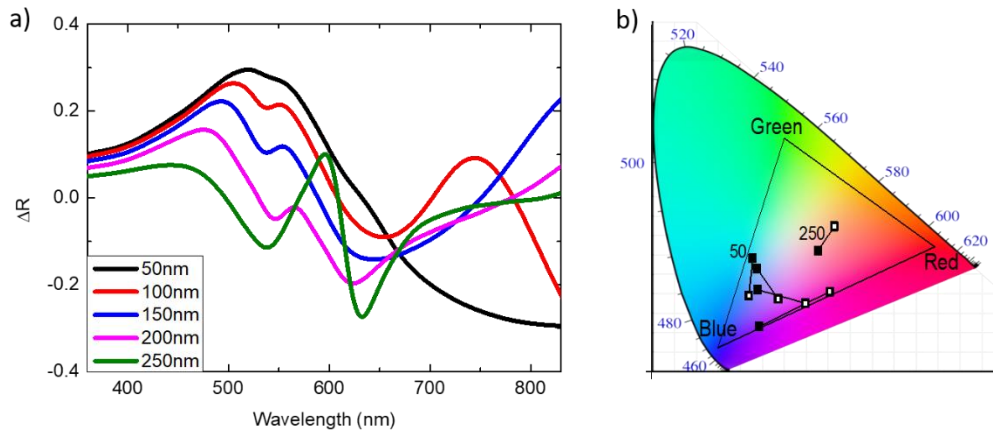


Figure 7.21: (a) ΔR values for phase change of the VO₂ layer from the semiconducting to metallic phase as a function of disc diameter. (b) CIE colour-map for each diameter of 50-250 nm, with phase change of VO₂ from semiconducting (black dot) to metallic (white dot).

Figure 7.21 (a) illustrates the ΔR in the structure as a function of wavelength for each diameter of disc examined. The maximum ΔR values do not appear to shift as diameter increases when compared to the ΔR values achieved in Section 7.1.2, in Figure 7.9 (a). The maximum ΔR value in Figure 7.19 for the 250 nm diameter illustrates further the difference in reflectance spectra due to the narrow peak present at this diameter.

The CIE colour map is also shown in Figure 7.21 (b), for each diameter of disc. The values are largely grouped in the Blue primary area of the colour-space, with the 250 nm diameter case appearing closer to the centre of the CIE space than the other points. There is approximately equal separation between phases for the 50, 100 and 150 nm diameter cases, with the 200 nm diameter showing the largest separation yet achieved in these nanostructures that combine Au particles with VO₂. This structure configuration has also shown the largest gamut yet observed in structures with varying disc diameter in this chapter, demonstrating potential for the structure to generate a larger range of colours.

7.1.5 Particle shapes imbedded in VO₂

This section investigates the introduction of Au particles of various shapes to the structure explored in Section 7.1.4. This is a similar progression to that between Section 7.1.2 and 7.1.3. The shapes used are the same as those in section 7.1.3, with a box, hexagon, star, and triangle examined, with the disc response also included for comparison. All particles are 30 nm thick, and are equivalent in volume to the 150 nm diameter disc, according to Equation 7.2. The structure resembles the architecture introduced in Section 7.1.4, shown in Figure 7.18 (a), with Si substrate, 100nm Ag layer, 30 nm SiO₂, and VO₂ layer.

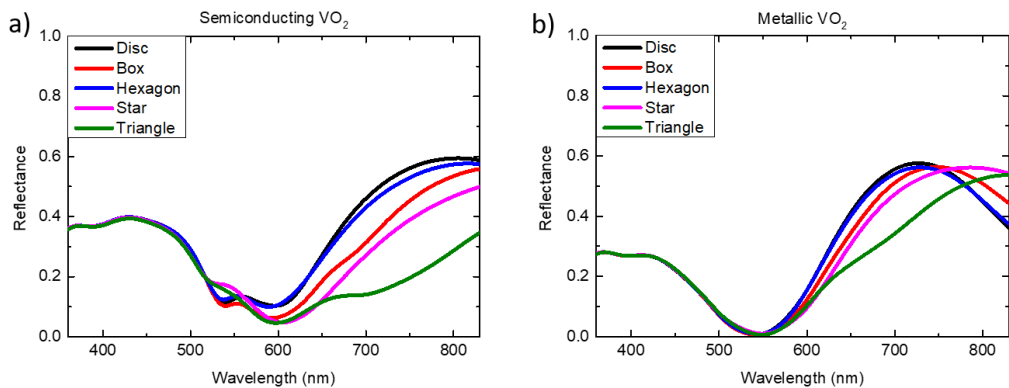


Figure 7.22: Reflectance spectra for the nanostructure with the disc, box, hexagon, star, and triangle shaped nanoparticles, imbedded in VO₂, in the (a) semiconducting, and (b) metallic phase. sRGB values are not shown, as the spectra significantly overlap and produce similar colour hues.

The reflectance for these shapes imbedded in the VO₂ layer are shown in Figure 7.22. Similar to Figure 7.11, which presents the spectra for the same shapes, of 100 nm thickness on-top of the VO₂ layer, sRGB colour values are not used in this plot. These values are not included as the spectral changes overlap across a wide range, making them hard to distinguish. Similar to the disc of 150 nm diameter shown in Figure 7.19, the hue of these spectra is blue in the semiconducting phase, and a pink in the metallic phase of VO₂, with a similar luminance throughout. A wide dip, centred at approximately 550-600 nm for all shapes, dominates the majority of the visible region in every shape examined.

In the case of the box, star and triangle, the minimum reflectance in the dip observed is a notable decrease in reflectance at approximately 600 nm in the semiconducting phase. The second dip noted in the circle, box, and hexagon structures at 540 nm is not observed in star and triangle structures, and instead appears as a point of inflection, or shoulder for the feature in the same wavelength range. Similar to the secondary peak in the star and triangle structures in Section 7.1.2, this is due to the sharper geometries of these shapes. This sharpness leads to a difference in the LSPR generated in the particles, with a larger field enhancement observed in sharper particles.

The positions of the maximum electric fields experienced in the side profiles of this architecture are hard to determine, due to the maxima occurring off of the central axis of the particles in most shapes examined. This is demonstrated in the xy plane E field maps in Figures 7.24 and 7.25, with the faces of the particles exhibiting the largest enhancement.

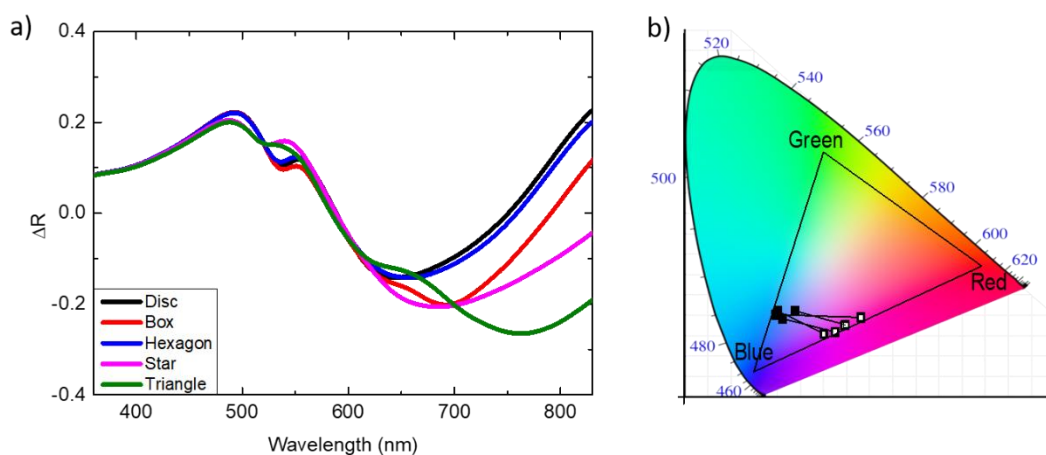


Figure 7.23: (a) ΔR values for phase change of the VO_2 layer from the semiconducting to metallic phase for each particle shape. (b) CIE colour-map for shape, with phase change of VO_2 from semiconducting (black dot) to metallic (white dot).

Figure 7.23 further demonstrates the similarity in performance of the structure as a function of particle shape, with close correlation between the ΔR values for all shapes across the visible region. These spectra overlap significantly more than that of the particles on-top of the VO_2 layer, shown in Figure 7.13 (a). This is due to the

damping effect of the highly absorbing VO₂ layer surrounding the nanoparticles, leading to smaller E field magnitudes, particularly for the sharper particles.

The CIE plot shown in Figure 7.23 (b) illustrates the grouping of the colour values in these structures in the region of the blue primary. Upon phase transition, all values move towards the midpoint of the blue-red primaries. This is due to the increase in the stimulation of the long (red) colour cones in the metallic phase of VO₂. The separation of all values is second only to the 200 nm diameter disc in Figure 7.21 (b), demonstrating the high performance of the structure with all shapes examined. These values are also in a region of the CIE with high colour saturation, an improvement on the positions available to the thin film structure examined in Chapter 6, as demonstrated by the values achieved in Figure 6.17 (b).

As mentioned in Section 7.1.4, the purpose of imbedding particles is the potential to maximise the field interaction with the thin film, as the largest fields have been observed at the top corners of the particles in previous examinations in the Chapter. Top-down electric field profiles are shown for all shapes examined in this Section in Figures 7.24 and 7.25. The electric profiles for the (a) disc, (b) hexagon, and (c) box are shown in Figure 7.24.

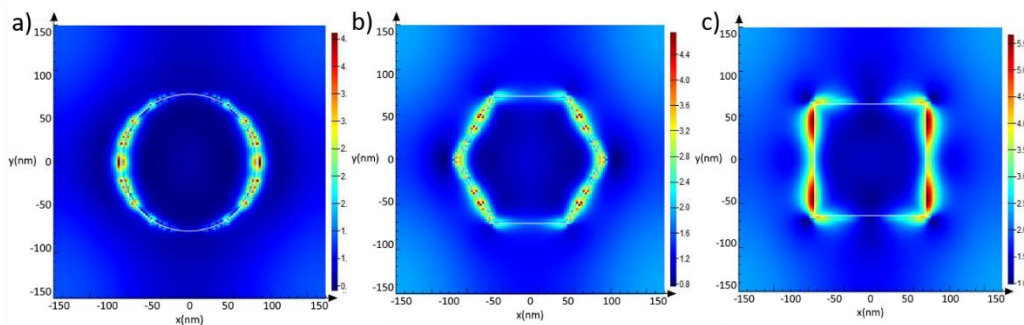


Figure 7.24: 2-dimensional wavelength dependent top-down electric field profile, positioned at the top surface of the (a) disc, (b) hexagon, and (c) box particles at 600 nm. VO₂ in the semiconducting phase.

Figure 7.24 reveals the difficulty in realising the maximum electric field profiles for the electric field enhancement for these imbedded structures, as the maxima are located off the central axis of the particle in most cases.

The maximum observed E field for the (a) disc, (b) hexagon, and (c) box are 4.0, 4.4 and 5.5 V/m, respectively. This follows the same trend for maxima observed in the discs on-top of the VO_2 layer in Figure 7.14. However, the areas of high electric field enhancement for this configuration occur on the plane interfaces of the particle and VO_2 , and not the corners, as was observed in the particles on-top. It is also clear that the field enhancement is approximately half that of the particles on-top of the VO_2 layer. This can be attributed to the reduced scattering cross-section potential of the particles, as they are fully imbedded, and the absorption caused by the surrounding material being significantly lossy.

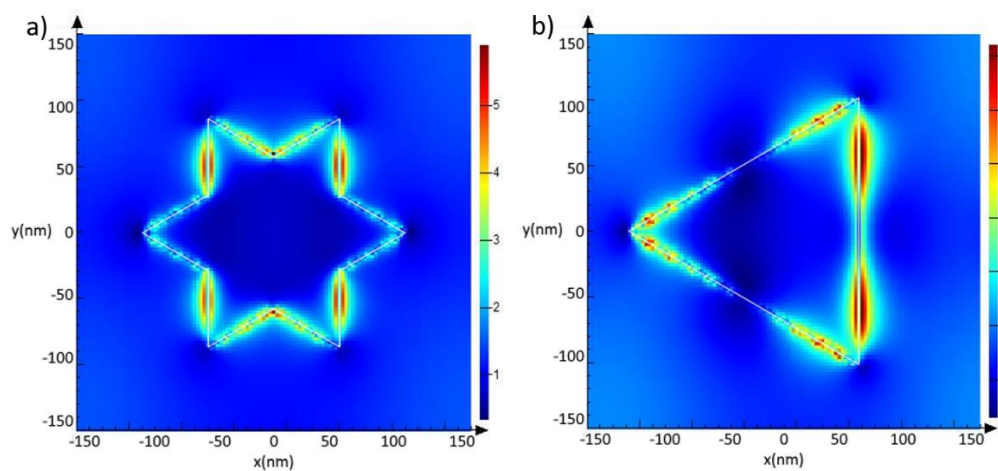


Figure 7.25: 2-dimensional wavelength dependent top-down electric field profile, positioned at the top surface of the (a) star, and (b) triangle particles at 600 nm. VO_2 in the semiconducting phase.

A similar trend is noted in Figure 7.25, with maxima of approximately 5.9 and 7 V/m electric field strength. These maxima are also positioned at the interfaces of the Au and VO_2 , and not the sharp points of the structures. It is clear from this, that imbedding the particles does not lead to the large field enhancement observed in structures with particles on-top of VO_2 . However, performance has been increased with imbedded particles, in terms of the change in CIE colour-space position in the structures with imbedded particles. Overall, performance of imbedded structures shows improvement over those of the thin film design in Chapter 6.

Further study may be required to expand the gamut of the structures, by creating structures that result in CIE values closer to the red, green, and blue colour

primaries. Improvements may also be possible in the luminance and colour saturation, by generating spectral features that are sharper, and with larger reflectance intensity.

7.2 Conclusion

Au particles have been incorporated into a VO₂ thin film nanostructures to determine colour change potential of a combined nanostructure architecture. The highly sensitive, strong LSPR in the visible, and field enhancement around the Au nanoparticle have led to strong interaction with the VO₂ layer, altering reflectance spectra of the structure. Change in reflectance of the thin film VO₂ stack, as well as the LSPR of the disc component, combine to increase the colour change of the overall structure. Au discs of varying diameter on-top of the VO₂ layer have shown that low overall reflectance, and weak interaction of the evanescent field with the layer lead to colours with high saturation, but low luminance and small colour change upon phase change of VO₂. Incorporation of different shapes of the same volume, including a box, hexagon, star, and triangle, increase the field enhancement, though have little impact on the reflectance measured, as the LSPR of the particles are similar across the visible region.

Imbedding of the Au particles into the VO₂ has led to an increase of field interaction with the layer, but a decrease in overall field enhancement, due to the high absorption of VO₂. The colour gamut achieved with disc diameter change upon phase transition was shown to increase substantially, when compared to that of discs on-top of the VO₂, and the thin film design of Chapter 6. The inclusion of the box, hexagon, star, and triangle shaped nanoparticles have, again, lead to increased field enhancement, but have minimal impact on colour change in the structure.

Conclusion

Summary

This thesis has explored a number of metallic nanostructure architectures for structural colour. Possibilities for dynamic colour for use in passive display applications have also been explored.

The commercial FDTD tool Lumerical has been validated in **Chapter 4**, by simulating and comparing the structure published by Kumar *et al.*[6] An aluminium-based nanodisc-nanohole plasmonic array has been realised, similar in configuration to previous Aluminium nanodisc-nanohole structures[11,37,58]. In FDTD simulation, a strong interaction between the disc and hole components by a Fano resonance interference effect has been observed. Variation of a number of key geometry parameters has been carried out, including disc diameter, cell pitch, and pillar height. These parameter variations were used to determine the origin of spectral features, and to optimise the structure for fabrication. Arrays fabricated by EBL include a 5 mm square array sample consists of a dielectric pillar of 200 nm diameter and 100 nm height, with a pitch of 400 nm. An aluminium coating the top of the pillar and the backreflector form the disc and hole components. A strong agreement is found between simulated and measured spectra in fabricated sample. The 5 mm square array size of the fabricated sample is much larger than that of nanodisc and nanohole array samples fabricated by EBL in the literature, with the vast majority measuring below to 150 μm [6,11,20,37,51,188]. This was done to determine if visibility of the array colour under ambient illumination without the use of microscope optics. A high angular sensitive colour phenomenon was observed in this structure before and after metal deposition. This effect was examined, and established to be a diffraction effect caused by the array periodicity. A first order diffraction profile was observed, with grating constant of 400 nm, consistent with the array pitch.

The hybrid metal nanostructure examined in **Chapter 5** consisted of Au discs on a polymer thin film and Ag backreflector. This has been the first demonstration of a hybrid MIM structure, that combines the strong LSPR response of Au, with the high reflectivity of planar Ag. However, similar MIM structures with single metal configurations for both the discs and continuous backreflector have been previously investigated[11,12,20,42,190–196]. A disc diameter of 150 nm, cell pitch of 300 nm, and material thicknesses of 100 nm was considered as the “typical” configuration, with a wide variation of these parameters in simulation to determine colour trends and the origin of spectral features. This structure maintained a smaller unit cell footprint than the Aluminium structure, in order to minimise angular effects in reflectance, and the thin film polymer component increased potential for the incorporation of other materials to the structure. A strong interference effect has also been observed in this structure, between the disc LSPR and reflectance from the Ag backreflector, generating sharp spectral features in reflectance that are highly sensitive to parameter variation. A cyclical colour trend was observed in the structure as polymer layer thickness was varied, with a repetition periodicity every 180 nm thickness change. 100 μm arrays have been fabricated using EBL, with two polymer thicknesses. To our knowledge, this has been the first demonstration of EBL on a polymer layer. Good agreement was found between the simulated structures and those fabricated by EBL.

In **Chapter 6**, a thin film stack structure was examined, incorporating a PCM in order to produce dynamic colour. Literature studies utilising a number of chalcogenide based thin film structures were examined[72,73], and VO_2 was selected as an alternative low-power material[17], with the goal of increasing the sensitivity of VO_2 in the visible region, producing a structure with comparable performance. A thin film stack ITO with an intermediate VO_2 layer, and Ag backreflector was examined, similar in configuration to that of the chalcogenide based structures. The sensitivity of the visible reflectance spectrum to the change in phase of a 30nm VO_2 layer increased after incorporation to the thin film stack, with

comparable performance the chalcogenide designs. An increase in maximum ΔR was observed. A 30% change is observed in a 10-30-25-100 ITO-VO₂-ITO-Ag thin film stack, compared with 20% recorded in similar structures containing GST and AIST. CIE separation was also shown to increase in this VO₂ stack configuration. Inclusion of a top ITO layer was also shown to increase the chromaticity change on phase transition. This chapter has illustrated the potential for VO₂ in the visible region, as research has predominantly been focused on applications in the IR[19,83–89,93–96].

The inclusion of nanoparticle arrays to a thin film VO₂ structure was examined in **Chapter 7**, following on from the thin film design proposed in Chapter 6. The high sensitivity of the LSPR response and electric field distribution surrounding the Au nanoparticles to the surrounding media were exploited to maximise colour change on phase transition. VO₂ structures incorporating patterned Ag nanodisc arrays have been previously investigated with applications in the visible[103]. However, the performance of these structures has been limited. In this Chapter, several Au nanoparticle shapes were investigated, in positions on-top of the VO₂ layer and imbedded within it. These shapes included discs, boxes, hexagons, stars and triangles, of the same volume. Change in reflectance of the thin film VO₂ stack, as well as the LSPR of the disc component as the surrounding media is altered, combined to increase the colour change of the overall structure. Imbedded particles were shown to result in the decrease of the maximum ΔR , to 20%. However, this architecture resulted in the largest separation in CIE values of any architecture examined, with particle shape having little impact on the colour change observed.

In conclusion, structural colour has been realized in two plasmonic structures, which have been simulated to determine dependencies on a number of geometric parameters of the structure. A Fano resonance interaction between components of both structures has been shown to contribute to the generation of sharp spectral features in reflectance. These structures have also been fabricated by EBL, with good agreement between simulation and experiment. Dynamic structure colour has been

achieved in simulation of two PCM systems containing VO₂, one based on a thin film stack design, and the other incorporating a metallic nanoparticle component. Improvement to the colour switching potential has been demonstrated as a result of the nanoparticle presence in the structure, due to the sensitive LSPR formed by the particle interacting with the VO₂. Therefore, these nanoparticle-VO₂ structures have potential for dynamic colour generation with comparable, and in some cases improved performance, over other PCM structures. This could lead to the incorporation of nanoparticle-VO₂ structures in display, colour printing, and anti-counterfeit technologies, to name but a few.

Outlook

The work carried out in this thesis on structural colour has highlighted the importance of the sensitivity of nanoparticle LSPR to, structural parameters, proximity of other particles, and the properties of the surrounding media. Dynamic colour generation has been established in simulation to be feasible, both in thin film, and nanoparticle incorporated architectures.

Looking forward, the focus of this research toward dynamic structural colour with regards to the use of VO₂, is paramount. Fabrication of thin film structures to verify the results achieved in Chapter 6 is a key point for the realisation of VO₂ as a phase change material in colour applications. Resulting validation of the thin film stack method for sensitisation of the VO₂ in the visible, as well as development of a fabrication techniques for future structures that incorporate VO₂ to expand research opportunities.

Due to the expansive geometry and materials space available when considering even only a handful of geometry and material composition parameters, the development of a minimization algorithm for simulation would generate an advantageous position in future research efforts. This would allow an increase in the scope of the simulation space, with qualitative analysis of performances.

In the case of the VO₂ structures examined to date, only a small fraction of the available geometry space has been examined, and in only the configurations shown here. There is potential for far greater gains in performance, and exploration of the full sRGB colour gamut available for these structures, and further efforts into uncovering some of these gains would be prudent. This is especially true regarding the development of an optimal structure before fabrication, due to the potential cost in fabrication of the many configurations possible. With regards to this structure, only square arrays of uniform Au nanoparticles have been considered currently. Inclusion of nanoparticles of different composition and distribution also provides possibilities in expanding the colour gamut. Fabrication methods of nanoparticle

distributions within a chalcogenide PCM layer has been shown in recent efforts to be possible with scalable laser heating[100], highlighting great potential for low cost manufacture. There is also potential for further enquiry of other contacting methods for these structures for the application of electrical actuation. To date, switching methods have been postulated, based on the research of others in the field for chalcogenide based materials. VO₂-based structures may benefit from other electrical contacting systems, which may further increase colour change potential, as observed in Chapter 6 with the top ITO contact.

More generally within the scope of nanoparticle-PCM systems in the future, there are applications for other areas, namely sensing, colour filters, absorbers, and light harvesting are just a few examples. While focus here is on sharp, intense spectral features in the visible, these structures have responses that extend into both the UV and IR, with applications in both. VO₂ has been used extensively in the past for IR applications, due to its larger refractive index change in that region. Sensitisation of the material in the IR is as beneficial as it is in the visible region.

Ultimately these structures have shown great potential for both static and dynamic structural colour, and the results shown here are only the beginning of the exploration of their potential. Moving forward, there is much to be done to further improve the technology, and implement it into devices for future use.

Appendix A

Supplementary Information

Here, supplementary simulation results are presented for the nanoparticle-VO₂ structure introduced in Chapter 7. These represent intermediate structures that were investigated for the structure, as well as variables that were considered as potentially significant, but did not significantly impact performance of the nanostructure.

A.1 Thin discs on VO₂

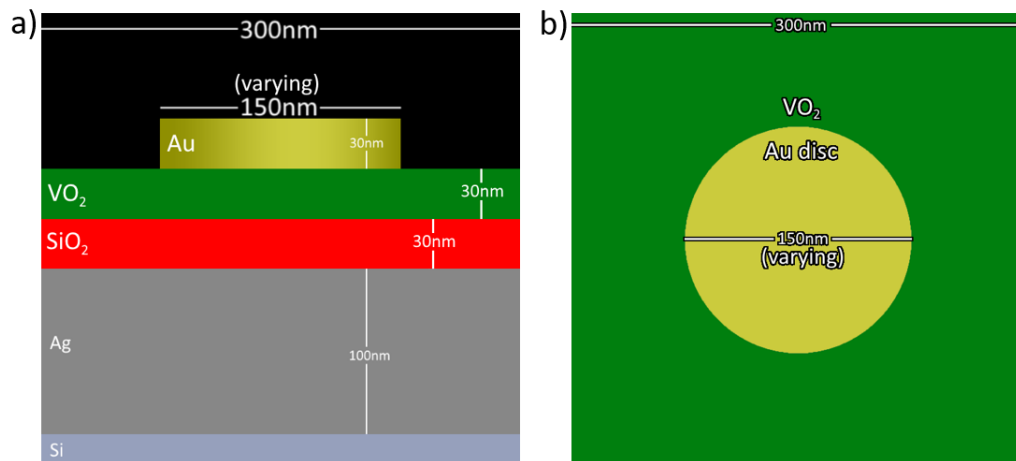


Figure A.1: (a) Schematic profile of the nanostructure on Si substrate, with Ag thickness of 100 nm, Au, SiO₂ and VO₂ thicknesses of 30 nm. The Au disc is on-top of the VO₂ layer. (b) Top-down schematic of the structure unit cell, with 150 nm diameter Au disc and 300 nm pitch.

Figure A.1 illustrates an intermediate structure considered in Chapter 7 with discs of 30 nm thickness on-top of the VO₂ layer. Results are shown here, as the structure may be considered an intermediate configuration, and results from the structure merit discussion.

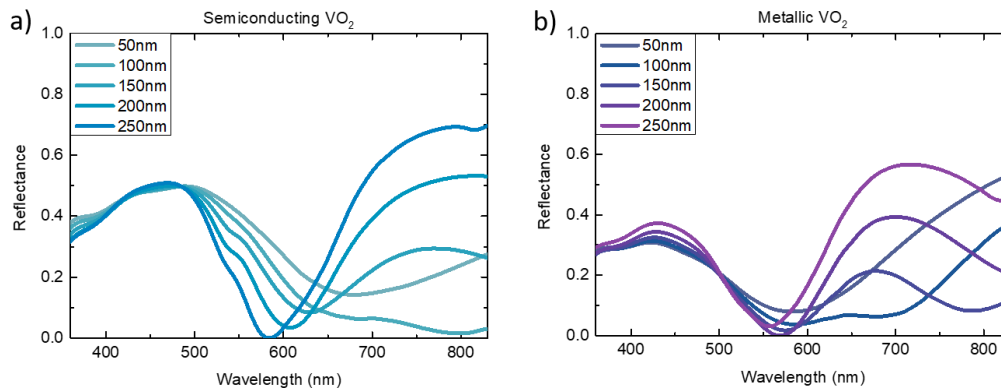


Figure A.2: Reflectance spectra of five structures with varying disc diameter 50-250 nm in 50 nm steps, for the (a) Semiconducting and (b) Metallic phases. The line for each spectrum is shown in the sRGB colour.

Figure A.2 shows the structure with 30 nm Au thick nanodiscs in both the (a) semiconducting, and (b) metallic phase of VO₂. In this configuration, the SiO₂ and VO₂ thicknesses remain at 30 nm. With an Au disc diameter of 50 nm, the structure resembles the thin film VO₂ reflectance noted in Figure 6.11 (b) in both phases. A similar reflectance is observed in the 50 nm disc example in Figure 7.7, where the discs are 100 nm thickness. As the key difference between this structure, and the one explored in Section 7.1.2 is the particle volume, it would be expected that the trend in spectra shape would be similar for both structures. However, this is not observed. As disc diameter increases, the peak position and intensity at short wavelengths, below 500 nm, remains largely unchanged. The dip noted at approximately 680 nm in the semiconducting phase blue-shifts and deepens, reaching a near-zero reflection at 585 nm in the 250 nm diameter disc case. This near-zero reflection is also observed in the metallic phase, at 570 nm in the 250 nm diameter case. In the structure examined in Section 7.1.2, the peak position red-shifts by approximately 80 nm, and varies in reflectance from 30 to 60% as diameter is varied.

In Figure A.2, the rising reflectance noted at longer wavelengths with increasing diameter is attributed to the disc high reflectivity. At longer wavelengths, the high reflectivity has more impact as the fill factor of the disc in the unit cell increases.

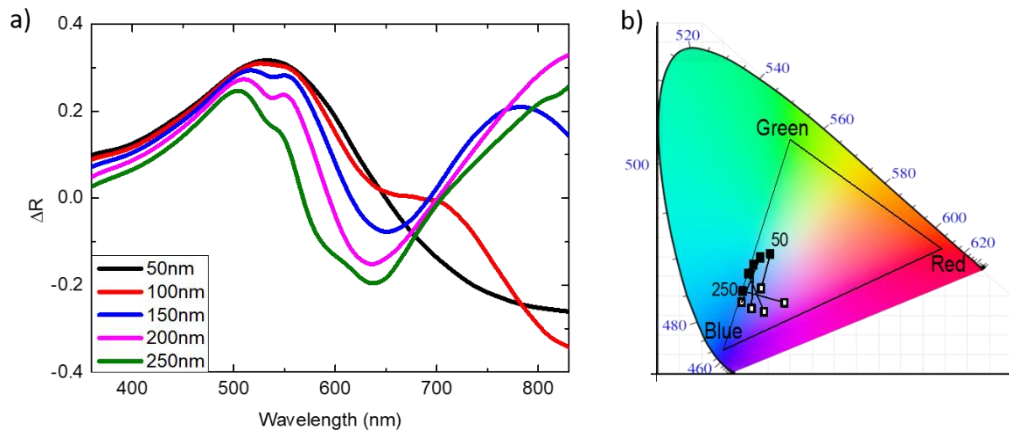


Figure A.3: (a) ΔR values for phase change of the VO₂ layer from the semiconducting to metallic phase as a function of disc diameter. (b) CIE colour-map for each diameter of 50-250 nm, with phase change of VO₂ from semiconducting (black dot) to metallic (white dot) phase.

Figure A.3 illustrates the ΔR in the structure as a function of wavelength for each diameter of disc examined. A higher ΔR is maintained as diameter increased when compared to the ΔR values achieved in Section 7.1.2, in Figure 7.8 (a). The ΔR values in Figure A.3 (a) do not red-shift with increased disc diameter, as was the case in Figure 7.8 (a).

The CIE colour map is also shown in Figure A.3 (b), for each diameter of disc. The values are grouped in the Blue primary area of the colour-space, with approximately equal separation between phases for each diameter. This, together with the ΔR values, indicate that the structure is not significantly impacted by the variation of Au disc diameter on-top of the VO₂ layer, other than the tuning of initial colour observed by the structure, in particular when compared to the structure employed in Section 7.1.2. However, disc diameter is limited by the unit cell boundaries, and so further tuning would not be expected by exploring the parameter space further.

A.2 Encapsulation of Au nanoparticle

In Section 7.1.4 of Chapter 7 the nanodisc array was imbedded in the VO₂ layer to maximise the field interaction with the thin film, as the largest fields were observed at the top corners of the discs. As the LSPR is highly sensitive to the refractive index of the surrounding media, full encapsulation of a nanoparticle in a PCM is expected

to significantly impact the position and intensity of the LSPR reflectance peak upon phase transition. Here, the impact of fully encapsulating the discs in the VO₂ layer was considered by reducing the Au disc thickness by 5 nm, resulting in a 25 nm thick disc, with diameter 150 nm, in a 300 nm pitch array. The structure is presented in Figure A.4. The VO₂ thickness is fixed at 30 nm, due to the significant colour change observed as VO₂ thickness is varied, illustrated in Figure 6.14.

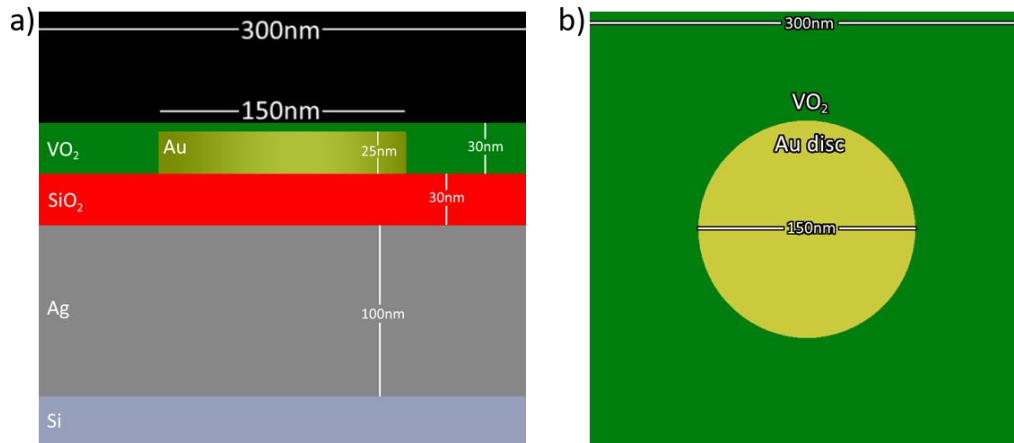


Figure A.4: (a) Schematic profile view of the nanostructure on Si substrate, with Ag thickness of 100 nm, VO₂ and SiO₂ thicknesses of 30 nm, and Au disc thickness of 25 nm. (b) Top-down schematic of the structure unit cell, with 150 nm diameter Au disc and 300 nm pitch.

The reflectance spectra for this structure, with VO₂ in the semiconducting and metallic phase are shown in Figure A.3. This structure is compared to that of the disc imbedded in the VO₂ layer, where Au and VO₂ are of the same thickness, as shown in Figure 7.17.

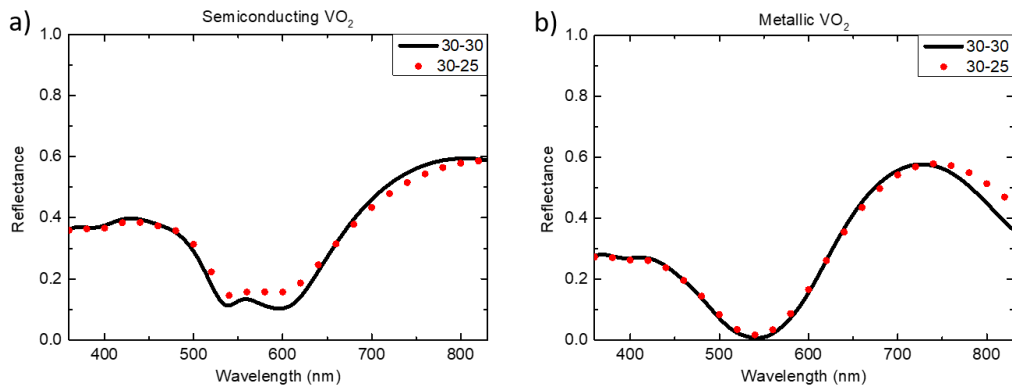


Figure A.5: Reflectance spectra with for VO₂ thickness of 30 nm, and Au disc thickness of 30 nm and 25 nm. These spectra are for VO₂ in the (a) Semiconducting and (b) Metallic phases. The line for each spectrum is not shown in the sRGB colour, as the significant overlap leads to similar colours that are difficult to distinguish.

The reflectance spectra in Figure A.5 do not include sRGB colour values as the spectra significantly overlap across the visible, making them hard to distinguish. The spectra illustrate that the encapsulation of the disc has a negligible impact on the response of the structure, indicating that encapsulation does not lead to an observable impact on the colour change performance of the structure.

A.3 Polarisation dependency

The nanoparticle-VO₂ structures investigated in Section 7.1.3 and 7.1.5 of Chapter 7 have considered arrays of nanoparticles of varying shape in place of discs. In the case of the triangle and star shaped particles, there is a significant difference length of the particle when rotated 90°. This has the potential to introduce polarisation dependencies in the structure, which is considered here.

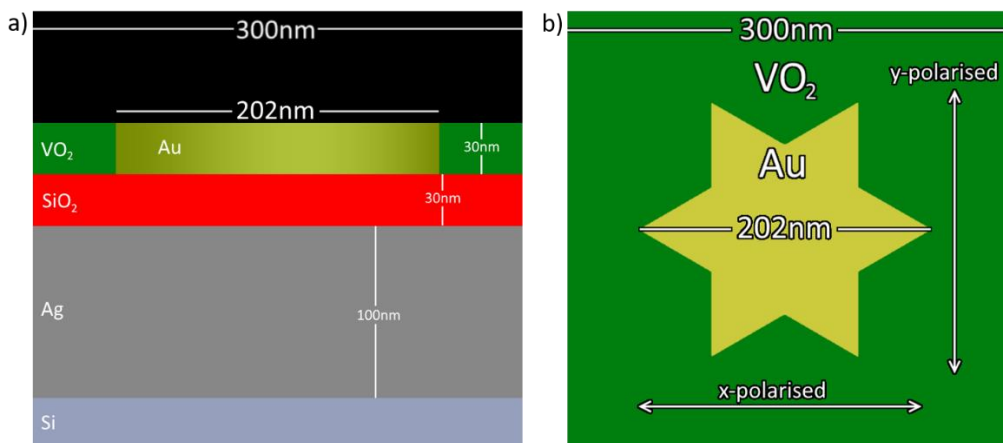


Figure A.6: (a) Schematic profile view of the nanostructure on Si substrate, with Ag thickness of 100 nm, VO₂, SiO₂, and Au disc thicknesses of 30 nm. (b) Top-down

schematic of the structure unit cell, with 150 nm diameter Au disc and 300 nm pitch.

Indication of x and y polarisation axes is also included.

Figure A.6 shows the schematic of the structure under consideration. This is the imbedded structure with a star disc shape, as examined in Section 7.1.5 in Chapter 7. Here, x and y polarised light is used in simulation of the structure, to determine the polarisation dependence.

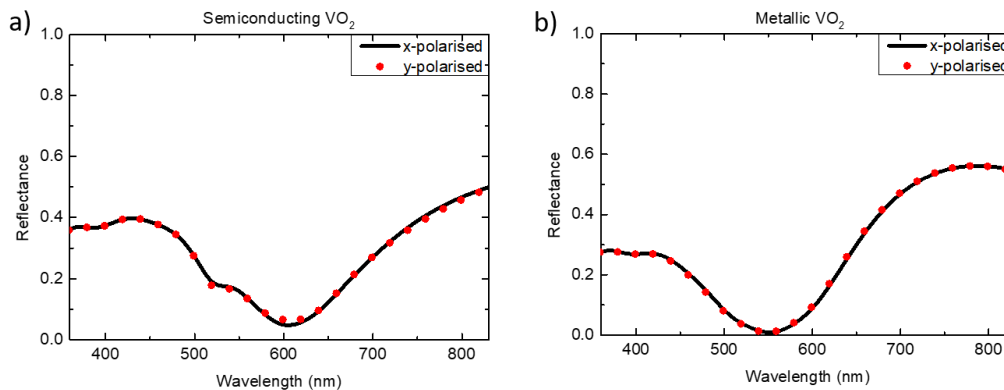


Figure A.7: Reflectance spectra with imbedded Au star structure in x-polarised and y-polarised light, with VO₂ in the (a) Semiconducting and (b) Metallic phases. The line for each spectrum is not shown in the sRGB colour, as the significant overlap leads to colours of similar chromaticity that are difficult to distinguish.

The reflectance spectra from the polarisation simulations are revealed in Figure A.7. These spectra show a significant overlap for both polarisations over the visible region, and indicate that the structure does not exhibit a strong polarisation dependence with the imbedded star structure.

A.4 Array pitch

As with the structure considered in Chapter 4 and 5, the influence of inter-disc interaction was examined, by varying the array pitch with a fixed disc diameter of 150 nm. This was considered with the imbedded disc structure, to determine the influence of the highly absorbing VO₂ layer. The structure is shown in Figure A.8.

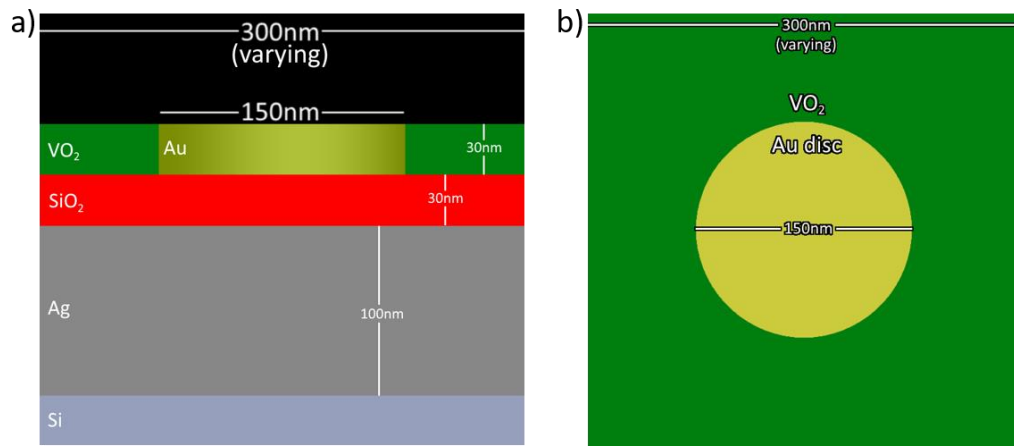


Figure A.8: (a) Schematic profile view of the nanostructure on Si substrate, with Ag thickness of 100 nm, VO₂, SiO₂, and Au disc thicknesses of 30 nm. (b) Top-down schematic of the structure unit cell, with 150 nm diameter Au disc and 300 nm pitch.

The structure consisted of a 100 nm Ag layer on an Si substrate, with a SiO₂, VO₂, and Au disc thickness of 30 nm. The discs were imbedded in the VO₂ layer, and had a fixed diameter of 150 nm, as the gap between discs was varied from 0-300 nm in 50 nm steps.

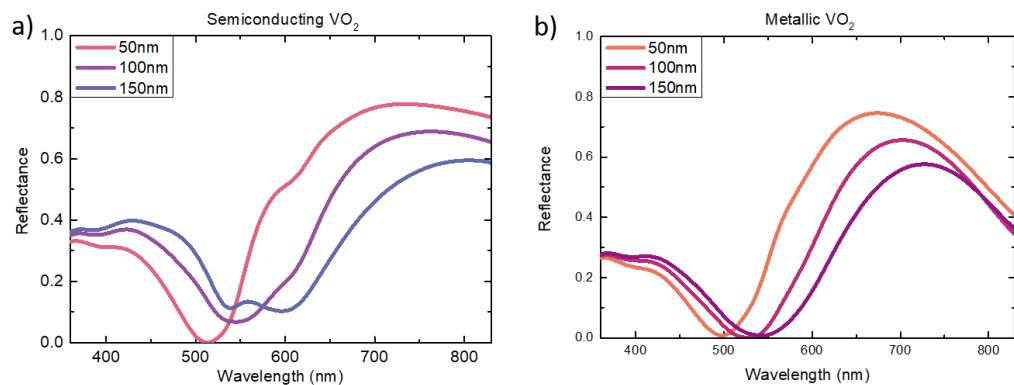


Figure A.9: Reflectance spectra of the imbedded Au disc structure with fixed diameter of 150 nm and varying disc gap of 50 nm, 100 nm, and 150 nm, with VO₂ in the (a) Semiconducting and (b) Metallic phases. The line for each spectrum is shown in the sRGB colour.

Reflectance spectra are revealed in Figure A.9 (a) for structures with gaps of 50 nm, 100 nm, and 150 nm. A red-shift in the dip position is observed as the gap is increased, as well as a decrease in the peak reflectance at long wavelengths. This is attributed to the decrease in the fill factor of the Au disc in the unit cell as the gap is increased. This is further demonstrated in the CIE plot Figure A.10.

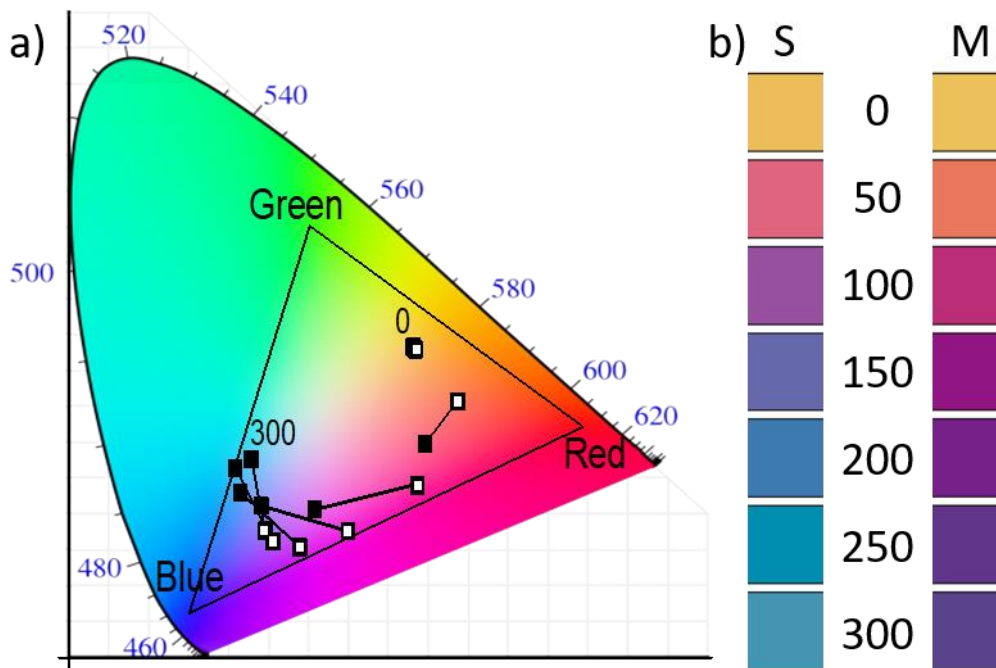


Figure A.10: (a) CIE plot from the spectra of the imbedded Au disc structure with varying disc gap of 0-250 nm, with VO₂ in the (black dot) Semiconducting and (white dot) Metallic phases. (b) sRGB colour swatches of both phases.

Figure A.10 shows the CIE plot of the structure with a fixed diameter of 150 nm and gap of 0-300 nm in 50 nm steps. Also included are the colour swatches for both phases of VO₂. The discs are in direct contact in the 0 nm case, resulting in a large fill factor of Au in the unit cell, and a reflectance that closely resembles a planar Au film. As the separation is increased, the fill factor reduces, and trends towards the response of the thin film observed in Figure 6.11 (b). There is no evidence of spectra features that are sensitive to the gap variation, that would be indicative of inter-disc interaction.

Appendix B

Sample recipes

Here, sample recipes for the preparation of the Aluminium structure in Chapter 4, and the hybrid Au-Ag structure in Chapter 5 are described.

B.1 Aluminium nanostructure sample preparation

- 10x12 mm SiO₂ substrates were cut from a 1 mm thick microscope slide.
- Substrates were cleaned in solutions of Acetone, Methanol and Isopropyl Alcohol (IPA), respectively, for 20 minutes each.
- Substrates were dried with a nitrogen gun.
- ma-N 2401 was spin coated for 60 seconds at 3000 rpm.
- Substrates were placed on a hotplate at 90°C for 60 seconds.
- E-Spacer was deposited by spin coating for 60 seconds at 3000rpm.
- Nanodisc arrays were patterned using Elionix 7700 TFE-SEM.
- An accelerating voltage of 15 kV was used at a working distance of 5 mm, with a beam current of 50.9 pA and aperture of 10 μm delivering an area dose of 140 μC/cm² over an array area of 50 μm.
- E-Spacer was removed by rinsing in de-ionised water for 10 seconds.
- Patterns were developed by submerging the sample in ma-D 525 developer for 10 seconds.
- Samples were rinsed with deionised water for 60 seconds, then IPA for 10 seconds, before an air gun was used to remove the IPA.
- Thin film Al was deposited on the substrates using a Temescal FC-2000 EB-PVD, with a 20nm layer at a deposition rate of 0.5 Å/s.

B.2 Hybrid nanostructure sample preparation

- 10x12 mm Si substrates were cut from were cut from plane (100) 10 cm diameter wafers.
- Substrates were cleaned in solutions of Acetone, Methanol and Isopropyl Alcohol (IPA), respectively, for 20 minutes each.
- Substrates were dried with a nitrogen gun.
- Thin film Ag was deposited on the substrates using a Temescal FC-2000 EB-PVD, with a 100nm layer at a deposition rate of 0.5 Å/s.
- Tafmer polymer deposited using a simple spin coating process at 3000 rpm for 30 seconds.
- PMMA was spin coated 3000 rpm for 60 seconds.
- Substrates were placed on a hotplate at 180°C for 120 seconds.
- E-Spacer was deposited by spin coating for 60 seconds at 3000rpm.
- Nanodisc arrays were patterned using Carl Zeiss Supra FE-SEM.
- An accelerating voltage of 15 kV was used at a working distance of 5 mm, with a beam current of 35.6 pA and aperture of 10 μm delivering an area dose of 250 μC/cm² over an array area of 100μm.
- E-Spacer was removed by rinsing in de-ionised water for 10 seconds.
- Patterns were developed by submerging the sample in a 1:3 solution of Methyl Isobutyl Ketone (MIBK) to IPA for 45 seconds.
- Samples were immediately submerging IPA for 10 seconds to stop development, then IPA for 10 seconds, before an air gun was used to remove the IPA.
- 100nm thick Au layer was deposited by EB-PVD, at a deposition rate of 0.5 Å/s.
- Lift-off was carried out by submersion of the samples in Acetone solution heated to approximately 40°C on a hot plate for 10 minutes
- Samples were rinsed in IPA to stop lift-off process.

Appendix C

Colour data

Here, colour data pertaining to all spectra presented within the thesis is tabulated, where applicable. This includes the CIE xyY, sRGB values, and sRGB colour swatches. Also included is an example calculation, converting XYZ to xyY, and XYZ to sRGB. These are the transforms described in Section 3.1.5 of Chapter 3. First, an example XYZ value of **30 50 10** is presented. This is a typical output of the integrating functions in Equations 3.24a-c. These are divided by 100, and the matrix transform for XYZ to RGB is applied:

$$R_{linear} = (0.3 \times 3.2405) + (0.5 \times -1.5371) + (0.1 \times -0.4985) = 0.15375$$

$$G_{linear} = (0.3 \times -0.9693) + (0.5 \times 1.8706) + (0.1 \times -0.0416) = 0.64035$$

$$B_{linear} = (0.3 \times 0.0556) + (0.5 \times -0.2040) + (0.1 \times 1.0572) = 0.02040$$

These values are examined, to determine if they fall below the threshold value of 0.0031308. In this case, none fall below the threshold, so the higher gamma correction value is applied to all three, to make the values non-linear.

$$R_{sRGB} = (1.055 \times (0.15375^{\frac{1}{2.4}})) - 0.055 = 0.428532$$

$$G_{sRGB} = (1.055 \times (0.64035^{\frac{1}{2.4}})) - 0.055 = 0.821179$$

$$B_{sRGB} = (1.055 \times (0.02040^{\frac{1}{2.4}})) - 0.055 = 0.153416$$

These values are then multiplied by 255 and rounded, to form the 8-bit sRGB values.


The CIE xyY values are calculated by:

$$x = \frac{X}{X + Y + Z} = \frac{30}{30 + 50 + 10} = 0.3333$$

$$y = \frac{50}{30 + 50 + 10} = 0.5555$$

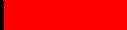



$$Y = 50$$

The XYZ, sRGB, and xyY values are presented below, along with a colour swatch:

X	Y	Z	R	G	B	x	y	Y	Colour
30	50	10	109	209	39	0.3333	0.5555	50	

Below is the tabulated CIE xyY, sRGB values and sRGB swatches for spectra shown throughout the thesis; listed in the order they appear, segmented by Chapter, and labelled by Figure in which the spectra are presented.

First, the values for the maximum of R, G, and B, as well as white sRGB values is shown:

	R	G	B	x	y	Y	Colour
Red	255	0	0	0.6401	0.3300	21.26	
Green	0	255	0	0.3000	0.6000	71.52	
Blue	0	0	255	0.1500	0.0600	7.22	
White	255	255	255	0.3127	0.3290	100.00	

Chapter 4

Figure 4.3 (a): Kumar et al.[6] varying diameter with a fixed gap.











Diameter (nm)	R	G	B	x	y	Y	Colour
50	228	214	204	0.3301	0.3400	68.95	
60	204	167	149	0.3645	0.3521	42.64	
70	163	103	114	0.3831	0.3116	18.70	
80	113	44	108	0.3288	0.2018	6.39	
90	52	43	116	0.2081	0.1425	3.72	
100	40	54	119	0.1976	0.1581	4.42	
110	44	93	108	0.2341	0.2888	9.45	
120	67	122	101	0.2737	0.3779	16.05	
130	73	100	84	0.2954	0.3705	11.17	
140	127	158	127	0.3103	0.3814	30.50	

Figure 4.3 (c): FDTD simulation validation, varying diameter with a fixed gap.











Diameter (nm)	R	G	B	x	y	Y	Colour
50	214	166	123	0.3991	0.3818	43.00	
60	211	131	116	0.4235	0.3481	31.34	
70	196	72	127	0.4201	0.2601	17.90	
80	176	75	136	0.3768	0.2431	16.04	
90	137	109	141	0.3102	0.2738	18.18	
100	113	137	144	0.2809	0.3164	23.42	
110	136	159	144	0.3040	0.3531	32.04	
120	152	172	143	0.3188	0.3725	38.16	
130	187	181	141	0.3510	0.3822	45.54	
140	199	188	140	0.3607	0.3897	50.00	

Figure 4.6 (b): Disc component, varying diameter with fixed pitch of 400 nm.




Diameter (nm)	R	G	B	x	y	Y	Colour
100	43	41	30	0.3512	0.3807	2.19	
150	23	97	66	0.2628	0.4273	9.12	
200	177	137	58	0.4403	0.4356	27.54	

Figure 4.7 (b): Hole component, varying diameter with fixed pitch of 400 nm.

Diameter (nm)	R	G	B	x	y	Y	Colour
0	239	238	236	0.3146	0.3310	85.56	
100	230	207	219	0.3216	0.3161	66.56	
150	214	177	214	0.3147	0.2864	50.60	
200	202	154	205	0.3128	0.2671	40.08	
200 (no pillar)	221	185	206	0.3263	0.3052	54.53	

Figure 4.8 (b): Full structure, varying diameter with fixed pitch of 400 nm.

Diameter (nm)	R	G	B	x	y	Y	Colour
100	223	174	139	0.3892	0.3706	47.82	
150	131	72	173	0.2646	0.1718	12.48	
200	103	184	159	0.2695	0.3687	39.67	

Figure 4.12: Diameter variation, fixed gap of 200 nm.

Diameter (nm)	R	G	B	x	y	Y	Colour
0	239	238	236	0.3146	0.3310	85.56	
25	238	236	234	0.3153	0.3310	84.11	
50	234	231	218	0.3231	0.3426	79.71	
75	232	202	190	0.3455	0.3424	63.11	
100	183	138	138	0.3633	0.3292	30.08	
125	41	126	86	0.2682	0.4285	16.07	
150	56	103	159	0.2108	0.2159	13.04	
175	0	153	185	0.2091	0.2728	26.29	
200	103	184	159	0.2695	0.3687	39.67	
225	172	195	113	0.3543	0.4394	48.99	
250	209	182	160	0.3548	0.3561	49.55	
275	228	147	206	0.3369	0.2630	41.82	
300	217	118	222	0.3131	0.2139	32.98	

Figure 4.13: Diameter variation, fixed pitch of 400 nm.

Diameter (nm)	R	G	B	x	y	Y	Colour
0	239	238	236	0.3146	0.3310	85.56	
25	239	237	235	0.3153	0.3310	84.92	
50	237	235	229	0.3178	0.3352	83.08	
75	234	222	202	0.3349	0.3505	74.00	
100	223	174	139	0.3892	0.3706	47.82	
125	193	83	127	0.4119	0.2714	19.06	
150	131	72	173	0.2646	0.1718	12.48	
175	70	146	178	0.2271	0.2732	25.07	
200	103	184	159	0.2695	0.3687	39.67	
225	153	201	125	0.3286	0.4357	50.03	
250	189	206	89	0.3790	0.4704	55.68	
275	215	200	74	0.4130	0.4654	56.25	
300	234	186	96	0.4267	0.4255	53.45	

Figure 4.14: Gap variation, fixed diameter of 200 nm.

Gap (nm)	R	G	B	x	y	Y	Colour
0	224	217	181	0.3429	0.3693	68.81	
25	209	221	212	0.3101	0.3391	70.02	
50	192	208	199	0.3070	0.3398	60.44	
75	174	190	189	0.3006	0.3303	49.50	
100	147	171	190	0.2776	0.3020	39.05	
125	97	163	191	0.2405	0.2850	32.50	
150	0	175	186	0.2196	0.3104	34.21	
175	0	185	177	0.2283	0.3420	37.87	
200	103	184	159	0.2695	0.3687	39.67	
225	129	180	141	0.3000	0.3900	39.23	
250	140	174	176	0.2825	0.3260	38.98	
275	149	169	216	0.2611	0.2661	39.72	
300	152	169	230	0.2545	0.2505	40.76	

Figure 4.15: Pillar height, fixed diameter of 200 nm and fixed pitch of 400 nm.

Pillar height (nm)	R	G	B	x	y	Y	Colour
0	239	238	236	0.3146	0.3310	85.56	
20	235	236	233	0.3139	0.3321	83.54	
40	210	232	220	0.3054	0.3422	76.58	
60	168	219	196	0.2922	0.3576	62.97	
80	126	201	174	0.2771	0.3677	49.26	
100	103	184	159	0.2695	0.3687	39.67	
120	111	168	160	0.2712	0.3419	33.92	
140	131	151	177	0.2716	0.2886	30.13	
160	153	125	196	0.2732	0.2283	25.43	
180	170	94	207	0.2785	0.1842	21.06	
200	180	94	209	0.2874	0.1868	22.31	

Figure 4.20: FDTD simulation vs fabricated sample.

	R	G	B	x	y	Y	Colour
Simulation	129	181	156	0.2891	0.3673	40.12	
Sample	129	171	148	0.2946	0.3655	35.93	

Figure 4.22 (b): Diffraction spectra of Al sample.

Angle (°)	R	G	B	x	y	Y	Colour
20	0	0	15	0.1500	0.0600	0.03	
24	0	10	46	0.1649	0.1135	0.41	
28	0	20	45	0.1814	0.1728	0.69	
32	0	40	33	0.2370	0.3733	1.63	
36	0	73	44	0.2586	0.4509	4.95	
40	0	82	29	0.2808	0.5308	6.12	
44	49	72	0	0.3694	0.5449	5.29	
48	76	52	0	0.4810	0.4563	3.99	
52	80	23	0	0.5840	0.3745	2.32	
56	70	0	0	0.6401	0.3300	1.30	
60	49	0	0	0.6401	0.3300	0.65	
64	29	0	0	0.6401	0.3300	0.26	
68	14	0	0	0.6401	0.3300	0.09	
72	5	0	0	0.6401	0.3300	0.03	
76	2	0	0	0.6401	0.3300	0.01	
80	1	0	0	0.6401	0.3300	0.01	

Chapter 5

Figure 5.3 (b): Disc component, varying diameter with fixed pitch of 300 nm.

Diameter (nm)	R	G	B	x	y	Y	Colour
100	68	75	30	0.3755	0.4648	6.35	
150	166	144	61	0.4185	0.4476	28.39	
200	226	1733	86	0.3014	0.5982	6391.30	

Figure 5.4 (b): Disc & polymer component, varying polymer thickness.

Thickness (nm)	R	G	B	x	y	Y	Colour
100	187	82	24	0.5484	0.3860	16.67	
2000	192	74	34	0.5556	0.3682	16.22	

Figure 5.6 (b): Hole component, varying diameter with fixed pitch of 300 nm.

Diameter (nm)	R	G	B	x	y	Y	Colour
0	222	222	239	0.3018	0.3110	74.00	
100	223	222	239	0.3025	0.3110	74.16	
150	223	222	238	0.3031	0.3120	74.10	
200	224	221	237	0.3044	0.3120	73.67	

Figure 5.7 (b): Full structure, 150 nm diameter with fixed pitch of 300 nm.

Diameter (nm)	R	G	B	x	y	Y	Colour
150	171	185	157	0.3228	0.3674	45.79	

Figure 5.9: Polymer thickness variation (0-300 nm).

Height (nm)	R	G	B	x	y	Y	Colour
0	222	96	71	0.5168	0.3550	24.35	
20	222	93	91	0.4942	0.3317	24.11	
40	194	91	138	0.3930	0.2671	20.79	
60	168	111	176	0.3077	0.2368	22.83	
80	146	158	190	0.2753	0.2828	34.28	
100	171	185	157	0.3228	0.3674	45.79	
120	190	168	109	0.3867	0.4077	40.06	
140	239	135	58	0.5026	0.4017	35.98	
160	225	102	10	0.5541	0.3945	25.53	
180	178	84	39	0.5252	0.3826	15.95	
200	181	60	103	0.4491	0.2726	14.03	
220	191	46	158	0.3673	0.1988	15.50	
240	185	88	171	0.3357	0.2202	20.23	
260	167	141	144	0.3381	0.3246	29.28	
280	167	164	101	0.3721	0.4210	35.71	
300	191	146	64	0.4418	0.4325	32.00	

Figure 5.10: Polymer thickness variation (0-1000 nm).

Polymer thickness (nm)	R	G	B	x	y	Y	Colour
0	222	96	71	0.5168	0.3550	24.35	
25	118	186	172	0.2710	0.3500	41.95	
50	209	117	211	0.3157	0.2203	30.98	
75	205	146	215	0.3072	0.2474	38.44	
100	171	185	157	0.3228	0.3674	45.79	
125	182	161	96	0.3939	0.4185	36.28	
150	247	114	35	0.5448	0.3894	31.93	
175	182	81	28	0.5428	0.3849	15.91	
200	181	60	103	0.4491	0.2726	14.03	
225	161	52	165	0.3141	0.1763	12.75	
250	133	119	161	0.2838	0.2595	20.75	
275	109	167	113	0.3049	0.4233	32.08	
300	191	146	64	0.4418	0.4325	32.00	
325	215	118	64	0.4952	0.3882	27.77	
350	243	72	113	0.4952	0.2916	24.88	
375	198	47	154	0.3832	0.2082	16.37	
400	141	91	147	0.3088	0.2356	15.25	
425	110	138	111	0.3092	0.3807	22.64	
450	116	158	80	0.3386	0.4662	28.75	
475	153	129	94	0.3824	0.3870	23.28	
500	187	97	124	0.4028	0.2917	20.57	
525	226	83	141	0.4298	0.2657	24.28	
550	222	77	132	0.4415	0.2689	22.50	
575	171	111	108	0.3983	0.3339	21.11	
600	118	142	100	0.3282	0.4071	24.12	
625	127	140	113	0.3258	0.3775	24.46	
650	152	106	130	0.3444	0.2893	18.60	
675	173	91	127	0.3820	0.2757	17.90	
700	204	103	110	0.4411	0.3205	23.66	
725	208	113	104	0.4471	0.3406	26.22	
750	192	122	113	0.4113	0.3417	26.32	
775	160	126	121	0.3603	0.3371	23.78	
800	146	104	124	0.3449	0.2947	17.47	
825	146	95	106	0.3747	0.3098	15.34	
850	165	107	101	0.4027	0.3388	19.45	
875	194	121	103	0.4269	0.3536	26.12	
900	203	120	112	0.4264	0.3397	27.30	
925	195	100	120	0.4174	0.3026	22.07	
950	175	74	131	0.3840	0.2481	15.65	
975	154	79	139	0.3396	0.2341	14.33	
1000	159	105	137	0.3445	0.2783	19.28	

Figure 5.11: Diameter variation, fixed pitch of 300 nm.

Diameter (nm)	R	G	B	x	y	Y	Colour
0	247	246	244	0.3146	0.3310	92.22	
25	247	245	243	0.3152	0.3310	91.55	
50	244	235	237	0.3175	0.3270	84.76	
75	234	217	224	0.3203	0.3216	72.50	
100	198	199	204	0.3083	0.3230	57.21	
125	180	189	180	0.3122	0.3407	49.39	
150	171	185	157	0.3228	0.3674	45.79	
175	169	183	137	0.3373	0.3934	44.11	
200	172	178	120	0.3553	0.4105	41.97	
225	165	174	110	0.3581	0.4216	39.40	
250	157	171	109	0.3522	0.4218	37.40	
275	141	177	116	0.3296	0.4236	38.37	
300	200	170	128	0.3788	0.3833	42.59	

Figure 5.12: Diameter variation, fixed gap of 150 nm.

Diameter (nm)	R	G	B	x	y	Y	Colour
0	247	246	244	0.3146	0.3310	92.22	
25	248	243	239	0.3184	0.3330	90.29	
50	251	229	226	0.3300	0.3321	82.04	
75	243	203	208	0.3403	0.3238	66.32	
100	224	183	188	0.3440	0.3233	53.35	
125	204	175	170	0.3432	0.3353	46.40	
150	171	185	157	0.3228	0.3674	45.79	
175	148	209	147	0.3094	0.4148	54.00	
200	174	215	143	0.3306	0.4216	59.58	
225	207	205	145	0.3582	0.4011	58.97	
250	218	191	146	0.3717	0.3824	54.24	
275	201	185	146	0.3585	0.3783	49.19	
300	178	184	158	0.3282	0.3640	46.21	

Figure 5.13: Gap variation, fixed diameter of 150 nm.

Gap (nm)	R	G	B	x	y	Y	Colour
0	198	183	124	0.3746	0.4042	47.33	
25	165	165	90	0.3786	0.4380	35.65	
50	215	141	91	0.4475	0.3887	34.25	
75	229	145	109	0.4404	0.3704	38.01	
100	222	152	127	0.4107	0.3592	39.52	
125	198	162	145	0.3640	0.3514	39.89	
150	171	185	157	0.3228	0.3674	45.79	
175	135	209	167	0.2879	0.3877	53.54	
200	155	220	176	0.2959	0.3863	61.29	
225	191	218	189	0.3125	0.3638	64.89	
250	213	211	201	0.3212	0.3404	64.95	
275	214	208	208	0.3172	0.3290	63.96	
300	197	212	212	0.3018	0.3290	63.71	

Figure 5.15 (a): Gold-Gold disc-backreflector structure.

Polymer thickness (nm)	R	G	B	x	y	Y	Colour
0	219	103	0	0.5511	0.4006	24.76	
20	222	109	0	0.5451	0.4054	26.47	
40	192	118	41	0.4915	0.4178	24.32	
60	161	137	88	0.3937	0.4056	26.17	
80	149	158	108	0.3496	0.4085	31.93	
100	186	161	98	0.3963	0.4145	36.81	
120	210	144	68	0.4600	0.4168	34.07	
140	254	113	14	0.5574	0.3915	32.91	
160	211	91	0	0.5622	0.3918	21.33	
180	175	75	0	0.5609	0.3929	14.15	
200	182	57	56	0.5397	0.3308	13.16	
220	189	61	96	0.4724	0.2861	15.00	
240	185	96	109	0.4237	0.3111	19.78	
260	178	132	92	0.4133	0.3872	26.74	
280	184	140	60	0.4433	0.4332	29.27	
300	203	123	5	0.5097	0.4316	26.87	

Figure 5.15 (b): Silver-silver disc-backreflector structure.

Polymer thickness (nm)	R	G	B	x	y	Y	Colour
0	231	191	178	0.3567	0.3438	57.46	
20	222	197	181	0.3453	0.3475	58.80	
40	145	180	197	0.2723	0.3053	42.69	
60	198	163	189	0.3226	0.2964	41.87	
80	204	156	147	0.3701	0.3407	38.72	
100	248	177	97	0.4447	0.4107	52.26	
120	247	197	77	0.4406	0.4449	60.24	
140	255	177	88	0.4567	0.4154	53.41	
160	205	135	116	0.4146	0.3538	31.57	
180	146	142	128	0.3313	0.3521	27.02	
200	177	147	161	0.3302	0.3094	32.79	
220	207	152	169	0.3519	0.3078	38.59	
240	224	158	109	0.4266	0.3863	41.41	
260	236	161	109	0.4359	0.3866	44.43	
280	234	187	121	0.4078	0.4023	54.41	
300	238	213	121	0.3971	0.4266	67.15	





Figure 5.15 (c): Gold-Aluminium disc-backreflector structure.

Polymer thickness (nm)	R	G	B	x	y	Y	Colour
0	216	90	84	0.5004	0.3361	22.55	
20	206	80	64	0.5270	0.3465	19.23	
40	184	66	66	0.5167	0.3296	14.48	
60	181	57	110	0.4369	0.2598	13.88	
80	184	83	166	0.3416	0.2197	19.13	
100	193	140	179	0.3296	0.2782	33.35	
120	169	173	140	0.3370	0.3761	40.22	
140	219	153	92	0.4408	0.4002	38.62	
160	248	122	47	0.5303	0.3913	34.08	
180	195	97	31	0.5293	0.3966	20.25	
200	173	77	70	0.4866	0.3392	14.63	
220	186	50	130	0.4080	0.2301	14.33	
240	191	55	169	0.3496	0.1942	16.67	
260	179	108	163	0.3359	0.2523	22.95	
280	164	153	128	0.3482	0.3669	32.23	
300	175	158	84	0.3986	0.4328	34.21	

Figure 5.15 (d): Copper-Aluminium disc-backreflector structure.

Polymer thickness	R	G	B	x	y	Y	Colour
0	192	101	44	0.5113	0.3942	20.70	
20	169	78	60	0.4965	0.3545	14.21	
40	129	22	79	0.4387	0.2369	5.81	
60	140	0	119	0.3618	0.1767	6.91	
80	153	26	162	0.3070	0.1551	10.12	
100	178	124	155	0.3417	0.2848	26.25	
120	169	177	99	0.3693	0.4386	40.78	
140	221	179	14	0.4563	0.4724	47.64	
160	239	132	0	0.5275	0.4193	34.85	
180	176	76	6	0.5576	0.3916	14.41	
200	116	39	59	0.4604	0.2894	5.48	
220	121	0	109	0.3465	0.1683	5.17	
240	134	22	143	0.3054	0.1545	7.63	
260	133	89	135	0.3137	0.2471	13.88	
280	129	140	99	0.3423	0.4026	24.32	
300	152	168	46	0.3910	0.4969	34.88	

Figure 5.20: FDTD simulation vs fabricated samples.

	R	G	B	x	y	Y	Colour
Simulation (70 nm)	183	122	178	0.3218	0.2536	27.20	
Sample (70 nm)	89	65	152	0.2312	0.1618	8.17	
Simulation (196 nm)	206	66	72	0.5285	0.3235	17.49	
Sample (196 nm)	151	68	51	0.5007	0.3555	10.95	

Chapter 6

Figure 6.3: AIST structure, varying bottom ITO contact thickness.







Amorphous AIST	R	G	B	x	y	Y	Colour
10-7-70	107	143	177	0.2505	0.2728	25.95	
10-7-110	170	193	168	0.3128	0.3625	49.51	
10-7-160	195	125	120	0.4042	0.3361	27.63	
Crystalline AIST							
10-7-70	104	98	144	0.2649	0.2401	13.69	
10-7-110	125	181	189	0.2638	0.3172	41.08	
10-7-160	203	170	83	0.4191	0.4346	42.07	

Figure 6.5: GST structure, varying bottom ITO contact thickness.







Amorphous AIST	R	G	B	x	y	Y	Colour
10-7-70	96	135	179	0.2385	0.2545	23.07	
10-7-120	193	213	152	0.3397	0.4040	61.19	
10-7-180	182	63	156	0.3559	0.2090	15.90	
Crystalline AIST							
10-7-70	99	92	147	0.2547	0.2221	12.41	
10-7-120	154	208	184	0.2898	0.3608	55.44	
10-7-180	208	125	111	0.4301	0.3470	29.22	

Figure 6.8: Simple VO₂ structure, varying VO₂ thickness.







Semiconducting VO ₂	R	G	B	x	y	Y	Colour
10-10	250	235	128	0.3914	0.4357	81.30	
10-20	243	173	0	0.4826	0.4550	48.94	
10-30	191	113	124	0.4004	0.3141	24.34	
Metallic VO ₂							
10-10	249	233	151	0.3776	0.4128	80.65	
10-20	241	180	0	0.4735	0.4622	51.34	
10-30	208	100	59	0.5133	0.3739	22.84	

Figure 6.10: ITO-VO₂-ITO-Ag structure, fixed VO₂ thickness.

Semiconducting VO ₂	R	G	B	x	y	Y	Colour
10-30-40	169	206	207	0.2853	0.3277	57.08	
10-30-35	158	199	201	0.2810	0.3263	52.33	
10-30-30	146	190	195	0.2756	0.3221	46.88	
10-30-25	134	180	188	0.2704	0.3174	41.34	
10-30-20	126	167	181	0.2673	0.3076	35.41	
10-30-15	127	153	172	0.2724	0.2989	30.27	
10-30-10	139	136	161	0.2913	0.2889	25.67	
10-30-5	163	120	146	0.3352	0.2891	23.29	
10-30-0	191	113	124	0.4004	0.3141	24.34	
Metallic VO ₂							
10-30-40	103	165	191	0.2447	0.2886	33.56	
10-30-35	93	152	181	0.2406	0.2810	28.12	
10-30-30	89	137	172	0.2388	0.2677	22.99	
10-30-25	96	121	161	0.2472	0.2559	18.73	
10-30-20	112	103	149	0.2702	0.2440	15.32	
10-30-15	134	85	134	0.3168	0.2421	13.29	
10-30-10	160	73	116	0.3882	0.2616	13.50	
10-30-5	185	78	93	0.4617	0.3094	16.55	
10-30-0	208	100	59	0.5133	0.3739	22.84	

Figure 6.12: ITO-VO₂-ITO-Ag structure, fixed stack thickness.

Semiconducting VO ₂	R	G	B	x	y	Y	Colour
10-10-45	195	205	208	0.3031	0.3254	59.82	
10-20-35	158	187	194	0.2847	0.3195	46.70	
10-30-25	134	180	188	0.2704	0.3174	41.34	
10-40-15	121	177	183	0.2642	0.3199	38.93	
10-50-5	114	175	175	0.2643	0.3289	37.33	
Metallic VO ₂							
10-10-45	182	182	197	0.3011	0.3099	47.43	
10-20-35	133	142	171	0.2771	0.2830	27.27	
10-30-25	96	121	161	0.2472	0.2559	18.73	
10-40-15	67	110	155	0.2240	0.2387	14.71	
10-50-5	46	104	149	0.2113	0.2325	12.65	

Figure 6.14: ITO-VO₂-ITO-Ag structure, fixed ITO thickness.

Semiconducting VO ₂	R	G	B	x	y	Y	Colour
10-10-25	233	179	143	0.3926	0.3701	51.55	
10-20-25	159	162	172	0.3013	0.3146	36.19	
10-30-25	134	180	188	0.2704	0.3174	41.34	
10-40-25	149	195	192	0.2802	0.3330	49.23	
10-50-25	168	204	182	0.3009	0.3576	54.89	
Metallic VO ₂							
10-10-25	223	164	114	0.4172	0.3878	43.45	
10-20-25	160	113	138	0.3427	0.2896	21.12	
10-30-25	96	121	161	0.2472	0.2559	18.73	
10-40-25	58	141	171	0.2231	0.2742	22.89	
10-50-25	67	157	170	0.2346	0.3061	28.21	

Figure 6.16: ITO top contact.

Semiconducting VO ₂	R	G	B	x	y	Y	Colour
0-30-35	136	187	202	0.2640	0.3081	45.04	
10-30-25	134	180	188	0.2704	0.3174	41.34	
Metallic VO ₂							
0-30-35	73	129	180	0.2206	0.2391	20.41	
10-30-25	96	121	161	0.2472	0.2559	18.73	

Chapter 7

Figure 7.3: Hybrid structure with VO₂.

	R	G	B	x	y	Y	Colour
Semiconducting	140	179	150	0.3023	0.3729	40.02	
Metallic	62	168	152	0.2473	0.3574	31.30	

Figure 7.8: Varying disc diameter on VO₂.

Semiconducting VO ₂	R	G	B	x	y	Y	Colour
50	115	174	178	0.2628	0.3227	37.13	
100	97	160	140	0.2740	0.3644	29.58	
150	109	161	89	0.3241	0.4578	29.46	
200	143	180	55	0.3695	0.5053	38.76	
250	178	198	79	0.3792	0.4783	50.42	
Metallic VO ₂							
50	85	99	141	0.2466	0.2421	12.78	
100	28	106	111	0.2295	0.3158	11.70	
150	28	134	76	0.2723	0.4706	17.82	
200	94	166	67	0.3242	0.5059	30.06	
250	160	189	91	0.3606	0.4653	44.62	

Figure 7.10: Particle shapes in free space.

Particle shapes in free space	R	G	B	x	y	Y	Colour
Disc	202	99	22	0.5374	0.3997	21.54	
Box	188	143	58	0.4460	0.4363	30.64	
Hexagon	165	143	61	0.4182	0.4470	27.98	
Star	200	116	56	0.4902	0.3990	25.06	
Triangle	200	102	55	0.5076	0.3826	22.06	

Figure 7.11: Particle shapes on VO₂.

Semiconducting VO ₂	R	G	B	x	y	Y	Colour
Disc	109	161	89	0.3241	0.4578	29.46	
Box	118	171	92	0.3279	0.4617	33.75	
Hexagon	108	163	92	0.3205	0.4555	30.16	
Star	133	179	102	0.3323	0.4501	38.19	
Triangle	127	173	104	0.3269	0.4417	35.40	
Metallic VO ₂							
Disc	28	134	76	0.2723	0.4706	17.82	
Box	60	138	80	0.2893	0.4600	19.72	
Hexagon	24	134	78	0.2692	0.4662	17.79	
Star	88	130	92	0.3045	0.4110	18.81	
Triangle	79	120	94	0.2925	0.3889	15.90	

Figure 7.17: Thin discs in free space, fixed pitch of 300 nm.

30 nm thick discs	R	G	B	x	y	Y	Colour
100	80	67	0	0.4482	0.4823	5.72	
150	202	99	22	0.5374	0.3997	21.54	
200	229	117	61	0.5112	0.3844	29.72	

Figure 7.19: Varying disc diameter imbedded in VO₂.

Semiconducting VO ₂	R	G	B	x	y	Y	Colour
50	65	164	185	0.2284	0.2940	31.18	
100	91	143	179	0.2377	0.2681	25.12	
150	101	105	171	0.2394	0.2130	15.81	
200	106	17	156	0.2431	0.1174	5.87	
250	169	112	122	0.3759	0.3138	21.43	
Metallic VO ₂							
50	68	84	146	0.2198	0.1973	9.64	
100	118	62	139	0.2858	0.1890	9.16	
150	145	21	130	0.3473	0.1776	8.17	
200	160	20	116	0.4023	0.2075	9.23	
250	178	128	95	0.4128	0.3774	25.73	

Figure 7.22: Particle shapes imbedded in VO₂.

Semiconducting VO ₂	R	G	B	x	y	Y	Colour
Disc	101	105	171	0.2394	0.2130	15.81	
Box	70	99	171	0.2114	0.1941	13.17	
Hexagon	100	105	171	0.2385	0.2127	15.75	
Star	43	110	170	0.2018	0.2126	14.57	
Triangle	37	106	170	0.1974	0.2038	13.60	
Metallic VO ₂							
Disc	145	21	130	0.3473	0.1776	8.17	
Box	132	12	130	0.3244	0.1608	6.78	
Hexagon	144	22	130	0.3455	0.1772	8.11	
Star	120	25	131	0.3005	0.1560	6.33	
Triangle	116	24	131	0.2932	0.1514	6.00	

Appendix A simulations

Figure A.2: Thin discs on VO₂, fixed pitch of 300 nm.

Semiconducting VO ₂	R	G	B	x	y	Y	Colour
50	112	175	187	0.2553	0.3107	37.69	
100	72	170	187	0.2325	0.3013	33.72	
150	41	161	188	0.2177	0.2834	29.59	
200	0	150	190	0.2055	0.2597	25.53	
250	0	128	193	0.1929	0.2146	19.29	
Metallic VO ₂							
50	81	96	149	0.2347	0.2217	12.28	
100	27	86	151	0.1910	0.1861	9.12	
150	71	75	154	0.2133	0.1696	8.70	
200	102	64	158	0.2416	0.1605	8.96	
250	141	70	164	0.2875	0.1841	12.72	

Figure A.5: Encapsulated discs.

Semiconducting VO ₂ -Au	R	G	B	x	y	Y	Colour
30-30	101	105	171	0.2394	0.2130	15.81	
30-25	115	117	169	0.2575	0.2404	19.23	
Metallic VO ₂ -Au							
30-30	145	21	130	0.3473	0.1776	8.17	
30-25	146	39	129	0.3493	0.1932	9.15	

Figure A.7: Star polarisation.

Semiconducting VO ₂	R	G	B	x	y	Y	Colour
x-polarised	43	110	170	0.2018	0.2126	14.57	Blue
y-polarised	56	109	170	0.2076	0.2123	14.68	
Metallic VO ₂							
x-polarised	120	25	131	0.3005	0.1560	6.33	Purple
y-polarised	117	27	132	0.2934	0.1538	6.23	

Figure A.9: Varying gap, fixed diameter of 150 nm.

Semiconducting VO ₂	R	G	B	x	y	Y	Colour
0	237	189	90	0.4310	0.4324	55.14	Yellow
50	225	100	126	0.4434	0.2998	26.63	Pink
100	150	80	159	0.3060	0.2076	14.72	Purple
150	101	105	171	0.2394	0.2130	15.81	Blue
200	61	122	175	0.2137	0.2315	18.01	Blue
250	0	142	176	0.2073	0.2661	22.48	Blue
300	67	149	178	0.2268	0.2785	25.90	Blue
Metallic VO ₂							
0	237	193	90	0.4281	0.4361	56.88	Yellow
50	233	119	91	0.4834	0.3591	31.27	Orange
100	187	45	118	0.4338	0.2415	13.75	Pink
150	145	21	130	0.3473	0.1776	8.17	Purple
200	117	33	136	0.2873	0.1550	6.65	Purple
250	97	53	138	0.2537	0.1628	6.92	Purple
300	90	66	140	0.2442	0.1784	7.96	Purple

References

- [1] V. K. Zworykin, "Television system," US1691324A, 1928.
- [2] P. Kordt, J. J. M. van der Holst, M. Al Helwi, W. Kowalsky, F. May, A. Badinski, C. Lennartz, and D. Andrienko, "Modeling of organic light emitting diodes: From molecular to device properties," *Adv. Funct. Mater.*, vol. 25, no. 13, pp. 1955–1971, 2015.
- [3] G. E. Blomgren, "The development and future of lithium ion batteries," *J. Electrochem. Soc.*, vol. 164, no. 1, pp. A5019–A5025, 2017.
- [4] S. Guddala, R. Kumar, and S. A. Ramakrishna, "Thermally induced nonlinear optical absorption in metamaterial perfect absorbers," *Appl. Phys. Lett.*, vol. 106, no. 11, pp. 10–15, 2015.
- [5] A. Kristensen, J. K. W. Yang, S. I. Bozhevolnyi, S. Link, P. Nordlander, N. J. Halas, and N. A. Mortensen, "Plasmonic colour generation," *Nat. Rev. Mater.*, vol. 2, p. 16088, 2016.
- [6] K. Kumar, H. Duan, R. S. Hegde, S. C. W. Koh, J. N. Wei, and J. K. W. Yang, "Printing colour at the optical diffraction limit," *Nat. Nanotechnol.*, vol. 7, no. 9, pp. 557–561, 2012.
- [7] Y. Gu, L. Zhang, J. K. W. Yang, S. P. Yeo, and C.-W. Qiu, "Color generation via subwavelength plasmonic nanostructures," *Nanoscale*, vol. 7, no. 15, pp. 6409–6419, 2015.
- [8] J. E. Bjorkholm, "EUV Lithography – The successor to optical lithography?," *Intel Technol. J.*, pp. 1–8, 1998.
- [9] D. Xia, Z. Ku, S. C. Lee, and S. R. J. Brueck, "Nanostructures and functional materials fabricated by interferometric lithography," *Adv. Mater.*, vol. 23, no. 2, pp. 147–179, 2011.
- [10] M. Ye, L. Sun, X. Hu, B. Shi, B. Zeng, L. Wang, J. Zhao, S. Yang, R. Tai, H.-J.

- Fecht, J.-Z. Jiang, and D.-X. Zhang, "Angle-insensitive plasmonic color filters with randomly distributed silver nanodisks," *Opt. Lett.*, vol. 40, no. 21, p. 4979, 2015.
- [11] S. J. Tan, L. Zhang, D. Zhu, X. M. Goh, Y. M. Wang, K. Kumar, C. W. Qiu, and J. K. W. Yang, "Plasmonic color palettes for photorealistic printing with aluminum nanostructures," *Nano Lett.*, vol. 14, no. 7, pp. 4023–4029, 2014.
- [12] J. Olson, A. Manjavacas, L. Liu, W.-S. Chang, B. Foerster, N. S. King, M. W. Knight, P. Nordlander, N. J. Halas, and S. Link, "Vivid, full-color aluminum plasmonic pixels," *Proc. Natl. Acad. Sci. U. S. A.*, vol. 111, no. 40, pp. 14348–53, 2014.
- [13] M. Kahraman, P. Daggumati, O. Kurtulus, E. Seker, and S. Wachsmann-Hogiu, "Fabrication and characterization of flexible and tunable plasmonic nanostructures," *Sci. Rep.*, vol. 3, no. 1, p. 3396, 2013.
- [14] S. Olcum, A. Kocabas, G. Ertas, A. Atalar, and A. Aydinli, "Tunable surface plasmon resonance on an elastomeric substrate.," *Opt. Express*, vol. 17, no. 10, pp. 8542–8547, 2009.
- [15] F. Huang and J. J. Baumberg, "Actively tuned plasmons on elastomerically driven Au nanoparticle dimers," *Nano Lett.*, vol. 10, no. 5, pp. 1787–1792, 2010.
- [16] T. Cao, C. Wei, R. E. Simpson, L. Zhang, and M. J. Cryan, "Broadband polarization-independent perfect absorber using a phase-change metamaterial at visible frequencies," *Sci. Rep.*, vol. 4, no. 1, p. 3955, 2015.
- [17] P. Cormier, T. V. Son, J. Thibodeau, A. Doucet, V.-V. Truong, and A. Haché, "Vanadium dioxide as a material to control light polarization in the visible and near infrared," *Opt. Commun.*, vol. 382, pp. 80–85, Jan. 2017.
- [18] M. Rudé, V. Mkhitarian, A. E. Cetin, T. A. Miller, A. Carrilero, S. Wall, F. J. G. de Abajo, H. Altug, and V. Pruneri, "Ultrafast and broadband tuning of resonant optical nanostructures using phase-change materials," *Adv. Opt. Mater.*, vol. 4, no. 7, pp. 1060–1066, 2016.

- [19] P. Markov, R. E. Marvel, H. J. Conley, K. J. Miller, R. F. Haglund, and S. M. Weiss, "Optically Monitored Electrical Switching in VO₂," *ACS Photonics*, vol. 2, no. 8, pp. 1175–1182, 2015.
- [20] A. S. Roberts, A. Pors, O. Albrektsen, and S. I. Bozhevolnyi, "Subwavelength plasmonic color printing protected for ambient use," *Nano Lett.*, vol. 14, no. 2, pp. 783–787, 2014.
- [21] G. Zheng, H. Mühlenbernd, M. Kenney, G. Li, T. Zentgraf, and S. Zhang, "Metasurface holograms reaching 80% efficiency," *Nat. Nanotechnol.*, vol. 10, no. 4, pp. 308–312, 2015.
- [22] P. Genevet and F. Capasso, "Holographic optical metasurfaces: A review of current progress," *Reports Prog. Phys.*, vol. 78, no. 2, p. 024401, 2015.
- [23] J. R. Fan and W. G. Wu, "Metal-dielectric-metal plasmonic nanohelms as broad-color-gamut tunable pixels for vivid display," in *MEMS January 2016, Shanghai, China*, pp. 226–229.
- [24] S. M. Wells, A. Polemi, N. V. Lavrik, K. L. Shuford, and M. J. Sepaniak, "Efficient disc on pillar substrates for surface enhanced Raman spectroscopy," *Chem. Commun.*, vol. 47, no. 13, p. 3814, 2011.
- [25] A. F. Smith and S. E. Skrabalak, "Metal nanomaterials for optical anti-counterfeit labels," *J. Mater. Chem. C*, vol. 5, no. 13, pp. 3207–3215, 2017.
- [26] M. A. Kats, R. Blanchard, P. Genevet, and F. Capasso, "Nanometre optical coatings based on strong interference effects in highly absorbing media," *Nat. Mater.*, vol. 12, no. 1, pp. 20–24, 2012.
- [27] M. A. Kats and F. Capasso, "Optical absorbers based on strong interference in ultra-thin films," *Laser Photonics Rev.*, vol. 10, no. 5, pp. 735–749, 2016.
- [28] C. J. R. Sheppard, "Approximate calculation of the reflection coefficient from a stratified medium," *Pure Appl. Opt. J. Eur. Opt. Soc. Part A*, vol. 4, no. 5, pp. 665–669, 1995.

- [29] H. Sugawara, K. Itaya, and G. Hatakoshi, "Characteristics of a distributed Bragg reflector for the visible-light spectral region using InGaAlP and GaAs: Comparison of transparent- and loss-type structures," *J. Appl. Phys.*, vol. 74, p. 3189, 1993.
- [30] K. a Diest, J. a. Dionne, and M. Spain, "Tunable color filters based on metal-insulator-metal resonators," *Nano Lett.*, vol. 9, no. 7, pp. 2579–2583, 2009.
- [31] C. F. Bohren and D. R. Huffman, *Absorption and Scattering of Light by Small Particles*. 1998.
- [32] A. B. Evlyukhin, S. I. Bozhevolnyi, A. L. Stepanov, R. Kiyon, C. Reinhardt, S. Passinger, and B. N. Chichkov, "Focusing and directing of surface plasmon polaritons by curved chains of nanoparticles.," *Opt. Express*, vol. 15, no. 25, pp. 16667–80, 2007.
- [33] M. D. McMahon, R. Lopez, H. M. Meyer, L. C. Feldman, and R. F. Haglund, "Rapid tarnishing of silver nanoparticles in ambient laboratory air," *Appl. Phys. B Lasers Opt.*, vol. 80, no. 7, pp. 915–921, 2005.
- [34] N. Liu, M. Mesch, T. Weiss, M. Hentschel, and H. Giessen, "Infrared perfect absorber and its application as plasmonic sensor," *Nano Lett.*, vol. 10, no. 7, pp. 2342–2348, 2010.
- [35] Y. Chu and K. B. Crozier, "Experimental study of the interaction between localized and propagating surface plasmons," *Opt. Lett.*, vol. 34, no. 3, pp. 244–246, 2009.
- [36] Y. Montelongo, J. O. Tenorio-Pearl, W. I. Milne, and T. D. Wilkinson, "Polarization switchable diffraction based on subwavelength plasmonic nanoantennas," *Nano Lett.*, vol. 14, no. 1, pp. 294–298, 2014.
- [37] X. M. Goh, Y. Zheng, S. J. Tan, L. Zhang, K. Kumar, C.-W. Qiu, and J. K. W. Yang, "Three-dimensional plasmonic stereoscopic prints in full colour," *Nat. Commun.*, vol. 5, p. 5361, 2014.

- [38] C. Zhang, X. Huang, H. Liu, S. J. Chua, and C. A. Ross, "Large-area zinc oxide nanorod arrays templated by nanoimprint lithography: control of morphologies and optical properties," *Nanotechnology*, vol. 27, no. 48, p. 485604, 2016.
- [39] E. L. Warren, E. A. Makoutz, K. A. W. Horowitz, A. Dameron, A. G. Norman, P. Stradins, J. D. Zimmerman, and A. C. Tamboli, "Selective area growth of GaAs on Si patterned using nanoimprint lithography," *Proc. 43rd IEEE Photovoltaics Spec. Conf.*, pp. 1–4, 2016.
- [40] D. Gerard, S. K. Gray, D. Gérard, and S. K. Gray, "Aluminium plasmonics," *J. Phys. D. Appl. Phys.*, vol. 48, no. 18, p. 184001, 2015.
- [41] T. Gong and J. N. Munday, "Aluminum-based hot carrier plasmonics," *Appl. Phys. Lett.*, vol. 110, no. 2, pp. 1–6, 2017.
- [42] C. Langhammer, M. Schwind, B. Kasemo, and I. Zoric, "Localized surface plasmon resonances in aluminum nanodisks," *Nano Lett.*, vol. 8, no. 5, pp. 1461–1471, 2008.
- [43] R. B. Waterhouse, "The formation, structure, and wear properties of certain non-metallic coatings of metals," *Wear*, vol. 8, no. 6, pp. 421–447, 1965.
- [44] G. D. Sulka and K. G. Parkoła, "Anodising potential influence on well-ordered nanostructures formed by anodisation of aluminium in sulphuric acid," *Thin Solid Films*, vol. 515, no. 1, pp. 338–345, 2006.
- [45] M. J. McClain, A. E. Schlather, E. Ringe, N. S. King, L. Liu, A. Manjavacas, M. W. Knight, I. Kumar, K. H. Whitmire, H. O. Everitt, P. Nordlander, and N. J. Halas, "Aluminum Nanocrystals," *Nano Lett.*, vol. 15, no. 4, pp. 2751–2755, 2015.
- [46] M. W. Knight, N. S. King, L. Liu, H. O. Everitt, P. Nordlander, and N. J. Halas, "Aluminum for plasmonics," *ACS Nano*, vol. 8, no. 1, pp. 834–840, 2014.
- [47] E. Eizner, O. Avayu, R. Ditcovski, and T. Ellenbogen, "Aluminum

nanoantenna complexes for strong coupling between excitons and localized surface plasmons," *Nano Lett.*, vol. 15, no. 9, pp. 6215–6221, 2015.

- [48] G. H. Chan, J. Zhao, G. C. Schatz, and R. P. Van Duyne, "Localized surface plasmon resonance spectroscopy of triangular aluminum nanoparticles," *J. Phys. Chem. C*, vol. 112, no. 36, pp. 13958–13963, 2008.
- [49] J. Martin, M. Kociak, Z. Mahfoud, J. Proust, D. Gérard, and J. Plain, "High-resolution imaging and spectroscopy of multipolar plasmonic resonances in aluminum nanoantennas," *Nano Lett.*, vol. 14, no. 10, pp. 5517–5523, 2014.
- [50] M. W. Knight, L. Liu, Y. Wang, L. Brown, S. Mukherjee, N. S. King, H. O. Everitt, P. Nordlander, and N. J. Halas, "Aluminum plasmonic nanoantennas," *Nano Lett.*, vol. 12, no. 11, pp. 6000–6004, 2012.
- [51] V. R. Shrestha, S. S. Lee, E. S. Kim, and D. Y. Choi, "Aluminum plasmonics based highly transmissive polarization-independent subtractive color filters exploiting a nanopatch array," *Nano Lett.*, vol. 14, no. 11, pp. 6672–6678, 2014.
- [52] F. Cheng, X. Yang, D. Rosenmann, L. Stan, D. Czaplewski, and J. Gao, "Enhanced structural color generation in aluminum metamaterials coated with a thin polymer layer," *Opt. Express*, vol. 23, no. 19, p. 25329, 2015.
- [53] Y. W. Huang, W. T. Chen, W. Y. Tsai, P. C. Wu, C. M. Wang, G. Sun, and D. P. Tsai, "Aluminum plasmonic multicolor meta-hologram," *Nano Lett.*, vol. 15, no. 5, pp. 3122–3127, 2015.
- [54] T. Ellenbogen, K. Seo, and K. B. Crozier, "Chromatic plasmonic polarizers for active visible color filtering and polarimetry," *Nano Lett.*, vol. 12, no. 2, pp. 1026–1031, 2012.
- [55] Z. Xu, L. Y. M. Tobing, Y. Xie, J. Tong, P. Ni, S. Qiu, T. Yu, and D. H. Zhang, "Aluminum based structures for manipulating short visible wavelength in-plane surface plasmon polariton propagation," *Opt. Express*, vol. 23, no. 17, p. 22883, 2015.

- [56] E. Højlund-Nielsen, X. Zhu, M. S. Carstensen, M. K. Sørensen, C. Vannahme, N. Asger Mortensen, and A. Kristensen, "Polarization-dependent aluminum metasurface operating at 450 nm," *Opt. Express*, vol. 23, no. 22, p. 28829, 2015.
- [57] N. S. King, L. Liu, X. Yang, B. Cerjan, H. O. Everitt, P. Nordlander, and N. J. Halas, "Fano resonant aluminum nanoclusters for plasmonic colorimetric sensing," *ACS Nano*, vol. 9, no. 11, pp. 10628–10636, 2015.
- [58] J. S. Clausen, E. Højlund-Nielsen, A. B. Christiansen, S. Yazdi, M. Grajower, H. Taha, U. Levy, A. Kristensen, and N. A. Mortensen, "Plasmonic metasurfaces for coloration of plastic consumer products," *Nano Lett.*, vol. 14, no. 8, pp. 4499–4504, Jul. 2014.
- [59] L. Duempelmann, D. Casari, A. Luu-Dinh, B. Gallinet, and L. Novotny, "Color rendering plasmonic aluminum substrates with angular symmetry breaking," *ACS Nano*, vol. 9, no. 12, pp. 12383–12391, 2015.
- [60] G. W. Burr, M. J. Breitwisch, M. Franceschini, D. Garetto, K. Gopalakrishnan, B. Jackson, B. Kurdi, C. Lam, L. A. Lastras, A. Padilla, B. Rajendran, S. Raoux, and R. S. Shenoy, "Phase change memory technology," vol. 28, no. 2, pp. 223–262, 2010.
- [61] N. Raeis-Hosseini and J. Rho, "Metasurfaces based on phase-change material as a reconfigurable platform for multifunctional devices," *Materials (Basel)*, vol. 10, no. 9, 2017.
- [62] Y. C. Her, H. Chen, and Y. S. Hsu, "Effects of Ag and In addition on the optical properties and crystallization kinetics of eutectic $\text{Sb}_{70}\text{Te}_{30}$ phase-change recording film," *J. Appl. Phys.*, vol. 93, no. 12, pp. 10097–10103, 2003.
- [63] Y. Ikuma, Y. Shoji, M. Kuwahara, X. Wang, K. Kintaka, H. Kawashima, D. Tanaka, and H. Tsuda, "Reversible Switching of an Optical Gate Using Phase-Change Material and Si Waveguide," in *Integrated Photonics Research, Silicon and Nanophotonics and Photonics in Switching*, 2010, p. IWA6.
- [64] M. Gurvitch, S. Luryi, A. Polyakov, A. Shabalov, M. Dudley, G. Wang, S. Ge,

and V. Yakovlev, "VO₂ films with strong semiconductor to metal phase transition prepared by the precursor oxidation process," *J. Appl. Phys.*, vol. 102, no. 3, 2007.

- [65] X. Chen, Q. Lv, and X. Yi, "Smart window coating based on nanostructured VO₂ thin film," *Optik (Stuttg.)*, vol. 123, no. 13, pp. 1187–1189, 2012.
- [66] J. Orava, A. L. Greer, B. Gholipour, D. W. Hewak, and C. E. Smith, "Characterization of supercooled liquid Ge₂Sb₂Te₅ and its crystallization by ultrafast-heating calorimetry," *Nat. Mater.*, vol. 11, no. 4, pp. 279–283, 2012.
- [67] L. Perniola, V. Sousa, A. Fantini, E. Arbaoui, A. Bastard, M. Armand, A. Fargeix, C. Jahan, J. F. Nodin, A. Persico, D. Blachier, A. Toffoli, S. Loubriat, E. Gourvest, G. Betti Beneventi, H. Feldis, S. Maitrejean, S. Lhostis, A. Roule, O. Cueto, G. Reibold, L. Poupinet, T. Billon, B. De Salvo, D. Bensahel, P. Mazoyer, R. Annunziata, P. Zuliani, and F. Boulanger, "Electrical behavior of phase-change memory cells based on GeTe," *IEEE Electron Device Lett.*, vol. 31, no. 5, pp. 488–490, 2010.
- [68] T. Matsunaga, J. Akola, S. Kohara, T. Honma, K. Kobayashi, E. Ikenaga, R. O. Jones, N. Yamada, M. Takata, and R. Kojima, "From local structure to nanosecond recrystallization dynamics in AgInSbTe phase-change materials," *Nat. Mater.*, vol. 10, no. 2, pp. 129–134, 2011.
- [69] Y.-J. Huang, T.-C. Chung, C.-H. Wang, and T.-E. Hsieh, "Phase transition behaviors of AgInSbTe-SiO₂ nanocomposite thin films for phase-change memory applications," *MRS Proc.*, vol. 1251, no. 7, Jan. 2010.
- [70] X. Jiao, J. Wei, F. Gan, and M. Xiao, "Temperature dependence of thermal properties of Ag₈In₁₄Sb₅₅Te₂₃ phase-change memory materials," *Appl. Phys. A*, vol. 94, no. 3, pp. 627–631, 2009.
- [71] A. Dun, "Laser direct writing pattern structures on AgInSbTe phase change thin film," vol. 9, no. 8, pp. 8–11, 2011.
- [72] P. Hosseini, C. D. Wright, and H. Bhaskaran, "An optoelectronic framework

- enabled by low-dimensional phase-change films," *Nature*, vol. 511, no. 7508, pp. 206–211, 2014.
- [73] C. Ríos, P. Hosseini, R. A. Taylor, and H. Bhaskaran, "Color depth modulation and resolution in phase-change material nanodisplays," *Adv. Mater.*, pp. 4720–4726, 2016.
- [74] Y. Lu, S. Song, Y. Gong, Z. Song, F. Rao, L. Wu, B. Liu, and D. Yao, "Ga-Sb-Se material for low-power phase change memory," *Appl. Phys. Lett.*, vol. 99, no. 24, pp. 1–4, 2011.
- [75] C. N. Afonso, J. Solis, F. Catalina, and C. Kalpouzos, "Ultrafast reversible phase change in GeSb films for erasable optical storage," *Appl. Phys. Lett.*, vol. 60, no. 25, pp. 3123–3125, 1992.
- [76] B. Lee, G. W. Burr, R. M. Shelby, S. Raoux, C. T. Rettner, S. N. Bogle, K. Darmawikarta, S. G. Bishop, and J. R. Abelson, "Observation of the role of subcritical nuclei in crystallization of a glassy solid," *Science (80-.)*, vol. 326, no. 5955, pp. 980–984, 2009.
- [77] S. Sundar and J. Chakravarty, "Antimony toxicity," *Int. J. Environ. Res. Public Health*, vol. 7, no. 12, pp. 4267–4277, 2010.
- [78] B. G. Chae, H. T. Kim, D. H. Youn, and K. Y. Kang, "Abrupt metal-insulator transition observed in VO₂ thin films induced by a switching voltage pulse," *Phys. B Condens. Matter*, vol. 369, no. 1–4, pp. 76–80, 2005.
- [79] Y. Zhou, X. Chen, C. Ko, Z. Yang, C. Mouli, and S. Ramanathan, "Voltage-triggered ultrafast phase transition in vanadium dioxide switches," *IEEE Electron Device Lett.*, vol. 34, no. 2, pp. 220–222, 2013.
- [80] A. a. Stabile, S. K. Singh, T.-L. Wu, L. Whittaker, S. Banerjee, and G. Sambandamurthy, "Separating electric field and thermal effects across the metal-insulator transition in vanadium oxide nanobeams," *Appl. Phys. Lett.*, vol. 107, no. 1, p. 013503, 2015.

- [81] G. Stefanovich, A. Pergament, and D. Stefanovich, "Electrical switching and Mott transition in VO₂," *J. Phys. Condens. Matter*, vol. 12, no. 41, pp. 8837–8845, 2000.
- [82] B. V Venkataraman and S. Sudha, "Vanadium toxicity," *Asian J. Exp. Sci*, vol. 19, no. 2, pp. 127–134, 2005.
- [83] A. Crunteanu, M. Fabert, J. Givernaud, V. Kermene, A. Desfarges-Berthelemot, J. Orlianges, C. Champeaux, and A. Catherinot, "Vis-IR optical switching/modulation based on the electrically-activated phase transition of VO₂ thin films," in *Conference on Lasers and Electro-Optics 2010*, p. JWA88.
- [84] R. A. Soref, "Phase-change materials for electro-optical switching in the near and mid-infrared," in *Advanced Photonics 2015*, p. IW1A.3.
- [85] S. D. Ha, Y. Zhou, C. J. Fisher, S. Ramanathan, and J. P. Treadway, "Electrical switching dynamics and broadband microwave characteristics of VO₂ radio frequency devices," *J. Appl. Phys.*, vol. 113, no. 18, p. 184501, 2013.
- [86] S. Chen, X. Yi, H. Ma, H. Wang, X. Tao, M. Chen, and C. Ke, "A novel structural VO₂ micro-optical switch," *Opt. Quantum Electron.*, vol. 35, no. 15, pp. 1351–1355, 2003.
- [87] J. Hiltunen, J. Puustinen, A. Sitomaniemi, S. Pearce, M. Charlton, and J. Lappalainen, "Self-modulation of ultra-fast laser pulses with 1550 nm central wavelength in VO₂ thin films," *Appl. Phys. Lett.*, vol. 102, no. 12, p. 121111, Mar. 2013.
- [88] H. Jerominek, "Vanadium oxide films for optical switching and detection," *Opt. Eng.*, vol. 32, no. 9, p. 2092, 1993.
- [89] E. Strelcov, Y. Lilach, and A. Kolmakov, "Gas sensor based on metal-insulator transition in VO₂ nanowire thermistor," *Nano Lett.*, vol. 9, no. 6, pp. 2322–2326, 2009.
- [90] P. U. Jepsen, B. M. Fischer, A. Thoman, H. Helm, J. Y. Suh, R. Lopez, and R.

- F. Haglund, "Metal-insulator phase transition in a VO₂ thin film observed with terahertz spectroscopy," *Phys. Rev. B - Condens. Matter Mater. Phys.*, vol. 74, no. 20, pp. 1–9, 2006.
- [91] T. T. Lv, Y. X. Li, H. F. Ma, Z. Zhu, Z. P. Li, C. Y. Guan, J. H. Shi, H. Zhang, and T. J. Cui, "Hybrid metamaterial switching for manipulating chirality based on VO₂ phase transition," *Sci. Rep.*, vol. 6, no. 1, p. 23186, 2016.
- [92] M. Zhou, J. Bao, M. Tao, R. Zhu, Y. Lin, X. Zhang, and Y. Xie, "Periodic porous thermochromic VO₂(M) films with enhanced visible transmittance," *Chem. Commun.*, vol. 49, no. 54, p. 6021, 2013.
- [93] L. Liu, L. Kang, T. S. Mayer, and D. H. Werner, "Hybrid metamaterials for electrically triggered multifunctional control," *Nat. Commun.*, vol. 7, p. 13236, Oct. 2016.
- [94] K. Appavoo and R. F. Haglund, "Detecting nanoscale size dependence in VO₂ phase transition using a split-ring resonator metamaterial," *Nano Lett.*, vol. 11, no. 3, pp. 1025–1031, 2011.
- [95] M. S. Weimer, I. S. Kim, P. Guo, R. D. Schaller, A. B. F. Martinson, and A. S. Hock, "Oxidation state discrimination in the atomic layer deposition of vanadium oxides," *Chem. Mater.*, vol. 29, no. 15, pp. 6238–6244, 2017.
- [96] M. A. Kats, D. Sharma, J. Lin, P. Genevet, R. Blanchard, Z. Yang, M. M. Qazilbash, D. N. Basov, S. Ramanathan, and F. Capasso, "Ultra-thin perfect absorber employing a tunable phase change material," *Appl. Phys. Lett.*, vol. 101, no. 22, 2012.
- [97] G. Xu, P. Jin, M. Tazawa, and K. Yoshimura, "Tailoring of luminous transmittance upon switching for thermochromic VO₂ films by thickness control," *Japanese J. Appl. Physics, Part 1 Regul. Pap. Short Notes Rev. Pap.*, vol. 43, no. 1, pp. 186–187, 2004.
- [98] U. Kreibig and M. Volmerr, *Optical Properties of Metal Clusters*, Vol. 25., vol. 25, no. 25. Springer-Verlag, 1995.

- [99] K. L. Kelly, E. Coronado, L. L. Zhao, and G. C. Schatz, "The optical properties of metal nanoparticles: The influence of size, shape, and dielectric environment," *J. Phys. Chem. B*, vol. 107, no. 3, pp. 668–677, 2003.
- [100] H. Huang, L. Zhang, Y. Wang, X. Han, Y. Wu, Z. Zhang, and F. Gan, "Locally formation of Ag nanoparticles in chalcogenide phase change thin films induced by nanosecond laser pulses," *Mater. Chem. Phys.*, vol. 135, no. 2–3, pp. 467–473, 2012.
- [101] T. Hira, T. Homma, and T. Saiki, "Giant surface plasmon resonance switching of gold nanoparticles based on ultrafast phase change of GeSbTe," *E*Pcos*, vol. 2, no. September 2011, pp. 1–4, 2011.
- [102] T. Hira, T. Homma, T. Uchiyama, K. Kuwamura, and T. Saiki, "Switching of localized surface plasmon resonance of gold nanoparticles on a GeSbTe film mediated by nanoscale phase change and modification of surface morphology," *Appl. Phys. Lett.*, vol. 103, no. 24, p. 241101, Dec. 2013.
- [103] F.-Z. Shu, F.-F. Yu, R.-W. Peng, Y.-Y. Zhu, B. Xiong, R.-H. Fan, Z.-H. Wang, Y. Liu, and M. Wang, "Dynamic plasmonic color generation based on phase transition of vanadium dioxide," *Adv. Opt. Mater.*, vol. 7, p. 1700939, 2018.
- [104] M. Yi, C. Lu, Y. Gong, Z. Qi, and Y. Cui, "Dual-functional sensor based on switchable plasmonic structure of VO₂ nano-crystal films and Ag nanoparticles," *Opt. Express*, vol. 22, no. 24, p. 29627, 2014.
- [105] G. Xu, Y. Chen, M. Tazawa, and P. Jin, "Surface plasmon resonance of silver nanoparticles on vanadium dioxide," *J. Phys. Chem. B*, vol. 110, no. 5, pp. 2051–2056, 2006.
- [106] G. Xu, C.-M. Huang, P. Jin, M. Tazawa, and D.-M. Chen, "Nano-Ag on vanadium dioxide. I. Localized spectrum tailoring," *J. Appl. Phys.*, vol. 104, no. 5, p. 053101, Sep. 2008.
- [107] G. Xu, C.-M. Huang, M. Tazawa, P. Jin, and D.-M. Chen, "Nano-Ag on vanadium dioxide. II. Thermal tuning of surface plasmon resonance," *J. Appl.*

Phys., vol. 104, no. 5, p. 053102, Sep. 2008.

- [108] M. J. Dicken, K. Aydin, I. M. Pryce, L. A. Sweatlock, E. M. Boyd, S. Walavalkar, J. Ma, and H. A. Atwater, "Frequency tunable near-infrared metamaterials based on VO₂ phase transition," *Opt. Express*, vol. 17, no. 20, p. 18330, 2009.
- [109] D. Y. Lei, K. Appavoo, F. Ligmajer, Y. Sonnefraud, R. F. Haglund, and S. A. Maier, "Optically-triggered nanoscale memory effect in a hybrid plasmonic phase changing nanostructure," *ACS Photonics*, vol. 2, no. 9, pp. 1306–1313, 2015.
- [110] P. Markov, K. Appavoo, R. F. Haglund, and S. M. Weiss, "Hybrid Si-VO₂-Au optical modulator based on near-field plasmonic coupling," *Opt. Express*, vol. 23, no. 5, p. 6878, 2015.
- [111] J. D. Ryckman, V. Diez-Blanco, J. Nag, R. E. Marvel, B. K. Choi, R. F. Haglund, and S. M. Weiss, "Photothermal optical modulation of ultra-compact hybrid Si-VO₂ ring resonators," *Opt. Express*, vol. 20, no. 12, p. 13215, 2012.
- [112] B. A. Kruger, A. Joushaghani, and J. K. S. Poon, "Design of electrically driven hybrid vanadium dioxide (VO₂) plasmonic switches," *Opt. Express*, vol. 20, no. 21, p. 23598, 2012.
- [113] K. Appavoo, D. Y. Lei, Y. Sonnefraud, B. Wang, S. T. Pantelides, S. a Maier, and R. F. Haglund, "Role of defects in the phase transition of VO₂ nanoparticles probed by plasmon resonance spectroscopy," *Nano Lett.*, vol. 12, no. 2, pp. 780–6, 2012.
- [114] J. Beynon, *Introductory University Optics*. 1996.
- [115] O. S. Heavens, *Introduction to optics*, vol. 21, no. 5. 1989.
- [116] S. A. Maier, *Plasmonics Fundamentals and Applications*, vol. 677, no. 1. Springer, 2007.
- [117] F. Wooten, "Optical Properties of Solids," *Am. J. Phys.*, vol. 70, p. 1269, 2002.
- [118] G. R. Fowles, *Introduction to Modern Optics*, 2nd ed. 1975.

- [119] F. Della Sala and S. D'Agostino, *Handbook of molecular plasmonics*. 2013.
- [120] L. Novotny and B. Hecht, *Principles of Nano-Optics*, vol. 19, no. 24. Cambridge: Cambridge University Press, 2006.
- [121] H. S. P. Wong, S. Raoux, S. Kim, J. L. Liang, J. P. Reifenberg, B. Rajendran, M. Asheghi, and K. E. Goodson, "Phase Change Memory," *Proc. Ieee*, vol. 98, no. 12, pp. 2201–2227, 2010.
- [122] N. Yamada, "Origin, secret, and application of the ideal phase-change material GeSbTe," *Phys. Status Solidi Basic Res.*, vol. 249, no. 10, pp. 1837–1842, 2012.
- [123] E. Janod, J. Tranchant, B. Corraze, M. Querré, P. Stoliar, M. Rozenberg, T. Cren, D. Roditchev, V. T. Phuoc, M.-P. Besland, and L. Cario, "Resistive switching in Mott insulators and correlated systems," *Adv. Funct. Mater.*, vol. 25, no. 40, pp. 6287–6305, Oct. 2015.
- [124] T. Yao, O. Yoshio, and N. Yamamoto, "A structural study of the high-temperature phase of VO₂," *J. Solid State Chem.*, vol. 112, no. 1, pp. 196–198, 1994.
- [125] F. Béteille and J. Livage, "Optical Switching in VO₂ Thin Films," *Journal Sol-Gel Sci. Technol.*, vol. 13, no. 1, pp. 915–921, 1998.
- [126] S. S. Kanu and R. Binions, "Thin films for solar control applications," *Proc. R. Soc. A Math. Phys. Eng. Sci.*, vol. 466, no. 2113, pp. 19–44, 2010.
- [127] V. Eyert, "The metal-insulator transitions of VO₂: A band theoretical approach," *Ann. der Phys.*, vol. 11, no. 9, pp. 650–702, 2002.
- [128] K. A. Willets and R. P. Van Duyne, "Localized surface plasmon resonance spectroscopy and sensing," *Annu. Rev. Phys. Chem.*, vol. 58, no. 1, pp. 267–297, 2007.
- [129] A. V. Zayats, I. I. Smolyaninov, and A. A. Maradudin, "Nano-optics of surface plasmon polaritons," *Phys. Rep.*, vol. 408, no. 3–4, pp. 131–314, 2005.

- [130] J. a Sanchez-Gil and a a Maradudin, "Near field and far field scattering of surface plasmon polaritons by one-dimensional surface defects," *Phys. Rev. B*, vol. 60, no. 11, p. 10, 1999.
- [131] W. L. Barnes, T. W. Preist, S. C. Kitson, and J. R. Sambles, "Physical origin of photonic energy gaps in the propagation of surface plasmons on gratings," *Phys. Rev. B*, vol. 54, no. 9, pp. 6227–6244, Sep. 1996.
- [132] S. C. Kitson, W. L. Barnes, and J. R. Sambles, "Full photonic band gap for surface modes in the visible," *Phys. Rev. Lett.*, vol. 77, no. 13, pp. 2670–2673, 1996.
- [133] W. L. Barnes, A. Dereux, and T. W. Ebbesen, "Surface plasmon subwavelength optics," *Nature*, vol. 424, no. 6950, pp. 824–830, 2003.
- [134] A. G. Brolo, R. Gordon, B. Leathem, and K. L. Kavanagh, "Surface plasmon sensor based on the enhanced light transmission through arrays of nanoholes in gold films.," *Langmuir*, vol. 20, no. 17, pp. 4813–4815, 2004.
- [135] J. D. Jackson and J. Schwinger, *Classical Electrodynamics*. 1998.
- [136] U. Kreibig, M. Volmerr, and M. Vollmer, *Optical properties of metal clusters*, Vol. 25., vol. 25, no. 25. Springer-Verlag, 1995.
- [137] C. F. Bohren and Huffman D R, *Absorption and scattering of light by small particles*. 1983.
- [138] S. M. Bilankohi, "Optical scattering and absorption characteristics of silver and silica/silver core/shell nanoparticles," *Orient. J. Chem.*, vol. 31, no. 4, pp. 2259–2263, 2015.
- [139] D. Boyer, "Photothermal imaging of nanometer-sized metal particles among scatterers," *Science (80-.)*, vol. 297, no. 5584, pp. 1160–1163, 2002.
- [140] B. Wu, N. Mathews, and T.-C. Sum, "Surface plasmon resonance," in *Plasmonic organic solar cells*, 2016, p. 30.
- [141] A. Lovera, B. Gallinet, P. Nordlander, and O. J. F. Martin, "Mechanisms of

- Fano resonances in coupled plasmonic systems," *ACS Nano*, vol. 7, no. 5, pp. 4527–4536, 2013.
- [142] A. E. Miroschnichenko, S. Flach, and Y. S. Kivshar, "Fano resonances in nanoscale structures," *Rev. Mod. Phys.*, vol. 82, no. 3, pp. 2257–2298, 2010.
- [143] Y. Shen, V. Rinnerbauer, I. Wang, V. Stelmakh, J. D. Joannopoulos, and M. Soljačić, "Structural colors from Fano resonances," *ACS Photonics*, vol. 2, no. 1, pp. 27–32, 2015.
- [144] A. Cusano, F. Arregui, M. Giordano, and A. Cutolo, *Optochemical Nanosensors*. 2016.
- [145] U. Fano, "Effects of configuration interaction on intensities and phase shifts," *Phys. Rev.*, vol. 124, no. 6, pp. 1866–1878, 1961.
- [146] J. Chen, Z. Li, Z. Fan, and F. Yang, "Finite element beam propagation method for analysis of plasmonic waveguide," *Chinese Opt. Lett.*, vol. 6, no. 8, pp. 572–574, 2008.
- [147] B. Luk'yanchuk, N. I. Zheludev, S. A. Maier, N. J. Halas, P. Nordlander, H. Giessen, and C. T. Chong, "The Fano resonance in plasmonic nanostructures and metamaterials," *Nat. Mater.*, vol. 9, no. 9, pp. 707–715, 2010.
- [148] T. Pakizeh, C. Langhammer, I. Zorić, P. Apell, and M. Käll, "Intrinsic Fano interference of localized plasmons in Pd nanoparticles," *Nano Lett.*, vol. 9, no. 2, pp. 882–886, 2009.
- [149] L. Pedrotti, F. L. Pedrotti, and L. M. S. Pedrotti, *Introduction to Optics*. Pearson, 2006.
- [150] M. R. Gartia, A. Hsiao, A. Pokhriyal, S. Seo, G. Kulsharova, B. T. Cunningham, T. C. Bond, and G. L. Liu, "Colorimetric plasmon resonance imaging using nano *Lycurgus cup* arrays," *Adv. Opt. Mater.*, vol. 1, no. 1, pp. 68–76, 2013.
- [151] J. M. McMahon, J. Henzie, T. W. Odom, G. C. Schatz, and S. K. Gray, "Tailoring the sensing capabilities of nanohole arrays in gold films with

- Rayleigh anomaly-surface plasmon polaritons," *Opt. Express*, vol. 15, no. 26, p. 18119, 2007.
- [152] M. R. Pointer and R. W. G. Hunt, *Measuring Colour*. John Wiley & Sons, 2011.
- [153] R. Choudhury and A. Kumar, *Principles of colour and appearance measurements*. Woodhead, 2014.
- [154] O. Noboru and A. R. Robertson, "CIE standard colorimetric system," in *Colorimetry*, Chichester, UK: John Wiley & Sons, Ltd, 2006, pp. 63–114.
- [155] J. Schanda, "CIE colorimetry," in *Colorimetry*, Hoboken, NJ, USA: John Wiley & Sons, Inc., 2007, pp. 25–78.
- [156] F. L. Pedrotti, L. M. S. Pedrotti, L. M. S. Pedrotti, and Pedrotti, *Introduction to optics (3rd edition)*. Pearson, 2006.
- [157] W. Croswell, *Antenna theory, analysis, and design*, vol. 24, no. 6. IEEE Antennas and Propagation Society Newsletter, 1982.
- [158] J. H. Poynting, "On the transfer of energy in the electromagnetic field," *Philos. Trans. R. Soc. London*, vol. 175, no. 0, pp. 343–361, 1884.
- [159] B. T. Draine and P. J. Flatau, "Discrete-dipole approximation for scattering calculations," *J. Opt. Soc. Am. A*, vol. 11, no. 4, p. 1491, 1994.
- [160] B. T. Draine and P. J. Flatau, "Discrete-dipole approximation for periodic targets: theory and tests," *J. Opt. Soc. Am. A*, vol. 25, no. 11, p. 2693, 2008.
- [161] E. D. Palik, *Handbook of optical constants of solids*. Academic press, 2012.
- [162] R. Hobbs, *Digital video and HD algorithms and interfaces*. Morgan Kaufmann, 2010.
- [163] J. Schanda, *Colorimetry: Understanding the CIE System*. Wiley, 2007.
- [164] R. Tetzlaff, *Cellular neural networks and their applications*. 2002.
- [165] E. Reinhard, E. Khan, A. Akyüz, and G. Johnson, *Color imaging: Fundamentals and applications*. A K Peters/CRC Press, 2008.

- [166] C. Oleari, *Standard colorimetry*. Chichester, UK: John Wiley & Sons, Ltd, 2015.
- [167] A. Ford and A. Roberts, "Colour space conversions," *Westminster Univ. London*, vol. 1998, pp. 1–31, 1998.
- [168] D. A. Kerr, "The CIE XYZ and xyY color spaces," no. 1, pp. 1–16, 2010.
- [169] D. C. Joy, *Helium ion microscopy*. New York, NY: Springer New York, 2013.
- [170] C. Vieu, F. Carcenac, A. Pepin, Y. Chen, M. Mejias, A. Lebib, L. Manin-Ferlazzo, L. Couraud, and H. Launois, "Electron beam lithography - Resolution limits and applications," *Appl. Surf. Sci.*, vol. 164, pp. 111–117, 2000.
- [171] M. T. Postek, A. Vladár, C. Archie, and B. Ming, "Review of current progress in nanometrology with the helium ion microscope," *Meas. Sci. Technol.*, vol. 22, no. 2, 2011.
- [172] B. W. Ward, J. A. Notte, and N. P. Economou, "Helium ion microscope: A new tool for nanoscale microscopy and metrology," *J. Vac. Sci. Technol. B Microelectron. Nanom. Struct.*, vol. 24, no. 6, p. 2871, 2006.
- [173] J. Notte, B. Ward, N. Economou, R. Hill, R. Percival, L. Farkas, and S. McVey, "An introduction to the helium ion microscope," *AIP Conf. Proc.*, vol. 931, no. 2007, pp. 489–496, 2007.
- [174] F. Cheng, J. Gao, L. Stan, D. Rosenmann, D. Czaplewski, and X. Yang, "Aluminum plasmonic metamaterials for structural color printing," *Opt. Express*, vol. 23, no. 11, pp. 14552–60, 2015.
- [175] "Zeiss HIL - ORION NanoFab." [Online]. Available: <https://www.zeiss.com/microscopy/int/products/multiple-ion-beam/orion-nanofab-for-materials.html>.
- [176] D. Winston, B. M. Cord, B. Ming, D. C. Bell, W. F. DiNatale, L. A. Stern, A. E. Vladar, M. T. Postek, M. K. Mondol, J. K. W. Yang, and K. K. Berggren, "Scanning-helium-ion-beam lithography with hydrogen silsesquioxane

- resist," *J. Vac. Sci. Technol. B Microelectron. Nanom. Struct.*, vol. 27, no. 6, p. 2702, 2009.
- [177] D. C. Bell, M. C. Lemme, L. A. Stern, J. R. Williams, and C. M. Marcus, "Precision cutting and patterning of graphene with helium ions," *Nanotechnology*, vol. 20, no. 45, pp. 1–6, 2009.
- [178] A. N. Abbas, G. Liu, B. Liu, L. Zhang, H. Liu, D. Ohlberg, W. Wu, and C. Zhou, "Patterning, characterization, and chemical sensing applications of graphene nanoribbon arrays down to 5 nm using helium ion beam lithography," *ACS Nano*, vol. 8, no. 2, pp. 1538–1546, 2014.
- [179] X. Shi and S. A. Boden, "Scanning helium ion beam lithography," 2016, pp. 563–594.
- [180] "Zeiss SEM - Gemini column." [Online]. Available: <https://www.zeiss.com/microscopy/int/products/scanning-electron-microscopes/geminisem.html>.
- [181] J. H. Kim, M. Seo, and S. Y. Kim, "Lithographically patterned breath figure of photoresponsive small molecules: dual-patterned honeycomb lines from a combination of bottom-up and top-down lithography," *Adv. Mater.*, vol. 21, no. 41, pp. 4130–4133, 2009.
- [182] X. Duan, Y. Huang, Y. Cui, J. Wang, and C. M. Lieber, "Indium phosphide nanowires as building blocks for nanoscale electronic and optoelectronic devices," *Nature*, vol. 409, no. 6816, pp. 66–69, 2001.
- [183] Y. W. Su, C. S. Wu, C. C. Chen, and C. D. Chen, "Fabrication of two-dimensional arrays of CdSe pillars using E-beam lithography and electrochemical deposition," *Adv. Mater.*, vol. 15, no. 1, pp. 49–51, 2003.
- [184] J. I. Goldstein, D. E. Newbury, P. Echlin, D. C. Joy, C. E. Lyman, E. Lifshin, L. Sawyer, and J. R. Michael, "Scanning Electron Microscopy and X-ray Microanalysis," *Scanning Electron Microsc. X-Ray Microanal.*, pp. 21–32, 2003.

- [185] H. Duan, H. Hu, K. Kumar, Z. Shen, and J. K. W. Yang, "Direct and reliable patterning of plasmonic nanostructures with sub 10 nm gaps," *ACS Nano*, vol. 5, no. 9, pp. 7593–7600, 2011.
- [186] H. Duan, H. Hu, H. K. Hui, Z. Shen, and J. K. W. Yang, "Free-standing sub-10 nm nanostencils for the definition of gaps in plasmonic antennas," *Nanotechnology*, vol. 24, no. 18, 2013.
- [187] J. Singh and D. E. Wolfe, "Nanostructured component fabrication by electron beam-physical vapor deposition," *J. Mater. Eng. Perform.*, vol. 14, no. 4, pp. 448–459, 2005.
- [188] D. Inoue, A. Miura, T. Nomura, H. Fujikawa, K. Sato, N. Ikeda, D. Tsuya, Y. Sugimoto, and Y. Koide, "Polarization independent visible color filter comprising an aluminum film with surface-plasmon enhanced transmission through a subwavelength array of holes," *Appl. Phys. Lett.*, vol. 98, no. 9, pp. 1–4, 2011.
- [189] J. Martin and J. Plain, "Fabrication of aluminium nanostructures for plasmonics," *J. Phys. D: Appl. Phys.*, vol. 48, no. 18, p. 184002, 2015.
- [190] B. Zhang, J. Hendrickson, and J. Guo, "Multi-spectral near perfect metamaterial absorbers using spatially multiplexed plasmon resonance metal square structures," *J. Opt. Soc. Am. B*, vol. 30, no. 3, pp. 656–662, 2013.
- [191] W. Kim, B. S. Simpkins, J. P. Long, B. Zhang, J. Hendrickson, and J. Guo, "Localized and nonlocalized plasmon resonance enhanced light absorption in metal-insulator-metal nanostructures," *J. Opt. Soc. Am. B*, vol. 32, no. 8, p. 1686, 2015.
- [192] S. Boujday, M. L. de la Chapelle, J. Srajer, and W. Knoll, "Enhanced vibrational spectroscopies as tools for small molecule biosensing," *Sensors (Switzerland)*, vol. 15, no. 9, pp. 21239–21264, 2015.
- [193] R. Nicolas, G. Lévêque, J. Marae-Djouda, G. Montay, Y. Madi, J. Plain, Z. Herro, M. Kazan, P.-M. Adam, and T. Maurer, "Plasmonic mode interferences

- and Fano resonances in metal-insulator-metal nanostructured interface," *Sci. Rep.*, vol. 5, no. 1, p. 14419, Nov. 2015.
- [194] L. Lin and Y. Zheng, "Optimizing plasmonic nanoantennas via coordinated multiple coupling," *Sci. Rep.*, vol. 5, p. 14788, Oct. 2015.
- [195] F. Zhou, Y. Liu, and W. Cai, "Huge local electric field enhancement in hybrid plasmonic arrays," *Opt. Lett.*, vol. 39, no. 5, pp. 1302–5, 2014.
- [196] B. Zhang, Y. Zhao, Q. Hao, B. Kiraly, I.-C. Khoo, S. Chen, and T. J. Huang, "Polarization-independent dual-band infrared perfect absorber based on a metal-dielectric-metal elliptical nanodisk array," *Opt. Express*, vol. 19, no. 16, p. 15221, 2011.
- [197] A. Joushaghani, "Micro- and nano-scale optoelectronic devices using vanadium dioxide," PhD Thesis, University of Toronto, 2014.
- [198] T. A. König, P. A. Ledin, J. Kerszulis, M. A. Mahmoud, M. A. El-sayed, J. R. Reynolds, and V. V. Tsukruk, "Electrically tunable plasmonic behavior of nanocube-polymer nanomaterials induced by a redox-active electrochromic polymer," *ACS Nano*, vol. 8, no. 6, pp. 6182–6192, 2014.
- [199] Y. Leterrier, L. Médico, F. Demarco, J. A. E. Månson, U. Betz, M. F. Escolà, M. K. Olsson, and F. Atamny, "Mechanical integrity of transparent conductive oxide films for flexible polymer-based displays," *Thin Solid Films*, vol. 460, no. 1–2, pp. 156–166, 2004.
- [200] H. Hosono, H. Ohta, M. Orita, K. Ueda, and M. Hirano, "Frontier of transparent conductive oxide thin films," *Vacuum*, vol. 66, no. 3–4, pp. 419–425, 2002.
- [201] L. Sánchez, A. Rosa, A. Griol, A. Gutierrez, P. Himm, B. Van Bilzen, M. Menghini, J. P. Locquet, and P. Sanchis, "Impact of the external resistance on the switching power consumption in VO₂ nano gap junctions," *Appl. Phys. Lett.*, vol. 111, no. 3, p. 031904, 2017.

- [202] A. Joushaghani, J. Jeong, S. Paradis, D. Alain, J. Stewart Aitchison, and J. K. S. Poon, "Voltage-controlled switching and thermal effects in VO₂ nano-gap junctions," *Appl. Phys. Lett.*, vol. 104, no. 22, 2014.
- [203] J. Sakai, M. Zaghrioui, V. Ta Phuoc, S. Roger, C. Autret-Lambert, and K. Okimura, "Pulsed laser-deposited VO₂ thin films on Pt layers," *J. Appl. Phys.*, vol. 113, no. 12, 2013.
- [204] P. Jin and S. Tanemura, "Formation and thermochromism of VO₂ films deposited by RF magnetron sputtering at low substrate temperature," *Jpn. J. Appl. Phys.*, vol. 33, no. Part 1, No. 3A, pp. 1478–1483, 1994.
- [205] F. C. Case, "Low temperature deposition of VO₂ thin films," *J. Vac. Sci. Technol. A Vacuum, Surfaces, Film.*, vol. 8, no. 3, pp. 1395–1398, May 1990.
- [206] J. Henson, J. Dimaria, and R. Paiella, "Influence of nanoparticle height on plasmonic resonance wavelength and electromagnetic field enhancement in two-dimensional arrays," *J. Appl. Phys.*, vol. 106, no. 9, 2009.